2017

ON THE ROLE OF AERATION, ELASTICITY AND WAVE-STRUCTURE INTERACTION ON HYDRODYNAMIC IMPACT LOADING

Mai, Tri Cao

http://hdl.handle.net/10026.1/9884

RESEARCH WITH PLYMOUTH UNIVERSITY

ON THE ROLE OF AERATION, ELASTICITY AND WAVE-STRUCTURE INTERACTION ON HYDRODYNAMIC IMPACT LOADING

by

MAI CAO TRÍ

A thesis submitted to Plymouth University
in partial fulfilment for the degree of

DOCTOR OF PHILOSOPHY

Marine Science and Engineering Doctoral Training Centre

August 2017

ACKNOWLEDGEMENTS

AUTHOR'S DECLARATION

At no time during the registration for the degree of *Doctor of Philosophy* has the author been registered for any other University award without prior agreement of the Graduate Sub-Committee.

Work submitted for this research degree at the Plymouth University has not formed part of any other degree either at Plymouth University or at another establishment.

Relevant scientific seminars and conferences were regularly attended at which work was often presented. As lead author, several papers have been prepared for publication.

Publications as lead author:

Mai, T., Greaves, D., Raby, A. and Taylor, P.H., 2016. "*Physical Modelling of Wave Scattering Around Fixed FPSOs*". Applied Ocean Research **61**, Pages 115-129, ISSN 0141-1187, http://dx.doi.org/10.1016/j.apor.2016.10.007.

Mai, T., Greaves, D. and Raby, A., 2017. "*Aeration Effects on Offshore Structure Wave Impacts*". Journal of Fluids and Structures. (*Writing up for submission*)

Mai, T., Greaves, D. and Raby, A., 2017. "*Hyroelasticity Effects on Offshore Structure Wave Impacts*". Journal of Fluids and Structures. (*Writing up for submission*)

Publications as co-author:

Ma, Z., Causon, D., Qian, L., Mingham, C., **Mai, T.**, Greaves, D. and Raby, A., 2016. "*Pure and Aerated Water Entry of a Flat Plate*". Physics of Fluids **28**(1): 016104. DOI: http://dx.doi.org/10.1063/1.4940043

Hu, Z.Z., **Mai, T.**, Greaves, D. and Raby, A., 2016. *Investigations of Offshore Breaking Wave Impacts on a Large Offshore Structure*. Journal of Fluids and Structure. (*Accepted for publication*)

Conference proceedings:

Hu, Z.Z., **Mai, T.**, Greaves, D. and Raby, A., 2016. *A Numerical and Experimental Study of a Simplified FPSO in Extreme Free Surface Waves*. Proceedings of the 26th International Ocean and Polar Engineering Conference (ISOPE2016).

Mai, T., Hu, Z. Z., Greaves, D. and Raby, A., 2015. *Investigation of Hydroelasticity: Wave Impact on a Truncated Vertical Wall*. Proceedings of the 25th International

Ocean and Polar Engineering Conference (ISOPE2015), Hawaii, USA. Vol.3, pp 647-654.

Ma, Q.W., Yan., S., **Mai, T.**, Greaves, D. and Raby, A., 2015. *Numerical and Experimental Studies on Nonlinear Interaction between FPSO and 3D Focusing Waves*. Proceedings of the 25th International Ocean and Polar Engineering Conference (ISOPE2015), Hawaii, USA. Vol.3, pp 655-662.

Ma, Z.H., Qian. L., Causon, D.M., Mingham, C.G., **Mai, T.**, Greaves, D. and Raby, A., 2015. *The role of fluid compressibility in predicting slamming loads during water entry of flat plates*. Proceedings of the 25th International Ocean and Polar Engineering Conference (ISOPE2015), Hawaii, USA. Vol.3, pp 642-646.

Hu, Z.Z., **Mai, T.**, Greaves, D. and Raby, A., 2015. *Hydroelastic Investigation of Extreme Wave Impact on a Truncated Vertical Wall*. Proceedings of the 7th International Conference on Hydroelasticity in Marine Technology, Split, Croatia, September 16th - 19th.

Mai, T., Greaves, D. and Raby, A., 2014. *Aeration effects on impact: Drop test of a flat plate*. Proceedings of the 24th International Ocean and Polar Engineering Conference (ISOPE2014), Busan, Korea. Vol 3, pp. 703-709.

Word count for the main body of this thesis: 35,898

Signed ……………………………………………………

Date …………………………………………………

ABSTRACT

On the role of aeration, elasticity and wave-structure interaction on hydrodynamic impact loading

Mai Cao Trí

Local and global loadings, which may cause the local damage and/or global failure and collapse of offshore structures and ships, are experimentally investigated in this study. The big research question is how the aeration of water and the elasticity of the structural section affect loading during severe environmental conditions. A further question is how the scattered waves from ships and offshore structures, the mooring line force and the structural response, which are known to affect local load and contribute to global load, will be affected by wave-structure interaction of a ship or offshore structure under non-breaking wave conditions. Three different experiments were undertaken in this study to try to answer these questions: (i) slamming impacts of a square flat rigid/elastic plate, which represents a plate section of the bottom or bow of ship structure, onto pure and aerated water surface with zero degree deadrise angle; (ii) wave impacts on a truncated vertical rigid/elastic wall in pure and aerated water, where the wall represents a plate section of a hull; and (iii) wave-structure interactions of different FPSO[1]-shaped models, where the models were fixed or taut moored. The experiments were carried out at Plymouth University's COAST Laboratory.

Spatial impact pressure distributions on the square plate have been characterised under different impact velocities. It was found that the impact pressures and force in pure water were proportional to the square of impact velocity. There was a significant reduction in both the maximum impact pressure and force for slamming in aerated water compared to that in pure water. An exponential relationship of the maximum force and the void fraction is proposed and its coefficients are found from drop test in this study. There was also a significant reduction in the first phase of the pressure and force impulse for slamming into aerated water compared with pure water. On the truncated wall, aeration also significantly reduced peak wave loads (both pressure and force) but impulses were not reduced by very much.

---

[1] FPSO: Floating Production Storage and Off-loading

For the case considered here, elasticity of the impact plate has a significant effect on the impact loads, though only at high impact velocities; here the impact loads were considerably reduced with increasing elasticity. Wave loading on the truncated wall was found to reduce with increasing elasticity of the wall for all investigated breaking wave types: high aeration, flip-through and slightly breaking wave impacts. In particular, impact pressure decreases with increasing elasticity of the wall under flip-through wave impact. As elasticity increases, the impulse of the first positive phase of pressure and force decreases significantly. This significant effect of hydroelasticity is also found for the total force impulse on the vertical wall under wave impacts.

Scattered waves were generated from the interaction of focused wave groups with an FPSO model. The results show that close to the bow of the FPSO model, the highest amplitude scattered waves are observed with the most compact model, and the third- and fourth-harmonics are significantly larger than the incident bound harmonic components. At the locations close to the stern, the linear harmonic was found to increase as the model length was decreased, although the nonlinear harmonics were similar for all three tested lengths, and the second- and third-harmonics were strongest with the medium length model. The nonlinear scattered waves increased with increasing wave steepness and a second pulse was evident in the higher-order scattered wave fields for the fixed and free floating models. In addition, the higher harmonics of the mooring line force, and the heave and pitch motions all increased with increasing wave steepness. Incident wave angles of 0 (head-on), 10 and 20 degrees were experimentally investigated in this study. As the incident wave angle between the waves and the long axis of the vessel was increased from 0 to 20 degrees, the third- and fourth-harmonic scattered waves reduced on the upstream side. These third- and fourth-harmonic diffracted waves are important in assessing wave run-up and loading for offshore structure design and ringing-type structural response in fixed and taut moored structures. The second-, third- and fourth-harmonics of the mooring line force, and the heave and pitch motions decreased as the incident wave angle increased from 0 to 20 degrees.

CONTENTS

LIST OF FIGURES

xviii

LIST OF TABLES

CHAPTER 1:   INTRODUCTION

1.1   General introduction

Offshore structures and platforms for oil and gas exploration have seen significant development in past decades (Frieze, 2011). Furthermore, development of renewable energy (wind, wave and tidal energy, etc.) has seen growth as the world's fastest-growing energy source, increasing by 2.6 %/year (U.S. Energy Information Administration, 2016). In addition to the onshore wind farms, the growing trend in the development of renewable energy has been towards offshore wind farms and wave energy converters (U.S. Energy Information Administration). Similarly, the development trend of the oil and gas industry has been to move further offshore (Frieze, 2011; Lefebvre and Collu, 2012).

In design, construction and operation of offshore structures and platforms, determination of wave-structure interaction is crucial. In the design process, the aim is to optimise the design of the structure to minimise wave induced loads on the structure; hence the cost of the initial investment will be minimised. During construction and operation, it is important to determine the actual wave loads which are needed for safety assessments and to increase operational safety. The extreme and fatigue loads need to be assessed during service lifetime of the structures and platforms to have a better forecast on structural durability and to make a better maintenance plan.

Stationkeeping of floating structures in deep and shallow water, ringing which is a transient response of structures in survival wave conditions, green water on deck of Floating Production Storage and Offloading (FPSO) vessels, wetdeck slamming and steep wave impact on offshore platforms have been found among others as important offshore engineering problems with possible hydroelastic effects (Faltinsen, 2014).

The motion response of a floating structure will often have low frequency, wave frequency and high frequency motion components. Hydrodynamic effects of importance for a single FPSO have been introduced in the recommended practice by Det Norske Veritas (DNV-RP-F205, 2010). These include the wave frequency loads, low frequency loads (due to slow-drift motions i.e. slowly varying wave and wind loads give rise to low frequency resonant horizontal motions which are dependent only on the first order quantities), loads in moonpool, slamming loads and green water loads, all of which must be taken into account in the analysis and design. The high frequency loads (ringing) are also important for tension leg platform (TLP) design.

Offshore floating models are usually large structures and therefore inertia dominated ($KC < 2$ and $D/L > 0.2$, where $KC = u_0T/D$ is the Keulegan-Carpenter number, u_0 is the maximum horizontal water particle velocity, T is the wave period, D is the diameter of the structure and L is the wave length). This implies that radiation/diffraction from the structure need to be investigated/ predicted as well.

1.2   Rationale of this research project

Hydrodynamics of a fluid medium is quite well understood, but the violent wave-structure impact in a water-air mixture still remains as a principle challenge for offshore engineering. It is essential to improve understanding of that problem in order to safely design offshore structures to prevent and minimise the loss of life and cost in offshore industry.

Nowadays, sea level rise and the occurrence of more frequent and severe storms around the UK and North-Western Europe as a result of climate change are well known (Gulev & Grigorieva, 2004; Grabemann & Weisse, 2008; Young et al., 2011; Bitner-Gregersen et al., 2013). This has significant effects on the safety of existing offshore structures and their ability to continue to operate safely under new conditions and for the safety assessment of the new offshore structures in deeper water planned for the UK. There are

some structures in UK waters that are up to 40 year old and need to be re-assessed to ensure that they will survive under more severe environment conditions caused by climate change, and to confirm that their life can be extended into the next 25 years. The reliability of hydrodynamic impact load predictions is critical for upgrade of existing structures and design of new structures. Owing to the hydrodynamic impact loads, sea walls, containers of sloshing liquids (e.g. Liquified Natural Gas carriers - LNG), FPSO vessels and offshore structures can be damaged (for example, wave impact induced the damage of the Foinaven and Schiehallion FPSOs, see Buchner et al., 2004).

There is still considerable uncertainty in predictions of extreme wave loading on offshore structures (Bitner-Gregersen et al., 2013). The Morison equation is applied to predict wave loading on a slender structure and the linear and second order diffraction theory works well for the large volume structures. In addition, the ringing load, which is nonlinear structural behaviour at triple linear wave frequency, of the offshore structure columns was found in the 1990s (Chaplin et al., 1997). For design process of offshore wind turbines in deeper water, this ringing load will be as a design problem.

The peak pressure is known to be unreliably predicted and unrepeatable in extreme conditions although surface elevations are well predicted and with carefully controlled laboratory experiments (Buchner et al., 2004; Voogt and Buchner, 2004; Xu et al., 2008a&b). It was found that the aeration and entrapment of air pockets play an important factor in pressure time histories under impact loading (Bullock et al., 2001 & 2007).

There are still a number of open questions to the fundamental physics of hydrodynamic impact loading and the available occurrence of the extremely pressure impulsive found from previous projects (Bullock et al, 2007; Lafeber et al., 2012; Guilcher et al., 2014). In particular, uncertainty exists in the understanding of the influence of: the presence of air in the water (both entrapped air pockets and entrained air bubbles) leading to

variability of wave impact pressures measured in experiments; flexibility of the structure leading to hydroelastic response; three dimensionality of the incident wave.

1.3 Research aim and objectives

This PhD research was part of the FROTH project, which was a close collaboration between five universities (Plymouth University, Manchester Metropolitan University, City University, Oxford University and University of Bath). The aim of the FROTH project was to investigate the physics of hydrodynamic impact loading and wave-structure interaction of offshore structures and ships through a carefully integrated programme of numerical modelling and physical experiments.

Within the FROTH Project, the specific aim of this PhD research was to:

- improve understanding of the physical effects of aeration, hydroelasticity and wave-structure interaction on the local and global loadings of offshore structures and ships through a series of laboratory experiments.

The overall aim is broken down into three underpinning objectives:

i. Investigate the aeration and hydroelasticity effects on slamming impact by means of free dropping a flat plate (rigid/elastic), from various heights, into pure and aerated water surfaces with zero degree deadrise angle, to:

   o Understand the distribution of impact pressures on the plate under different impact velocities and evaluate empirical factors of the relationship between slamming impact loading and impact velocity.

   o Assess the effect of aeration of air-water medium on the slamming impact loadings and then evaluate the empirical factors of the relationship between the impact loading and the aeration level.

   o Assess the effect of elasticity of the impact plate on the slamming impact loadings.

ii. Investigate the aeration and hydroelasticity effects on wave impact on a truncated vertical wall (rigid/elastic) in pure and aerated water media. Focused wave groups based on NewWave underlying JONSWAP spectrum were applied to generate different wave impact types, i.e. early broken, broken, high aeration (large air pocket), flip-through and slightly breaking waves, by changing the focused distance of the wave packet, to:

- o Identify characteristics of the tested wave impact types.

- o Assess the effect of aerated water on wave impact loadings on the vertical rigid wall.

- o Assess the effect of elasticity of the vertical wall on wave impact loadings.

iii. Investigate the wave-structure interactions of fixed or free floating FPSO-shaped bodies, in which various conditions were tested, including different model lengths, different wave steepness and different wave directions. Focused wave groups based on NewWave with underlying JONSWAP spectrum were applied in the experiment, to:

- o Assess the effect of structural geometry on scattered waves, which may induce ringing-type load on offshore structures and ships.

- o Improve the understanding of the effects of wave steepness and wave direction on scattered wave fields, mooring line force and structural motion.

1.4 General methodology

The main methodologies of the research are the design of a variety of physical models, the subsequent laboratory experiments and the analysis of resulting data. Physical models were conducted and implemented to investigate effects of aeration and hydroelasticity on slamming onto water surface as well as on wave impact on a

truncated vertical wall, which is used to represent a section of the hull of an FPSO. Physical modelling was also carried out to investigate wave-structure interactions of simplified FPSOs and wave scattering around different lengths of FPSO models. A set of non-breaking wave conditions, which correspond to the 100 year extreme significant wave height at the Cleeton platform in the Southern North Sea (Williams, 2008), were employed in these experiments by scaling. The experiments were conducted in a wave flume as well as in the Ocean Basin in the COAST laboratory at Plymouth University.

1.5   How to read this dissertation

The thesis is presented in seven chapters. Following the general introduction to wave loading on offshore structures and the objectives of the research presented here, a literature review on slamming, wave impact and wave-structure interaction is given in Chapter 2. Chapter 3 presents the experimental methodology applied in order to meet the research objectives, and a detailed description of the three test series is also given in this chapter. Results and discussions of aeration and hydroelasticity effects on slamming are given in Chapter 4. In Chapter 5, the effects of hydoelasticity and aeration on various wave impact types found from this research are presented. Experimental results of wave-structure interactions of FPSO-shaped models are given and discussed in Chapter 6. Finally, Chapter 7 gives overall conclusions and recommendations.

CHAPTER 2:   LITERATURE REVIEW

2.1   Slamming into water surface

Hydrodynamic impact problems are frequently encountered in natural hazards (Kay, 2014; Rodgers & Bryson, 2014), marine engineering (Faltinsen, 1993 & 2000; Kapsenberg, 2011) and water sports (Rubin, 1999). Slamming of high speed marine vessels on the water surface and wave impacts on ship bows both create vitally important environmental loads that must to be taken into account for practical design of those structures. In addition, the ditching of an aircraft on the water surface is another problem of water slamming on a body which can lead to damage to the aircraft and potential loss of life. Hydrodynamic impact and slamming is a complicated process in which compressibility of the water, the presence of an air cushion and air bubbles, and hydroelasticity may all be relevant (Faltinsen et al., 2004). Water slamming has been investigated over several decades using both theoretical and physical models. Von Karman (1929) developed the first theory to estimate pure water impact for a wedge and then for a horizontal plate. In 1932, Wagner (1932) developed the theory for a wedge with very small dead-rise angle which is small enough not to trap air under impact. There are a number of experimental studies undertaken to investigate water slamming by dropping a wedge (Chuang, 1966a; Zhu, 1995; Zhao et al., 1997), a horizontal body (Chuang, 1966b; Verhagen, 1967; Zhu, 1995; Faltinsen, 2000; Bullock et al., 2001; Kwon et al., 2003; Ermanyuk et al., 2005; Oh et al., 2009), a horizontal circular cylinder (Lange and Rung, 2011; Van Nuffel et al., 2014) or a pyramid onto a still pure water surface (Alaoui et al., 2012 & 2015). Furthermore, Smith et al. (1998) conducted a series of drop tests of a horizontal plate onto waves of different steepness.

If the compressibility of the water can be taken into account, then the peak pressure at the instant of the impact of a horizontal plate onto still water is equal to the acoustic pressure (von Karman, 1929) $p_a = \rho c v$, where ρ is the fluid density, c is the speed of sound in the fluid and v is the plate velocity just before the impact (also known as the impact velocity). In practice, the maximum acoustic pressure never occurs because an air layer is trapped between the flat plate and the water surface and this air layer acts as a cushion layer (Chuang, 1966a&b; Lewison and Maclean, 1968). In the experiment of Chuang (1966a&b) the maximum impact pressure is found to be proportional to $\rho c_a v$, where c_a is the speed of sound in air rather than in water. In the theory developed by Chuang (1966a&b), the compressibility of both the air and water was considered in a general solution of the problem. Since the maximum impact velocity was limited to 1.92 m/s, the finding in Chuang's tests may not necessarily apply to a higher impact velocity. The compressibility of the water and the elasticity of the body are neglected by Verhagen (1967). In his explanation, compressibility effects are neglected because the events of interest are expected to happen in a timescale of the order required by an acoustic wave in air to travel over a distance l, i.e., $\Delta t = l/c_a$, which is large compared with l/c (l is the half width of the flat plate). His experiments indicated that this assumption is fully justified. However, his experiments are limited to small values of the mass of the body compared with the added mass. From his experiment, he found that the maximum impact pressure was proportional to the square of the impact velocity for small value of $M/\rho l^2$, but this relationship will be linear if $M/\rho l^2 \gg 1$ (M is the mass per unit length of the impact plate). Zhu (1995) found that the slamming pressure coefficient, $C_p = p_{max}/(0.5\rho v)$, increases with the weight of the model due to the added mass of water induced, where p_{max} is the peak slamming pressure. The coefficient of weight has been defined as $C_m = m/A$, where m is the weight of the model and A is the flat impact area. It was found that there was a considerable amount of scatter in the peak

slamming pressures, but the pressure impulses of the first positive phase (the time integration of pressure from initial impact through to the first maximum and back to zero) were more or less the same (Zhu, 1995).

In open oceans and seas, bubbles are known to be created in the upper ocean through different mechanisms (Deane and Stokes, 1999), such as: (i) the action of breaking gravity and capillary waves (Longuet-Higgins, 1993); (ii) drop impact on the ocean surface (Franz, 1959; Pumphrey and Elmore, 1990) and (iii) melting snow (Blanchard and Woodcock, 1957). However, most bubbles near the ocean surface are caused by breaking waves under moderate wind conditions (Medwin, 1977; Dean and Stokes, 1999). The entrained bubbles in both field and laboratory have diameters of the order of millimetres and the rise velocity of those bubbles is nearly constant for bubble diameters ranging from 0.5 to 50 mm (Chanson et al., 2002; Chanson, 1997; Wood, 1991). A burst of sound is emitted at a frequency approximately given by Minnaert's equation after a bubble is first formed (Deane and Stokes, 1999; Minnaert, 1933). Bubbles produced by breaking waves are concentrated within a plume and this plume starts to dissipate through the processes of dissolution, diffusion, and degassing (Deane and Stokes, 1999). There are different phases of a bubble plume's life cycle such as α-plume, β-plume and γ-plume (Monahan, 1993). The α-plume is the phase of a plume formed when the majority of bubbles are created by breaking waves. This stage of the plume persists for a second in time and is characterised by high void fractions (order 10% of void fraction) and a broadband spectrum of bubble sizes (tens of microns to millimetres), see Monahan (1993) and Deane and Stokes (1999). Once the momentum of the combination of the downward moving jet and breaking wave dissipated, the most diffuse bubbles aggregate and then form the β-plume. As time moves on, the largest bubbles rise to the surface, the remaining smaller bubbles are spread by the turbulent diffusion over a greater volume, which is represented by the γ-plume (Monahan, 1993).

In the open ocean, breaking waves may be caused by constructive interference, wave-wave, wave-current and wind-wave interactions (Melville, 1996).

Hydroelasticity in marine applications can be found from the early works of Chuang (1970), Bishop and Price (1979) and Faltinsen (1997 & 2000). More recently, Temarel (2008) investigated the effects of hydroelasticity for a variety of marine structures such as ships, offshore platforms, very large floating structures and also aqua-culture structures. There is a significant body of research on high-speed craft related the localized hydroelasticity effects, for example how the slamming loads and structural responses are affected by the elasticity of the hull/panel (Aarsnes, 1994; Kvålsvold, 1994; Battley et al., 2009; Stenius, 2009; Stenius et al., 2011a,b and Stenius et al., 2013). With increasing ship size, craft speed, and severity of environmental loadings, the localized hydroelasticity effects have become more of an issue for achieving optimized structures. In general, hydroelasticity can be considered as a sub-category of fluid-structure interaction between flexible structure and liquid. A classic example being the hull-water impacts of high-speed craft which can produce large transient hydrodynamic impact loads on the hull/bottom structure. There is a critical influence of the impact velocity and the relative angle between the hull and water surface (the deadrise angle) on the impact loads: the impact loads increase with increasing impact velocity and decreasing deadrise angle. However, with small deadrise angles the impact pressure will be decreased by an air-cushioning effect (Verhagen, 1967; Lewison and Maclean, 1968; Faltinsen, 2004). A flexible structure will be deformed under hydrodynamic loading and this deformation of the structure will affect the local flow-field between the structure and water, and thereby the spatial and temporal pressure distributions on the structure. Kinematic and inertia effects have been identified as two types of hydroelasticity effects during an impact event (Stenius et al., 2013); kinematic effects are associated with the structure response, i.e. the structural deformation changes

the geometry, velocity and acceleration conditions at the fluid-structure boundary, and on the other hand inertia effects are associated with the loading rates of the structure. Kinematic and inertia effects are fundamentally combined and interrelated, however a distinction between them has been discussed by Stenius (2009) and Stenius et al. (2013).

In particular, uncertainty exists in the understanding of the influence of the presence of air in the water (both entrapped pockets and entrained bubbles) leading to variability of wave impact pressures and forces. There are limited experimental studies on the slamming impact onto aerated water (see Bullock et al., 2001; Lange and Rung, 2011). In this present study, aeration effects on impact were experimentally investigated by dropping a flat plate from various heights onto the water surface, in which the water was aerated to various degrees, to understand role of aeration effect on slamming impacts on ship and offshore structures. In addition, a spring system was connected between the impact plate and the carriage to form an elastic structure for investigating elasticity effect on slamming impacts with zero deadrise angle, which has rarely been done before. The springs could be changed to gain different elasticities of the tested plate (Elastic 1 and Elastic 2 in Table 3-1) and the impact velocity was varied from 1 m/s to 7 m/s by changing the drop height.

2.2 Wave impact on vertical structures

Breaking wave impacts on vertical structures can produce very high loads, which may lead to structural failure and damage. Wave impacts on coastal and offshore structures have been investigated experimentally and numerically for several decades. Most investigations have been carried out to improve understanding of the physics and characteristics of wave impacts on a vertical wall (Oumeraci et al., 1992 & 1993; Hattori et al., 1994; Bullock et al., 2007; Bredmose et al., 2010; Hofland et al., 2011; Lafeber et al., 2012; Guilcher et al., 2014) or a vertical mono-pile (Wienke and

Oumeraci, 2005). The physics and characteristics of the impact loading have been shown by researchers to depend significantly on the breaking wave conditions (Oumeraci et al., 1993; Hattori et al., 1994). Hattori et al. (1994) found in their experimental results that the smaller the amount of entrapped air between the breaking wave and the wall at the collision, the higher the impact pressures. However, the distinctions of low-aeration (small amount of entrapped air) and high-aeration (large amount of entrapped air) were considered by Bullock et al. (2007) and they found that a high aeration level, which is known as the large air-pocket wave impact, does not always reduce the peak pressure, and it can increase both the force and impulse on the structure. The previous studies also found that the highest impact pressures tend to occur around still water level (SWL) under regular wave conditions (Hattori et al., 1994; Bullock et al., 2007). Other researchers found the maximum peak pressure occurred at SWL for plunging breakers (Chan and Meville, 1988; Hull and Müller, 2002) and for flip-through, small and large air pocket (Oumeraci et al., 1995). However, Hofland et al. (2011) presented the location of the pressure peak was located above SWL under the tested wave impact types (broken, small and large air pockets, flip-through and slosh impacts) which were generated using the focussing wave technique.

Structural hydroelasticity effects have been investigated for many years, for example by dropping an elastic plate onto the water surface as reported by Chuang (1970) and Faltinsen (1997 & 2000). The research demonstrates interesting theoretical and experimental results that are significant for the design of offshore structures. The results show that the maximum bending stress of a structural plate section is proportional to the drop velocity and is neither sensitive to where the waves hit the wetdeck nor to the curvature of the wave crest in the impact region (Faltinsen, 1997 & 2000). More recently Kimmoun et al. (2009) have investigated hydroelasticity experimentally by considering wave impacts on a flexible vertical wall. Their study investigated pressure

distribution on the flexible wall, and deflection of the wall under various types of impact. Further, the kinematics of the fluid and fine details of the flow (air pocket) were investigated experimentally and theoretically. Their study showed fairly good agreement between these approaches.

There is limited research investigating the effect of aerated water on wave impacts in the literature. Kimmoun et al. (2012) carried out experiments to investigate the influence of a bubble curtain on wave impacts on a vertical wall with the soliton and focused wave techniques applied. They found that for the cases using the focused wave technique, the location of the bubble generator and the injected air flow rate make the wave breaking process more or less efficient, and the variation of loads is increased while the high loaded area size is decreased. In addition, they found that the compressibility of the aerated water does not seem to be of significant influence on wave impacts generated using the soliton wave technique (Kimmoun et al., 2012).

In this study, to gain a better understanding of the physical processes involved in breaking wave impacts on a large ship or offshore structure (where aeration of water-air mixture and elasticity of structure may have an important effect on wave impacts) various types of wave impact on a truncated vertical wall, considered to be part of a FPSO hull, have been experimentally investigated in this work, in both pure and aerated water. The truncated wall is an initially rigid wall that can be modified to an elastic wall by using a spring system on the rear side of the wall. Deflection of the springs, pressures and forces have been measured under the impact.

2.3 Wave-structure interactions

Another aspect of this study is the consideration of wave structure interaction with a fixed or taut moored structure. Wave-induced load components at integer harmonics of the dominant linear input wave frequency can excite high frequency resonant response for floating offshore structures (e.g. floating offshore wind turbine, floating wave

energy converter, floating production storage and off-loading vessels - FPSOs and floating platforms more generally) and also for bottom-fixed offshore structures (e.g. gravity-based structures - GBS). There may be a nonlinear transfer of energy to a higher-harmonic response of the structure owing to nonlinear wave-wave interaction effects and nonlinear wave-structure interaction effects. Therefore, waves with the incident spectral energy at peak frequency (f_p) can in principle excite structural responses at multiples of the linear peak frequency ($2f_p$, $3f_p$, $4f_p$ ...). These higher-harmonic frequencies are known to cause highly intense nonlinear structural behaviours called *springing* (at double frequency) and *ringing* (at triple frequency), which were first observed in a model test of the Hutton platform which was operated in the UK North Sea from 1984-2001 (Mercier, 1982). The second-order excitation at the double frequency dominates for springing, while the higher-order (3rd and 4th order) frequencies trigger the ringing of gravity-based platforms and tension leg platforms, which is a transient elastic response (Faltinsen, 1995 & 2014). Shao and Faltinsen (2014) used a new potential flow method (the harmonic polynomial cell method) to simulate the linear and higher-order harmonic force amplitudes and phases on a surface-piercing vertical cylinder standing on the sea floor in regular waves. Their results showed good agreement with the higher-harmonic experimental results by Huseby and Grue (2000). Bachynski and Moan (2014) simulated wave-structure interaction of different tension leg platform used to support wind turbines and their simulation results showed that the large extreme forces were caused by ringing loads, which also increased short-term fatigue damage in the tendons and tower.

Floating production storage and off-loading vessels (FPSOs) and floating platforms more generally - with 'soft' catenary-type mooring systems - are unlikely to be affected by sum harmonic forcing. However, a major load contribution to the design of their mooring systems is the second order frequency difference term, as well as current and

wind loading. Thus, nonlinear wave interactions are also important for floaters. A second area of where local hydrodynamics plays an important role is estimation of the likelihood and severity of green water.

For structures which give rise to substantial changes in the wavefield around them, Molin et al. (2005) found that the 3rd order interactions between the incident and reflected wave fields in regular waves lead to significant enhanced waves and run-up at a finite wall in regular waves. Their experiments and numerical simulations, accounting for third-order driven changes to the total (incident and diffracted) wave field, are in good agreement. But standard analysis methods for large volume offshore structures are generally restricted to 2nd order in wave amplitude, using codes such as WAMIT or DIFFRACT (Zang et al., 2006). It may be that Molin's 3rd order interactions are only important in regular waves; further work is required to investigate this.

Floating Production Storage and Off-loading (FPSO) vessels are important and commonly used as parts of offshore oil and gas production systems. In recent decades, oil and gas resources have been developed in increasingly deep water and it is necessary to understand wave-FPSO interactions in such water conditions, where physical model testing remains important. The interaction of waves with an FPSO-type body has been the subject of previous investigations, for example the wave scattering (Zang et al., 2006; Siddorn, 2012) and the response of an FPSO vessel in long- and short-crested seas (HR Wallingford Ltd, 2002). Zang et al. (2006) examined the effects of second order wave diffraction around the bow of a simplified FPSO. Their study found that at locations upstream of the bow there is a second-order bound harmonic of the incoming wave, then later radiated free waves well-separated from the incoming wave group, but no significant third-order harmonic components were observed. A significant second-order diffracted wave field was found in the fully nonlinear simulations of Siddorn (2012) based on a boundary element potential flow method with quadratic elements, but

again no evidence of the third-harmonic contributions at the bow or upstream. However, there was evidence of third-order diffraction off out to the sides and diagonally downstream of the stern of the FPSO.

Fitzgerald et al. (2014) studied higher harmonic diffracted wave fields around a surface-piercing column due to a focused wave group using NewWave theory (Tromans et al., 1991). They simulated wave-structure interaction of a focused wave group (with kA = 0.1, where k is the wavenumber corresponding to the spectral peak energy period, and A is the total amplitude of the linear harmonic) and a 0.25 m diameter cylinder, using a fully nonlinear higher-order BEM potential flow model. Their simulation showed the second and third harmonics of the total and scattered wave fields at locations upstream and downstream of the model. Their general phase-based harmonic separation method (Fitzgerald et al., 2014) is applied to decompose the local wave field in this work.

The importance of these scattered waves and the associated loads depends on the application. One of the principal loading components on FPSOs is the slow drift force - the 2nd order difference frequency loading - as this is a major loading component in the design of the spread moorings, together with current and wind. Double and higher frequency harmonics of force are less important here. However, another design condition for floating bodies, including FPSOs, is the occurrence and severity of loading arising from green water on deck (Barcellona et al., 2003; Greco et al., 2007; Schoenberg & Rainey, 2002). The onset of green water will be significantly influenced by 2nd order difference and sum (and higher harmonic) contributions to local surface elevation, as negative freeboard is required for green water to appear on the deck.

In the present work, those higher harmonic components of the scattered wave, force and structural responses are experimentally investigated to get a better understanding of how model geometry (i.e. model length), wave steepness and wave direction effects on the local scattered wave field, mooring line force and responses of FPSO-shaped body, may

affect local and global loads, which may cause damage to or failure of offshore structures and ships. Experiments were carried out using three FPSO models of different lengths, with waves of various steepness and with incident waves approaching from three different angles. The scattered wave field around the fixed and floating models is investigated in detail by applying the phase-based harmonic separation method (Fitzgerald et al., 2014) or the phase-inversion method to separate the harmonic components of the scattered wave (Baldock et al., 1996; Hunt et al., 2003; Zang et al, 2006). The linear, second, third and fourth harmonics of the evolution of the local wave field and the scattered wave amplitudes are presented and discussed. In addition, the linear and higher harmonics of the single mooring line force and the motions of the floating model are also presented and discussed in this study.

It is noted that the bodies used in the experimental programme reported here are rather compact compared to the wavelength ($D/L_p \sim 0.09$, where L_p is the wave length and D the body width). The body dimensions were selected to match the geometry of the 'wave scattering from a box' tests at Imperial College (Zang et al., 2006). Even for this compact geometry and a head-on wave approach direction, there were significant second order sum and difference contributions both at the body and also scattered away as free-radiation.

CHAPTER 3: EXPERIMENTAL METHODOLOGY

3.1 Slamming into water surface

The first series of experiments is designed to investigate aeration and hydroelasticity effects on slamming. It involves bodies slamming onto water, examples of which are the bottom and bow of a high speed vessel, ditching of an aircraft, impact of bottom and bow of large ships like FPSO. It will model these interactions by performing a drop test with zero degree deadrise angle.

3.1.1 Set up of the drop test experiments

The experimental work was carried out in the Ocean Basin at Plymouth University's COAST Lab. The ocean basin is 35 m long by 15.5 m wide and has a movable floor that allows operation at different water depths up to 3 m. For these tests the depth was set to 1m. The falling block included a rigid impact plate connected to a carriage produced by two driver plates with a total mass that could be varied from 32 kg to 52 kg. A spring system was used to form elastic plates and elasticity of the plate could be changed using different spring stiffness. The falling block could be freely dropped in a 4 m high vertical guide frame fixed on the gantry crossing over the ocean basin. After each test, the falling block was lifted up to the tested drop height by a crane (see Figure 3-1). The impact plate was 0.25 m long, 0.25 m wide and 0.012 m thick. The impact velocity varied between 1 m/s and 7 m/s by varying the drop height of the impact plate in the experiments in order to investigate the relationship between impact velocity, maximum pressure and force at impact. Pressures under the impact plate were measured by five miniature pressure transducers (FGP Sensors XPM10 having measurement range of up to 100 bar) installed at various locations on the impact plate. The velocity of impact was integrated from the measured data recorded by an accelerometer (Model 4610 with

range of up to 200*g* or 500*g*, in which *g* is the gravity acceleration) mounted on the top

of the impact plate. A displacement sensor (Model LVDT-GCA500) was used to

measure deflection of springs under slamming impact. The geometry of the impact

plate, the vertical distribution of mass and the configuration of the instrumentation on

the impact plate are presented in Figure 3-2, Figure 3-3 and Figure 3-4. The sampling

frequency was 50 kHz for pressure transducers, accelerometer and displacement

sensors. All drop test conditions in this study are presented in Table 3-1. Figure 3-5

shows the calibration of the tested springs. In addition, a high speed camera (frame rate

up to 10,000 fps) was used to visualise the jets produced at impact and two underwater

cameras (30 fps) were used to record the processes of air pocket entrapment and air

bubble entrainment under the impact plate.
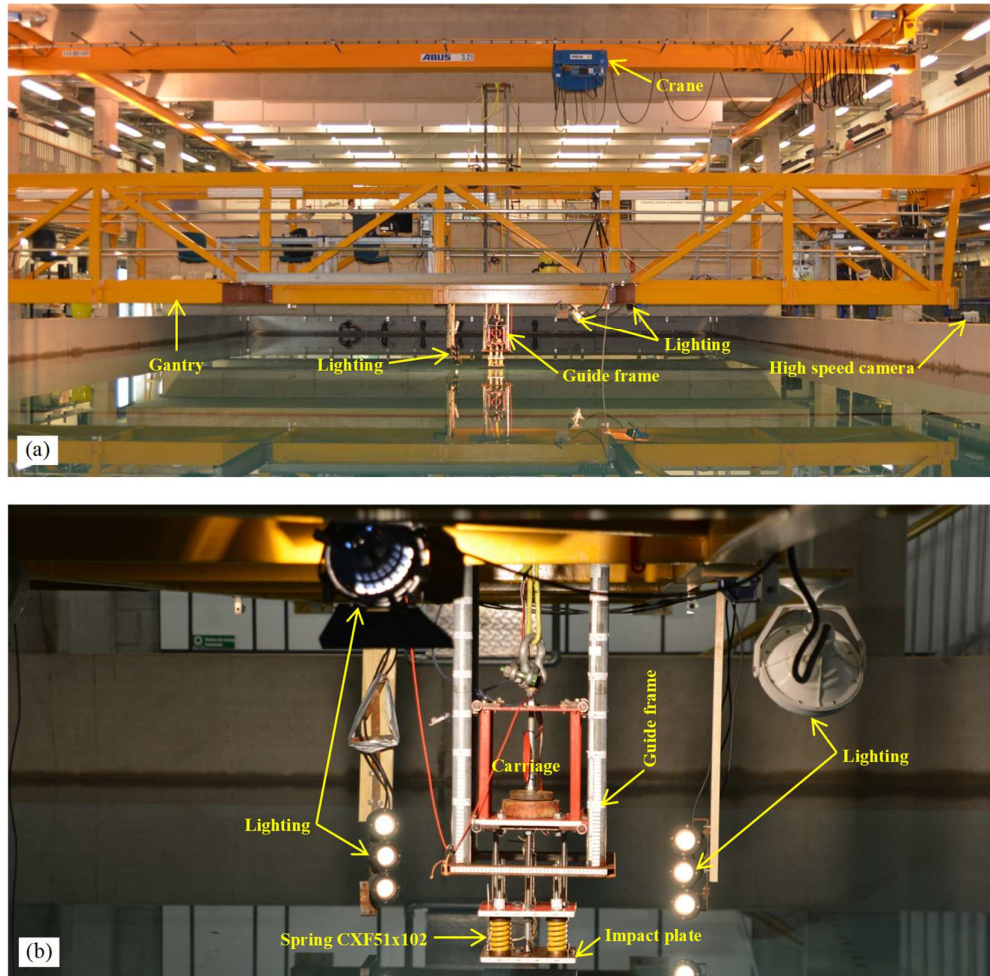
Figure 3-1. Configuration of drop test rig in the Ocean Basin: (a) Overview and (b) Closer view.

(a)   (b)   (c)
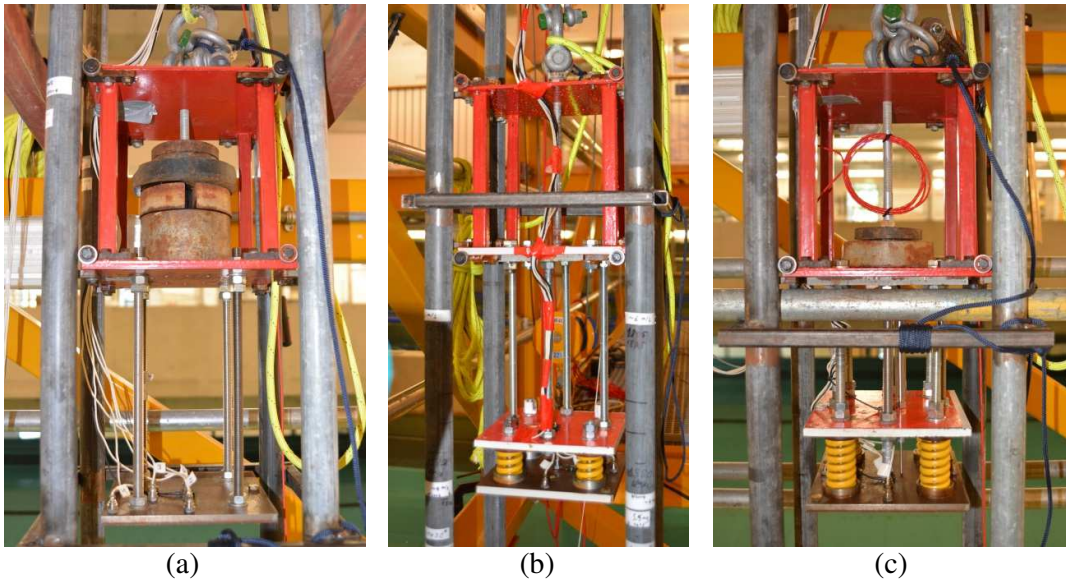
Figure 3-2. Configuration of the impact plates: (a) Rigid plate; (b) Elastic plate 1 - with springs CXF51x64 and (c) Elastic plate 2 - with springs CXF51x102.
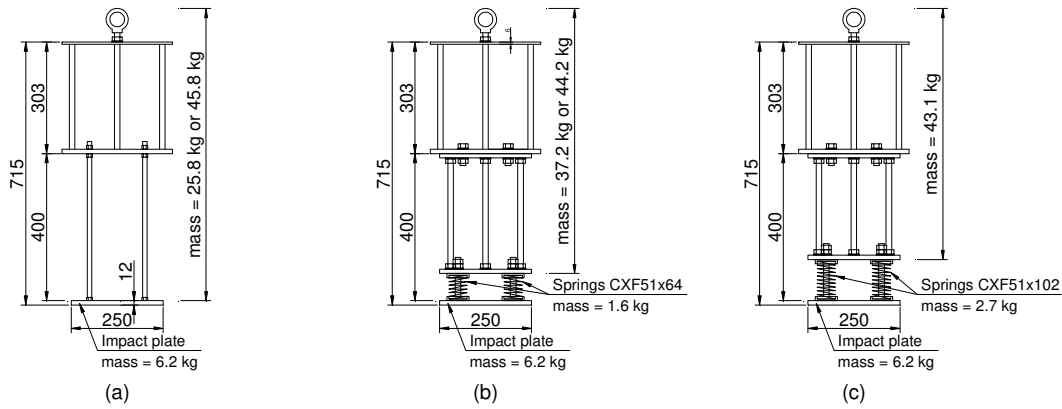
Figure 3-3. Vertical distribution of mass of the impact plates: (a) Rigid plate; (b) Elastic plate 1 - with springs CXF51x64 and (c) Elastic plate 2 - with springs CXF51x102.
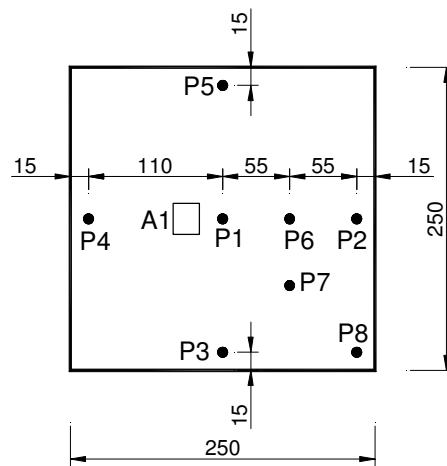
Figure 3-4. Configuration of instrumentation on the impact plate: P1 - P8 are pressure transducers; A1 is the accelerometer. Note units in mm.

20

Table 3-1: Drop test conditions.

Impact plates	Mass (kg)	Aeration levels			
		0	0.8 %	1 %	1.6 %
Rigid plate	32	v = 4 - 7m/s			
	52		v = 4 - 7 m/s		
Elastic plate 1: Springs CXF51x64 (k_1 = 4*765.5 N/mm)	45	v = 1 - 7m/s			
	52				
Elastic plate 2: Springs CXF51x102 (k_2 = 4*397.4 N/mm)	52				
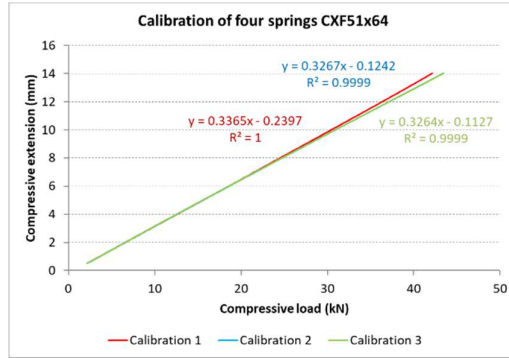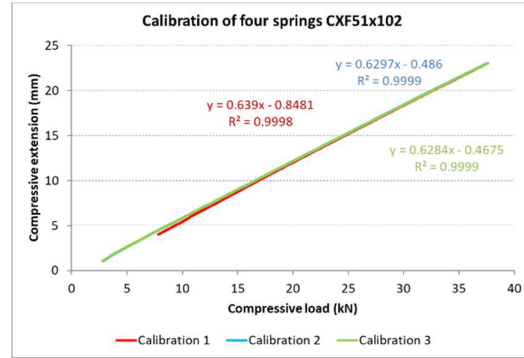
(a)   (b)

Figure 3-5. Calibration of the tested springs: (a) Springs CXF51x64; (b) Springs CXF51x102.

Evaluation of pure water in the Ocean Basin

The assumption of "pure water" in the ocean basin was re-evaluated by measuring the speed of sound in water used in the ocean basin. An Acoustic Systems Trainer (AST) for SONAR (**SO**und **NA**vigation and **R**anging) was used to measure speed of sound in water. Average speed of sound in the ocean basin water is 1471.90 m/s with standard deviation of 0.69 m/s for 14 measurements after the water surface was completely calm. This measured speed of sound is relatively close to the theoretical estimation value of 1475.79 m/s for pure water at 22 ºC according to Wilson (1960).

In addition, after each drop test in pure water, 15 minutes was allowed for the water surface to calm before running the next test. According to Stokes' theory (Detsch and Harris, 1989; Leger-Belair et al., 2000), a bubble of diameter 0.05 mm needs about 12.26 minutes to rise through a water depth of 1 m as used in the drop test (rise velocity of about 1.36 mm/s), and this bubble is degassed at the water surface. The Stokes'

theory and experiment presented by Leger-Belair et al. (2000) show that the rising velocity is proportional to the bubble radius. Therefore, after each test all bubbles of diameter larger than 0.05 mm will have risen to the water surface and have been degassed within the 15 minutes left between tests.

Bubble generation and void fraction estimations

In this study, aerated water was achieved using a bubble generation system to obtain different levels of void fraction. The bubble generator was made of a clear perforated plastic square top-plate (dimensions of 0.54 x 0.54 x 0.002 m). The bottom plate and the sides of the bubble generator were also made of clear plastic. Holes of 0.2 mm diameter were drilled in the top plate using a laser cutter. The holes were uniformly distributed with a spacing of 10 mm over a square area of 0.495 x 0.495 m^2. To generate aerated water, the air from an air compressor was injected into the bubble generator via four air inlets (see Figure 3-6). The bubble generator was placed on the floor of the Ocean basin at an operating depth of 1 m. Snapshots of the aerated water generated by different injection air pressures are presented in Figure 3-7, which clearly shows that the bubble density increases with injection pressure. In this study, bubbles were required to be as uniform in size as possible in order for comparison with numerical predictions presented by Ma et al. (2016). Average bubble size varies from 2.3 mm to 6.6 mm as estimated by Hancock (2014).

Different methodologies were applied to determine the void fraction of the aerated water: measurement of the speed of sound, a volumetric method, hydrostatic pressure in aerated water, and high speed photography, which can also be applied to estimate size, distribution and velocity of bubbles. Each of these methods has its own advantages and disadvantages (Mai et al., 2014).

In the present work, the void fraction (β) of aerated water was calibrated by the volumetric method (air flow rate measurement) using the following formula, which was

developed by Prof. Kurt Langfeld - Professor in Theoretical Physics, Plymouth University (see Appendix A for the derivation details of the formula).

$$\beta = \left(1 + \frac{1}{2\kappa}\frac{\Delta p}{p_a}\right)\frac{t_b}{t_{full}} \tag{3-1}$$

where κ is the adiabatic coefficient, Δp is the change in pressure given by the weight of the water column, p_a is the atmospheric pressure, t_b is the time a bubble needs to reach the surface after leaving the bubble generator, and t_{full} is the time needed to fill the cylinder with air completely. A clear plastic cylinder was used to measure the air flow rate through the water body as shown in Figure 3-8a&b. The air flow rate of each aeration level was measured at nine spatial locations indicated in Figure 3-8c. Injecting air pressures of 0.065 bar, 0.083 bar and 0.137 bar into the bubble generator, the water was respectively aerated at void fractions of 0.8±0.31 %, 1±0.39 % and 1.6±0.07 % as calibrated by the volumetric method at a depth of 25 cm from the water surface (Figure 3-9). These values are based on the mean of the nine measurements for each air pressure. It should be noted that the degree of aeration cannot be adequately defined by a single parameter because the degree of aeration varies in space (the measured depth level/location in water) and time. In this study, the degree of aeration is idealised by a representative single parameter, i.e. the tested void fraction was about 0.8%, 1% or 1.6%, enabling comparisons with the numerical simulation presented by Ma et al. (2016).
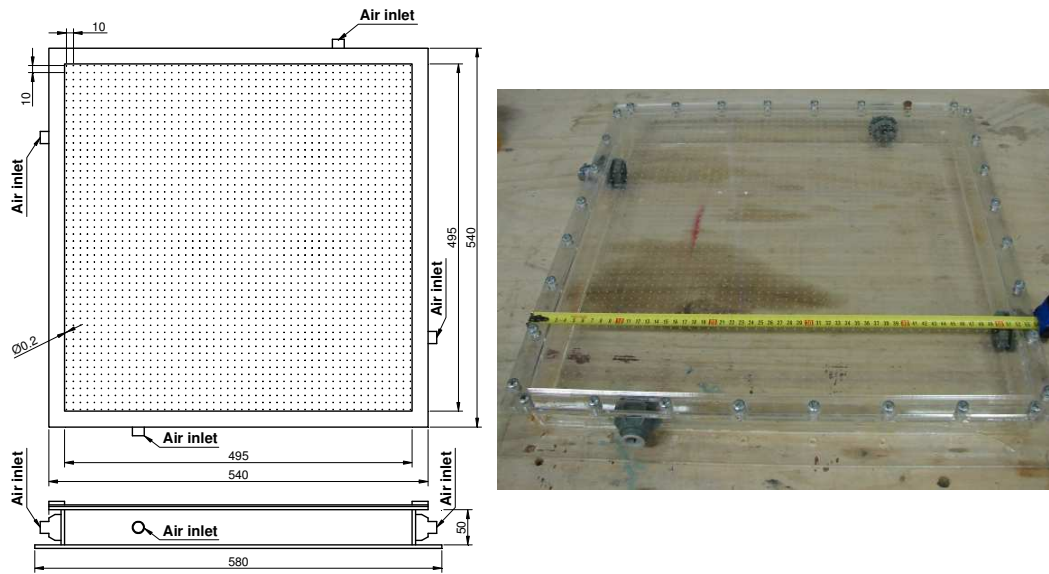
Figure 3-6. The bubble generator. Note units in mm.

(a)   (b)   (c)
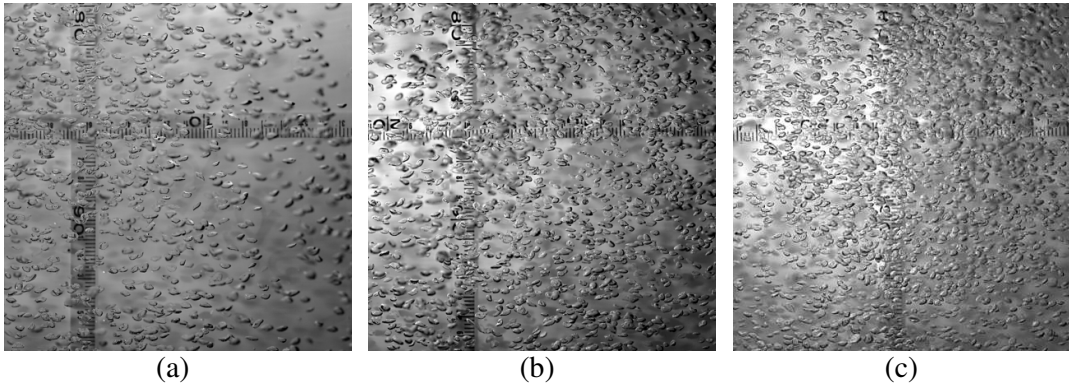
Figure 3-7. Aerated water at different injected air pressures: (a) 0.065 bar; (b) 0.083 bar; (c) 0.137 bar.

(a)   (b)   (c)
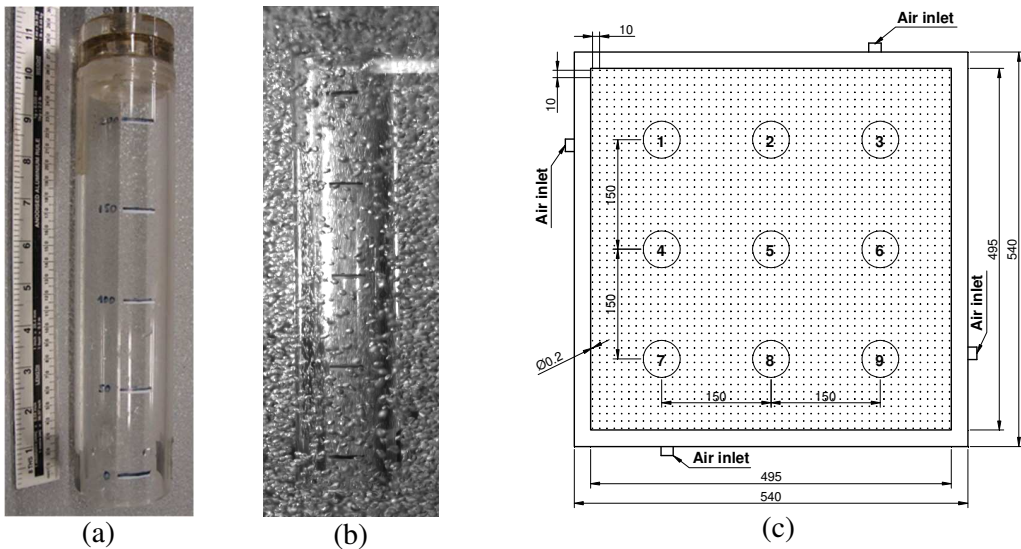
Figure 3-8. Volumetric method: (a) the clear plastic cylinder; (b) the cylinder in aerated water; and (c) the measured locations.
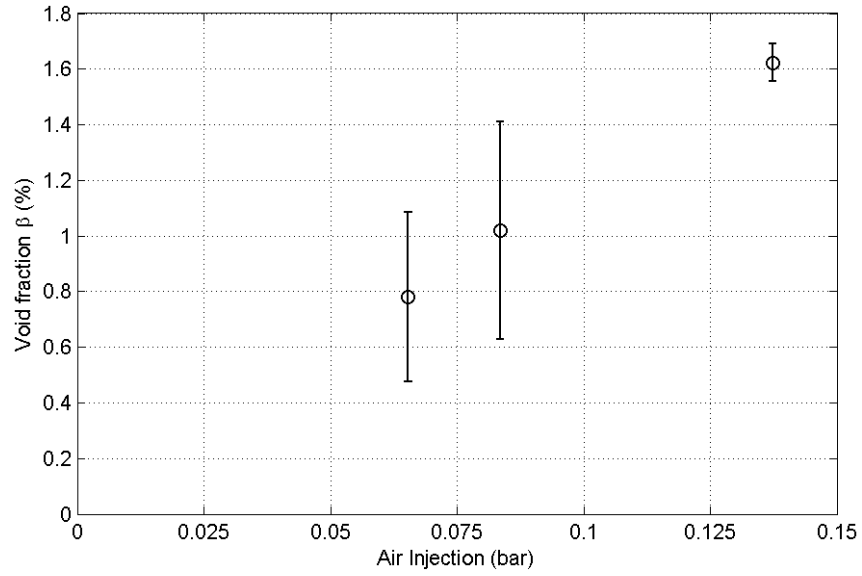
Figure 3-9. Void fraction calibrated in the Ocean Basin applying the volumetric method. Mean values are shown, with error bars representing the standard deviation of the nine measurements.

3.1.2 Plate kinematics

The time-varying velocity of the plate, $v(t)$, was integrated from the measured acceleration as follows

$$v(t) = v_0 + \int a(t)dt \qquad (3\text{-}2)$$

in which, v_0 is the initial velocity of the impact plate and $a(t)$ is the plate acceleration at time instant t.

The impact velocity can also be estimated from the drop height of the impact plate using the theoretical formula $v = \sqrt{2gh}$ (g is the gravity acceleration; h is the drop height) and an ideal free drop is assumed. By comparing this impact velocity with that of Equation (3-2), the effect of friction between the guide frame and the carriage can be observed. Due to friction the experimental velocities are smaller than the theoretical ones and the deviation from theory is greater for increased drop height and fall velocity (Figure 3-10).
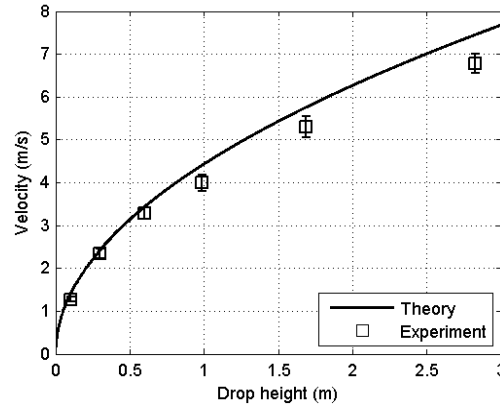
Figure 3-10. Theoretical and experimental impact velocities. The error bars represent the standard deviation of the repeated tests.

The displacement of the impact plate, $h(t)$ may also be determined from integration of the measured acceleration using the following formula:

$$h(t) = h_0 + \int a(t)dt^2 ,$$
(3-3)

in which, h_0 is the initial height of the impact plate.

3.1.3 Repeatability of the impact pressures

Repeatability of the measured impact pressures recorded in pure and aerated water was investigated and is illustrated in Figure 3-11 to Figure 3-13. Ten repeat tests of the impact experiments in pure water with the plate mass of 52 kg and impact velocity 3.45±0.04 m/s were performed and in Figure 3-11, results from 3 repeat tests are presented at each of 5 different pressure measurement locations (P1, P2, P6, P7 and P8 in Figure 3-4). It is shown that the pressure traces at the measured location are repeatable. Average impact pressures at P1, P2, P6, P7 and P8 are 9.16 bar, 3.45 bar, 7.79 bar, 7.33 bar and 2.77 bar, respectively. The standard deviations of the impact pressures at those locations vary from 0.14 bar to 0.72 bar (or 4 % to 9 % of the average values). In addition, repeatability of pressure at the central point (P1) and the four locations at the edge of the plate (P2, P3, P4 and P5) were also investigated and presented in Figure 3-12 for the case with impact velocity of 4.12 ± 0.1 m/s and plate mass of 52 kg. Pressures at these locations are also repeatable and at the edge locations

26

(P2, P3, P4 and P5) the maximum impact pressures are reasonably similar with the average value of 6.07 ± 0.4 bar (Figure 3-12b-e).

A selection of repeat tests with v = 4.09 ± 0.03 m/s for the plate in aerated water 1 % void fraction are shown in Figure 3-13 and show that the impact pressure is unrepeatable in both magnitude and behaviour. Impacts with this velocity were repeated 12 times and the standard deviation of impact pressures at all measured locations (P1, P2, P3, P4 & P5) varied from 27 % to 40 % of the average impact pressure. It was also observed that there was no clear relationship between the central impact pressure and the impact pressures at locations near the edge of the plate. This unrepeatability of the impact pressures in aerated water is due to the water surface being disturbed by the air bubbles rising through the water and breaking the surface such that the water is not perfectly flat as the plate impacts.
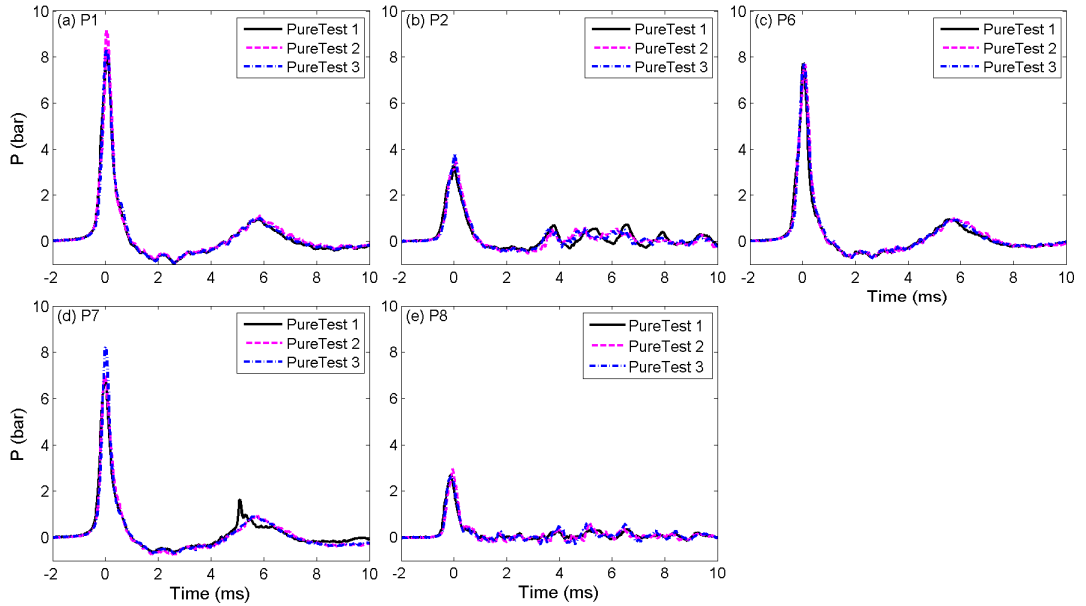
Figure 3-11. Pressure P1, P2, P6, P7 and P8 in pure water (Rigid plate; v = 3.45±0.04 m/s; m = 52 kg).
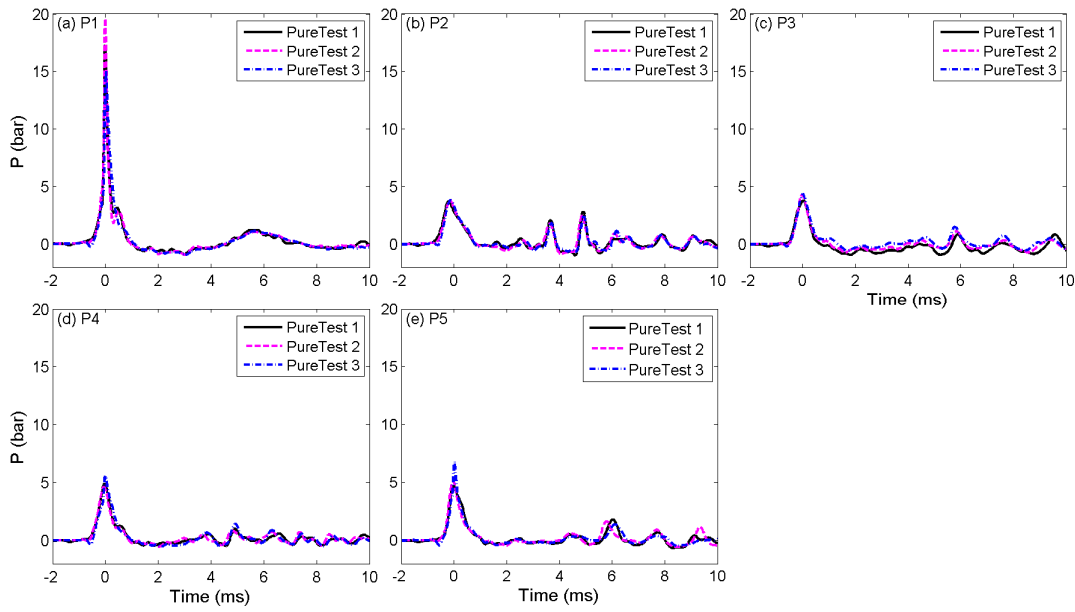
Figure 3-12. Pressures P1, P2, P3, P4 and P5 in pure water (Rigid plate; v = 4.12±0.1 m/s; m = 52 kg).
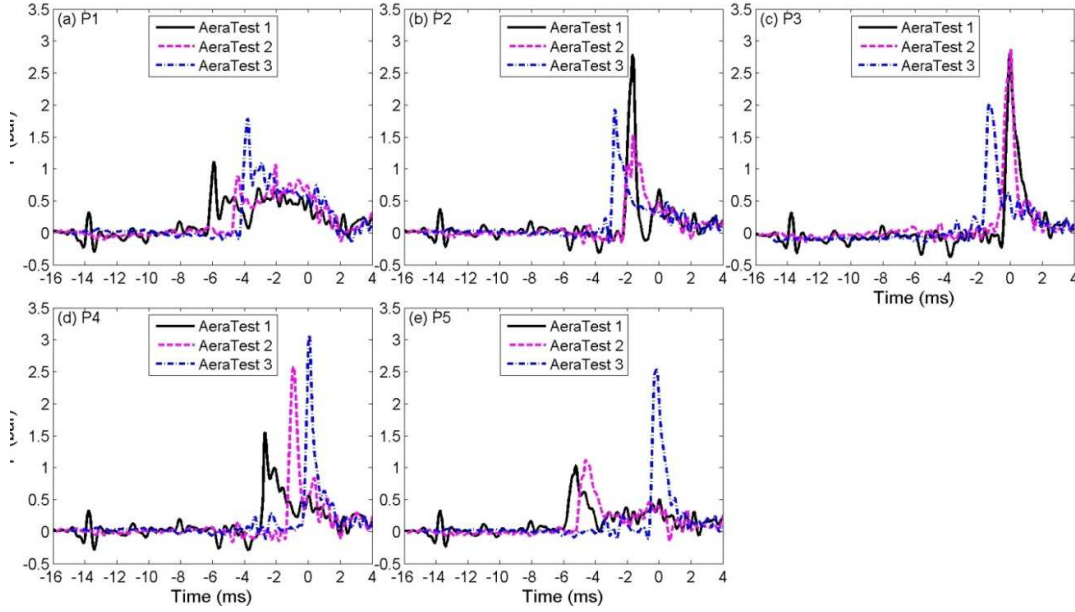
Figure 3-13. Pressure measurements in aerated water with void fraction β = 1 % (Rigid plate; v = 4.09±0.03 m/s; m = 32 kg).

3.1.4 Spatial integration of force from the measured pressures

The impact force has been determined by spatial integration of the measured pressures on the surface of the impact plate. The experiments were carried out in three separate series' and different pressure data were collected in each series, with P1 and P2 common to all tests. Four alternative spatial integrations were investigated (Figure 3-14), with the integrated forces resulting from each configuration presented in Figure

3-15 for comparison. In general, the integrated force F_2 is much higher than the others. F_4 is slightly higher than F_1 and F_3 at the highest impact velocity (v = 7.21 m/s). The integrated forces F_1 and F_3 are in good agreement for all impact velocities. Therefore, the integrated force F_1 will be presented in the remainder of this study due to the good quality and the availability of these data points for all tests.

(a) F_1 (b) F_2 (d) F_3 (c) F_4
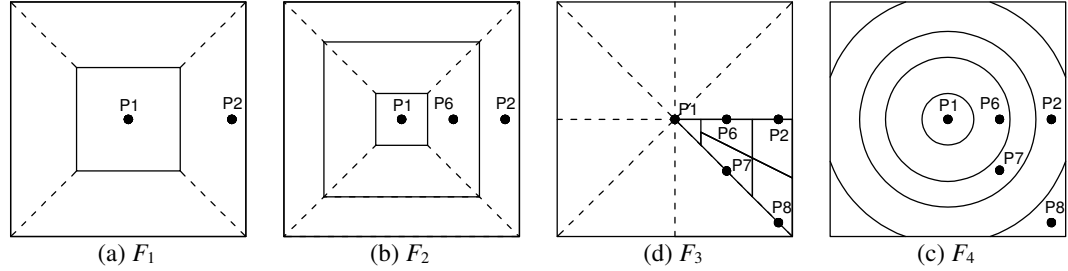
Figure 3-14. Alternatives of spatial integrating force from the measured pressures on a square plate.
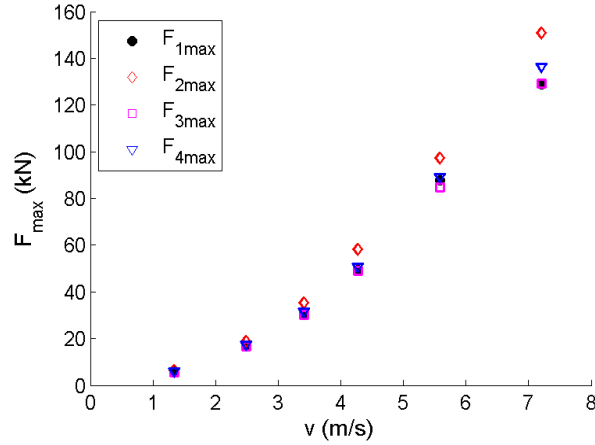
Figure 3-15. Integrating forces from the measured pressures on a square rigid plate.

3.2 Wave impact on a truncated vertical wall

The second series of experiments was the offshore breaking wave impacts on a truncated vertical wall, representing a hull section of an FPSO. Various types of wave impact were generated and tested to identify the most violent impact type for ship and offshore structures. Furthermore, aeration of water and elasticity of the wall were tested to investigate how they affected impact loadings on the structure.

3.2.1 Set up for the flume experiments

The experimental work was carried out in the sediment wave flume at Plymouth University's COAST Lab. The wave flume is 35 m long with a working section 0.6 m wide by 1.2 m high with a maximum still water depth of 0.8 m. A schematic of the physical model setup is given in Figure 3-16. The truncated vertical wall (Plate 1) is an aluminium plate of 0.56 m width by 0.6 m height and 0.012 m thickness connected to rigid elements (Plate 2 and 3) by four springs. Plate 2 and 3 were mounted on a support frame via a low profile load cell and Plate 4. There were 0.02 m gaps on both sides of the tested model to remove the friction between the model and the flume side walls, as friction can affect the free deformation of the springs and the load measurement. The spring system could incorporate springs of different stiffness and also can be locked to obtain a rigid wall model. Pressures under wave impact were measured by FGP XPM10 pressure sensors installed at 7 locations on the impact wall. A low profile load cell (stainless steel series) was used with an inline DC amplifier (Model 140) to measure total force on the wall. A displacement sensor (Model LVDT-GCA500) and accelerometers (Model 4610) were used to measure deflection of springs and vibration of the structure under wave impact, respectively. The configuration of the instrumentation on the impact plate is presented in Figure 3-17. The mass horizontal distribution of the tested walls are presented in Figure 3-18. The tested springs (CL51x102 and CL51x254) are calibrated and the calibrations are shown in Figure 3-19. The data of pressures, force, deflection and acceleration were sampled at 35 kHz frequency. This sampling frequency was smaller than that used in the drop test due to the larger number of the measured instruments and the RAM (Random-access memory) limitation of the computer used in this experiment.

Thirteen resistance-type wave gauges were used to measure water elevation along the wave flume, of which five wave gauges were used to measure the wave profile in front

of the model during impact (Figure 3-16b). The wave gauge data were sampled at 128 Hz frequency. In addition, a Photron SA4 high speed camera (frame rate up to 3600 fps at a resolution of 1024x1024) was used to visualise the air pockets, wave run-up and jets produced at impact.

The same bubble generation system was used as for the drop tests to generate aerated water with 0.6 % void fraction for these flume tests. The location of the bubble generator was just in front of the impact wall (Figure 3-16b).
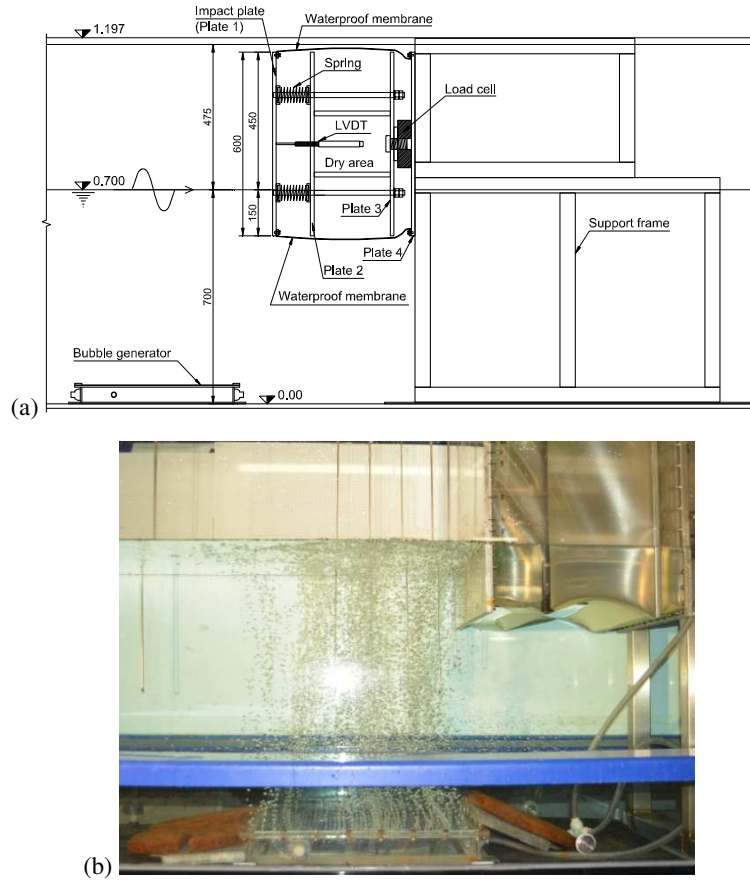
Figure 3-16: Side view of the tested model in the 35 m long wave flume.
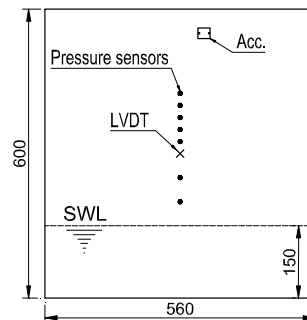
Figure 3-17: Configuration of instrumentation on the impact wall. Unit in mm.
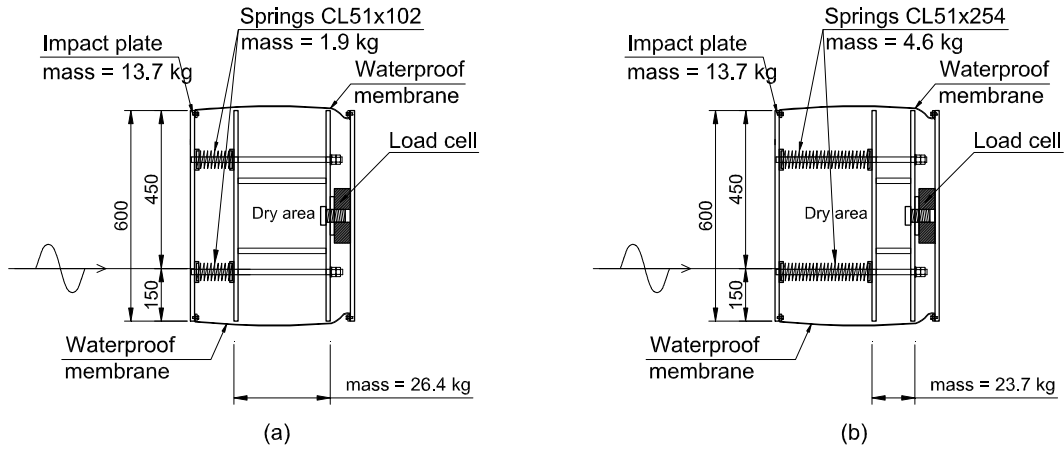
Figure 3-18: Mass horizontal distribution of the wall: (a) With springs CL51x102; (b) With springs CL51x254. Unit in mm.
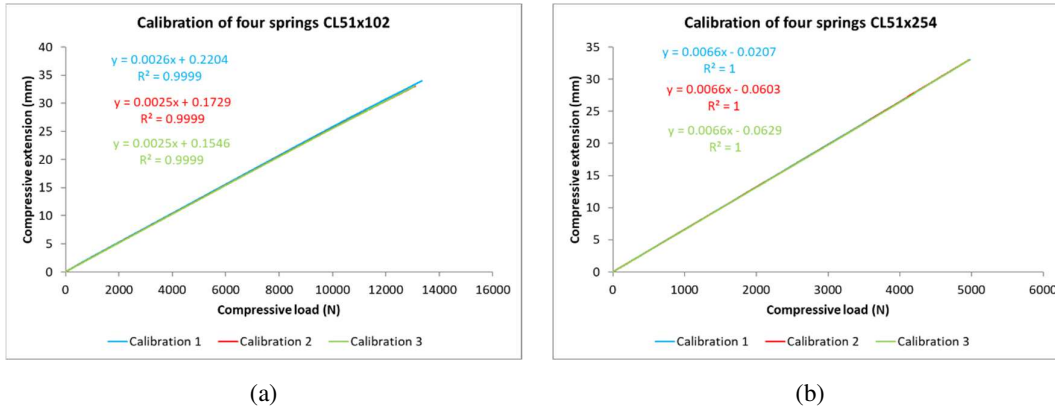
Figure 3-19. Calibration of the tested springs: (a) Springs CL51x102; (b) Springs CL51x254.

3.2.2 Wave conditions

A focusing technique was applied to generate different types of wave impact by changing the focus location X_f (Kimmoun et al., 2010). Focused wave groups were generated using NewWave focusing (Tromans et al., 1991) with an underlying JONSWAP spectrum ($\gamma = 3.3$). Wave conditions were scaled from prototype by a factor of 1:65 of the 100 year extreme significant wave height at the Cleeton platform in the Southern North Sea (Williams, 2008) to optimise the wave impact types in the wave flume. Five different types of wave impact were generated by changing the focal location from an absorbing piston paddle (0.5 m wide by 1 m high) in the wave flume with water depth, at the structure, of 0.625 m (with bubble generator in place) and 0.7 m (without bubble generator). The distance between the front impact plate (Plate 1) and

the wave paddle is 26.9 m. The target focus points are located downstream at 1.14 m, 1.64 m, 1.94 m, 2.14 and 2.54 m from the impact plate for the early broken wave, broken wave, high-aeration wave, flip-through wave and slightly breaking wave, respectively. The tested wave impacts are:

(1) Early broken wave impact: The target focus point is located at X_f = 28.04 m from the wave paddle (Figure 3-20a). This wave is broken far from the wall front. This early broken wave produces a large aerated water mass which hits the wall.

(2) Broken (nearer the structure) wave impact: X_f = 28.54 m (Figure 3-20b). This wave is broken nearer the front of the wall. This produces a smaller aerated water mass which hits the wall and is similar to that described by Bullock et al. (2007).

(3) High aeration wave impact: X_f = 28.84 m (Figure 3-20c). At the moment of impact, the wall and wave enclose a combined cloud of bubbles and a large air pocket (Bullock et al., 2007).

(4) Flip-through wave impact: X_f = 29.04 m (Figure 3-20d). At the moment of impact, uprush on the wall causes a jet just before the crest hits the wall (Bredmose et al., 2009; Kimmoun et al, 2010).

(5) Slightly breaking wave: X_f = 29.44 m (Figure 3-20e). This has its run-up higher than its crest and the crest is slightly broken when it reaches the wall (Bullock et al., 2007).

A summary of the tested conditions of wave impact on the rigid and elastic walls in the wave flume are presented in Table 3-2.

(a) Early broken   (b) Broken   (c) High aeration

(d) Flip-through   (e) Slightly breaking
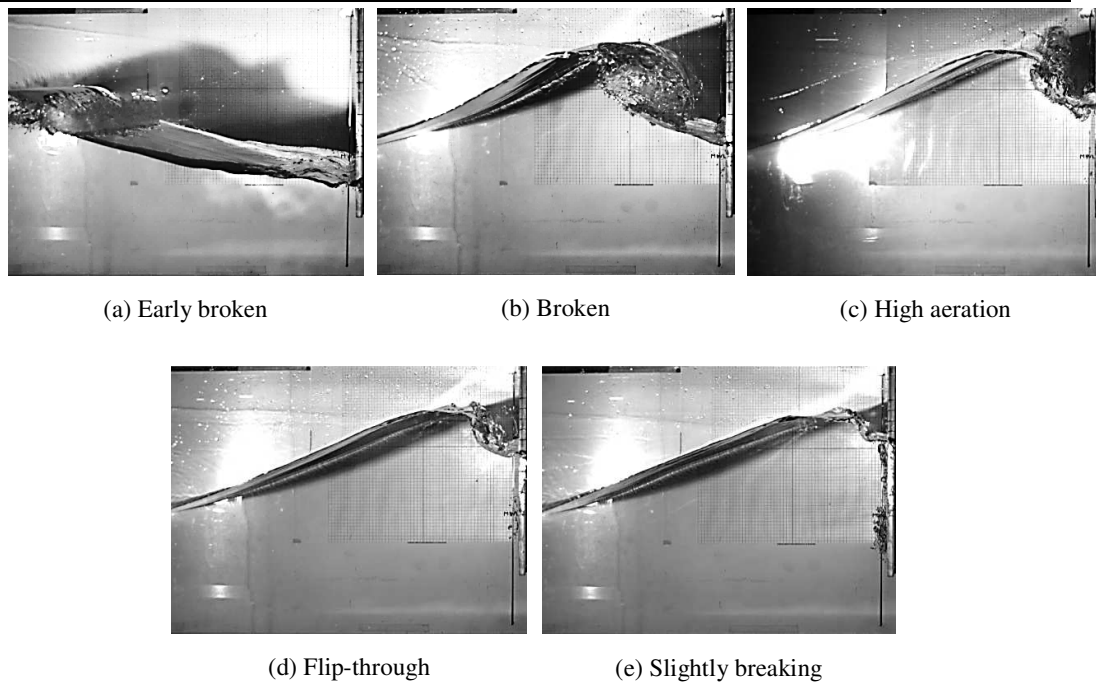
Figure 3-20: Five tested wave profiles.

Table 3-2: The tested conditions of wave impact on rigid and elastic walls.

Truncated walls	Water depth (m)	Wave impact types				
		Early Broken	Broken	High Aeration	Flip-Through	Slightly Breaking
Rigid wall	0.625	-	Aeration level: $\beta = 0$ & 0.6 %			
	0.7	Aeration level: $\beta = 0$				
Elastic wall 1 (with spring CL51x102: $k = 4*98.5$ N/mm) Elastic wall 2 (with spring CL51x254: $k = 4*37.7$ N/mm)	0.7	Aeration level: $\beta = 0$				

3.2.3 Water elevation in front of the wall

Water elevations in front of the wall at different instances in time are presented in Figure 3-21. Profiles of each of the five tested wave impacts (early broken, broken, high aeration, flip-through and slightly breaking waves) are produced using five wave gauges. Each plot shows the average water elevation of three test repeats and time t is defined relative to the time at which the maximum wave crest was measured by wave gauge WG11, which was located at $x = -0.15$ m from the wall front ($x = 0$). From each plot in Figure 3-21, the run-up velocity can be estimated around the impact, with the smallest interval time step $\Delta t = 0.0078$ s, which corresponds to the sample frequency of

128 Hz of the wave gauges for this experiment. Table 3-3 presents the run-up velocities as determined by wave gauges located at *x* = -0.015 m. The maximum run-up velocity was 5.87 m/s for the high aeration wave impact, when the water surface rose from *t* = -0.039 s to *t* = -0.031 s at location *x* = -0.015 m from the front wall (see Table 3-3). Overall, the run-up velocities at the location *x* = -0.015 m for the high aeration and flip-through impacts are higher than those for the other impacts (early broken, broken and slightly breaking).
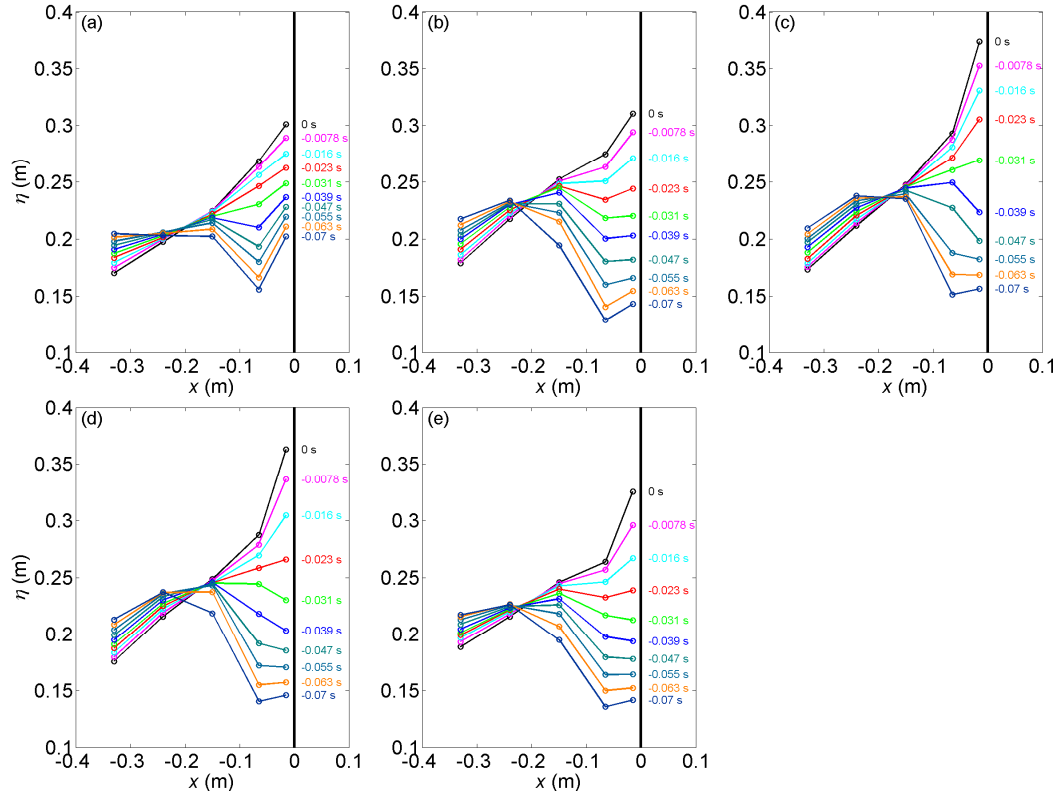
Figure 3-21: The measured water elevation in front of the wall during the impacts with *Δt* = 0.0078 s: (a) early broken; (b) broken; (c) high aeration; (d) flip-through; and (e) slightly breaking. The vertical thick line represents the vertical wall front at *x* = 0.

Table 3-3: Run-up velocity *v* (m/s) of water surface at *x* = -0.015 m.

t (s)	Early broken	Broken	High aeration	Flip-through	Slightly break
0.000	1.53	2.14	2.69	3.42	3.74
-0.008	1.80	2.95	2.82	4.09	3.74
-0.016	1.58	3.44	3.23	4.95	3.57
-0.023	1.77	3.04	4.66	4.57	3.35
-0.031	1.57	2.22	5.87	3.45	2.42
-0.039	1.11	2.69	3.21	2.26	2.02
-0.047	1.07	2.07	2.04	1.91	1.76
-0.055	1.11	1.45	1.76	1.71	1.52
-0.063	1.11	1.43	1.54	1.46	1.37
-0.070					

3.3 Wave-structure interactions of FPSO-shaped bodies

The last series of the experiments was the wave-structure interaction of FPSO-shaped bodies to understand how model geometry (i.e. model length), wave steepness and wave direction affected the local wave field around the models, the single mooring line force and the response of the models.

3.3.1 Set up of wave-structure interaction experiments

The experimental work was carried out in the Ocean Basin at Plymouth University's COAST Lab. A water depth of 2.93 m was used for this experiment. The FPSO models were made of aluminium and were fabricated at ~1:100 scale from a rectangular box with a half circular cylinder at the bow and stern for the longer models (Model 2 and 3) and purely a cylinder for Model 1. The tested models all had the same height and width of 0.3 m, and lengths of 0.3 m, 0.6 m and 1.2 m (Figure 3-22). The draft was 0.15 m for all of the models. The models were rigidly fixed to the gantry (which spans the width of the Ocean Basin) or free floating with a single mooring line system.

The input waves were focused wave groups generated using the NewWave methodology (Tromans et al., 1991) with an underlying JONSWAP spectrum (γ = 3.3), focusing at the bow of the models. Hence, the input wave group is a representation of the average shape of the largest (linear) waves in a random sea-state with a JONSWAP spectrum. A set of non-breaking wave conditions, which correspond to the 100-year extreme significant wave height at the Cleeton platform in the Southern North Sea (Williams, 2008), were employed in these experiments by scaling (1:100). The peak wave periods were chosen according to the guidance of the offshore technology report for UK water (Offshore Technology Report, 2001) to have a variety of wave steepness for investigation. The local wave steepness varied from 0.13 to 0.21, and the incident wave angle was from 0° to 20° where 0° corresponds to a head sea. The ratio of body size over wavelength (corresponding to T_p) varies between ~0.09 (cylinder) and ~0.43

(longest model). Test parameters are given in Table 3-4. Wave run-up on the models and the local wave field around the models were measured by 24 resistance wave gauges, as shown in Figure 3-23, with a sampling frequency of 128 Hz. In addition, a Qualisys system was used to track the motions of Model 3 in six degrees of freedom (6DOF) floating tests, and tension force of the single mooring line was measured by a tension load cell fixed on the basin floor (Figure 3-24).

Model 1   Model 2   Model 3
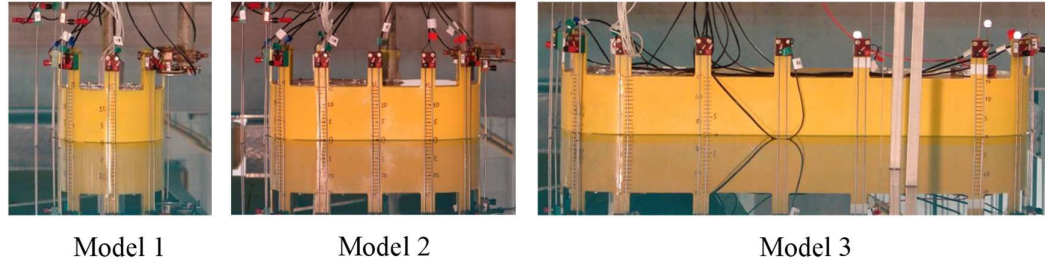
Figure 3-22. The tested models in the Ocean Basin.

Table 3-4. The tested wave conditions.

Parameters	Values
Amplitude, A (m)	0.069 - 0.094
Peak period, T_p (s)	1.330 - 1.440
Peak energy frequency, f_p (Hz)	0.694 - 0.750
High frequency cut-off (Hz)	2
Wave steepness, kA (-)	0.13 - 0.21
Wave direction, α (°)	0 - 20
Water depth, d (m)	2.93
Relative depth, kd (-)	5.68 - 6.63
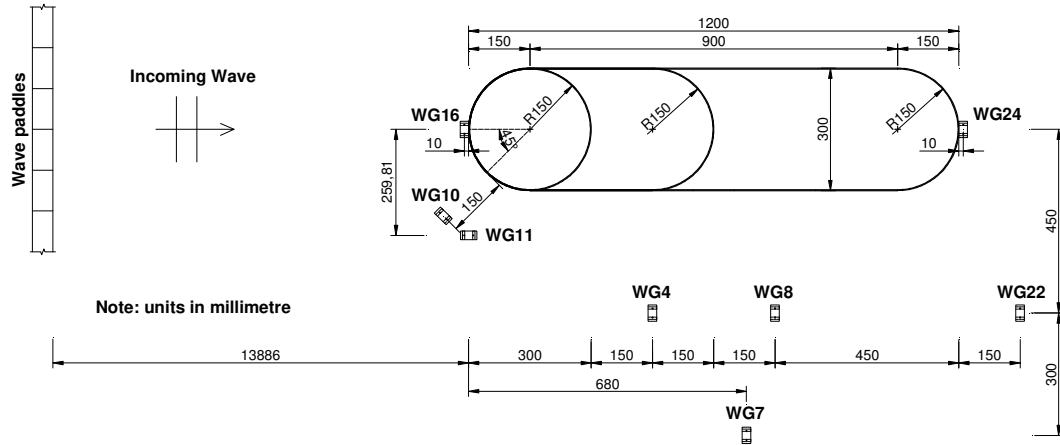
Figure 3-23. Layout of wave gauges around the tested models.
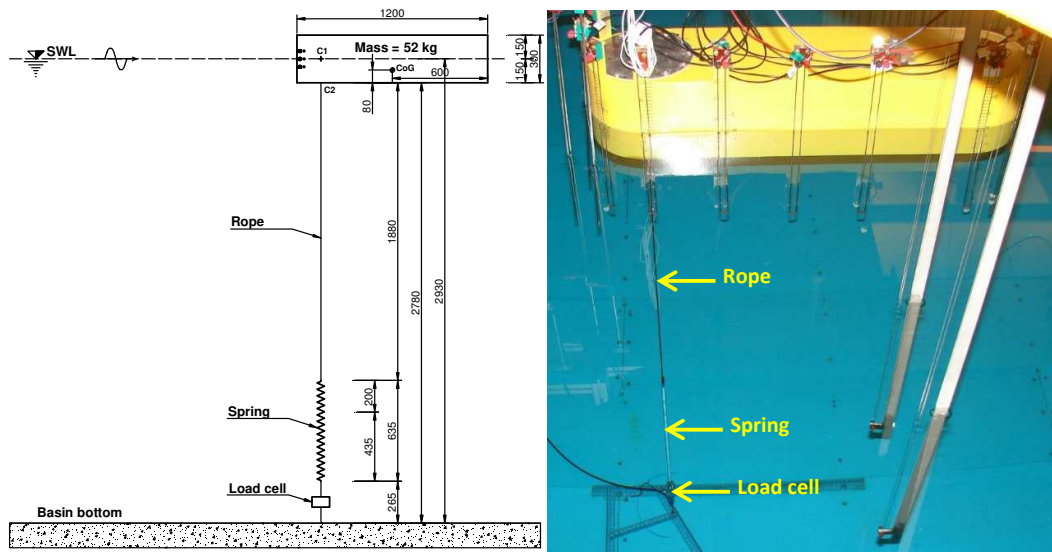
Figure 3-24. Single mooring line system of the free floating FPSO model (Model 3).

3.3.2 Phase-based harmonic separation method

In order to obtain higher-order components of the waves, a separation of components technique was required. Baldock et al. (1996) first presented a *phase-inversion* methodology; for applications see Hunt et al. (2003), Borthwick et al. (2006), Zang et al. (2006), Siddorn (2012), Fitzgerald et al. (2014) and Hann et al. (2014). The odd and even harmonic components can be extracted from the time histories of kinematic or dynamic quantities i.e. the free-surface elevation or wave force in the focus wave group interactions, in which two incident wave groups have identical wave component amplitudes and frequencies but inverted phase i.e. phase of 0° (crest-focused wave) and 180° (trough-focused wave). Then the individual harmonics e.g. linear and third-order, or second- and fourth-order can be separated from each other by frequency filtering.

In this study, however, the extended phase-based harmonic separation method (Fitzgerald et al., 2014) is applied to extract the linear and higher-order harmonic components of the free-surface elevation by applying simple linear combinations of the relevant time histories. This method requires the data from four incident focused wave groups that are each exactly 90° out of phase. There is then minimal post-processing applied to extract the linear, second-, third- and fourth-harmonics.

38

An incident wave group that has amplitude A and relative phase θ can be expressed as the classic Stokes perturbation expansion (Fenton, 1985), as follows

$$\eta(A, \theta) = B_{11} A \cos\theta + A^2 (B_{20} + B_{22} \cos 2\theta)$$

$$+ A^3 (B_{31} \cos\theta + B_{33} \cos 3\theta) + A^4 (B_{40} + B_{42} \cos 2\theta + B_{44} \cos 4\theta) + O(A^5) \qquad (3\text{-}4)$$

where B_{ij} are the coefficients in Fourier series for $\eta(A,\theta)$; i is the amplitude content order; and j is the frequency content order. Equation (3-4) can be rewritten in a more compact form as:

$$\eta(A, \theta) = \eta_{11} + (\eta_{20} + \eta_{22}) + (\eta_{31} + \eta_{33}) + (\eta_{40} + \eta_{42} + \eta_{44}) + O(A^5) \qquad (3\text{-}5)$$

where, η_{ij} are the jth-order harmonic components, $\eta_{ij} = A^i B_{ij} \cos(j\theta)$. If i and j are identical, then η_{ij} are the jth-order harmonic sum, e.g. the first-order sum η_{11}. On the other hand, if i and j are different, then η_{ij} are the jth-order harmonic difference, e.g. the term η_{31} is at the first-harmonic in frequency but 3$^{\text{rd}}$ order (cubic) in input wave amplitude. Henceforth, the subscript i is referred to as the (amplitude) order and j as the harmonic.

By considering four focused wave groups generated from the same wave amplitude components but with the phase of each Fourier component shifted 0°, 90°, 180° and 270° it is possible to obtain the four time histories of free-surface elevation η^0, η^{90}, η^{180} and η^{270} respectively. The linear combinations of these time histories and the Hilbert transforms of the 90° and 270° free-surface elevation time histories are applied to extract the linear and the first three superharmonics (2$^{\text{nd}}$, 3$^{\text{rd}}$ and 4$^{\text{th}}$ order); these are important for springing and ringing and are presented in Equations (3-6) - (3-9). A more detailed explanation of the separation method can be found in Fitzgerald et al. (2014).

$$(\eta^0 + H(\eta^{90}) - \eta^{180} - H(\eta^{270}))/4 = \eta_{11} + \eta_{31} \qquad (3\text{-}6)$$

$$(\eta^0 - \eta^{90} + \eta^{180} - \eta^{270})/4 = \eta_{22} + \eta_{42} \qquad (3\text{-}7)$$

$$(\eta^0 - H(\eta^{90}) - \eta^{180} + H(\eta^{270}))/4 = \eta_{33} \qquad (3\text{-}8)$$

$$(\eta^0 + \eta^{90} + \eta^{180} + \eta^{270})/4 = \eta_{20} + \eta_{40} + \eta_{44} \tag{3-9}$$

where H is the harmonic conjugate of the signal. Also note that due to the relatively weak nonlinearity of the difference components compared with the sum components, for example η_{31} compared with η_{11}, the difference components are likely to be negligible. The only exception to this is the 0th-order component η_{20} which represents the long wave set-*down* and can be cleanly separated using digital frequency filtering from components obtained in Equation (3-9). This long wave set-down also contains a 4th-order amplitude contribution η_{40} but in this application this additional contribution is small compared to the 2nd order term.

Figure 3-25 shows the time histories of the free-surface elevation η^0, η^{90}, η^{180} and η^{270} at the focus location (wave gauge WG11). The vertical axis is the dimensionless free-surface elevation (η/A), where η is the free-surface elevation and A is the linear amplitude at the focus location and time. The horizontal axis is the time scale with the focus time at $t = 0$ s. The focused wave groups shown in Figure 3-25 have a spectral peak energy period $T_p = 1.44$ s and total linear amplitude A of 0.069 m, the wave steepness is then $kA = 0.13$, where k is the wavenumber corresponding to T_p.

Applying the linear combinations presented in Equation (3-6) - (3-9) for η^0, η^{90}, η^{180} and η^{270} in Figure 3-25, the linear and the next three higher harmonic components have been obtained and presented in terms of their normalised amplitude spectra (Figure 3-26) and their separated time histories (Figure 3-27). Minimal post-processing (Fourier band-passing) has been applied to remove the leakage of the linear component in the higher harmonics. The higher-order sum frequency components ($\eta_{22}+\eta_{42}$, η_{33}, η_{44}) are derived from the experiments by applying the fast Fourier transform (FFT) to the measured data, removing the zero-frequency and linear frequency range of the amplitude spectrum, leaving the higher-order sum frequency ranges individually, and then performing an inverse FFT. Consequently, the linear and higher-order sum

harmonic components are very well separated using the extended phase-based harmonic separation method with a minimal post-processing. There was a double frequency error wave train off the wave paddles since only linear wave theory was used to create the waves. This can be seen at around $t = +13$ s for the second harmonic presented in Figure 3-27b.
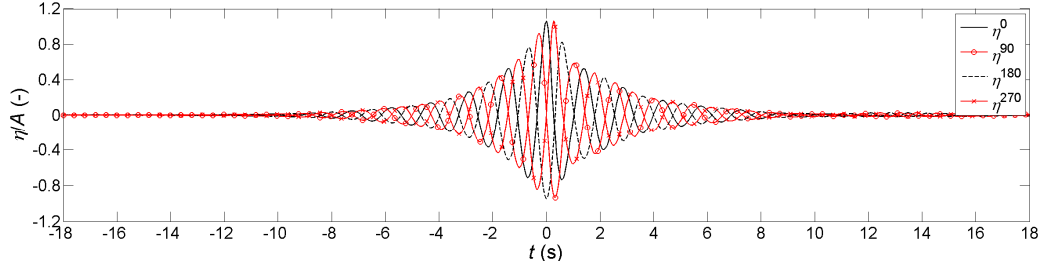
Figure 3-25. Wave profiles at the focus location (without model, $kA = 0.13$).
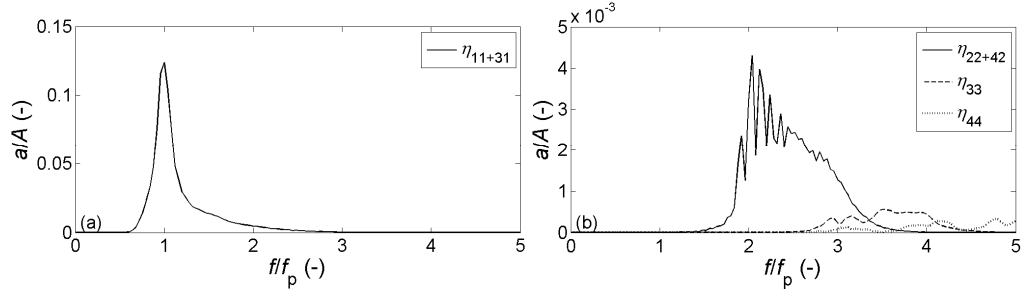
Figure 3-26. Amplitude spectra of the separated components at the focus location (without model, $kA = 0.13$). Note the different vertical scales.
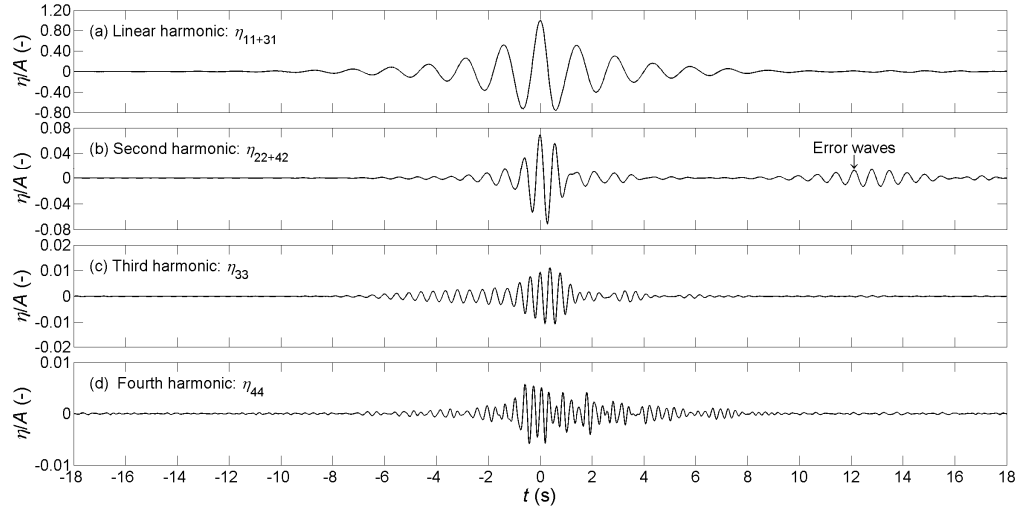
Figure 3-27. Time histories of the separated components at the focus location (without model, $kA = 0.13$). Note the different vertical scales.

3.3.3 Scattered wave field

The scattered or diffracted wave field can simply be extracted as the difference between the undisturbed incident wave and the measured wave in the presence of the model as follows

$$\eta_{ij}^{dif} = \eta_{ij}^{Model} - \eta_{ij}, \qquad (3\text{-}10)$$

where η_{ij}^{dif} is the $(i,j)^{th}$ component of the scattered/diffracted wave, η_{ij}^{Model} is the equivalent component with the model present, and η_{ij} is the undisturbed incident wave component measured at the same gauge location in the absence of the model.

3.3.4 Uncertainty and repeatability

Resistance wave gauges were used in the experiments. When the gauge operates, the resistance of the water between a pair of parallel rods/wires is measured and this is proportional to the immersion depth. The gauges were calibrated at the beginning of each test day and/or before the tests with each model in place. The linearity of the gauge measurement is very close to 1 over the entire range of surface elevation measured in the experiments. Repeatability of the unprocessed time history of measured water elevation at the presented locations is very high and is repeatable within the thickness of a line.

In the experiments, the focus location was predefined at the bow stagnation point. With each focus wave group, the input focus distance for the (linear) wave paddle was optimised to ensure that the waves focus at the predefined location without the FPSO model in place. The focus location was determined to be the point at which the troughs either side of the central crest are symmetric, i.e. of equal depth. WG11 was used to measure water elevation at the focus location. The input focus distances of the wave groups with kA = 0.13, 0.18 and 0.21 were 13.56 m, 13.25 m and 15.365 m, respectively. From the measured signals at WG11, the focused time t_f of each wave group was determined and then the time shift Δt_f estimated. Each wave group has it

group velocity c_g (a half of the phase velocity c_p), therefore the shift of the focus point is calculated by $\Delta X_f = c_g * \Delta t_f$. Consequently, the shift of the focus point is about 0.1 m between the wave groups with $kA = 0.13$ and 0.18 or about 2.5 m between the wave groups with $kA = 0.18$ and 0.21.

It should be noted that unless very steep near breaking waves are generated, the movement of the focus position and changes in wave structure are group properties - relative phase of the components is important but not absolute phase. Hence, the crest-trough phase combination will still work, and of course it would become immediately clear from the analysis if it was to breakdown - with large leakage of even harmonics into the odd harmonics. Although the harmonic extraction process is sensitive to the accuracy of the time alignment of the four phase combinations, the results presented here are very clearly separated between the different harmonics and there is no significant leakage between harmonics.

A timing (phase) error of E in the linear signal produces an equivalent relative error of nE for the n-th harmonic. Given that we didn't have absolute timing alignment, relative errors are certainly possible. But cross-correlation of the signals should allow the signals to be accurately aligned (to say 1/100-th of the main period -> 3.6deg for the linear but 14.4deg for the 4th harmonic). However, the results presented here are very clearly separated between the different harmonics and we cannot see any significant leakage between harmonics.

An example of the time alignment for the focus wave group with $kA = 0.13$ is shown in Figure 3-28 and Figure 3-29. Figure 3-28 shows the raw data of η^0, η^{90}, η^{180} and η^{270} with $t = 0$ is defined at the highest crest point (point A) of η^0. Figure 3-29 presents the signals after the time alignment by moving the lowest trough point of η^{180} (point B in Figure 3-28) horizontally to the vertical line at $t = 0$ and moving the point C in the signal of η^{90} to the point O (0,0).
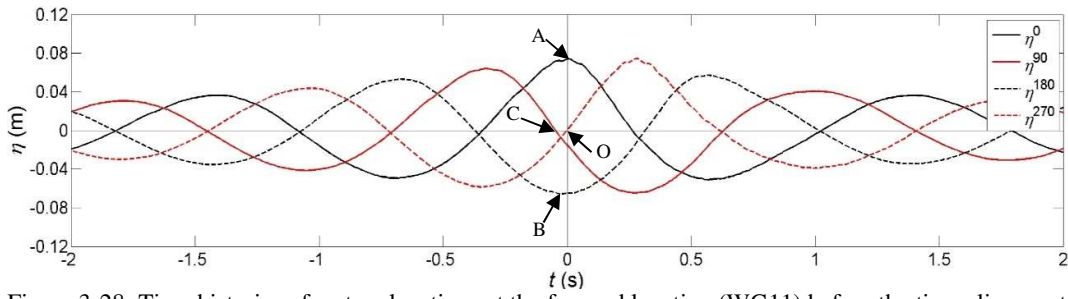
Figure 3-28: Time histories of water elevations at the focused location (WG11) before the time alignment.
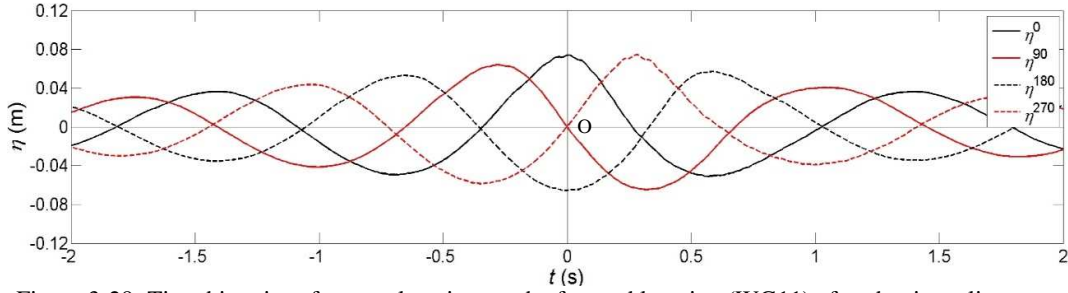
Figure 3-29: Time histories of water elevations at the focused location (WG11) after the time alignment.

CHAPTER 4:   AERATION AND HYDROELASTICITY EFFECTS ON SLAMMING IMPACTS

This chapter presents the results and discussions for the experimental investigation of aeration and hydroelasticity effects on slamming by dropping a flat square plate onto the water surface, in which the water was aerated to various degrees. The experiment is presented in detail in Section 3.1.

4.1 Characteristics of typical slamming impacts

4.1.1 Rigid plate on pure water

Motion time histories for the impact of the rigid plate in pure water with an impact velocity of 7.21 m/s and plate mass of 52 kg, are presented in Figure 4-1. N.B. Motion is defined as positive upwards. The maximum acceleration due to the impact was not captured by the $200g$ accelerometer as the signal was clipped from the moment that the plate hit water surface (Figure 4-1a). This indicates that, the maximum accelerations of the impacts in pure water were larger than $200g$ for the impact velocities were larger than 4 m/s in this experiment. Figure 4-1b shows that the velocity is zero at the start of the test and then increases linearly during the free falling of the impact plate until a maximum velocity is obtained. At the instant of reaching its maximum velocity, the impact plate starts to decelerate and this corresponds to first contact with the water surface. The velocity of the impact plate fluctuates for about 30 milliseconds, then decreases smoothly to zero and changes its direction due to the safety rope, which was connected to the carriage and used to stop the carriage from leaving the guide frame. In Figure 4-1c, the integrated displacement of the impact plate during the test is also shown.

45

Figure 4-2 presents the measured pressures and the integrated force (F_1) during impact for the test case presented in Figure 4-1. At the moment of impact, pressures start to increase up to their maximum values, with the time taken to reach a maximum value called the rise time. The maximum pressure at the centre of the impact plate (P1) is much higher than the maximum pressures near the edges (P2 & P8) and slightly higher than the maximum pressures at locations P6 & P7 located near the plate centre. The maximum pressures are attained at time instants between 1.24 ms and 1.32 ms after the moment of first contact of the impact plate with the water surface. It is observed that the maximum pressure at location P8 is always attained earlier than the maximum pressure P1 at the centre of the plate, by between about 0.08 ms under impact velocity $v = 7.21$ m/s and 0.38 ms under impact velocity $v = 1.33$ m/s. This observed phenomenon is similar to the previous work of Lewison and Maclean (1968). The results also show a second pressure peak under high impact velocity ($v = 7.21$ m/s) from this experiment and it appears at about 0.6 ms after the first peak (see Figure 4-2a). The second pressure peak may be due to the propagation of an acoustic shock wave either through air to the edge of the plate and back, over a distance $2l$, where l is the half width of the impact plate, or through water to the bottom of the basin and back, over a distance of twice the tested water depth, $2h$. The time-scale associated with propagation of the shock wave in water, namely $2h/c_w$ is 1.36 ms, where the measured speed of sound in pure water is c_w = 1471.90 m/s, whereas the propagation time needed for the shock wave travelling in air, $2l/c_a$ is 0.74 ms, where the speed of sound in air is taken to be $c_a = 340$ m/s. Based on these calculations, the scenario of shock wave travelling through the air gap along the width of the plate and back seems most likely as the time-scale is comparable to the observations (~0.6 ms) from the pressure time-histories of this experiment and the horizontal half-size of the trapped air region is less than l. Unfortunately, the trapped air

region cannot be observed in sufficient resolution from the low frequency underwater cameras (frame rate of 25 - 30 fps) used in this experiment.

Figure 4-1. Typical time-history of acceleration, velocity and displacement under impact of the 52 kg rigid plate in pure water ($v = 7.21$ m/s).

Figure 4-2. Typical time-history of pressures and force under impact of the 52 kg rigid plate in pure water ($v = 7.21$ m/s).

Distinct post-impact pressure oscillations have been observed and depicted in Figure 4-3 for the test under impact velocities of 1.33 m/s, 4.28 m/s and 7.21 m/s. The fast Fourier transform (FFT) has been applied to analyse the time histories of pressure signals presented in Figure 4-3. The purpose of the spectral analysis here is to identify

the oscillation frequencies of the pressure oscillations observed in the time history signals which are expected due to repeated compression and expansion of the trapped air between the impact plate and water surface. Therefore, the FFT should be an appropriate technique for spectral analysis to identify the pressure oscillation frequencies. The left hand plots (Figure 4-3a,c,e) are the time histories of pressures and the right plots (Figure 4-3b,d,f) are the respective FFTs plotted on the lin-log scale (with logarithmic scale for the y-axis) to show more detail of the spectral tail form. The pressures oscillations at the central point (P1) and near the plate centre (P6) are much more obvious than those near the edges of the plate (P2), at all impact velocities. The evolution of the impact pressure loading comprises distinct stages: the first shock loading, fluid expansion loadings (under atmosphere pressures) and re-loadings. This evolution of pressures due to impacts in pure water at high velocities (v = 5.5 m/s to 7 m/s) was also observed by Ma et al. (2016). The natural frequency of the falling block, carriage and support frame set-up is about 500 Hz and it is far from the observed oscillation frequencies which vary from 139.9 Hz to 319.7 Hz. These oscillations in pressure may due to repeated compression and expansion of the trapped air when the impact plate is about to hit the water surface (Verhagen, 1967; Lewison and Maclean, 1968) and/or due to reflection of the acoustic shock wave from the bottom of the basin (Lange and Rung, 2011). The time required for pressure wave transmission through twice the water depth is about 1.35 ms as calculated above, which corresponds to a frequency of 740 Hz. Under an impact velocity of 1.33 m/s the peak frequency of the oscillations is 319.7 Hz (Figure 4-3b). Under impact velocities of 4.28 m/s and 7.21 m/s, the peak frequencies of oscillations are approximately the same and of 139.9 Hz (Figure 4-3d,f). Those frequencies of the oscillations are much smaller than the frequency of 740 Hz, which is the estimated frequency of sound wave travels through twice the water depth. Therefore, it is believed that the post-oscillations of the pressure

48

are not due to shock wave reflected from the basin bottom. Table 4-1 presents the oscillation frequencies and their corresponding oscillation periods under different impact velocities. In addition, bubble sizes estimated from the oscillation frequencies applying Minnaert's equation (Minnaert, 1933) are also presented. It is shown in Figure 4-3 and Table 4-1 that as the impact velocity is increased, the frequency of these pressure oscillations reduces and the bubble size for a corresponding oscillation is increased. This suggests that the trapped air bubble, if this is indeed the effect being measured, is larger for higher impact velocity. As mentioned above, it is not possible to observe the trapped air bubble clearly in the underwater camera footage, but the size of trapped air bubble predicted by the theory is consistent, being of the order of the size of the plate. The FFTs presented in Figure 4-3(b,d,f) have shown many high frequency components of the corresponding discrete impact events in the pressure time histories presented in Figure 4-3(a,c,e).
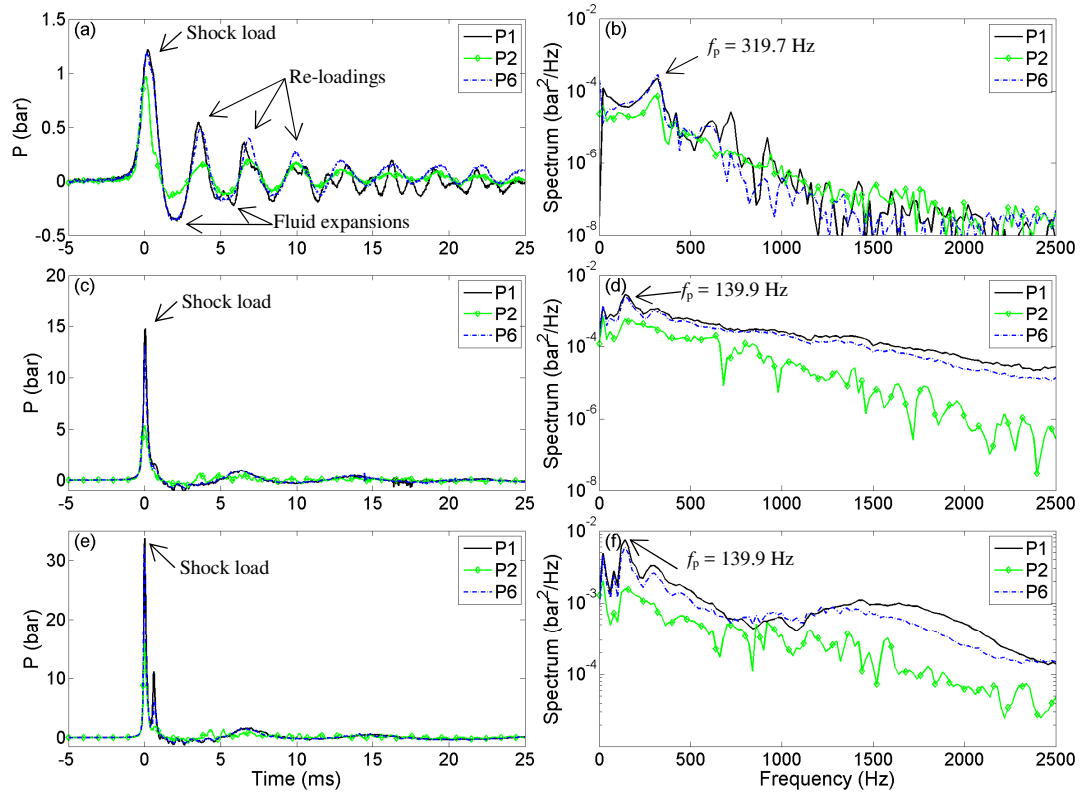
Figure 4-3. Oscillations of pressures (left) and their spectra (right) under impact of the 52 kg rigid plate in pure water: (a, b) v = 1.36 m/s; (c, d) v = 4.28 m/s; (e, f) v = 7.21 m/s. Note the different vertical scales.

Table 4-1: Distinct post-impact pressure oscillation frequencies and associated periods and bubble diameters.

V (m/s)	f (Hz)	T (ms)	D_{bubble} (Minnaert, 1933) (mm)
1.36	319.7	3.13	20.5
4.28	139.9	7.14	46.8
7.21	139.9	7.14	46.8

For structural design, it is essential to understand the maximum environmental load condition. By determining the distribution of maximum pressures on a plate, the local loads and requirement to strengthen parts of the plate can be established, in applications such as the hull of a high speed vessel, the bow of a ship or FPSO hulls (FPSO - Floating Production Storage and Offloading vessel). Spatial 2D-distributions of the maximum pressures on the square plate have been obtained from the available measured pressure points on the plate using the linear integration from the measured data points, which are represented by the dots shown in Figure 4-4. In Figure 4-4, an *xy* plane coordinate system is applied on the surface of the impact plate, with the plate centre at (*x/a*, *y/a*) = (0, 0) and *a* is the half width of the plate. The largest maximum pressure always occurred at the centre of the plate. Locations at about a half way from the centre to the edge of the plate have maximum pressures of about 70% to 80% of the highest pressure at the centre of the plate, while locations near the edges of the plate have maximum pressures of about 40% of the centre pressure.
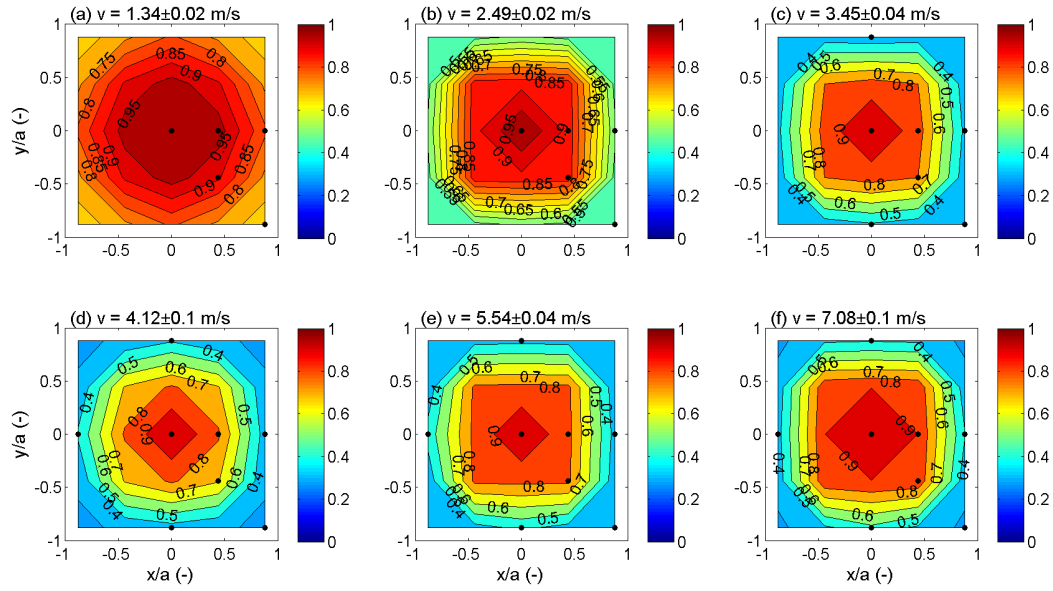
Figure 4-4. Spatial distribution of dimensionless maximum impact pressure ($P_{imax}/P_{I max}$) on the 52 kg rigid plate in pure water for a range of impact velocities. $P_{I max}$ is the maximum impact pressure at the centre of the plate and P_{imax} represents for all locations on the plate surface.

Figure 4-5 and Figure 4-6 present the maximum pressure *P1* measured at the centre of the impact plate and the maximum integrated force *F* against the impact velocity for the rigid tests in pure water with the plate mass of 32 kg and 52 kg, respectively. In each plot of Figure 4-5 and Figure 4-6, the circles represent the experimental maximum pressures (Figure 4-5a & Figure 4-6a) or maximum force (Figure 4-5b & Figure 4-6b) and the solid line represents fitted curves with functions as follows.

For pressure:

$$P_{\max} = a_P v^2 , \qquad (4\text{-}1)$$

or force:

$$F_{\max} = a_F v^2 , \qquad (4\text{-}2)$$

where the empirical coefficients a_P and a_F are estimated by the non-linear least-squares algorithm in Matlab to obtain the best curve fit to the experimental data. Empirical coefficients a_P, a_F and the correlation coefficient R^2 are presented within Figure 4-5 and Figure 4-6. It is clearly shown that the impact pressure and force are proportional to the square of the impact velocity. For the present experiment with $M/\rho l^2$

= 8.2 (for *m* = 32 kg) and 13.3 (for *m* = 52 kg), this relationship of the impact pressure and impact velocity is expected to be linear according to the numerical estimation of Verhagen (1967) for the case with $M/\rho l^2 \gg 1$. The theoretical formulae proposed by von Karman (1929) and Chuang (1966) are also included in Figure 4-5 and Figure 4-6 for comparison. Experimental results of the present study are much lower than the acoustic pressure estimation (von Karman, 1929). In contrast, the current results are much higher than the theory developed by Chuang (1966) at high impact velocities. This may be due to Chuang's theory which was experimentally validated up to impact velocities of 1.92 m/s only. This means that the magnitude of the maximum impact pressure might be considerably affected by any high impact velocity (Chuang, 1966), such as the tested velocities in the range of 2 m/s and 7 m/s in the present study.
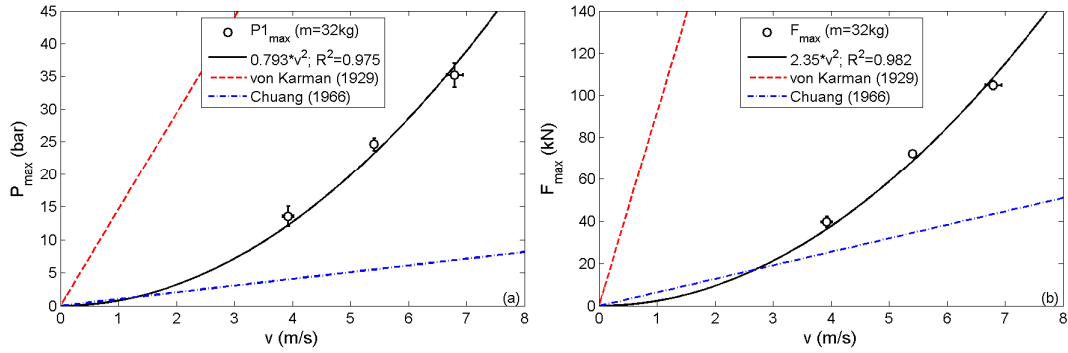
Figure 4-5. Impact pressure and force versus impact velocity for the 32 kg rigid plate in pure water. The error bars represent the standard deviation of the repeated tests.
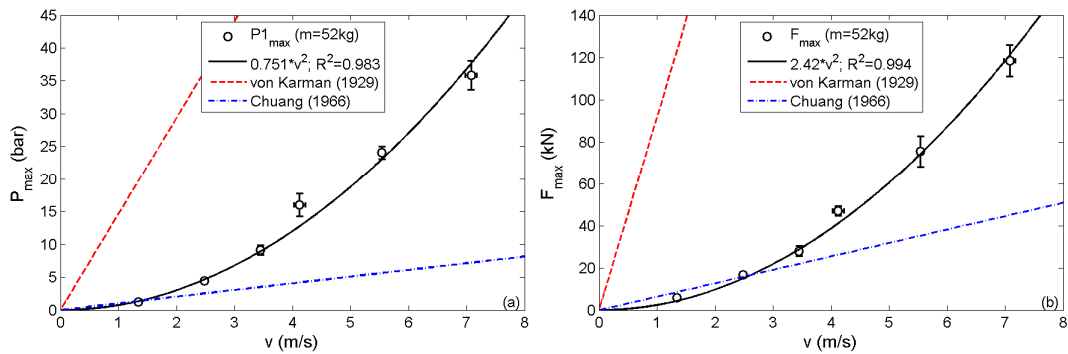
Figure 4-6. Impact pressure and force versus impact velocity for the 52 kg rigid plate in pure water. The error bars represent the standard deviation of the repeated tests.

4.1.2 Rigid plate on aerated water

Figure 4-7 shows the measured acceleration, the integrated velocity and displacement of an impact of the rigid plate in aerated water having a void fraction of 1.6%. The impact velocity was 7 m/s and the plate mass was 52 kg. It is clearly seen that the plate acceleration in aerated water (Figure 4-7a) is much less than in pure water (Figure 4-1a) for the same impact velocity and plate mass. The velocity of the plate decreases smoothly after the plate contacts with the water surface (Figure 4-7b) and the velocity trace after impact is found to be less complex than the impact in pure water presented in Figure 4-1b. The displacement trace of the impact plate in aerated water (Figure 4-7c) looks identical to the one for impact in pure water (Figure 4-1c). The water surface is unstable in this case as it is disturbed by the bubble generation, and the generated bubbles are expected to affect the pressure traces. The measured pressures and integrated force are presented in Figure 4-8. The peak pressures occur at different instances in time, separated by a few milliseconds (Figure 4-8a). Impact pressure and force under this impact case in aerated water are much lower than those in pure water in Figure 4-2. This significant reduction of the impact pressure in aerated water was also found from the experimental studies by drop tests of a circular plate by Bullock et al. (2001) and a cylinder at deadrise angle of 0° by Lange and Rung (2011).

Figure 4-9 presents the pressure traces after impact of the 52 kg rigid plate in aerated water (β = 1.6 %) with the impact velocities of 4.12 m/s and 7 m/s. There is no distinct oscillation of pressures after the impact in aerated water (Figure 4-9a,c) unlike what was observed from the impact in pure water (Figure 4-3a,c,e). It seems to be a quasi-hydrostatic pressure after the impact in aerated water. The associated pressure amplitudeFFT spectra are presented in Figure 4-9(b,d) and there is no high frequency peak unlike that observed in pure water due to the trapped air between the plate and water surface, and this is again likely to be due to the uneven free surface created by the

bubble generation. However, the FFTs in Figure 4-9(b,d) clearly show many high frequencies of the corresponding discrete impact events in the pressure time histories presented in Figure 4-9(a,c).
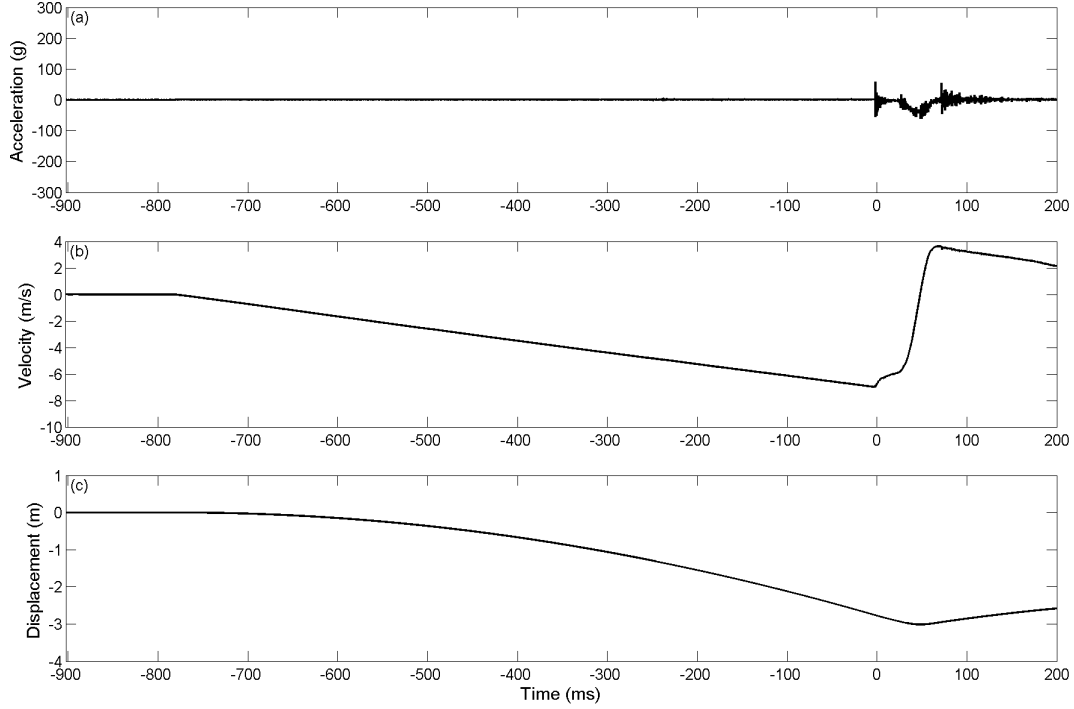
Figure 4-7. Typical time-history of acceleration, velocity and displacement under impact of the 52 kg rigid plate in aerated water $\beta = 1.6$ % ($v = 7$ m/s).
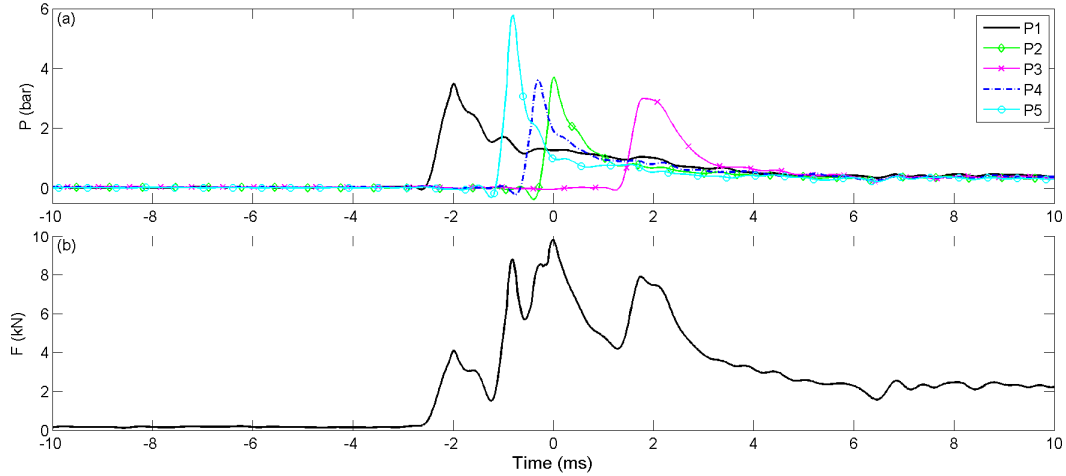
Figure 4-8. Typical time-history of pressures and force under impact of the 52 kg rigid plate in aerated water $\beta = 1.6$ % ($v = 7$ m/s).

54
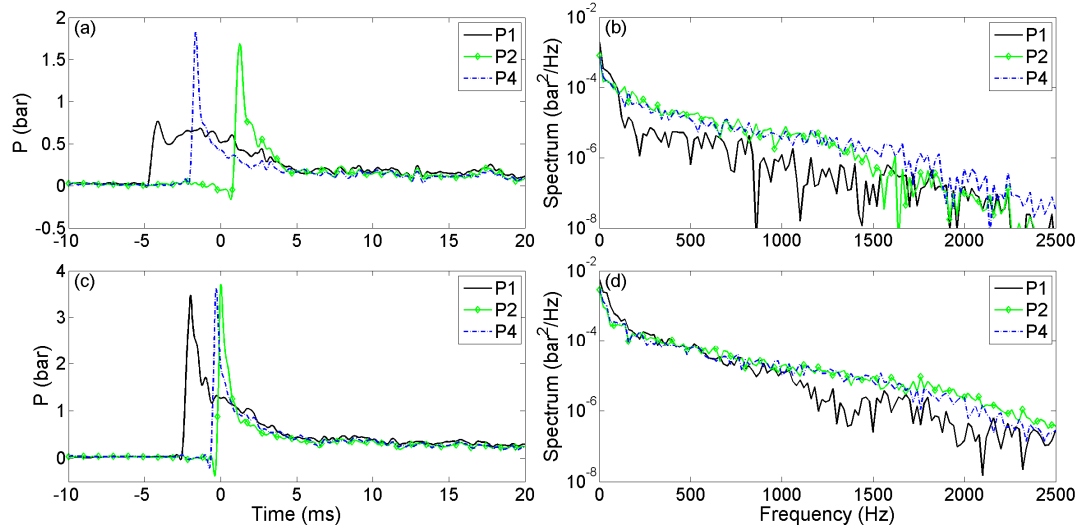
Figure 4-9. Oscillations of pressures (left) and their spectra (right) under impact of the 52 kg rigid plate in aerated water $\beta = 1.62$ %: (a, b) $v = 4.12$ m/s; (c, d) $v = 7.0$ m/s. Note the different vertical scales.

4.1.3 Elastic plates on pure water

Typical time-histories of the measured acceleration and the integrated velocity and displacement of the 52 kg elastic plates are shown in Figure 4-10 for the elastic plate 1 (using springs CXF51x54) with an impact velocity of 4.11 m/s and Figure 4-11 for the elastic plate 2 (using springs CXF51x102) with an impact velocity of 3.90 m/s. The acceleration of the elastic plates was measured by a 500g accelerometer and the maximum acceleration of the plates was found to be larger than 500g. The associated pressures and deflection of springs and the spatial integrated force are presented in Figure 4-12 and Figure 4-13 for the elastic plates 1 & 2, respectively. Figure 4-12a and Figure 4-13a present the pressures measured at locations P1 and P2 on the elastic plates 1 and 2 (see Figure 3-4 for the measured pressure locations). As was found for impact of the rigid plate, the impact pressures at locations near the edge (P2) are always attained earlier than the others at the centre of the impact plate (P1) and they are always much smaller than those at the plate centre under violent impacts. The spatially integrated force and the measured deflection of springs are respectively presented in Figure 4-12b and Figure 4-12c for the elastic plate 1, and in Figure 4-13b and Figure 4-13c for the elastic plate 2. The maximum force of 37.82 kN on the elastic plate 1 due

to impact with v = 4.11 m/s is very slightly higher than that on the elastic plate 2 due to impact with v = 3.90 m/s, where the maximum force was 37.00 kN. In contrast, the maximum deflection of the springs of the elastic plate 1 (D_{max} = 1.47 mm) is measurably smaller than that for the elastic plate 2 (D_{max} = 1.87 mm). The maximum deflection was attained at about from 2 ms to 3 ms after the impact (t = 0). This delay was also found in the drop test presented by Faltinsen (1997 & 2000). It may be due to the natural response period of the tested springs. The natural period of a spring can be estimated from $T = 2\pi (m_s/k)^{0.5}$, where m_s is the mass of spring in kg and k is the spring rate in N/m. Therefore, the natural periods of the springs CXF51x54 (m_{s1} = 0.41 kg) and CXF51x102 (m_{s2} = 0.66 kg) are calculated to be T_1 = 4.8 ms and T_2 = 8 ms, respectively. The rise time of the maximum deflections is about 2.2 ms for both spring types (Figure 4-12c and Figure 4-13c). This rise time is about a half of the natural period of the spring CXF51x54 (T_1 = 4.8 ms) and about one quarter of the natural period of the spring CXF51x54 (T_2 = 8 ms). Note that in this experiment the springs were allowed to compress only.
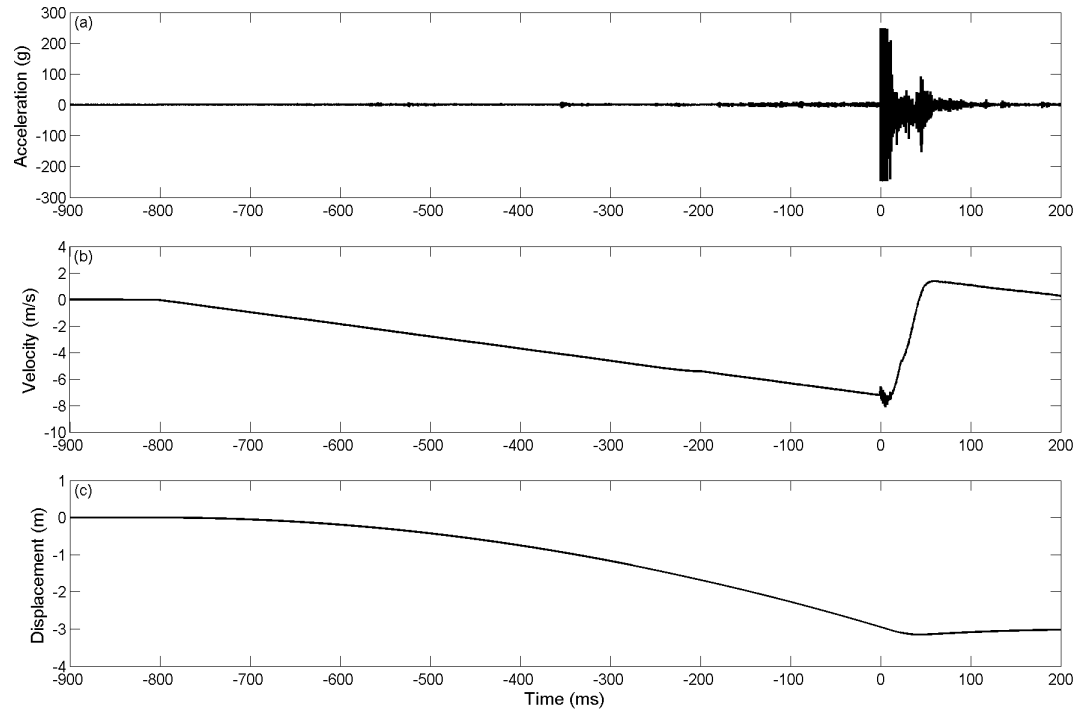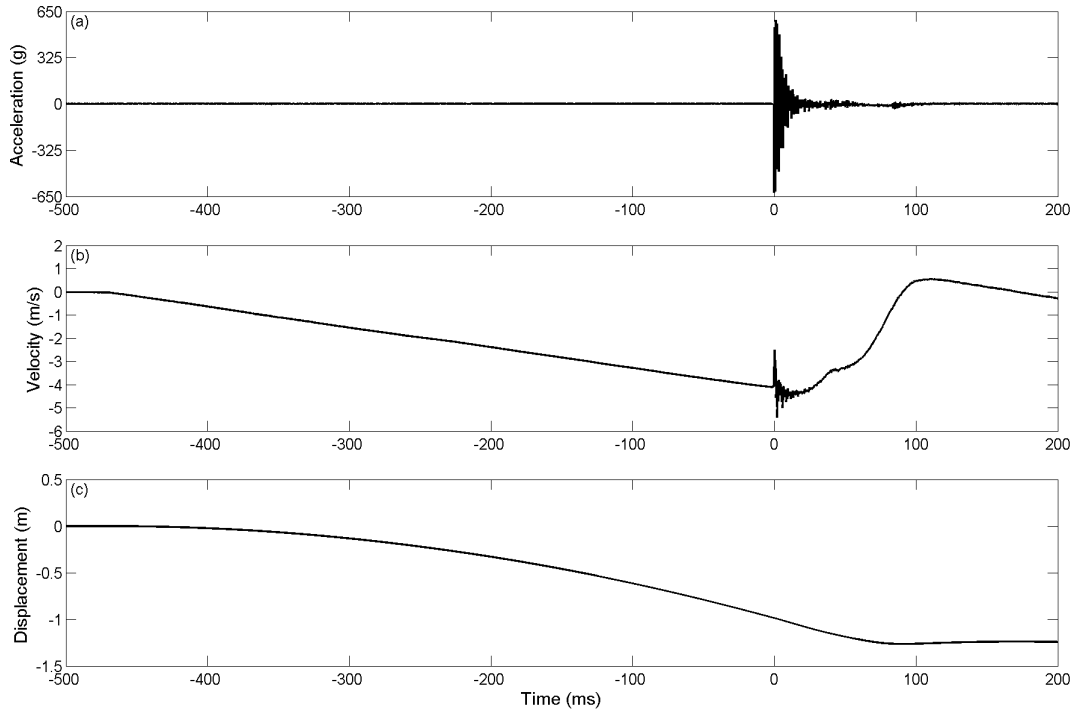

Figure 4-10. Typical time-history of acceleration, velocity and displacement of the 52 kg elastic plate 1 in pure water for v = 4.11 m/s.
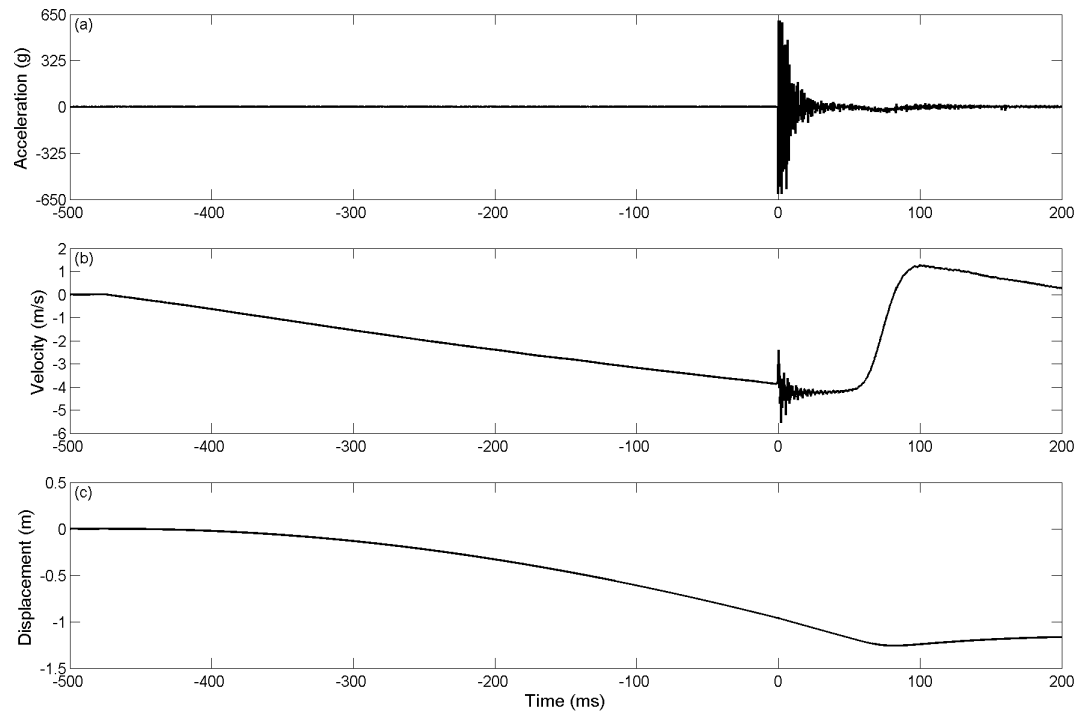
Figure 4-11. Typical time-history of acceleration, velocity and displacement of the 52 kg elastic plate 2 in pure water for v = 3.9 m/s.
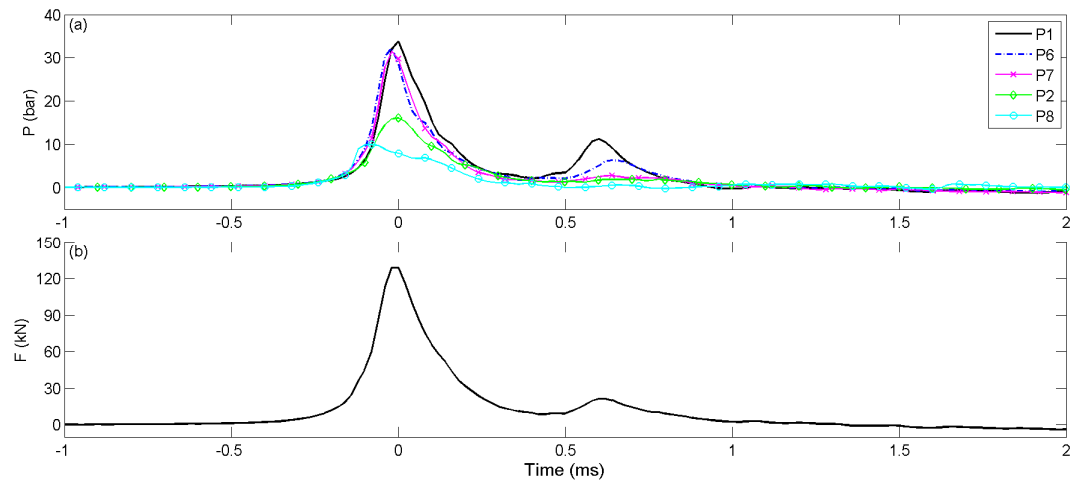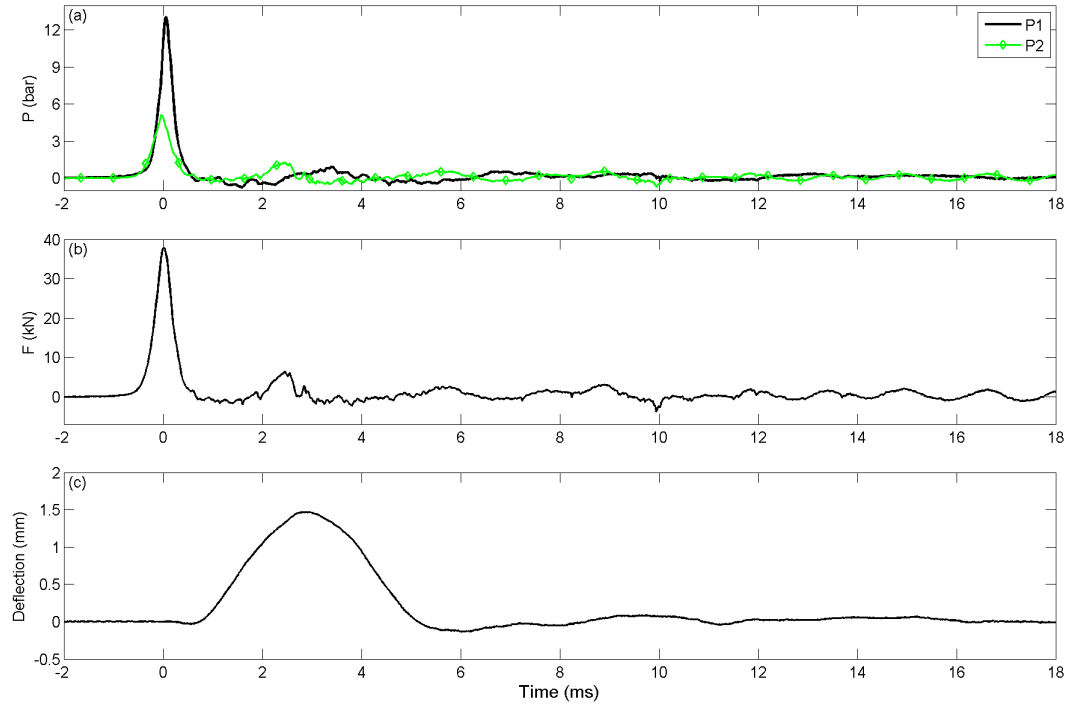

Figure 4-12. Typical time-history of pressures, force and deflection of springs of the 52 kg elastic plate 1 in pure water for v = 4.11 m/s.
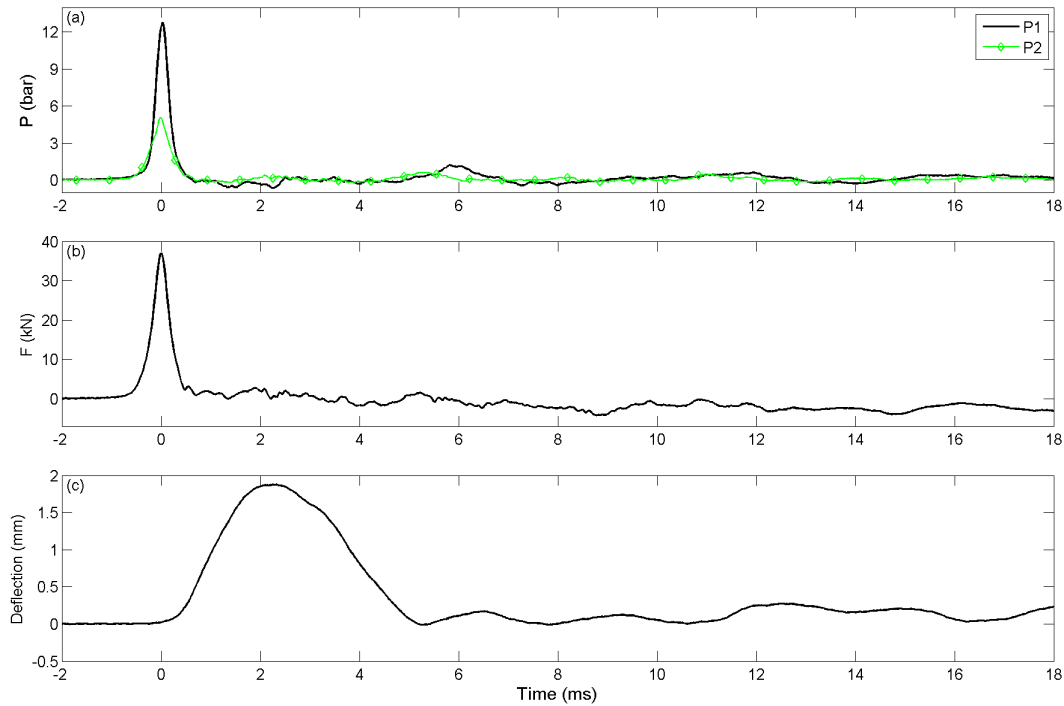
Figure 4-13. Typical time-history of pressures, force and deflection of springs of the 52 kg elastic plate 2 in pure water for *v* = 3.90 m/s.

Distinct post-impact pressure oscillations under impact of the elastic plates onto the water surface were also observed in this experiment. Pressure P1, P2 and P6 are presented and compared with the impact of the rigid plate in pure water in Figure 4-14 to Figure 4-16, in which the impact velocities were 1.28±0.07 m/s, 4.08±0.17 m/s and 6.96±0.18 m/s, respectively. In Figure 4-14, the first pressure peak on impact decreases with increasing elasticity of the plate. The oscillation after the impact is believed to be caused by the oscillation of the trapped air between the impact plate and water surface, which has been discussed in the previous sections. The FFT spectra of the measured pressures are given in the right hand plots in the figures. Under higher impact velocities (*v* = 4.08±0.17 m/s and 6.96±0.18 m/s), there are significant differences in the post-impact oscillations between the rigid plate and elastic plates with higher frequency peaks evidence for the elastic plates (Figure 4-15 and Figure 4-16). Significant differences between the pressure traces for rigid and flexible panels were also found from the controlled water slam test of composite hull panels presented by Battley et al. (2009), Stenius (2009) and Stenius et al. (2011a). Higher oscillation frequency of the

pressure under impact of an elastic plate was also observed by Tenzer et al. (2015). In the present study, it is clearly seen for the elastic plates that there are higher order frequencies in the pressure oscillations under high impact velocities and most of these oscillation frequencies are higher than the natural frequency of the impact plate (Figure 4-15 and Figure 4-16). As it was found in the impact of the rigid plate in pure water, the high peak frequencies (339.7 Hz and 139.9 Hz) of the post-impact pressures (Figure 4-14b,d,f; Figure 4-15b,d,f and Figure 4-16b,d,f) may due to the repeated compression and expansion of the different diameter trapped air bubbles when the impact plate is about to hit the water surface (see Table 4-1). As a result of the shock wave traveling through the air gap along the width of the rigid plate (Section 4.1.1), a second pressure shock was observed at an early stage ($t = 0.6$ ms) under impact velocity of 6.96±0.18 m/s (the solid lines in Figure 4-16a), but this second pressure shock does not seem to be evident in the elastic plate experiments (the dashed and dotted lines in Figure 4-16a). The second pressure peak appears coincident with the oscillations caused by the plate elasticity and the trapped air under the plate. There is also no evidence of this second pressure peak from the previous experimental drop test studies in which plates with large deadrise angles (5° and 10°) were used and so no air bubble could be trapped under the plate. Similar to the impact of the rigid plate in pure water, the impact of elastic plates in pure water have shown many high frequency peaks of the corresponding discrete impact pressure events and these high frequencies are slightly different between the rigid and elastic plates (Figure 4-14b,d,f; Figure 4-15b,d,f; Figure 4-16b,d,f).
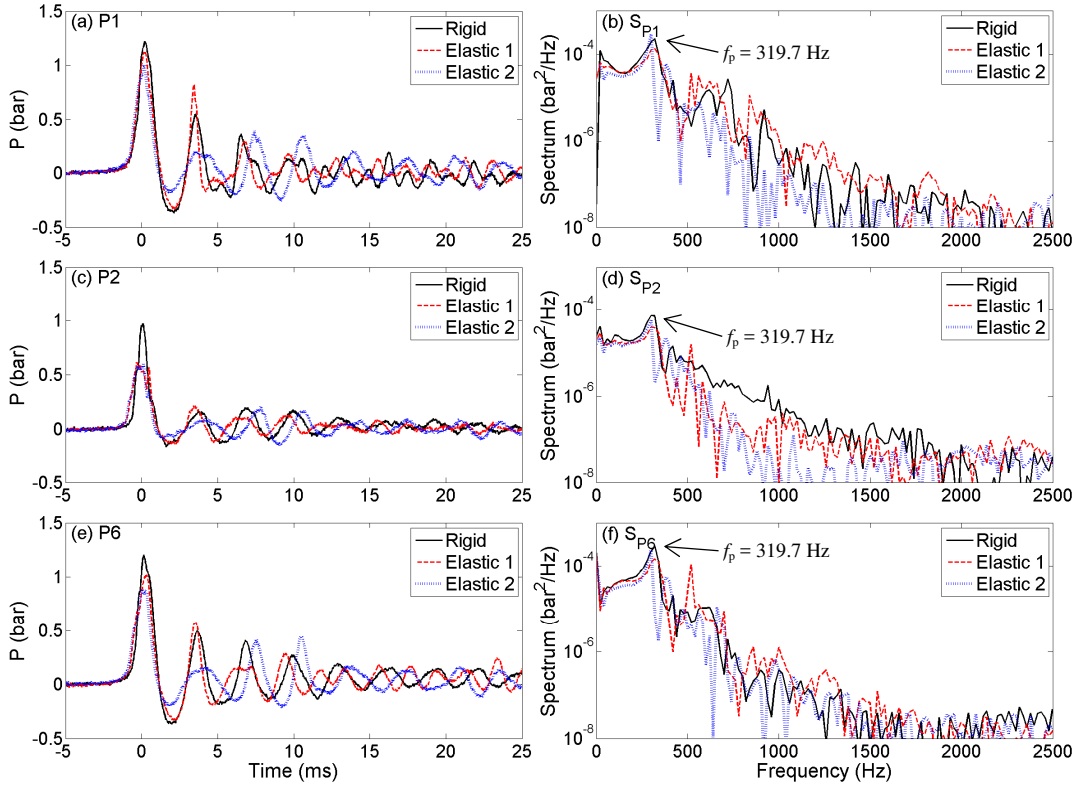
Figure 4-14. Oscillations of pressures (left) and their spectra (right) due to impact of rigid and elastic plates in pure water (v = 1.28±0.07 m/s, m = 52 kg). Note the different vertical scales.
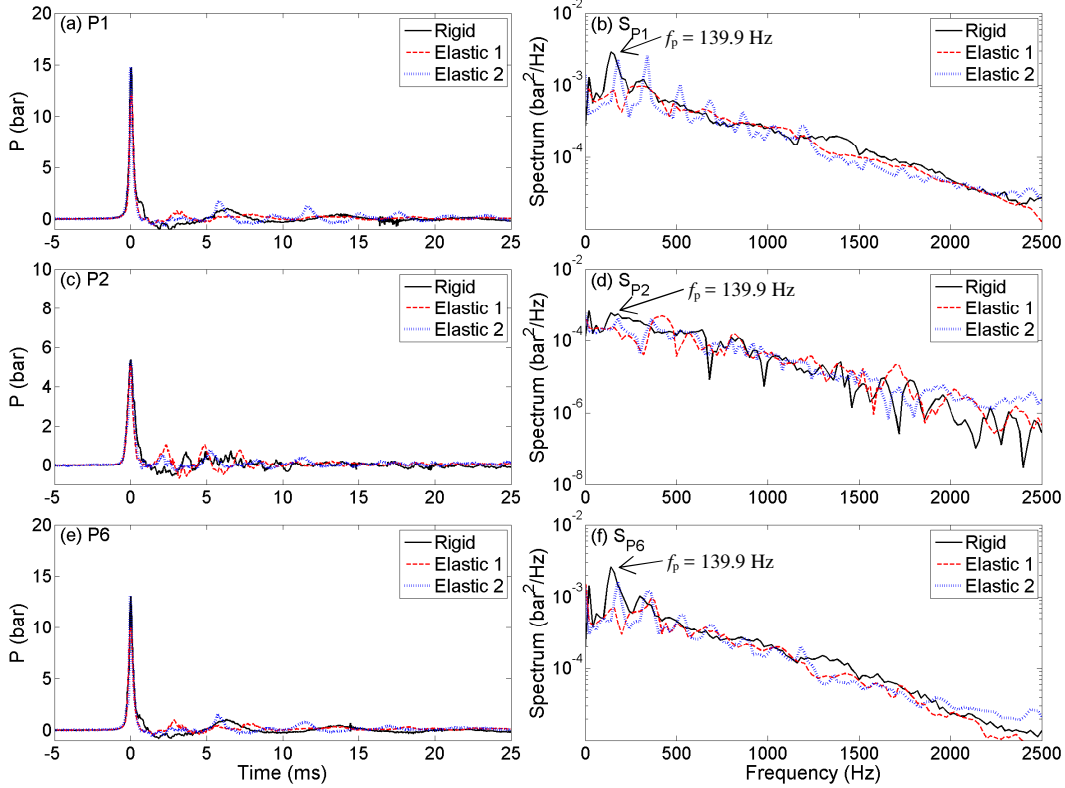
Figure 4-15. Oscillations of pressures (left) and their spectra (right) due to impact of rigid and elastic plates in pure water (v = 4.08±0.15 m/s, m = 52 kg). Note the different vertical scales.

60
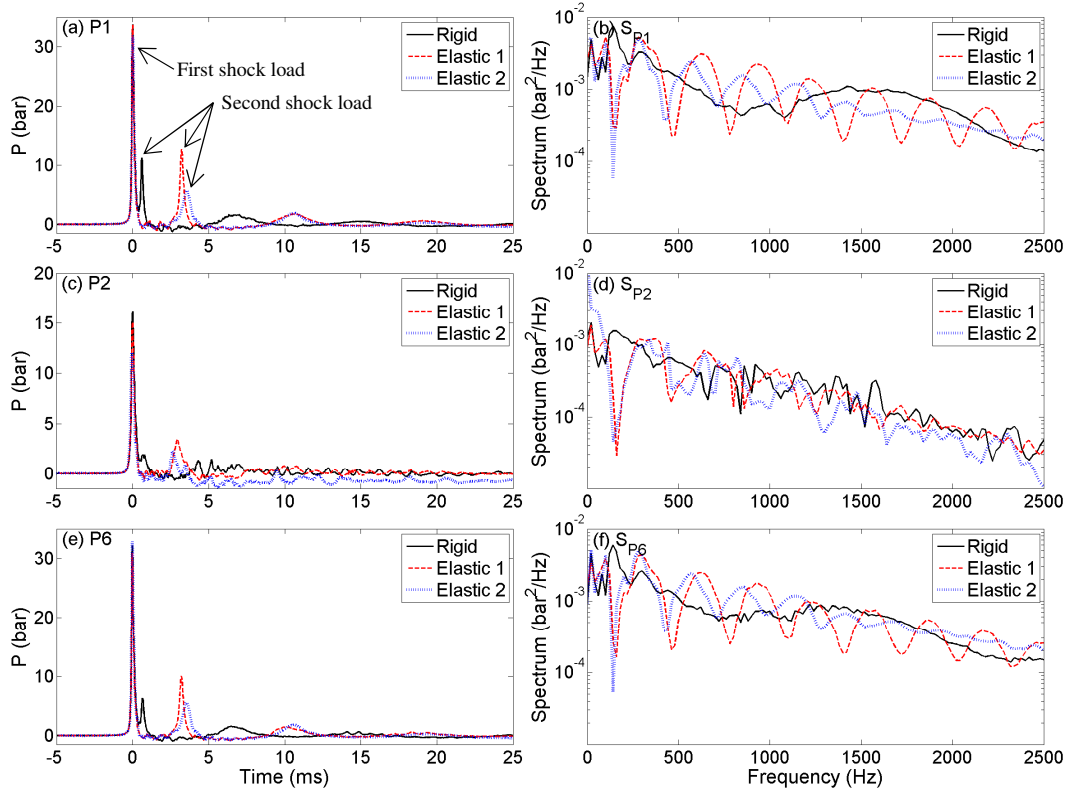
Figure 4-16. Oscillations of pressures (left) and their spectra (right) due to impact of rigid and elastic plates in pure water (v = 6.96±0.18 m/s, m = 52 kg). Note the different vertical scales.

4.1.4 Elastic plates on aerated water

Typical time-histories of pressures under impacts of the 52 kg elastic plates into aerated water (β = 1.6 %) are presented in Figure 4-17(a,c) and Figure 4-18(a,c). Similar to impact of the rigid plate in aerated water, the impact pressures under impact of the elastic plates varied temporally and spatially due to the presence of the generated bubbles and the disturbance of the water surface. Figure 4-17(b,d) and Figure 4-18(a,c) show the FFTs of the corresponding pressure signals presented in Figure 4-17(a,c) and Figure 4-18(a,c), respectively. It is seen that there is no distinct high frequency peak of the corresponding distinct post-impact pressure oscillations under the impact in aerated water and this is similar to the observation of pressures under impact of the rigid plate in aerated water (Figure 4-9). However, the FFTs show many high frequencies of the corresponding discrete impact pressure events.
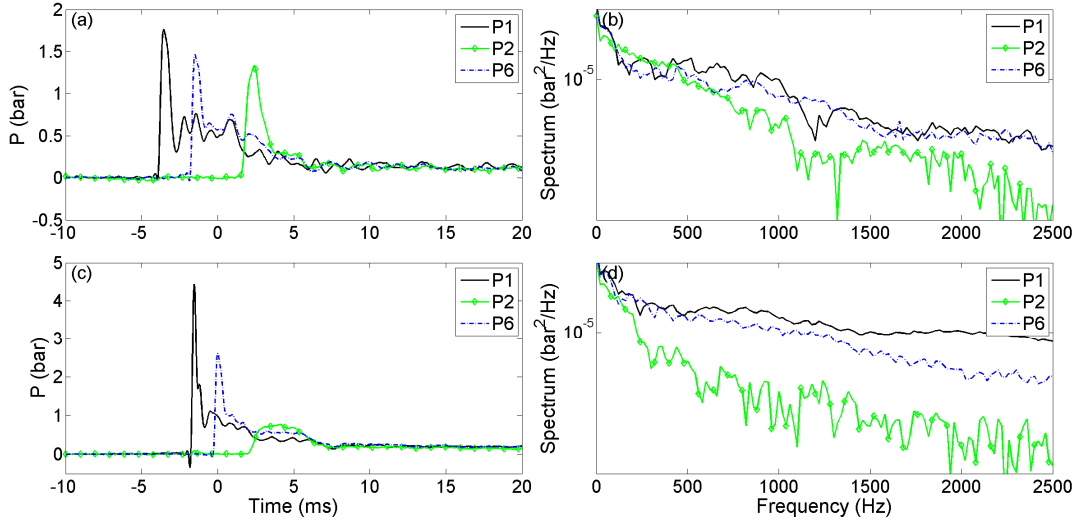
Figure 4-17. Pressure time histories (left) and their spectra (right) under impact in aerated water $\beta = 1.6$ %: (a, b) $v = 4.05$ m/s; (c, d) $v = 5.37$ m/s. Elastic plate 1: $m = 52$ kg. Note the different vertical scales.
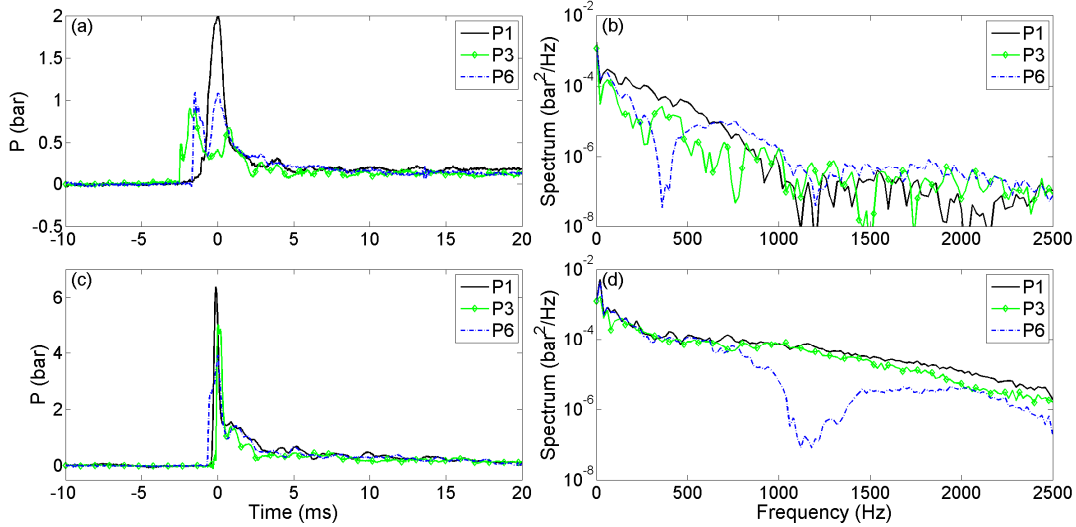
Figure 4-18. Pressure time histories (left) and their spectra (right) under impact in aerated water $\beta = 1.6$ %: (a, b) $v = 3.77$ m/s; (c, d) $v = 6.69$ m/s. Elastic plate 2: $m = 52$ kg. Note the different vertical scales.

4.2 Discussion of aeration effect on slamming impacts

4.2.1 Impact pressures and force using pure and aerated water

All maximum pressures measured at all locations for impacts in pure and aerated water are presented in Figure 4-19. Figure 4-19a and Figure 4-19b present the maximum pressures under impact of the 32 kg and 52 kg rigid plates, respectively. It is shown that the impact pressures in pure water (the black circles in plots) are much higher than those measured in aerated water of 0.8 %, 1 % and 1.6 % void fraction. With the presence of

air in the water the impact pressure in aerated water decreases significantly in comparison with the impact pressure in pure water. For example, for an impact velocity of 7 m/s and mass of 52 kg, the impact pressure in pure water $P1_{max}$ = 33.23 bar, is reduced to that of 4.45 bar when the water has an aeration level of 1.6 %. This shows that the aeration has an important role during impact and can reduce impact pressure significantly. In addition, the water surface distortion also affects the impact pressures for the tests in aerated water. The water surface was disturbed by the bubble generation system, therefore the impacts in aerated water were not perfectly flat impacts as in pure water. Because of the water surface distortion, the impacts in aerated water were reduced due to the small local deadrise angle, which is shown by others to cause the impact pressure to decrease (Chuang, 1966a; Lewison, 1969; Van Nuffel et al., 2014).
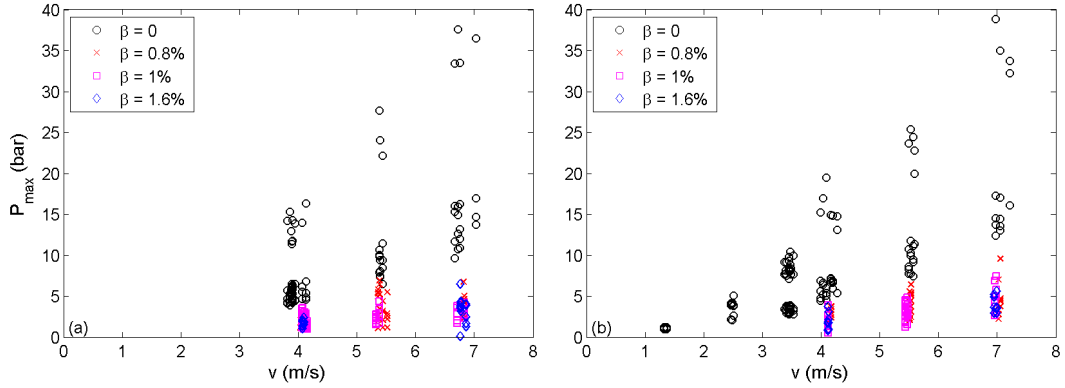
Figure 4-19. Impact pressures on rigid plate in pure and aerated water: (a) *m* = 32 kg; (b) *m* = 52 kg.

Both lognormal and extreme value models have been used to test the measurements with aerated water presented in Figure 4-19 to ascertain that no accidentally sampled measurements with a much higher probability of non-exceedance are included. Figure 4-20 to Figure 4-25 present the Cumulative Density Function (CDF or probability of non-exceedance) of lognormal and extreme value models applied to P_{max} measured in aerated water. The 95 % confidence intervals (CI) are also plotted for lognormal and extreme value models which are applied to each data set. The empirical CDF of P_{max} is estimated using Bernard's approximation for sample size less than 100: probability = (*i*-0.3)/(*N*+0.4), in which *i* is the index of event sorted in ascending order and *N* is the total

number of events (Stapelberg, 2009). In general, it is shown that the measured data fit quite well to a lognormal and/or extreme value model. All measured data are placed in the 95% confidence interval of the applied models. This means that no measured data with a much higher probability of non-exceedance are included in Figure 4-19.
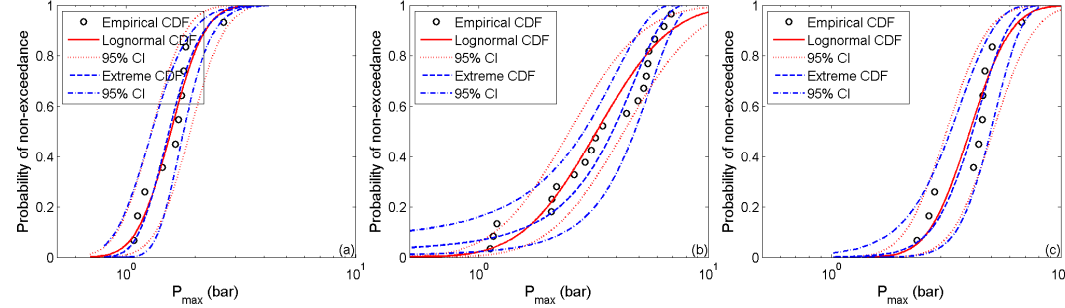
Figure 4-20. Probability of non-exceedance of P_{max} on the 32 kg rigid plate in aerated water (β = 0.8 %): (a) v = 4.02±0.14 m/s; (b) v = 5.25±0.44 m/s; (c) v = 6.78±0.19 m/s.
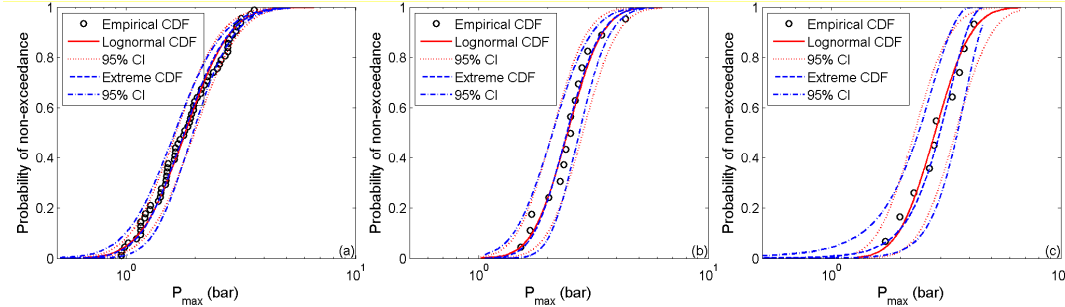
Figure 4-21. Probability of non-exceedance of P_{max} on the 32 kg rigid plate in aerated water (β = 1.0 %): (a) v = 4.02±0.14 m/s; (b) v = 5.25±0.44 m/s; (c) v = 6.78±0.19 m/s.

Figure 4-22. Probability of non-exceedance of P_{max} on the 32 kg rigid plate in aerated water (β = 1.6 %): (a) v = 4.02±0.14 m/s; (b) v = 6.78±0.19 m/s.
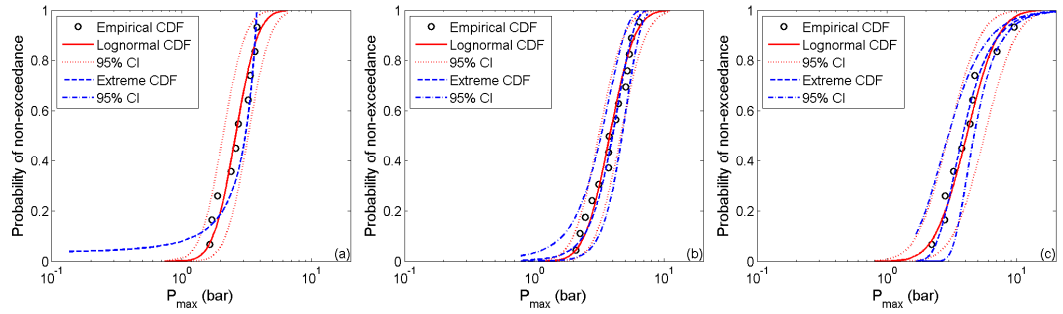
Figure 4-23. Probability of non-exceedance of P_{max} on the 52 kg rigid plate in aerated water ($\beta = 0.8$ %):

(a) $v = 4.02\pm0.14$ m/s; (b) $v = 5.25\pm0.44$ m/s; (c) $v = 6.78\pm0.19$ m/s.
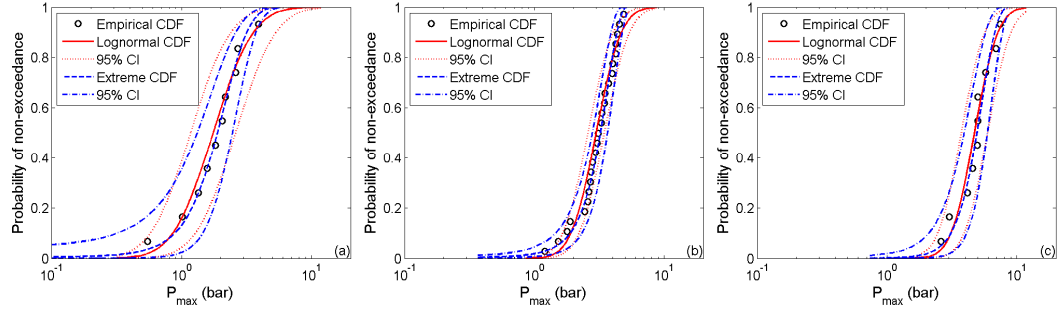
Figure 4-24. Probability of non-exceedance of P_{max} on the 52 kg rigid plate in aerated water ($\beta = 1.0$ %):

(a) $v = 4.02\pm0.14$ m/s; (b) $v = 5.25\pm0.44$ m/s; (c) $v = 6.78\pm0.19$ m/s.
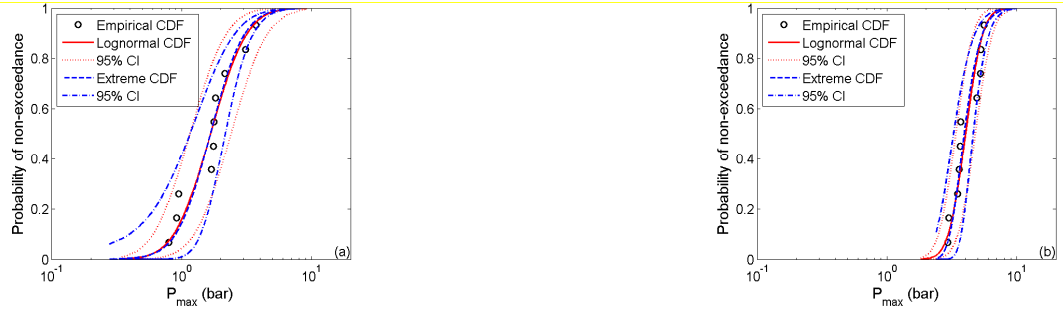
Figure 4-25. Probability of non-exceedance of P_{max} on the 52 kg rigid plate in aerated water ($\beta = 0.8$ %):

(a) $v = 4.02\pm0.14$ m/s; (b) $v = 6.78\pm0.19$ m/s.

Maximum forces in pure and aerated water are presented in Figure 4-26 for the tested rigid plates ($m = 32$ kg and 52 kg). The error bars in the plots of the figure indicate standard deviation obtained from 3 to 10 repeats. It shows that there is also significant reduction in the impact force from tests conducted in pure water in comparison with those conducted in aerated water. Figure 4-27 and Figure 4-28 show the maximum force versus void fraction (β) of the water for the rigid plate mass of 32 kg and 52 kg, respectively. Within the range of the experimental data in the present study, the maximum force appears to be as an exponential function of the void fraction, given by:

$$F_{max} = k_F e^{n\beta} \qquad , \qquad (4\text{-}3)$$

in which, coefficients k_F and n are estimated using the non-linear least-squares algorithm in Matlab to obtain the best curve fitted to the experimental data. This relationship is entirely empirical from the experimental data in this study from data fitting the results. The best fitted curve and its function are presented in each plot of Figure 4-27 and Figure 4-28 for each impact velocity. They show similar behaviour to the experimental results by Bullock et al. (2001) and simulations by Ma et al. (2016). These authors also found that there is significant reduction of the impact pressures even due to presence of a relatively small air content and that the aeration effect increased with the violence of the impact.
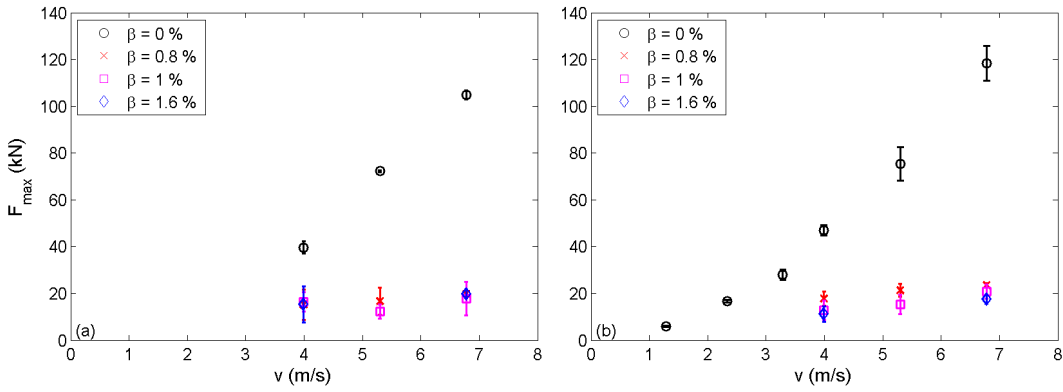
Figure 4-26. Impact force on rigid plate in pure and aerated water: (a) m = 32 kg; (b) m = 52 kg. Error bars indicating standard deviation.
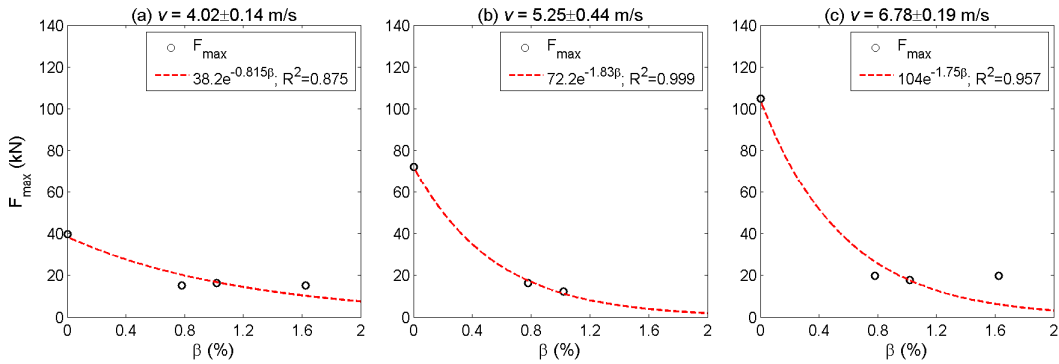
Figure 4-27. Impact force on rigid plate as a function of void fraction β (m = 32 kg).
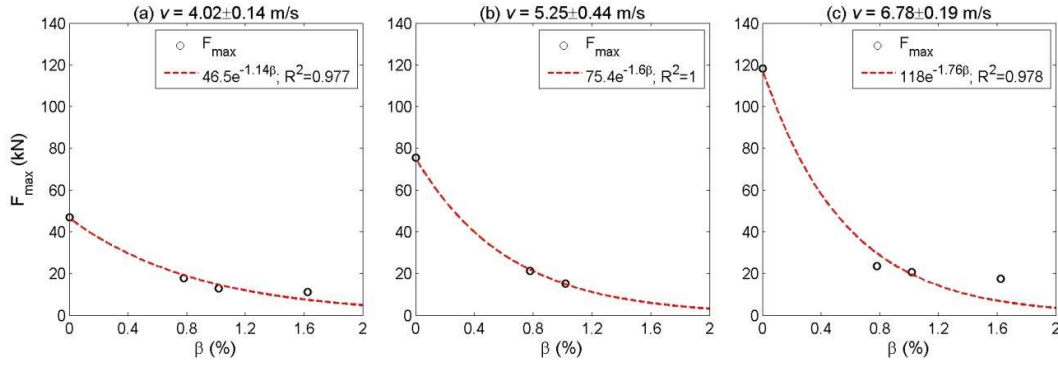
Figure 4-28. Impact force on rigid plate as a function of void fraction β (m = 52 kg).

4.2.2 Impulses (pressure and force) using pure and aerated water

Impulse, which is defined as the change in momentum of an object, can be obtained by integrating force values over the duration of the impact (Cooker & Peregrine, 1995; Bullock et al., 2007). The impulse is known less sensitive than the loading peak (Bullock et al., 2007), therefore it is useful to present results in terms of impulses. In the present study, the first impulse (I^{first}) of the impact is defined as the impulse of the first positive phase of the impact, i.e. the area A1 in Figure 4-29 and the total impulse (I^{total}) is integrated from the start of the impact until the signal falls back to the noise level, i.e. the sum of the areas A1 to A7 in Figure 4-29. It is noted that, the "total impulse" for the drop tests is calculated for a duration of time from the start time of an impact until the time when the impact plate was not restrained by the rope used to stop the plate falling onto the basin floor. Therefore, the "total impulse" used in this analysis does not consider the total impulse of the object brought to rest and therefore there may be a difference between the total impulses for various impacts.
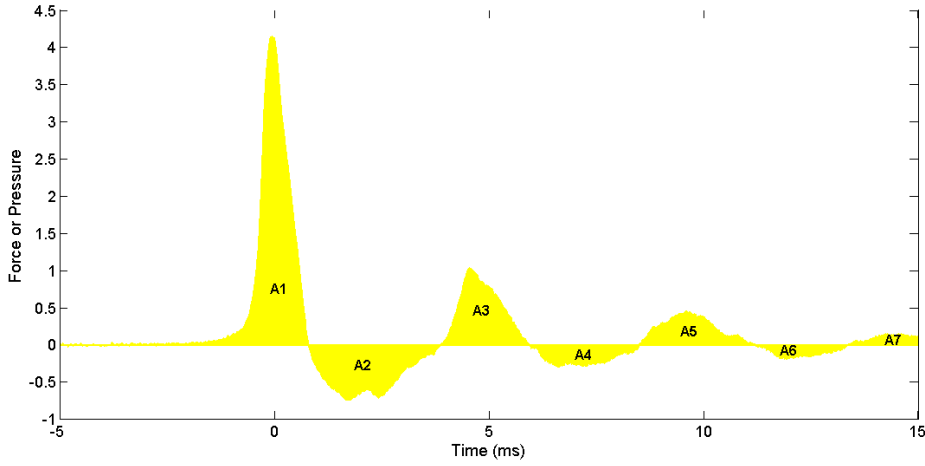
Figure 4-29. Definition sketch for the first impulse (I^{first}) and total impulse (I^{total}).

Pressure impulses of the rigid plate impact in pure and aerated water are presented in Figure 4-30 and Figure 4-31. It is shown that the first pressure impulses (I_P^{first}) of the impact in pure water are much higher than those in aerated water and there is a linear relationship between the first impulse and the impact velocity (Figure 4-30). In pure water, scattering of the first pressure impulse is much smaller than the scattering of the impact pressures P_{max} presented in Figure 4-19. This smaller scattering of the first pressure impulse was also found from the experimental work by Zhu (1995). In contrast, variation of the first pressure impulse is still as large as the variation of the impact pressures (Figure 4-19) for the aerated water. The total pressure impulses (I_P^{total}) are presented in Figure 4-31 and their variation in pure water is as large as the variation in aerated water. Additionally, there is no reduction of the total pressure impulses from pure water to aerated water for both the 32 kg and 52 kg rigid plates.

Figure 4-32 and Figure 4-33 present the first positive phase force impulse (I_F^{first}) and the total force impulse (I_F^{total}), respectively. Similar to the pressure impulse findings, the first force impulses in pure water are significantly larger than those in aerated water. In pure water, the variation of the first force impulse is larger than the variation of the first pressure impulse, especially at high impact velocities from 4 m/s to 7 m/s (see Figure 4-30 and Figure 4-32). Bullock et al. (2007) also presented the large variation of the

first force impulse from their experimental work of wave impacts. The total force impulses in pure and aerated waters are more or less the same, except the impacts of the 52 kg rigid plate show the total force impulses in aerated water are higher than those in pure water (see Figure 4-33b).
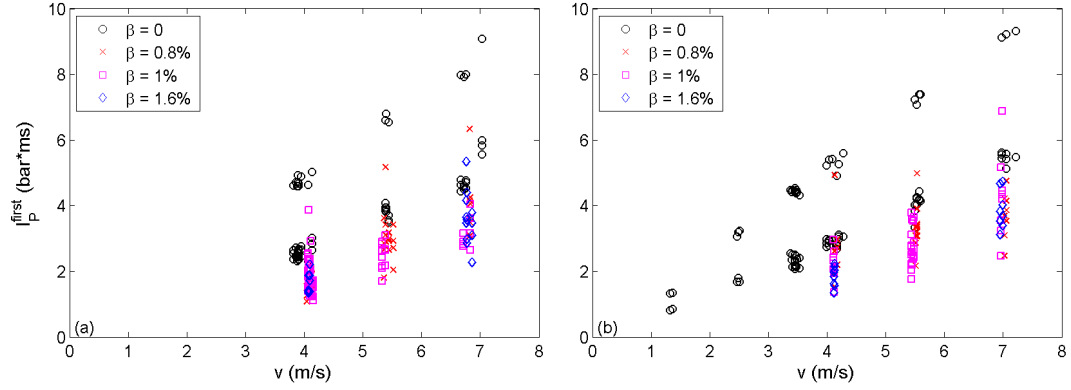
Figure 4-30. I_P^{first} of rigid plate impact in pure and aerated water: (a) $m = 32$ kg; (b) $m = 52$ kg.
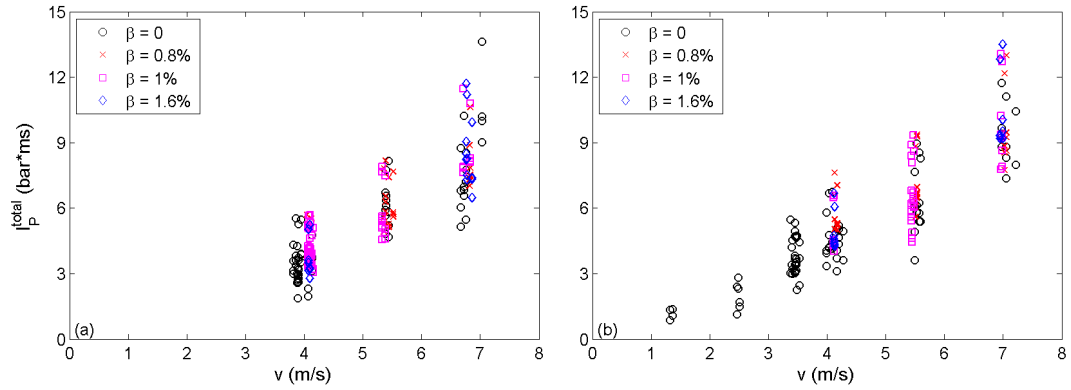
Figure 4-31. I_P^{total} of rigid plate impact in pure and aerated water: (a) $m = 32$ kg; (b) $m = 52$ kg.
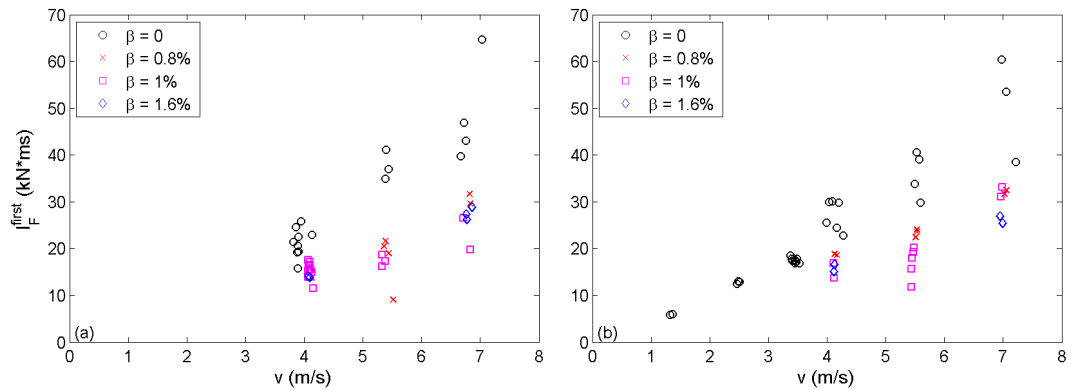
Figure 4-32. I_F^{first} of rigid plate impact in pure and aerated water: (a) $m = 32$ kg; (b) $m = 52$ kg.
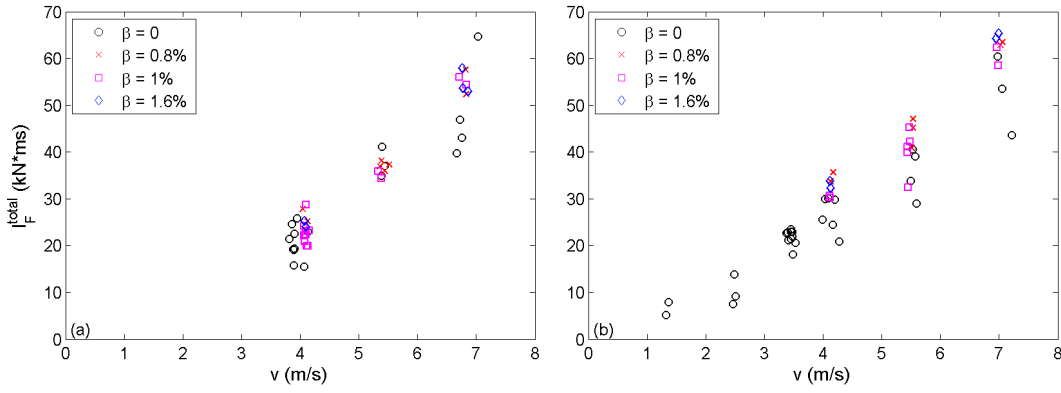
Figure 4-33. I_F^{total} of rigid plate impact in pure and aerated water: (a) $m = 32$ kg; (b) $m = 52$ kg.

4.3 Discussion of hydroelasticity effect on slamming impacts

4.3.1 Impact pressure and force on rigid and elastic plates

Figure 4-34 presents the impact pressures and forces under the impacts of the rigid and elastic plates in pure water. The impact pressures are presented in Figure 4-34a for the measured location at the centre of the plate (P1). The impact forces are shown in Figure 4-34b. In general, there is a slight reduction in impact pressure and force only at the higher velocities, beyond 5 m/s. This limited reduction may due to the stiffness of springs used to form the elastic plate 1 and 2. The results presented by Tenzer et al. (2015) also did not show a clear trend of hydroelasticity effects on pressure peaks, with the body they tested also being relatively stiff. Stenius et al. (2011a, b) showed that measured pressure magnitudes increase at the centre of the panel width of a wedge with increasing flexibility of the tested body with this trend being similar to their numerical simulations. They found a change of pressure magnitudes as a result of the local change in deadrise angle and impact velocity for a flexible body.
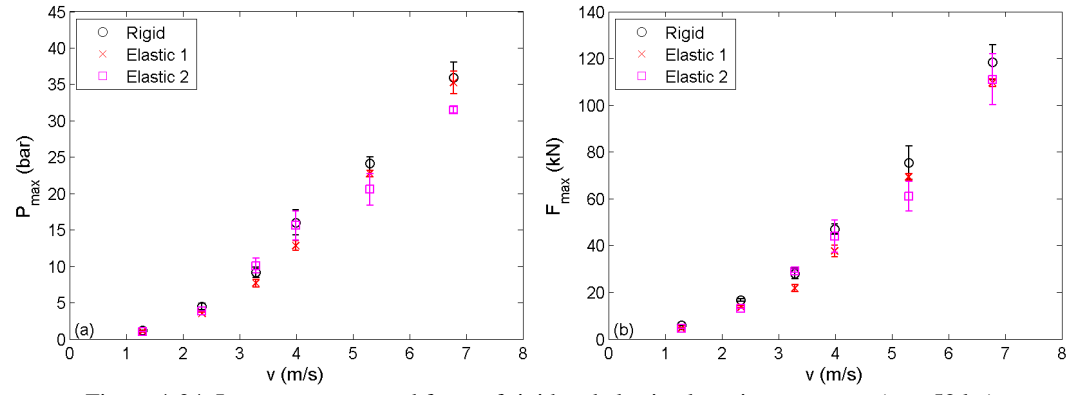
Figure 4-34. Impact pressure and force of rigid and elastic plates in pure water ($m = 52$ kg).

4.3.2 Impulses (pressure and force) on rigid and elastic plates

I_P^{first} and I_F^{first} of the rigid and elastic plates impact in pure water are presented in Figure 4-35. The masses of the plates are all of 52 kg. It is shown that I_P^{first} and I_F^{first} of the rigid plate are generally higher than those for the elastic plates. This can be seen most clearly at the high impact velocities beyond 4 m/s. However, the total impulses of pressure and force (I_P^{total} and I_F^{total}) presented in Figure 4-36 show there is no clear difference between the total impulses of the rigid and elastic plates.
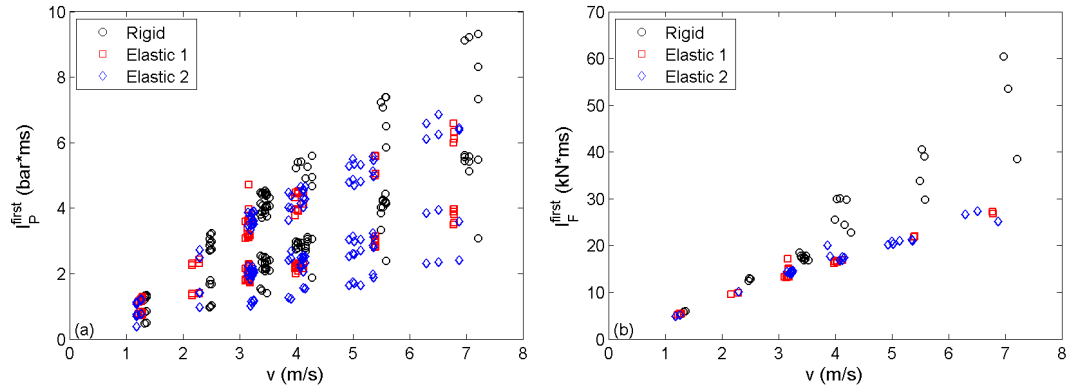
Figure 4-35. I_P^{first} (a) and I_F^{first} (b) of the rigid and elastic plates impact in pure water ($m = 52$ kg).
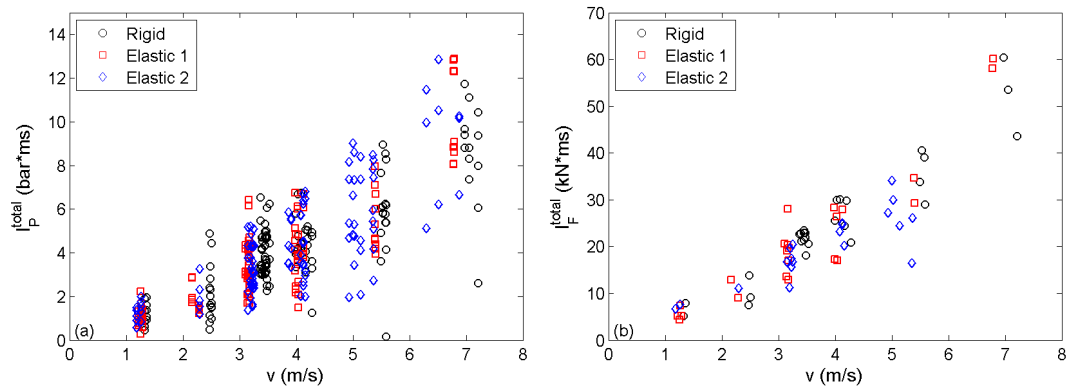
Figure 4-36. I_P^{total} (a) and I_F^{total} (b) of the rigid and elastic plates impact in pure water ($m = 52$ kg).

71

4.4 Discussion of combined aeration and hydroelasticity effect on slamming impacts

4.4.1 Impact pressure and force

The impact pressures (P_{max}) measured in aerated water have been tested with lognormal and extreme value models to ascertain that no accidentally sampled measurements with a much higher probability of non-exceedance are included in analysis. The results show that there is no sampled data are located outside of the 95% confidence intervals of lognormal and/or extreme value models which are used to test each data set of each impact velocity (see Appendix A.2).

Impact pressures and forces of the elastic plate 1 and 2 in pure and aerated water are shown in Figure 4-37, Figure 4-38 and Figure 4-39. Similar to the rigid plate, the impact pressures on the elastic plates due to impact in pure water are much higher than those in aerated water especially at and near the centre of the plate (Figure 4-37a, Figure 4-38a and Figure 4-39a). Large scatter of the impact pressures on the elastic plates is similar to that observed from the rigid plate which is presented in Figure 4-19. The impact forces on the elastic plates in pure and aerated water are presented in Figure 4-37b, Figure 4-38b and Figure 4-39b. In general, the impact forces in pure water are also much higher than those in aerated water. The impact pressure and force decrease with increasing the aeration level as was previously found for the rigid plate as well.
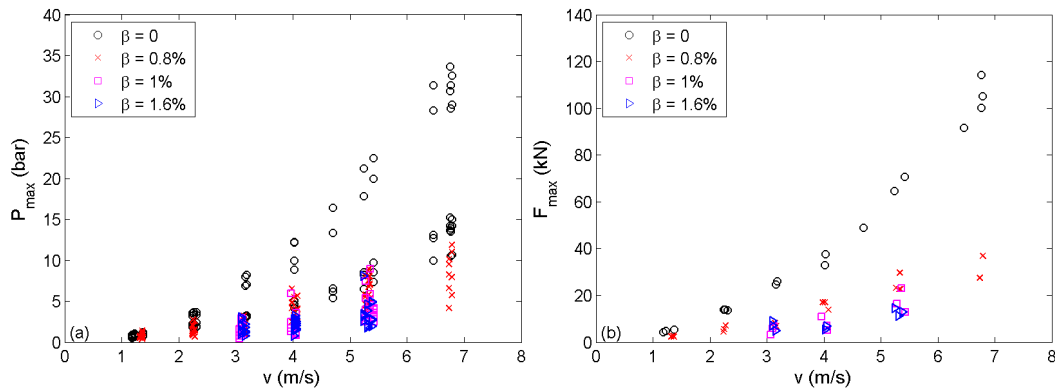
Figure 4-37. Impact pressure and force of elastic plate 1 (*m* = 45 kg) in pure and aerated water.

72
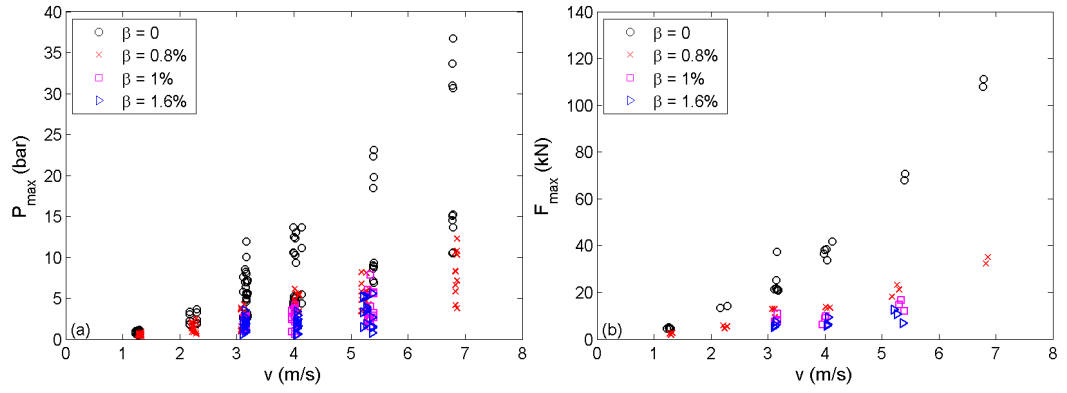
Figure 4-38. Impact pressure and force of elastic plate 1 ($m = 52$ kg) in pure and aerated water.
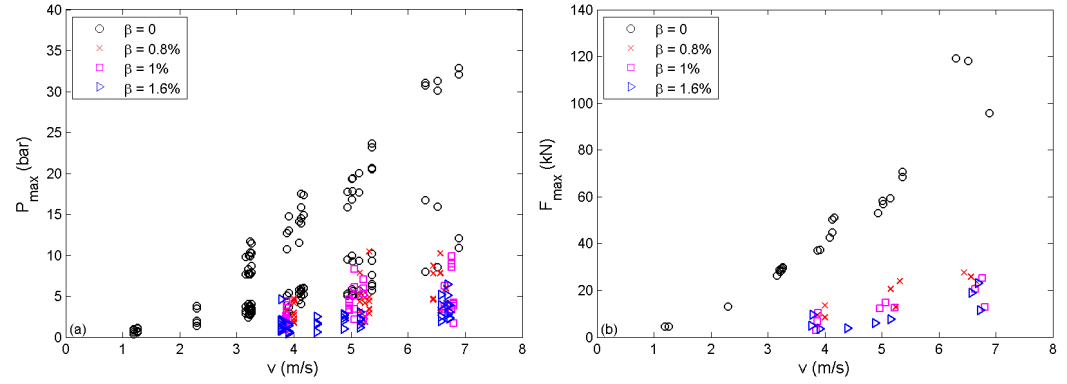
Figure 4-39. Impact pressure and force of elastic plate 2 ($m = 52$ kg) in pure and aerated water.

4.4.2 Impulses (pressure and force)

The first pressure and force impulses on the elastic plates due to impacts in pure and aerated water are shown in Figure 4-40, Figure 4-41 and Figure 4-42. It can be seen that there is no significant difference between the first impulses in pure and aerated water even though the first pressure impulses at and near the plate centre in pure water are slightly higher than those in aerated water (Figure 4-40a, Figure 4-41a and Figure 4-42a). In contrast, the first force impulses on the elastic plate 1 (with both $m = 45$ kg and 52 kg) in aerated water are higher than those in pure water under impact with high velocities ($v > 3$ m/s), see Figure 4-40b, Figure 4-41b. Average values of the first force impulses on the elastic plate 2 in pure water are slightly higher than the values in aerated water (Figure 4-42b).

The total pressure impulses are presented in Figure 4-43a, Figure 4-44a and Figure 4-45a, and it is shown that the total pressure impulses near the edges of the plates for

impact in pure water are lower than in aerated water, but at and near the plate centre they are more or less the same as in aerated water. Figure 4-43b, Figure 4-44b and Figure 4-45b present the total force impulses on the elastic and they show that the total force impulses in pure water are smaller than those in aerated water.

Scatter of the first and total force impulses in pure water are found to be less than those in aerated water, but for the pressure impulses (both the first and total impulses) the scatter is similar in pure and aerated water.
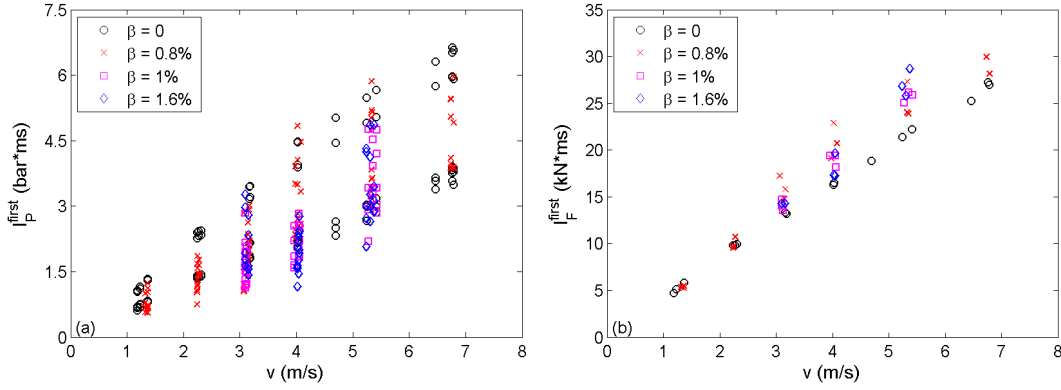
Figure 4-40. I_P^{first} (a) and I_F^{first} (b) of elastic plate 1 (m = 45 kg) impact in pure and aerated water.
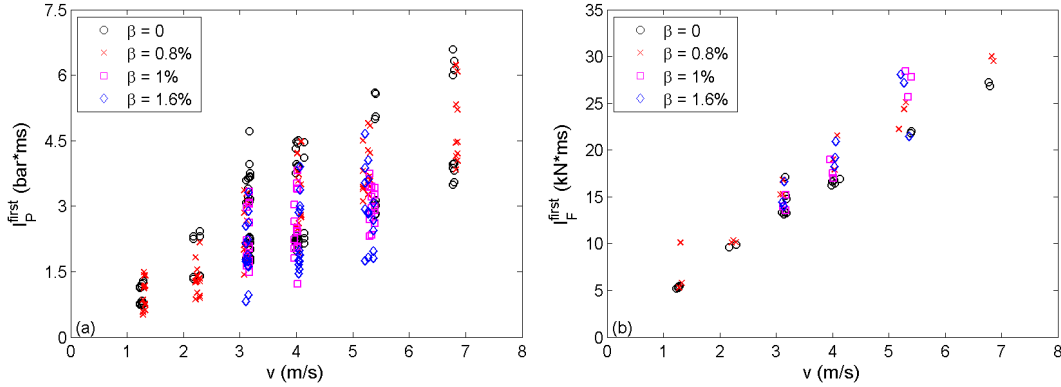
Figure 4-41. I_P^{first} (a) and I_F^{first} (b) of elastic plate 1 (m = 52 kg) impact in pure and aerated water.
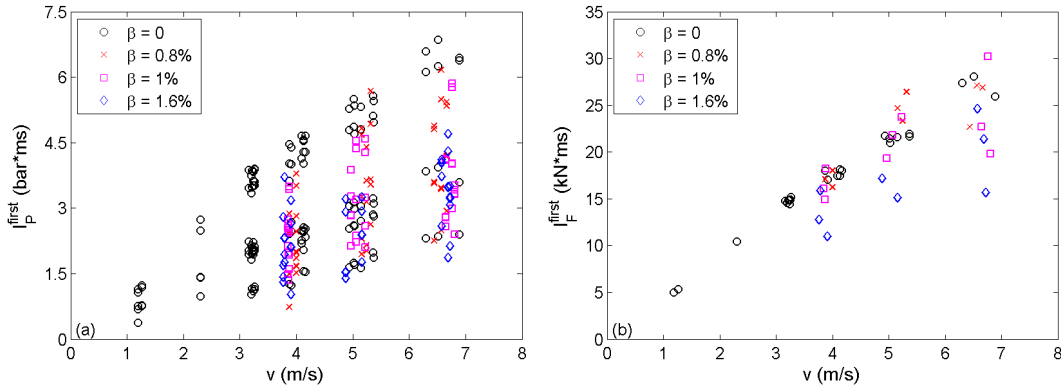
Figure 4-42. I_P^{first} (a) and I_F^{first} (b) of elastic plate 2 (m = 52 kg) impact in pure and aerated water.

74
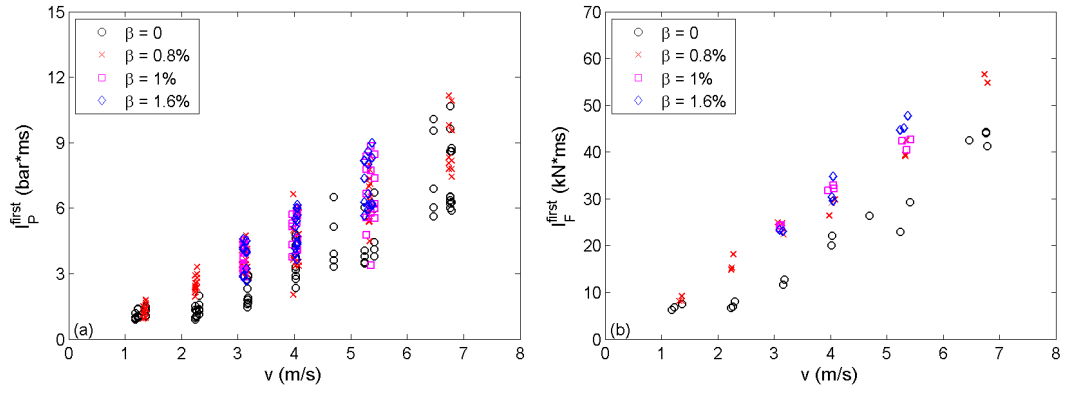
Figure 4-43. I_P^{total} (a) and I_F^{total} (b) of elastic plate 1 (m = 45 kg) impact in pure and aerated water.
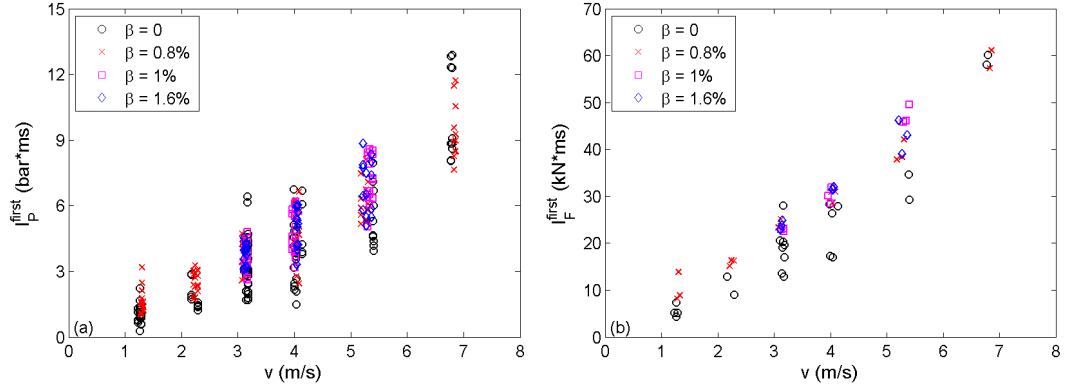
Figure 4-44. I_P^{total} (a) and I_F^{total} (b) of elastic plate 1 (m = 52 kg) impact in pure and aerated water.
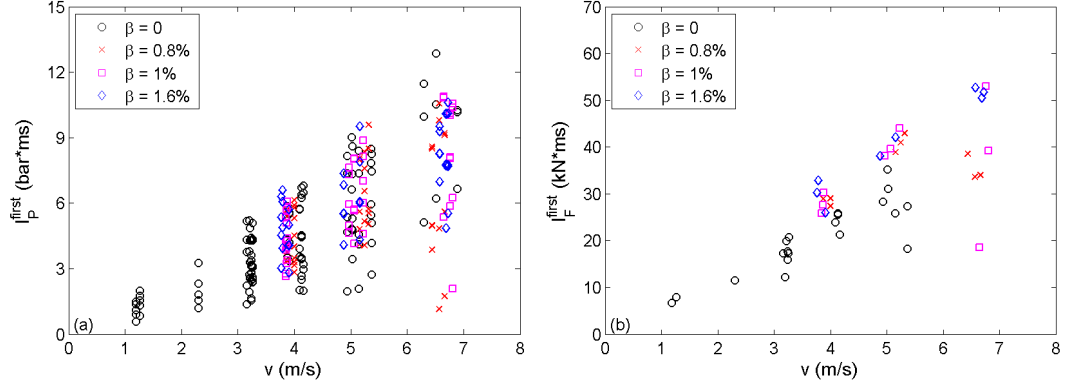
Figure 4-45. I_P^{total} (a) and I_F^{total} (b) of elastic plate 2 (m = 52 kg) impact in pure and aerated water.

4.5 Conclusions of slamming impacts

Slamming of rigid and elastic square flat plates in pure and aerated water were experimentally investigated in this chapter by means of a drop test which involved freely dropping a rigid or elastic plate having mass of between 32 kg and 52 kg from various heights to obtain various impact velocities. All tests were done with 0° deadrise

angle (flat impact). The water was aerated by using a bubble generation system to gain different aeration levels. The following are some conclusions of this experimental study:

- The spatial distribution of those impact pressures has been found under impact velocities varying from 1 m/s to 7 m/s and it is shown that the distribution of the maximum pressure depends on the impact velocity.

- An empirical relationship has been proposed to estimate the impact pressures and force on the square plate. The impact pressures (at the centre or near the edge of the plate) and force are proportional to the square of the impact velocity, i.e. $P_{i\max} = a_{iP}v^2$ or $F_{\max} = a_F v^2$, where a_{iP} and a_F are the empirical factors and depend on the impact body (rigidity, elasticity and mass of the body) and the location i on the plate.

- Pressure measurement under impact in pure water is repeatable. In contrast, for impacts in aerated water, the measured pressure is random in both magnitude and rise time. This unrepeatability in aerated water is believed to be caused by the unstable surface of the aerated water, which was disturbed by the bubble generation.

- There is a significant reduction in the impact pressure and force from those measured in pure water to those in aerated water. This reduction is not only due to the presence of air in water but also due to the water surface distortion.

- An exponential relationship of the maximum force and the void fraction has been proposed ($F_{\max} = k_F e^{n\beta}$) and its coefficients ($k_F$ and n) are found from this experimental study.

- The elasticity of the tested plates has a significant effect on the impact pressures and forces at high velocities only.

- Hydroelasticity affects the post-impact oscillations of the pressures under impact in pure water.

- Significant reductions of the pressure and force impulse of the first positive phase (I_P^{first} and I_F^{first}) were found from the impacts in pure water to aerated water. But there is no reduction of both the total pressure impulse (I_P^{total}) and the total force impulse (I_F^{total}).

- I_P^{first} and I_F^{first} of the impact of the elastic plates in pure water are much lower than those of the rigid plate. There is no clear difference in I_P^{total} and I_F^{total} between the impacts of the rigid and elastic plates.

CHAPTER 5: EFFECTS OF AERATION AND HYDROELASTICITY ON WAVE IMPACTS

This chapter presents results and discussions for the experimental investigation of wave impact on a truncated vertical wall, which represents a section of the hull of an offshore vessel such as an FPSO (Floating Production Storage and Off-loading) vessel, which is commonly used in the offshore oil and gas industry. In the experiments, the wall is a rigid aluminium plate and could be connected to a spring system to alternatively form an elastic wall. Water was either pure or aerated water, and the experimental details are given in Section 3.2.

5.1 Characteristics of wave impacts

5.1.1 Wave impacts in pure water

5.1.1.1 Early broken wave impact

Typical time-histories of accelerations, force and pressures due to early broken wave impact (focus distance X_f = 30.5 m) on the rigid wall in pure water are presented in Figure 5-1 and Figure 5-2. Accelerations up to 1.1g were measured on the impact wall (Plate 1 shown in Figure 3-16) for this particular test run (Figure 5-1a) and this is the highest acceleration recorded for early broken wave impact on the rigid wall. Plate 2 was rigidly fixed to the support frame as shown in Figure 3-16. The oscillation of the force signal after the impact is shown in Figure 5-1b and this oscillation frequency (~37 Hz) is close to the natural frequency of the complex model (f_N = 40 Hz). Figure 5-2 presents pressure traces, which were measured at various levels (z/d = 0.071 to 0.39, z is the pressure sensor level above SWL, d is the water depth at the structure) on the wall, and it shows that there are a number of impacts in a time period between t = -150 ms to

$t = 0$, in which $t = 0$ is denoted at the maximum impact force (see Figure 5-1b). The randomness of pressure traces was due to a relatively large volume of the aerated water generated under this type of wave impact. The maximum impact pressure and force due to the early broken waves was 0.12 bar (at level $z/d = 0.25$ at $t = -137.5$ ms) and 0.56 kN, respectively. Many high frequency oscillations were superimposed on the pressure time histories and these oscillations were caused by the oscillations of small bubbles within the aerated water produced by wave breaking. Similar oscillations to these have been observed in previous studies under broken wave impact, e.g. Bullock et al. (2007). Visualisation of irregular clouds of small bubbles during the process of early broken wave impact are shown in Figure 5-3 in sequential snapshots taken from $t = -100$ ms to $t = 50$ ms with $\varDelta t = 10$ ms. The impact wall is on the right hand side of each snapshot and the wave front come from the left hand side. It can be seen that the wave was already broken (before $t = -100$ ms) and produced a turbulent water-air mixture that impacts the wall. Because the wave has lost much of its energy in breaking before reaching the wall, it caused low impact pressures and force on the wall. Sub-atmospheric pressures were observed in the early broken wave impact presented in Figure 5-2, and these negative pressures were a common behaviour observed in the experiment and are thought to be due to the trapped air under wave impacts, as also mentioned by Oumeraci et al. (1993), Hattori et al. (1994) and Bullock et al. (2007). Repeatability of acceleration, force and pressures observed in five early broken wave impact tests are presented in Figure B-1 and Figure B-6 in Appendix B.1. Total force on the wall seems to be repeatable (Figure B-1b), but acceleration and pressures are unrepeatable (Figure B-1a and Figure B-6).

Figure 5-1: Time histories of force and accelerations due to early broken wave impact on rigid wall in pure water (*d* = 0.7 m).

Figure 5-2: Time histories of pressures due to early broken wave impact on rigid wall in pure water (*d* = 0.7 m). Note the different vertical scales.
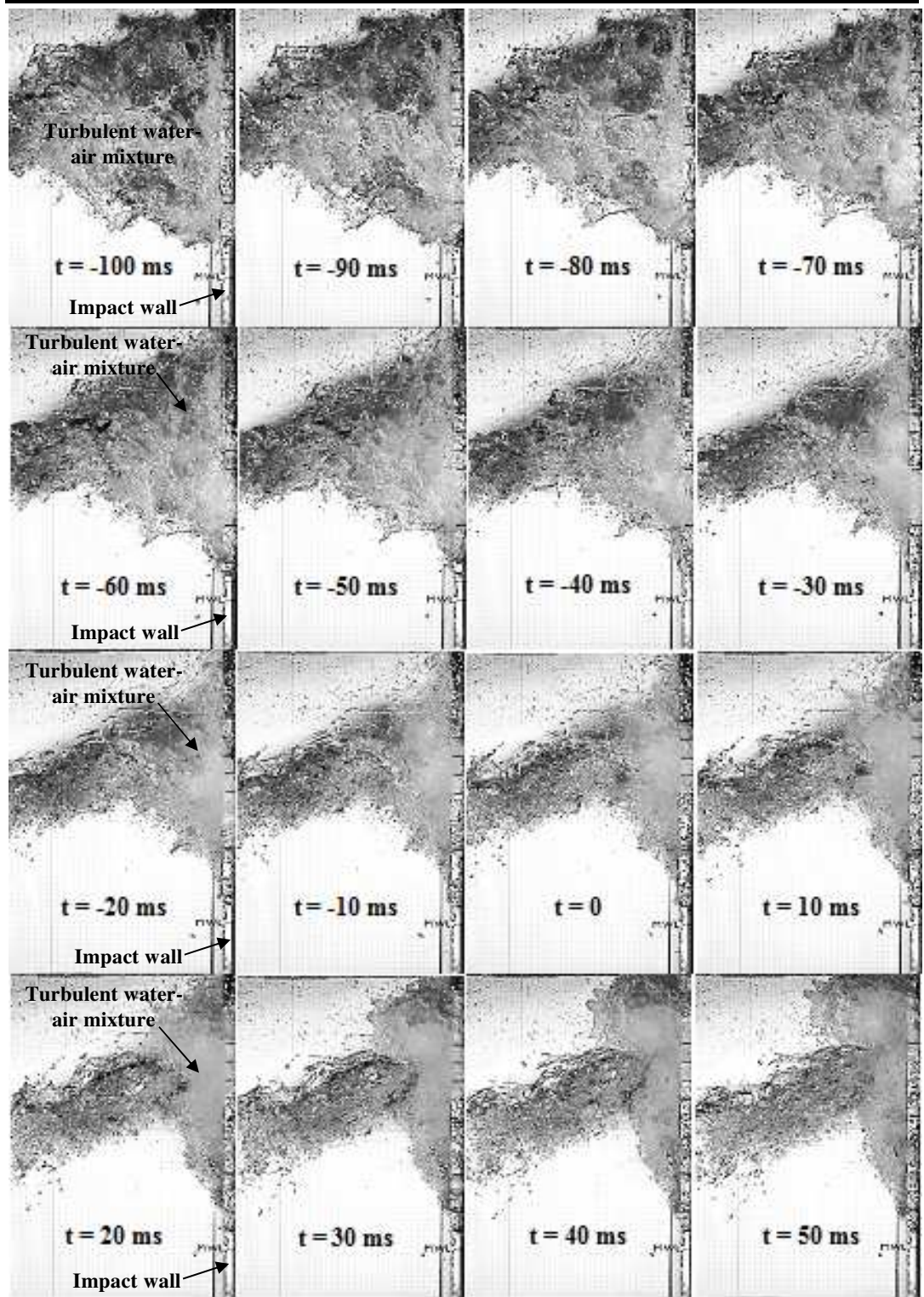
Figure 5-3: Snapshots of early broken wave impact on rigid wall in pure water ($d = 0.7$ m). In each snapshot, the wave was coming from the left and the wall was located on the right.

5.1.1.2 Broken wave impact

Figure 5-4 presents typical time-histories of accelerations and force under the broken wave impact (focus distance X_f = 31 m) on the rigid wall in pure water. In this case, the wave breaks just as it hits the wall. Accelerations up to 2.3g were recorded for the broken wave impacts and are presented in Figure 5-4a. The maximum impact force due to broken wave for this particular test was 0.81 kN (Figure 5-4b). The low frequency oscillation superimposed on the force time history is found to be close to the natural frequency of the model (f_N = 40 Hz). This low frequency oscillation was also observed in the force time histories of all broken wave impacts. Due to the chaotic nature of the broken wave turbulent flow as the wave hits the wall, there is considerable randomness apparent in the pressure time history under the broken wave impact as can be seen in Figure 5-5. At level z/d = 0.36, there was high impact pressure of 0.2 bar (the highest value that was observed for broken waves) at t = -53.83 ms (see Figure 5-5a). Many other test runs of broken wave impact show high impact pressures up to 0.18 bar that were attained at early times, around t = -100 ms. Similar to the early broken wave impacts presented in the previous section, there are high frequency oscillations which were superimposed on the pressure signals (see Figure 5-5a,b). These oscillations are likely to be due to the alternate expansion and compression of the dense cloud of bubbles seen in the image sequence of Figure 5-6 and also noted by Hattori et al. (1994) and Bullock et al. (2007). Figure 5-6 shows the sequential snapshots of the broken wave impact and a smaller volume of aerated water, in comparison with the early broken wave, can be seen in this case. The wave was coming from the left hand side and the impact wall was located on the right hand side of each snapshot. As shown in Figure 5-6, at t = -100 ms, a jet forms as the breaking wave hits the wall, causing high random impact pressures between t = -100 ms and t = 0. Similar to the early broken wave

impact, the acceleration and pressures on the wall are unrepeatable (Figure B-2a and

Figure B-7), but the total force on the wall seems to be repeatable (Figure B-2b).
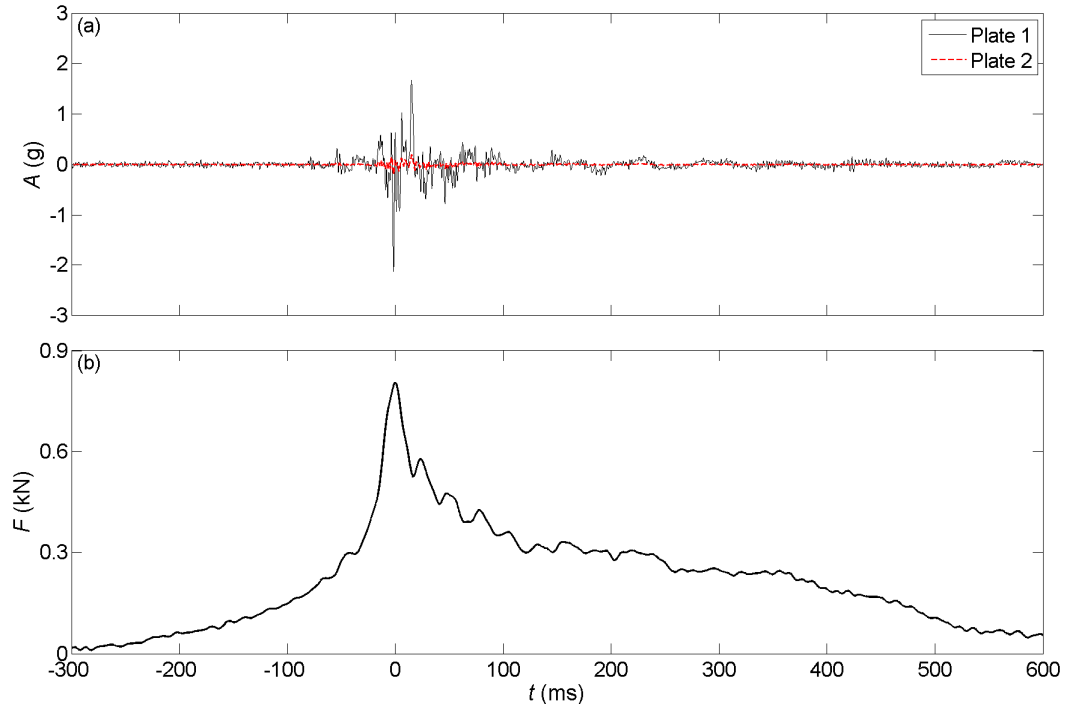
Figure 5-4: Time histories of force and accelerations due to broken wave impact on rigid wall in pure water (d = 0.7 m).
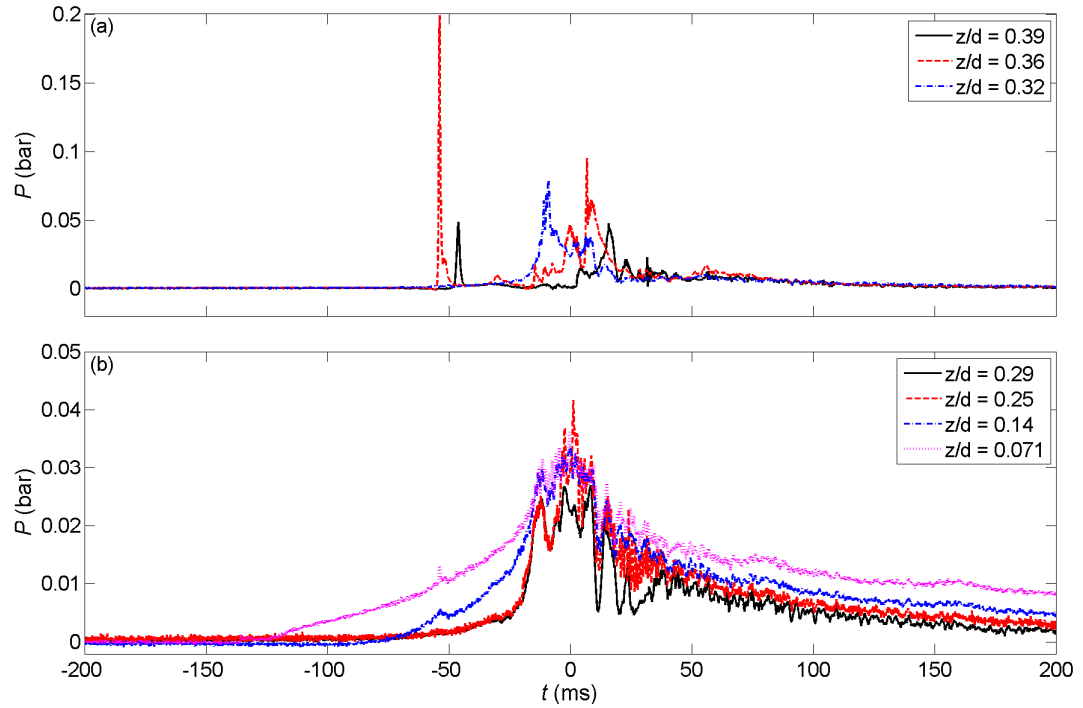
Figure 5-5: Time histories of pressures due to broken wave impact on rigid wall in pure water (d = 0.7 m). Note the different vertical scales.

Figure 5-6: Snapshots of broken wave impact on rigid wall in pure water (*d* = 0.7 m). In each snapshot, the wave was coming from the left and the wall was located on the right.

5.1.1.3 High aeration wave impact

Under high aeration wave impact (focus distance X_f = 31.3 m), the maximum acceleration of the wall is up to 6g for the case illustrated in Figure 5-7a. The time-history of the measured force on the wall under high aeration impact is presented in Figure 5-7b. The low frequency oscillations of the acceleration and force traces after the impact (between t = 0 ms and t = 500 ms in Figure 5-7a,b) can be seen and they are identical to the 40 Hz natural frequency of the structure. Associated time-histories of pressures on the wall at different levels are presented in Figure 5-8 for the test case presented in Figure 5-7. Higher impact pressures, in comparison with the previous wave impact types, are found and the time of peak pressure for each gauge is now nearly simultaneous under this wave impact type. The low frequency oscillation found in acceleration and force traces can also be observed from the pressure traces under the high aeration wave impact type (see Figure 5-8). It is shown that there are high frequency oscillations (~170 Hz to 880 Hz) of pressures after the impact (between t = 0 ms and t = 11 ms in Figure 5-8a,b). These high frequency oscillations may be due to the acoustic wave reflecting from the flume bottom and/or due to air-pocket and bubble oscillations. Using the theoretical natural frequency of air bubbles in water as derived by Minnaert (1933) and Hattori et al. (1994), the frequency of oscillation observed here corresponds to air-pocket and bubble radius of between 19.2 mm and 3.7 mm. This behaviour of the pressure time histories after the impact is similar to the previous findings for large air-pocket wave impacts (Hattori et al., 1994) or high aeration wave impacts (Bullock et al., 2007). Variation of pressure peaks due to high aeration impacts was very large as was also found by Hattori et al. (1994) and Bullock et al. (2007). The high aeration wave impact is presented in Figure 5-9 in sequential snapshots taken from t = -100 ms to t = 50 ms. It can be seen that the wave crest started to overturn at t = -100 ms and as time processing the jet of the breaking wave hit the wall and entrapped a

large air volume and a cloud of bubbles (see at time between $t = -30$ ms and $t = -10$ ms). Measurements of acceleration, force and pressures on the wall are shown in Figure B-3 and Figure B-8 for five high aeration wave impact tests. It is shown that the total force on the wall is well repeatable for the high aeration wave impact (Figure B-3b). Low frequency oscillation after impact on the acceleration and pressure traces is found to be repeatable, but the maximum acceleration and the impact pressure is unrepeatable (Figure B-3a and Figure B-8).
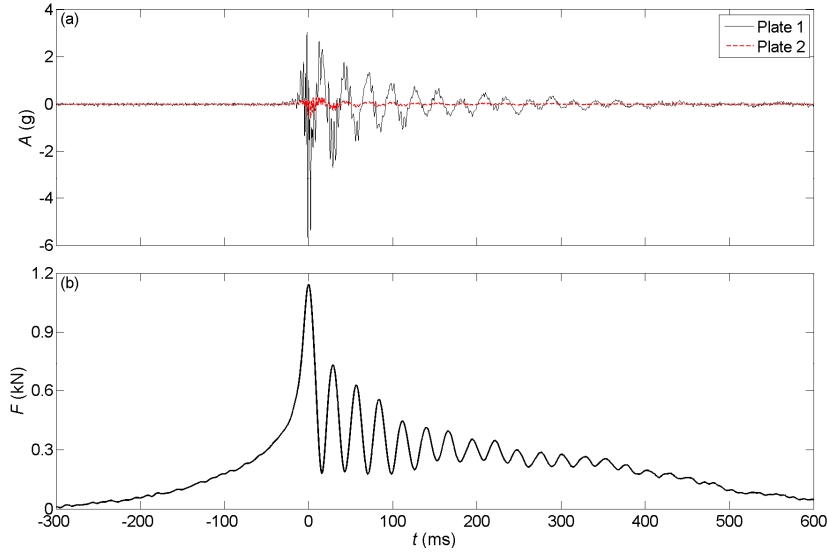
Figure 5-7: Time histories of force and accelerations due to high aeration wave impact on rigid wall in pure water ($d = 0.7$ m).
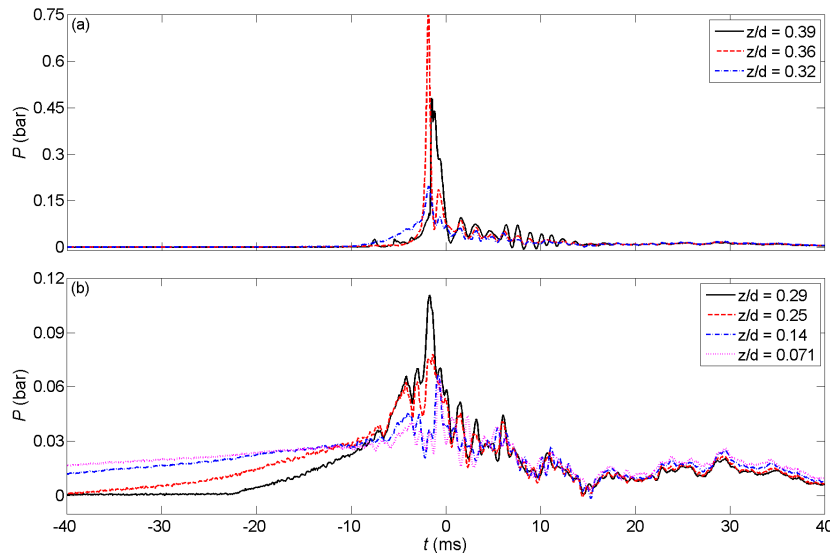
Figure 5-8: Time histories of pressures due to high aeration wave impact on rigid wall in pure water ($d = 0.7$ m). Note the different vertical scales.

86
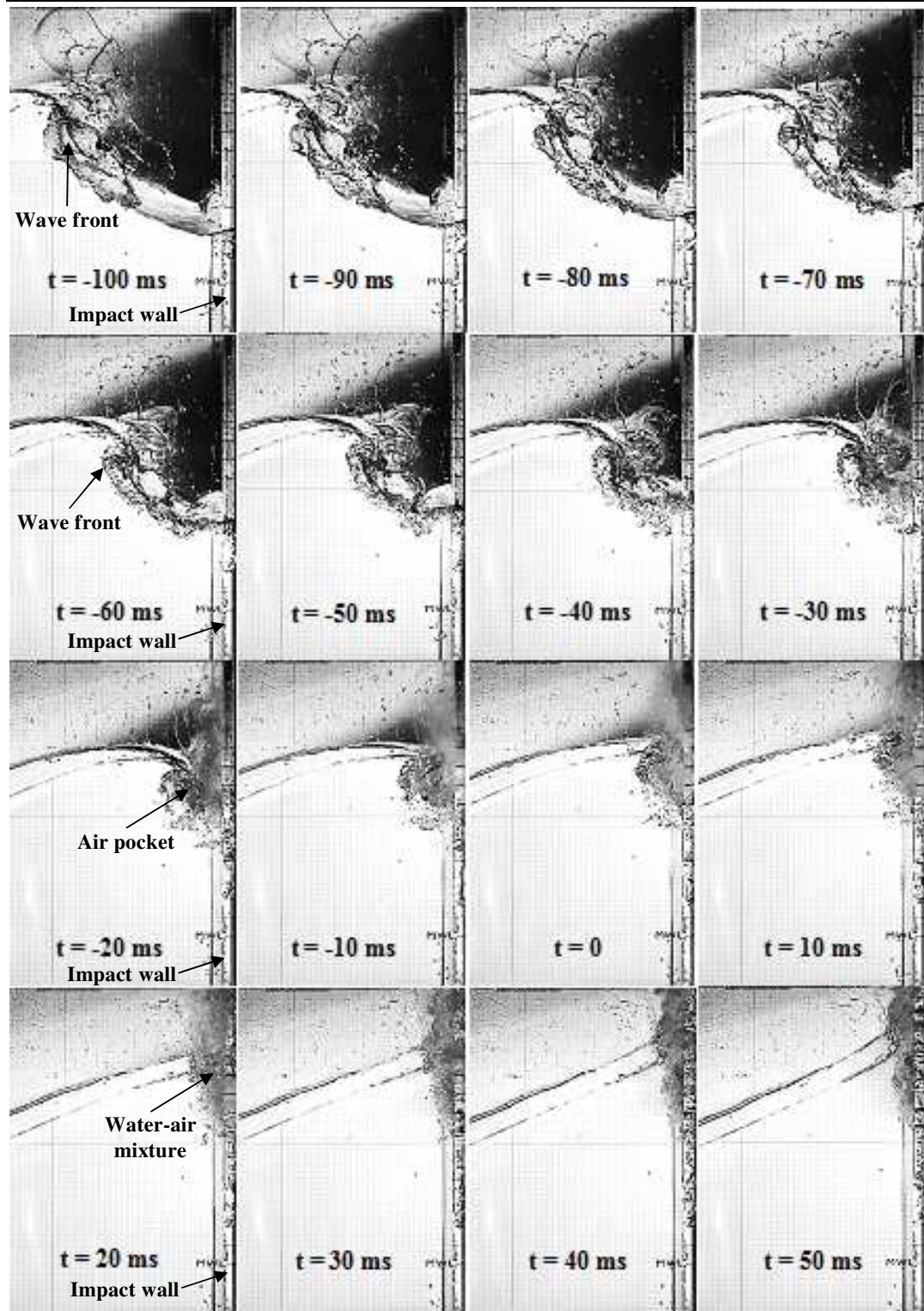
Figure 5-9: Snapshots of high aeration wave impact on rigid wall in pure water ($d = 0.7$ m). In each snapshot, the wave was coming from the left and the wall was located on the right.

5.1.1.4 Flip-through wave impact

Flip-through impact occurs if the air-pocket becomes zero and the wave strikes the wall with a vertical front face. This means the flip-through impact type lies between air-pocket impact and sloshing, where a sloshing wave rises up and down on the surface of a vertical wall. Flip-through impact was first identified by Cooker and Peregrine (1990) from their fully non-linear potential flow computation. Figure 5-10 and Figure 5-11 present time histories of the accelerations, force and pressures of a flip-through impact test case which caused the largest impact pressure (1.15 bar at level $z/d = 0.39$ in Figure 5-11a) obtained of any experiment presented here. The focus distance of $X_f = 30.5$ m was used to generate this flip-through wave impact type. The maximum acceleration of the wall on impact was recorded up to $4g$ for this particular case (Figure 5-10a). Similar to broken wave impacts and high aeration impact, evidence of the low frequency oscillation (~37 Hz) , which was due to the natural frequency vibration of the impact wall, was also found in the acceleration, force and pressure signals under the flip-through impacts. A high frequency oscillation (~620 Hz) was also observed after impact in pressure signals at all measured levels (Figure 5-11). This high frequency oscillation may be due to oscillation of 10.6 mm-diameter air bubble or a bubble cloud which was enclosed during the flip-through impact due to turbulence of the water surface. The high frequency oscillation of pressures after impact might also be caused by sound wave reflected from the flume bed. Phase differences of the high frequency oscillations in the pressure traces were observed and this may be due to the different distances between the pressure sensors and the impact point, where the air bubble was formed and sound wave started to transmit. Figure 5-12 presents snapshots of the flip-through impact at different instant times and it shows clearly the turbulence associated with the flip-through wave impact in this experimental work. Similar to the high aeration wave impact, the total force on the wall is well repeatable (Figure B-4b). However, acceleration and pressures

cannot be repeated, except the low frequency oscillation after the impact which is known to be due to the natural frequency vibration of the wall (Figure B-4a and Figure B-9).
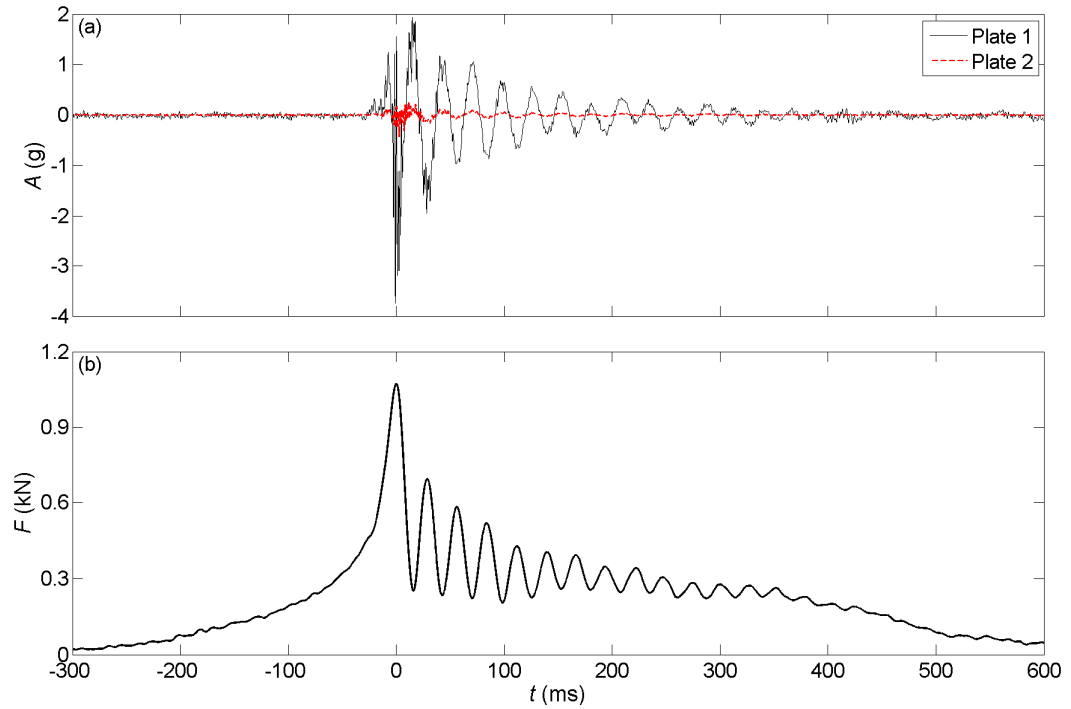
Figure 5-10: Time histories of force and accelerations due to flip-through impact on rigid wall in pure water ($d = 0.7$ m).
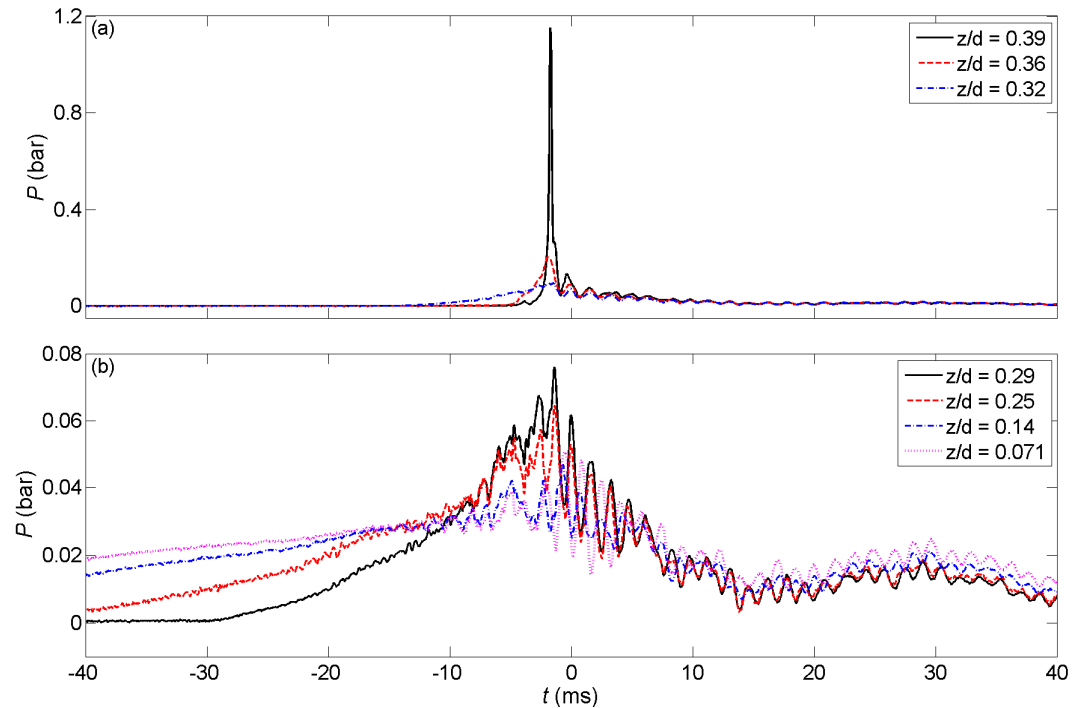
Figure 5-11: Time histories of pressures due to flip-through impact on rigid wall in pure water ($d = 0.7$ m). Note the different vertical scales.

89

Wave front

t = -100 ms

Impact wall

t = -90 ms

t = -80 ms

t = -70 ms

Wave front

t = -60 ms

Impact wall

t = -50 ms

t = -40 ms

t = -30 ms

Wave front

t = -20 ms

Impact wall

t = -10 ms

t = 0

t = 10 ms

t = 20 ms

Impact wall

t = 30 ms

t = 40 ms

t = 50 ms
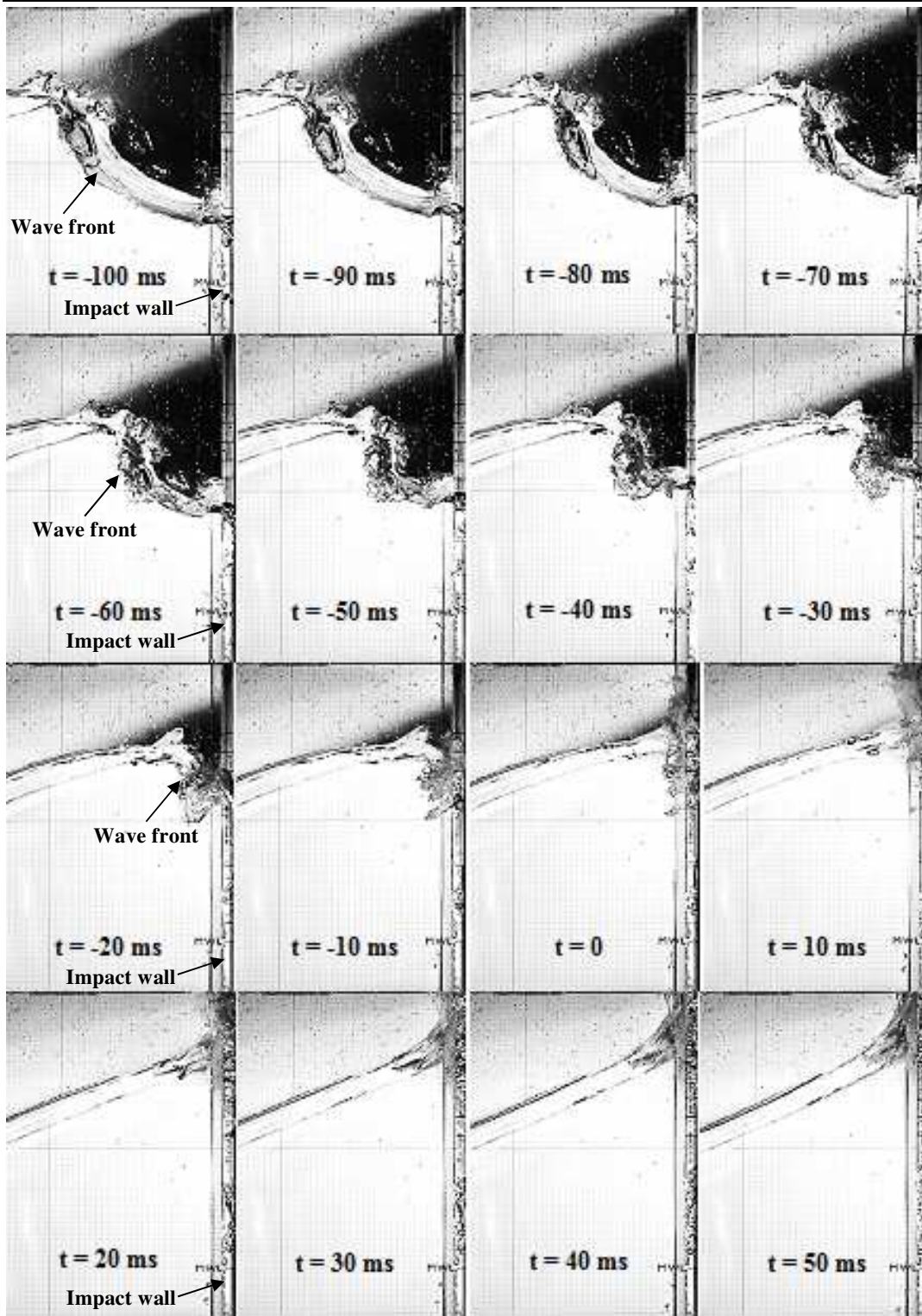
Figure 5-12: Snapshots of flip-through wave impact on rigid wall in pure water (d = 0.7 m). In each snapshot, the wave was coming from the left and the wall was located on the right.

5.1.1.5 Slightly breaking wave impact

Increasing the focus distance up to X_f = 31.9 m leads to the run-up on the wall being higher than the crest and the crest is slightly broken when it reaches the wall. Accelerations, force and pressures under the slightly breaking wave impact are presented in Figure 5-13 and Figure 5-14. A maximum acceleration of 0.7 g was recorded after the impact for this particular slightly breaking wave impact (Figure 5-13a). There is also a low frequency oscillation evident in the force signal (see Figure 5-13b) but the amplitude of this oscillation is much weaker than that due to other wave impacts (early broken, broken, high aeration and flip-through impacts). As can be seen in the pressure time histories presented in Figure 5-14, the pressure peak tends to decrease as the level z/d increases, except at the level z/d = 0.32 and 0.36 whereas the wave crest hits the wall, high pressures are caused. A preceding single impact was found on the pressure trace at level z/d = 0.36 and this is due to slightly breaking of the wave crest which can be seen in the snapshots in Figure 5-15, where the visualisation of this wave impact condition is illustrated by sequential snapshots recorded from the high speed camera. The time interval between two snapshots presented in Figure 5-15 is 10 ms and the figure presents snapshots from t = -100 ms to t = 50 ms. Acceleration, total force and pressures on the wall due to five slightly breaking wave impacts are illustrated in Figure B-5 and Figure B-10, and show clear lack of repeatability of acceleration and pressures on the wall as findings from other wave impact types (Figure B-5a and Figure B-10). However, total force on the wall also seems to be repeatable for the slightly breaking wave impact, see Figure B-5b.
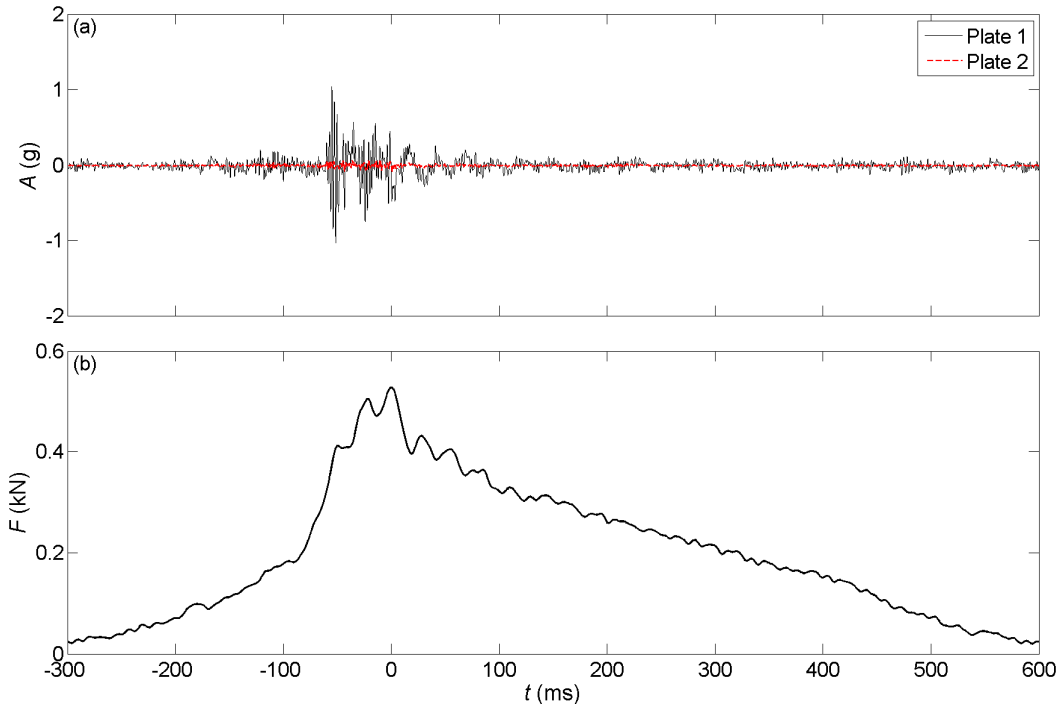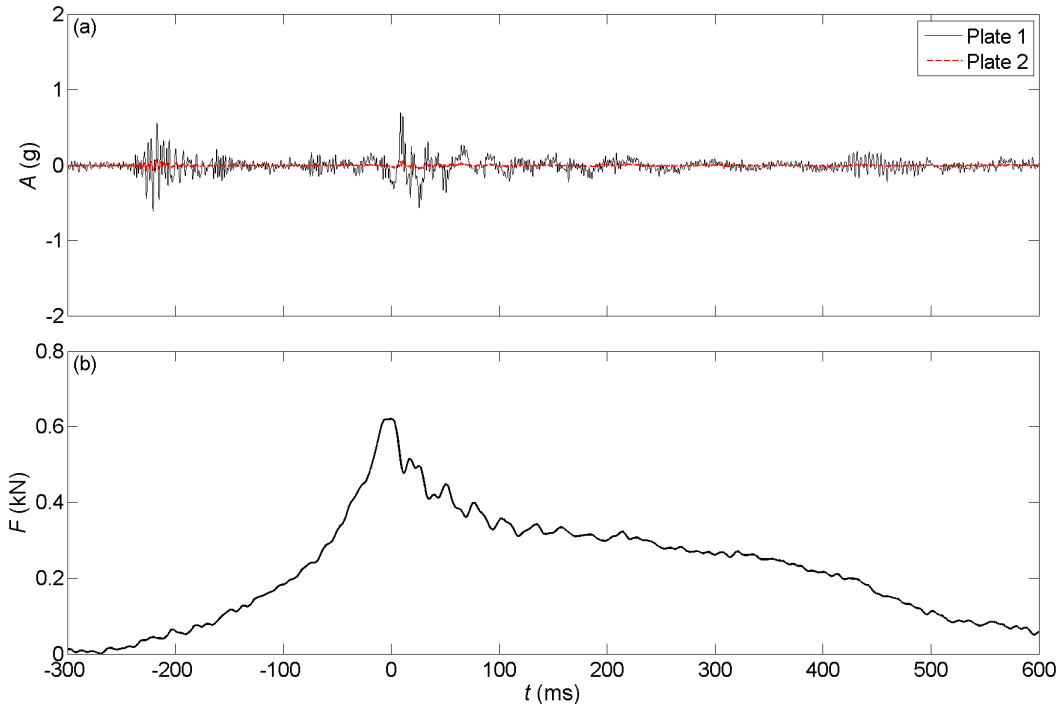
Figure 5-13: Time histories of force and accelerations due to slightly breaking wave impact on rigid wall in pure water ($d = 0.7$ m).
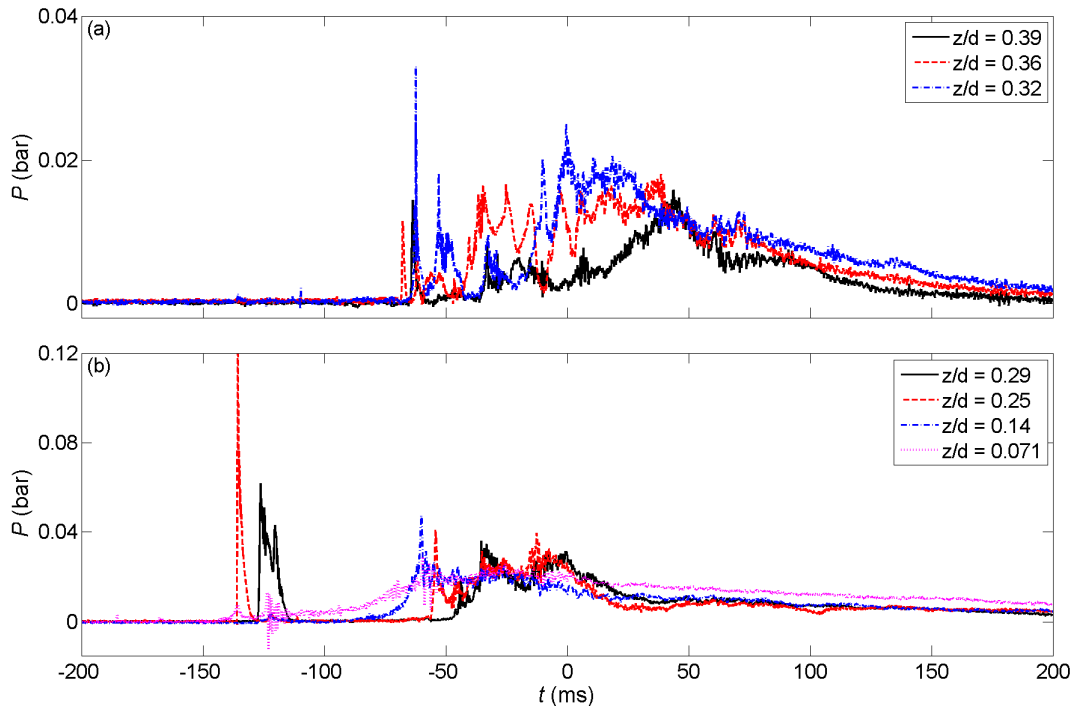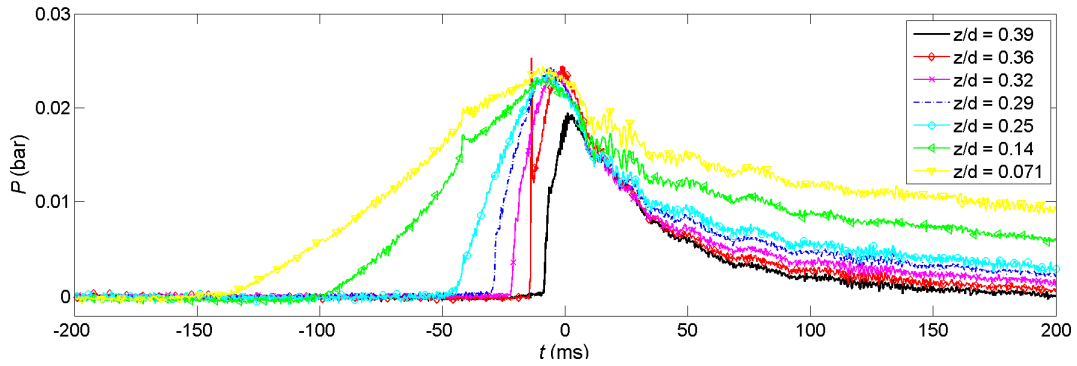

Figure 5-14: Time histories of pressures due to slightly breaking wave impact on rigid wall in pure water ($d = 0.7$ m).
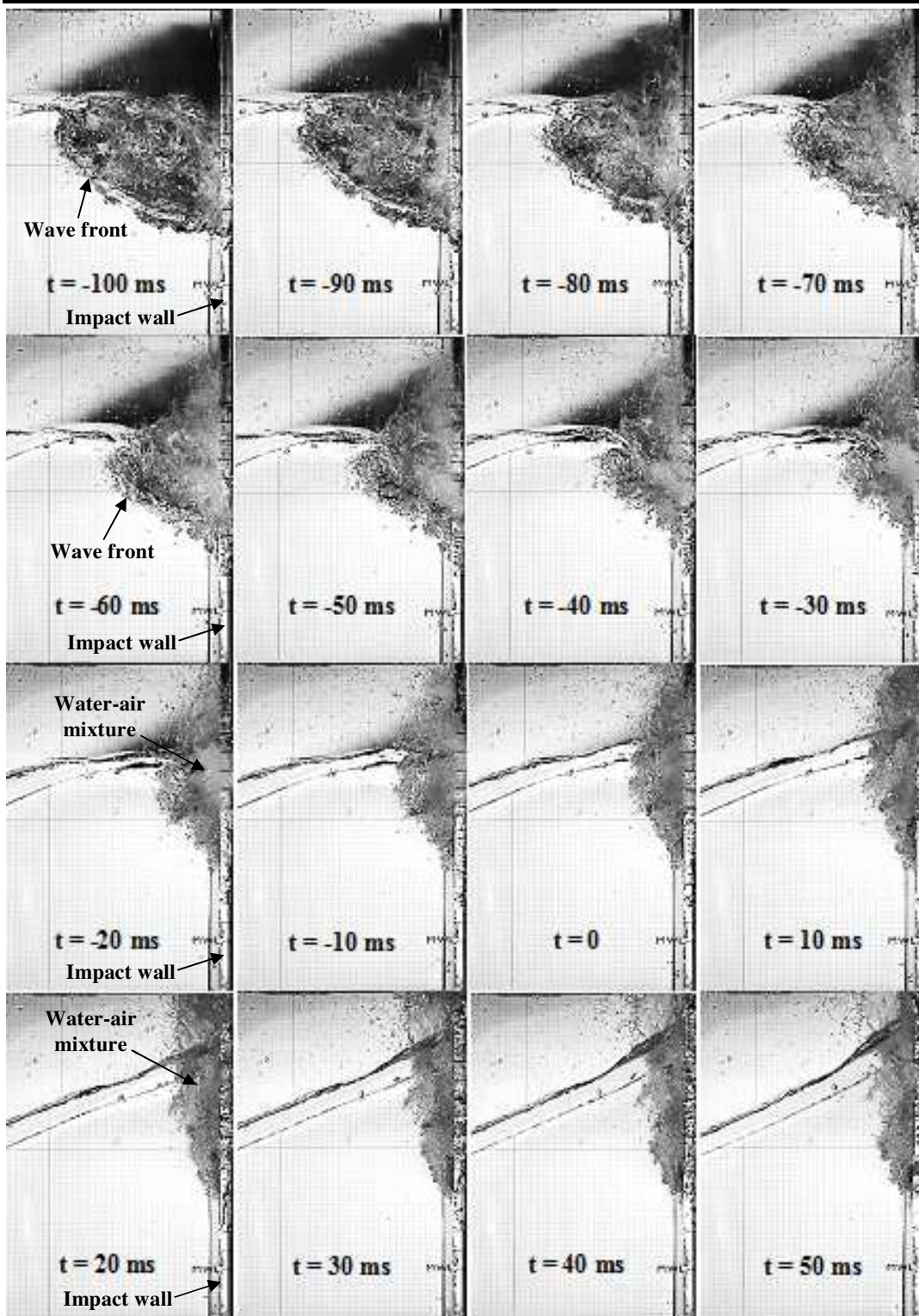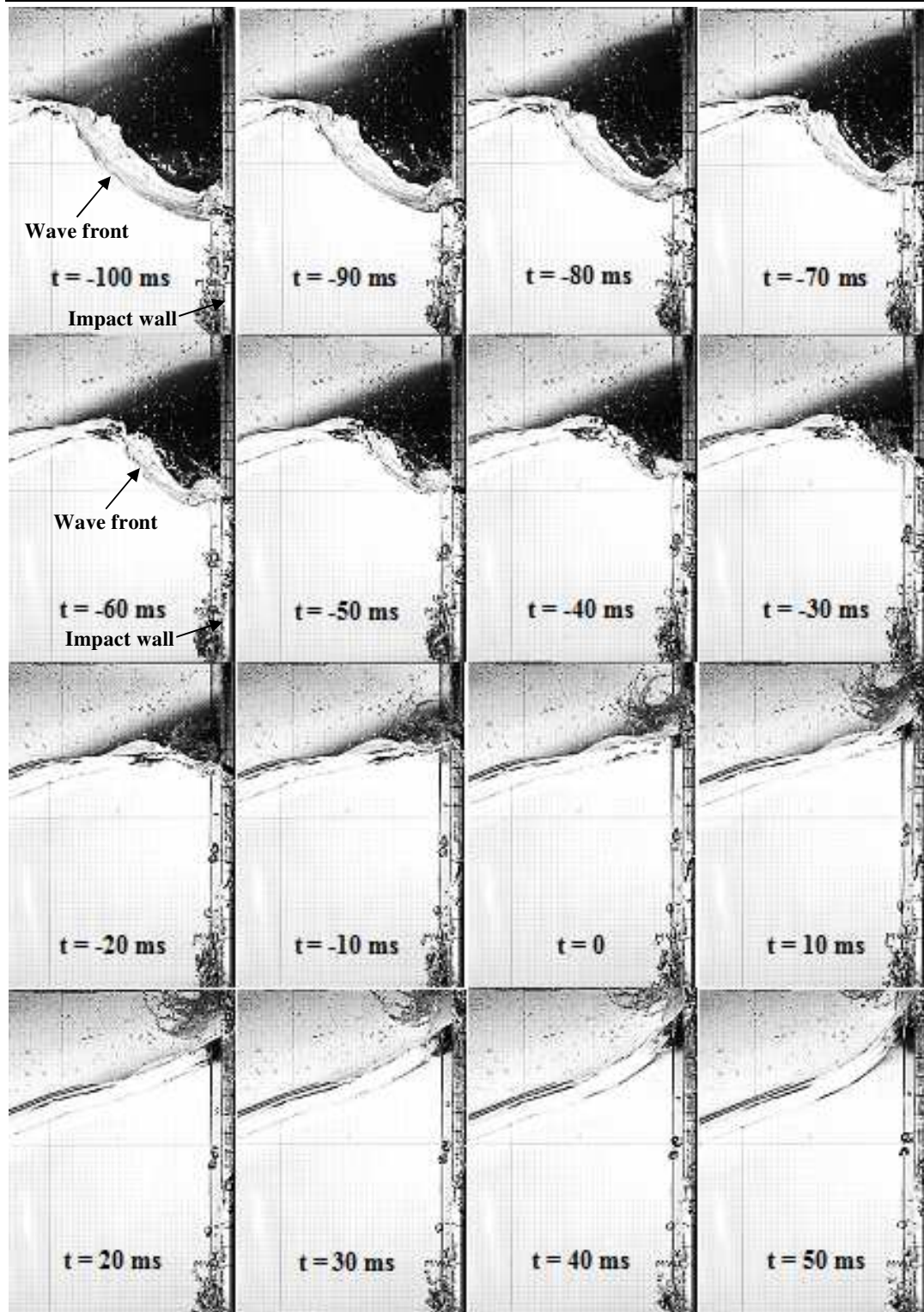
Figure 5-15: Snapshots of slightly breaking wave impact on rigid wall in pure water (d = 0.7 m). In each snapshot, the wave was coming from the left and the wall was located on the right.

5.1.1.6 Comparison of five wave impact types

Comparing time histories of acceleration, force and pressures on the rigid wall under the five tested wave impact types, which are previously presented in Section 5.1.1.1 to Section 5.1.1.5, are made and illustrated in Figure 5-16 and Figure 5-17. It is shown that the maximum acceleration and force due to the high aeration and flip-through wave impacts are much higher than those for the early broken, broken and slightly breaking wave impacts (Figure 5-16). In addition, Figure 5-16 shows that amplitude of the low frequency oscillation after impact in the acceleration and force traces due to the high aeration and flip-through wave impacts are significantly higher than those under the other tested wave impact types. Very high impact pressures due to the high aeration and flip-through wave impacts, in comparison with the early broken, broken and slightly breaking wave impacts, can be clearly seen in Figure 5-17a,b,c. On the other hand, high impact pressures are found at the time between $t = -150$ ms to $t = 0$ ms for the early broken and broken wave impacts, while those are found around $t = 0$ ms for the other impact types (Figure 5-17b-g). Evidence of the low frequency oscillation after impact is also found in the time histories of pressures due to the high aeration and flip-through wave impacts (Figure 5-17d-g). Repeatability of the total force on the wall due to high aeration and flip-through wave impacts (Figure B-3b and Figure B-4b) are much better than for the early broken, broken and slightly breaking wave impact types, which produce higher turbulence of the flow (Figure B-1b, Figure B-2b and Figure B-5b). Acceleration and pressures of all wave impacts on the wall cannot be repeated, except the low frequency oscillation after impact (Figure B-1a to Figure B-5a and Figure B-6 to Figure B-10).
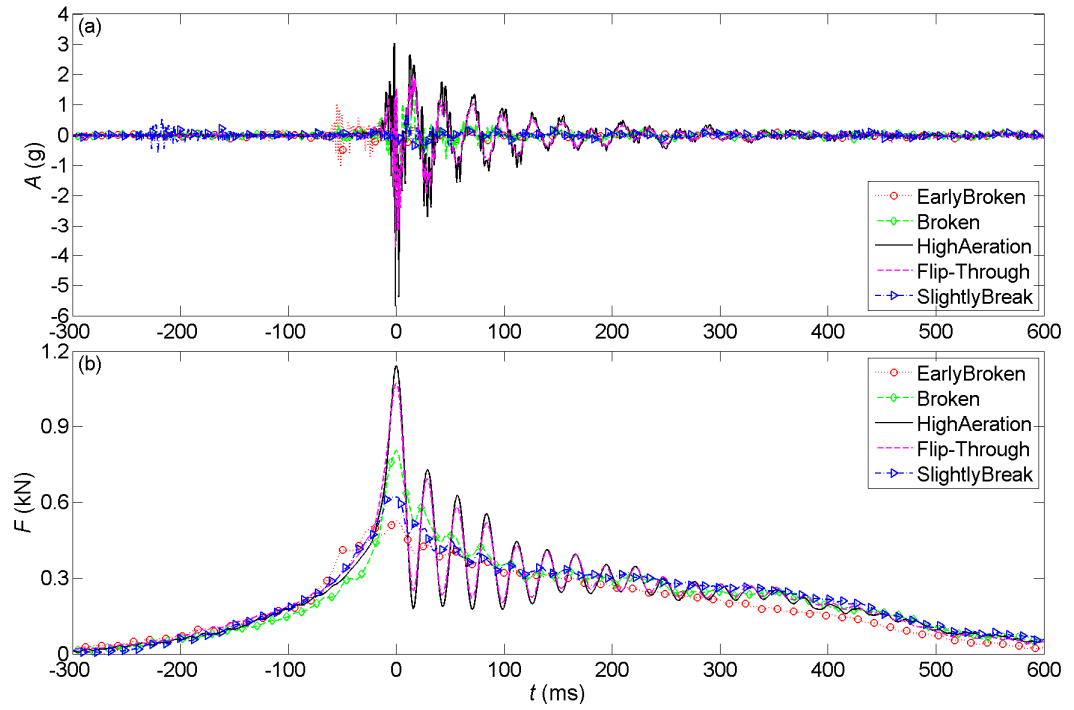
Figure 5-16: Comparison of acceleration and force traces on rigid wall under five tested wave impact types in pure water (d = 0.7 m).
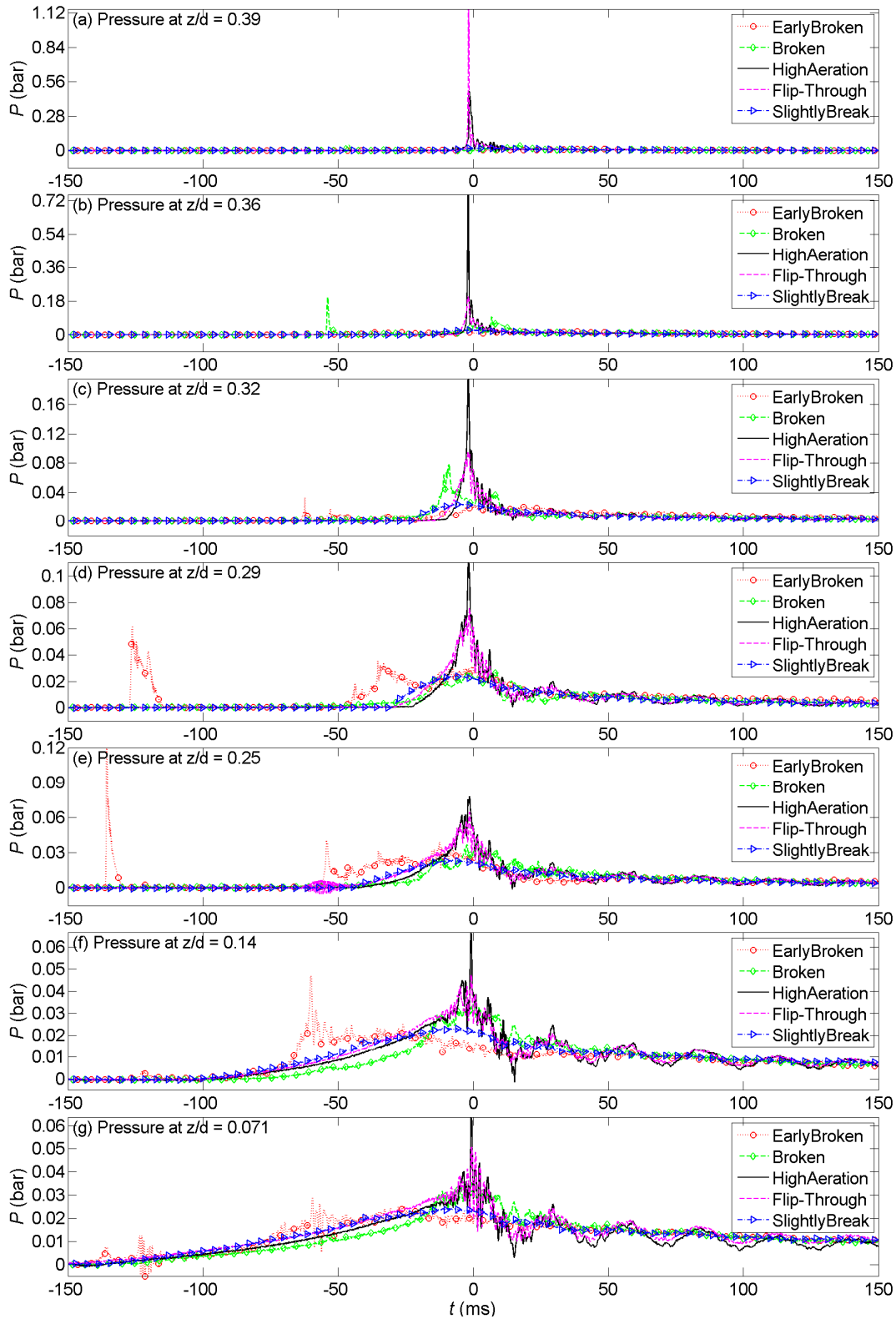
Figure 5-17: Comparison of pressure traces on rigid wall under five tested wave impact types in pure water (d = 0.7 m). Note the different vertical scales.

5.1.2 Wave impacts in aerated water

Investigation of different wave impacts on the rigid wall in pure and aerated water are presented in this section. The bubble generator was used to generate air bubbles in front of the impact wall, therefore the water depth in front of the wall was decreased to $d =$ 0.625 m (see Figure 3-16). Water was aerated to achieve a void fraction of 0.6 %. The pressure sensor mounted at level $z/d = 0.29$ was removed from the impact wall and used to calibrate and control the injection air pressure for the bubble generator. Therefore, the number of the measured pressure points on the impact wall was reduced to six points which were at $z/d = 0.071$, 0.14, 0.25, 0.32, 0.36 and 0.39. Because of the time limitation, the number of wave impact types was also reduced to four wave impact types: broken, high aeration, flip-through and slightly breaking (see Table 3-2).

Typical time histories of accelerations, force and pressures on the rigid wall in the aerated water for the four wave impact types are illustrated in Figure 5-18 to Figure 5-21. Comparisons of wave profiles between the test in pure and aerated water have been made and presented in Figure 5-22 to Figure 5-23 for the four wave impact types. Figure 5-24 to Figure 5-25 show the sequential snapshots during the wave impacts in aerated water.

Figure 5-18(a, b) to Figure 5-21(a, b) show the accelerations and force during the impacts. The low frequency oscillation (~37 Hz) is evident in the acceleration and force traces but its amplitude is rather smaller than that in pure water. Looking at the pressure traces in Figure 5-18c to Figure 5-21c, there are no significant high pressure peaks such as those obtained in pure water under the impacts presented in Section 5.1. High frequency oscillations after the impacts were also observed in the pressure traces and these oscillations are considered to be due to the expansion and compression and pressure wave transmitted through the water-air mixture body. Repeatability of wave impacts in aerated water is presented in Appendix B.2 for four wave impact types.

Similar to wave impact in pure water, the total force on the wall is repeatable, and acceleration and pressures are unrepeatable.
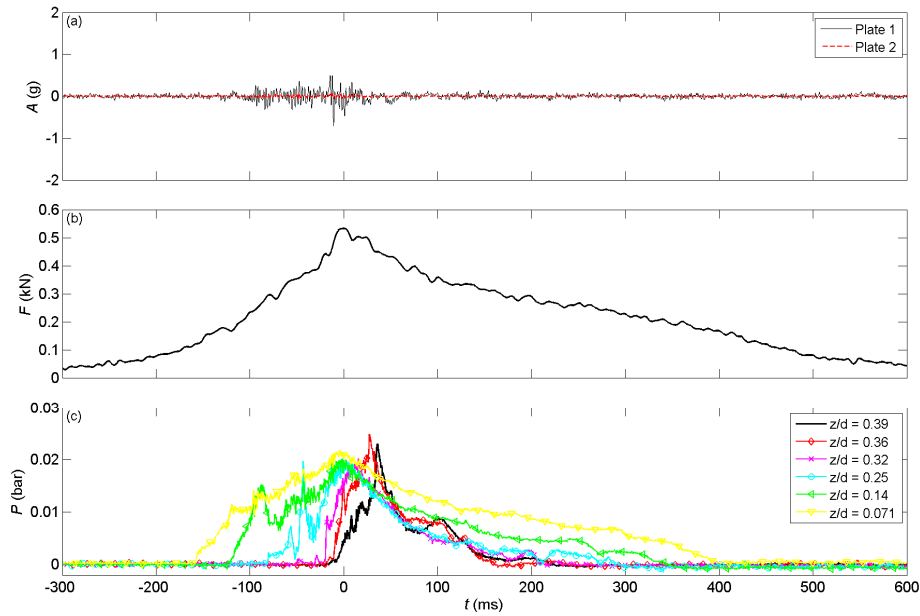
Figure 5-18: Typical time histories of accelerations, force and pressures on rigid wall under broken wave impact in aerated water ($d = 0.625$ m).
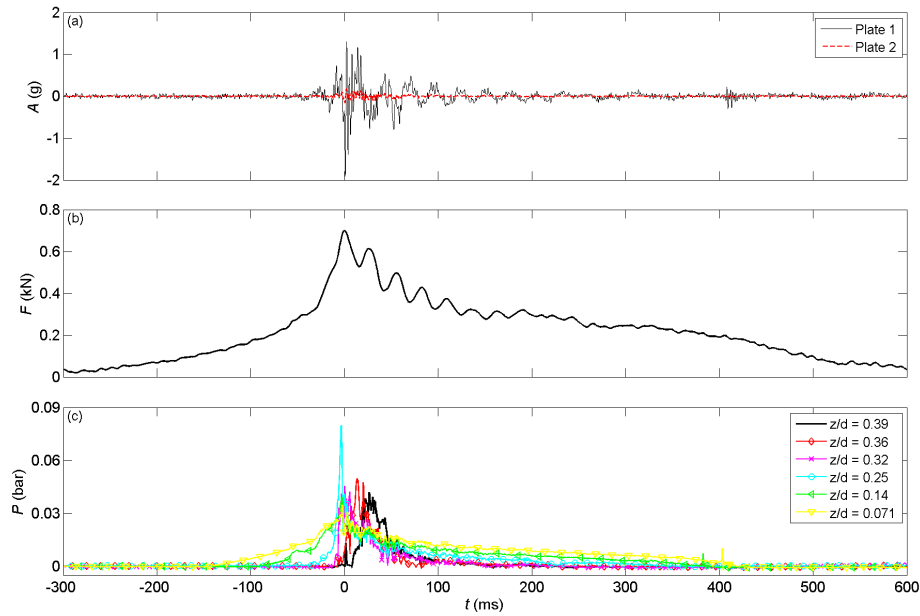
Figure 5-19: Typical time histories of accelerations, force and pressures on rigid wall under high aeration wave impact in aerated water ($d = 0.625$ m).
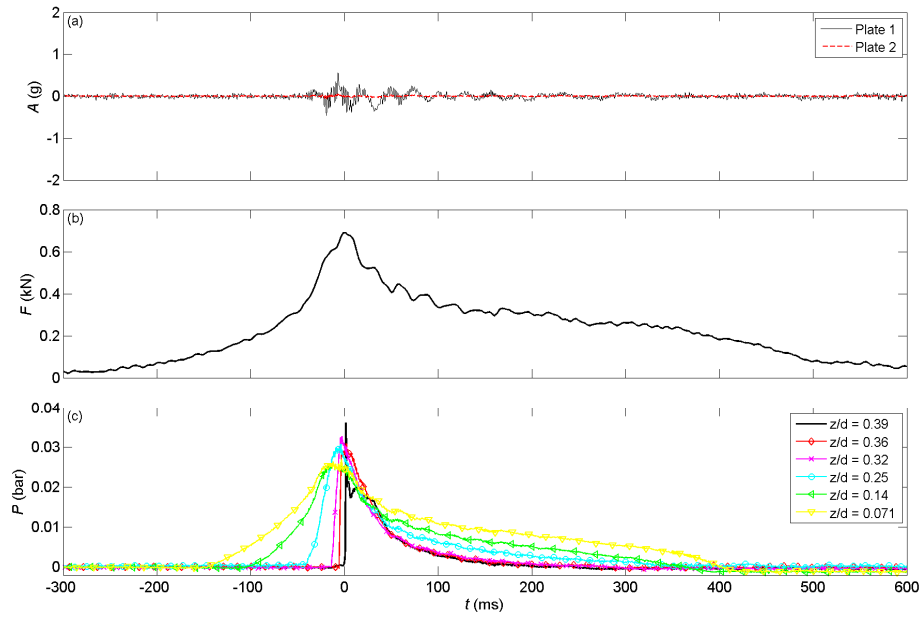
Figure 5-20: Typical time histories of accelerations, force and pressures on rigid wall under flip-through wave impact in aerated water ($d = 0.625$ m).
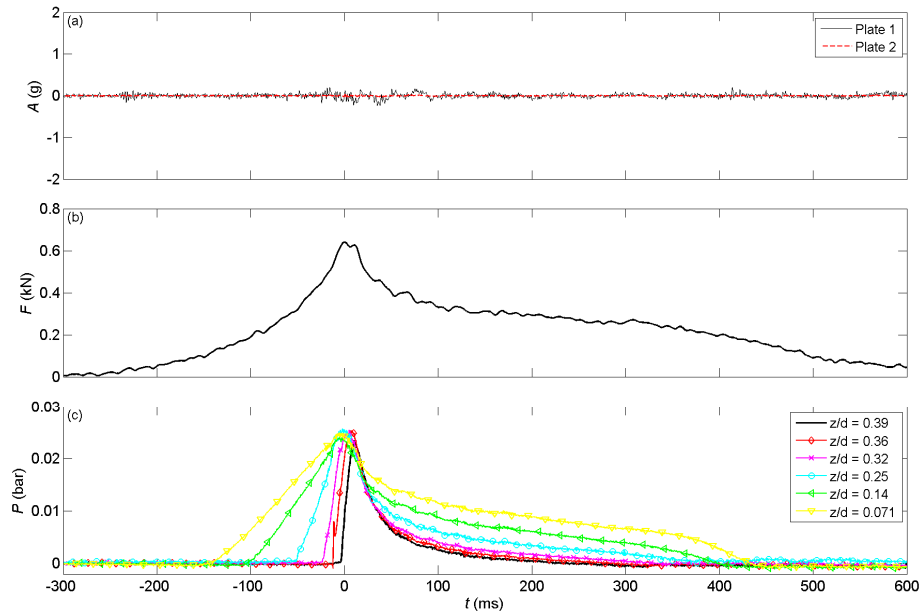
Figure 5-21: Typical time histories of accelerations, force and pressures on rigid wall under slightly breaking wave impact in aerated water ($d = 0.625$ m).

Wave profiles of the same wave impact types in pure and aerated water at location $x = -0.065$ m and -0.15 m ($x = 0$ at the front of the impact wall) are presented in Figure 5-22 and Figure 5-23. The air was injected into the bubble generator via four inlets to generate the aerated water. This air flow was expelled from the bubble generator, came into the water body and generated a flow, which was first in vertical direction and then in horizontal direction. Consequently, there was a surface current which was opposite to

the incoming wave direction. This flow has its effect on the incoming waves and this is clearly shown in Figure 5-22 and Figure 5-23. The effect of the flow formed by the bubble generation system, tended to change the incoming wave in the aerated water (dashed line in plots) so that it travelled up to 0.08 s slower than that in the pure water (solid line). Therefore, the surface current induced by the bubble generator slowed down the wave leading to decrease in the wave steepness. The difference between the maximum wave crest elevations in pure and aerated waters, at $x = -0.065$ m and -0.15 m, was up to 0.01 m. The disturbance of the wave crest due to presence of a bubble curtain was studied by Kimmoun et al. (2012) and they showed that the disturbance could lead to a decrease in impact pressure on a vertical wall such as is found in the experiments presented here. The influence of the bubble generation on the water surface can be seen in Figure 5-24 to Figure 5-25.
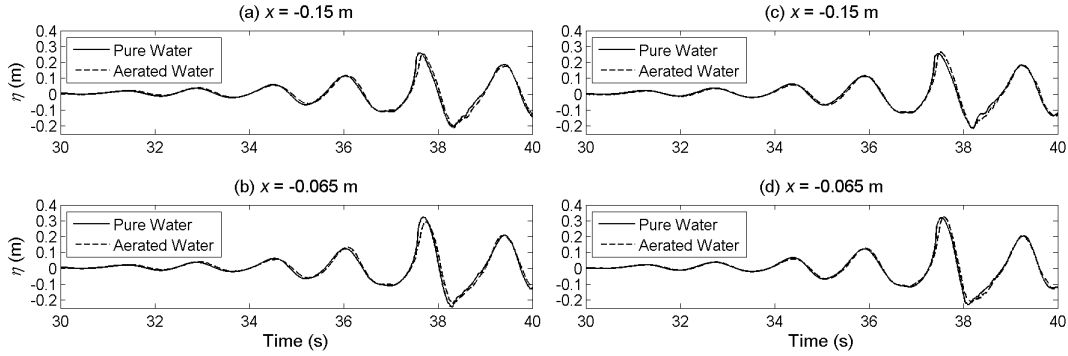
Figure 5-22: Comparison of wave profiles of broken wave (a, b) and high aeration wave (c, d) in pure and aerated water ($d = 0.625$ m).
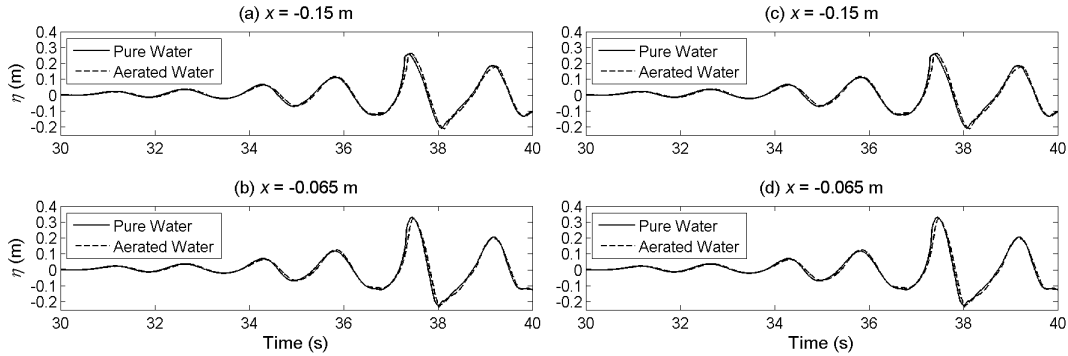
Figure 5-23: Comparison of wave profiles of flip-through (a, b) and slightly breaking (c, d) in pure and aerated water ($d = 0.625$ m).
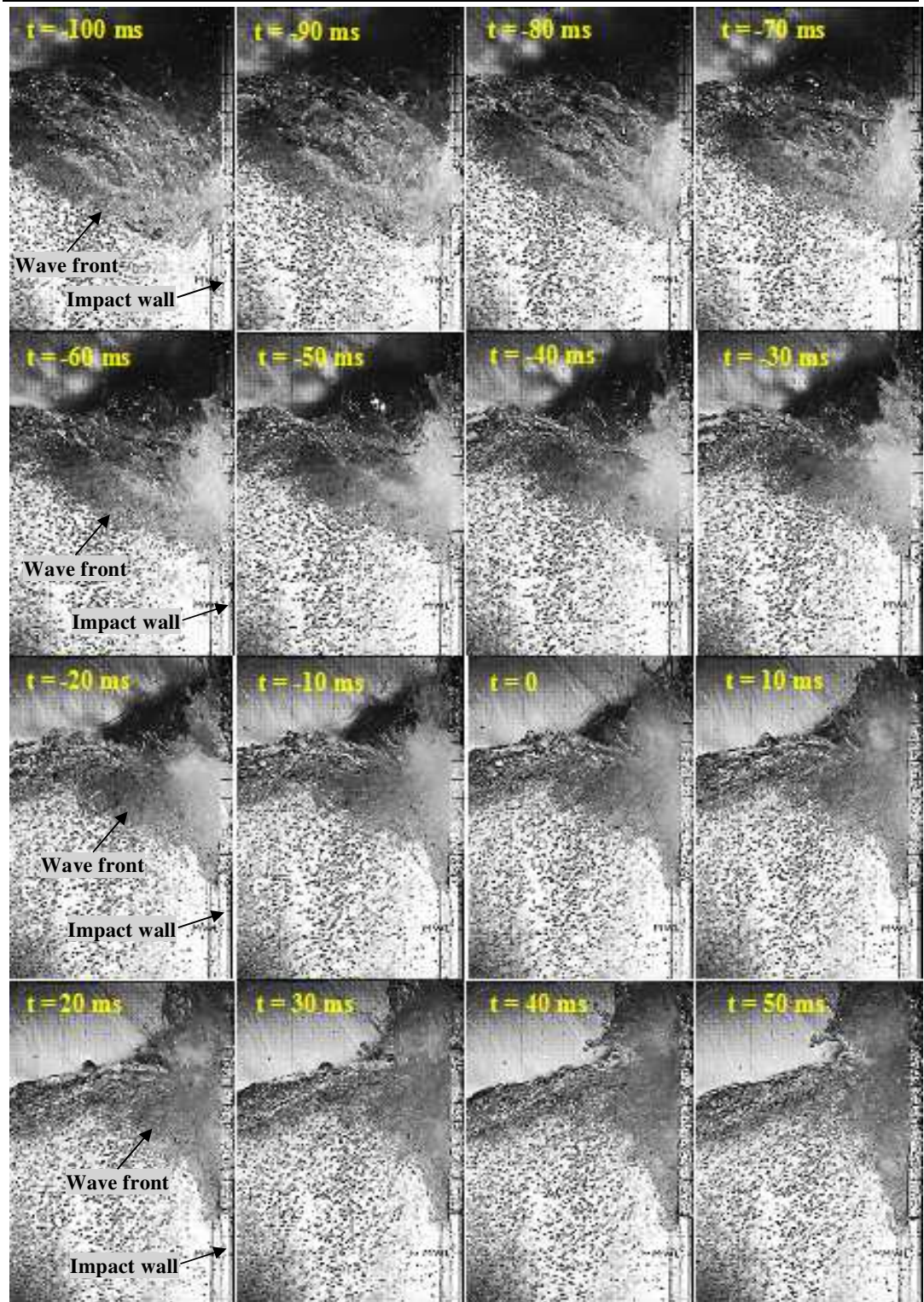
Figure 5-24: Snapshots of broken wave impact in aerated water (d = 0.625 m). In each snapshot, the wave was coming from the left and the wall was located on the right.
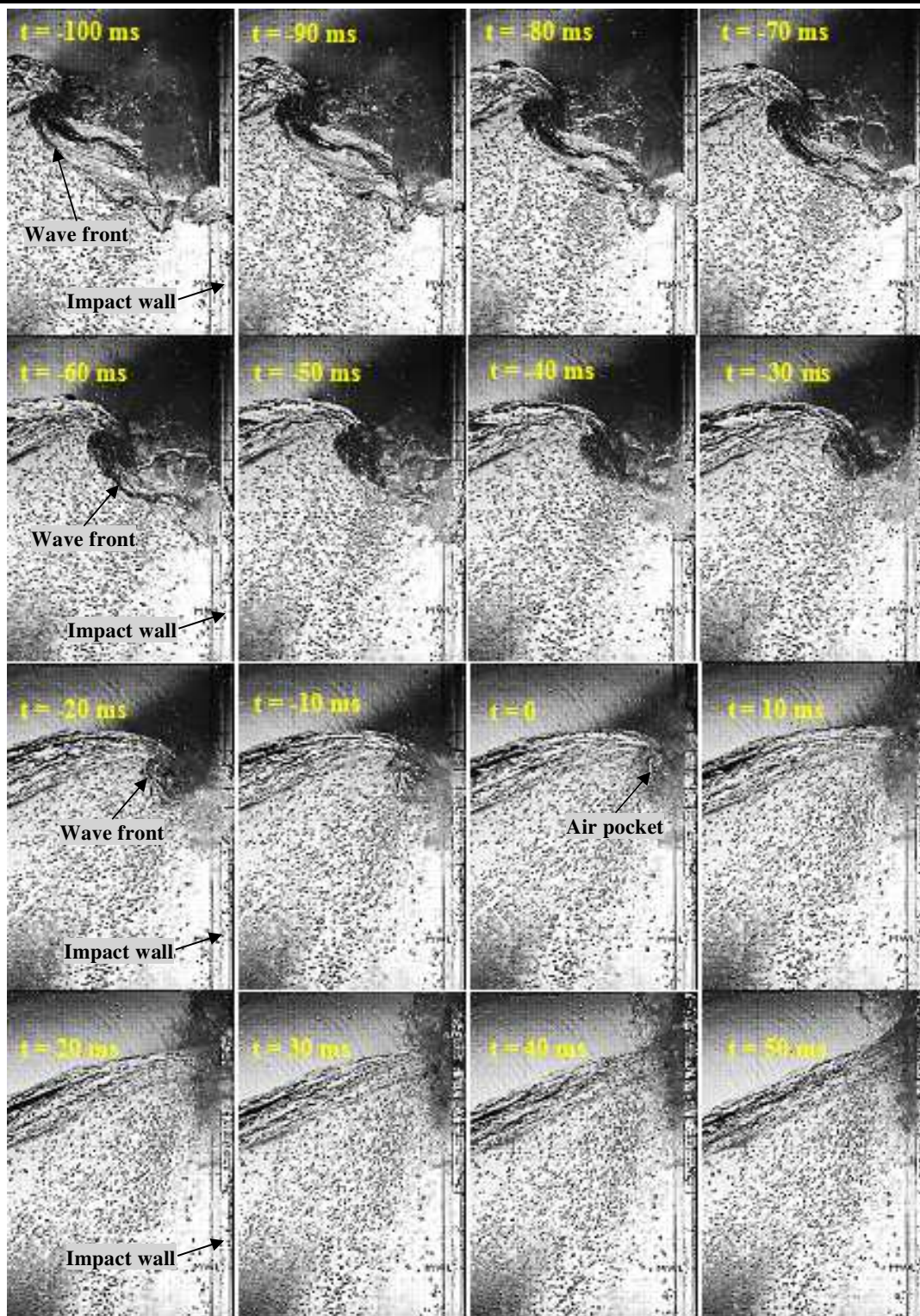
Figure 5-25: Snapshots of high aeration wave impact in aerated water ($d = 0.625$ m). In each snapshot, the wave was coming from the left and the wall was located on the right.
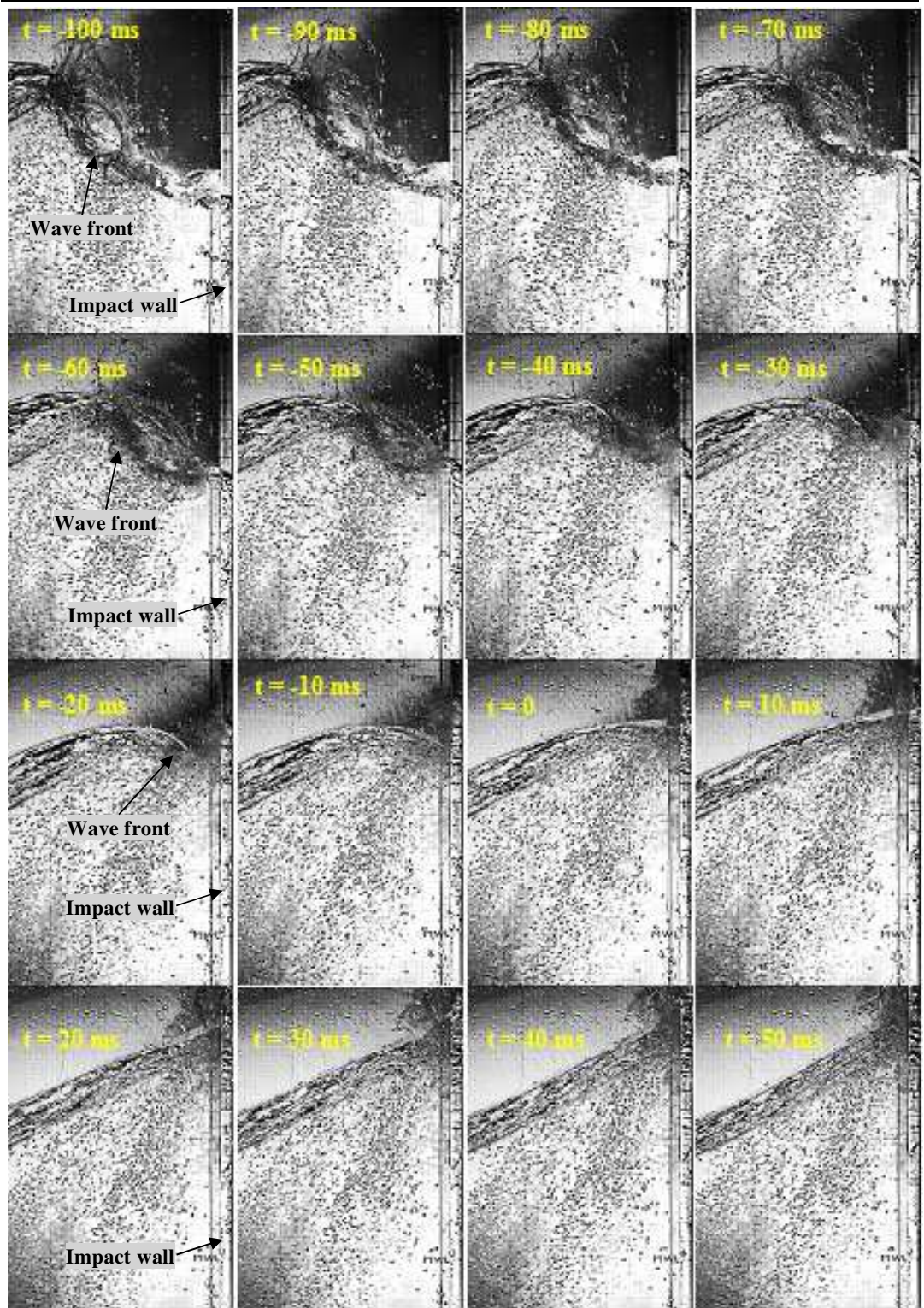
Figure 5-26: Snapshots of flip-through wave impact in aerated water (d = 0.625 m). In each snapshot, the wave was coming from the left and the wall was located on the right.
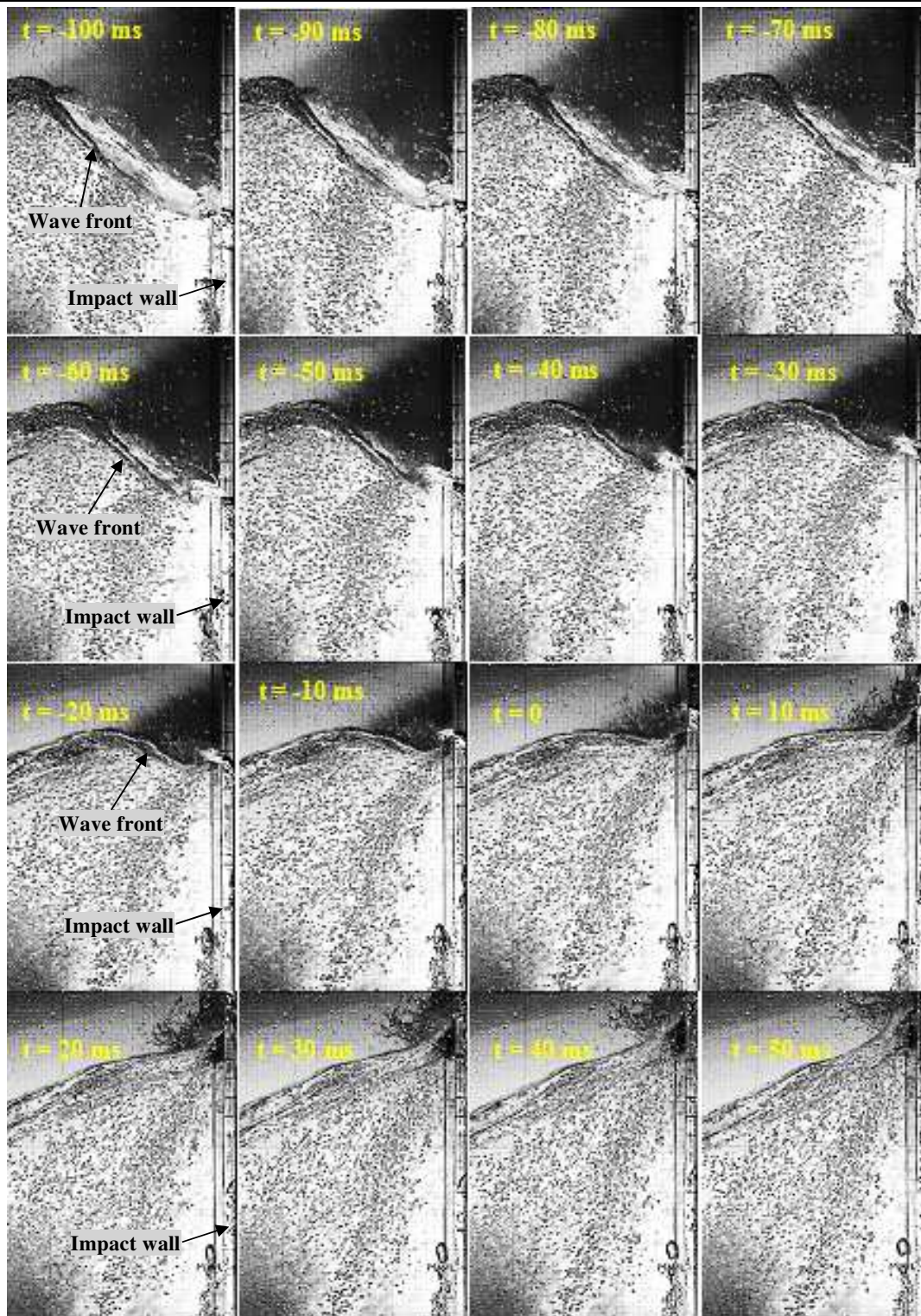
Figure 5-27: Snapshots of slightly breaking wave impact in aerated water (d = 0.625 m). In each snapshot, the wave was coming from the left and the wall was located on the right.

5.2 Discussion of aeration effect on wave impacts

5.2.1 Impact pressure and impulse in pure and aerated water

The wave impact pressures (P_{max}) due to broken, high-aeration, flip-through and slightly breaking wave impacts in aerated water have been tested with lognormal and extreme value models to ascertain that no accidentally measured data with a much higher probability of non-exceedance are included in analysis. It is shown that no sampled data are placed outside of the 95% confidence intervals of lognormal and/or extreme value models which are used to test each data set at each level *z/d* (see Appendix C:).

The maximum pressures at various levels on the rigid wall are presented in Figure 5-28 for wave impacts in pure and aerated waters with water depth *d* = 0.625 m. The vertical axis is the dimensionless level *z/d* of the measured points on the wall and the SWL (Still Water Level) is represented by *z/d* = 0. The horizontal axis is the logarithm of dimensionless impact pressure, $P_{max}/\rho gd$. The black diamonds are the impact pressures in pure water and the red pluses are the impact pressures in the aerated water with 0.6% of void fraction. The solid and dashed lines are the mean values of data points at each level on the rigid wall in pure and aerated waters, respectively. Maximum impact pressures were found to occur at vertical positions above SWL for impacts in 0.625 m water depth and this is similar to the finding by Hofland et al. (2011). It is clearly seen from Figure 5-28 that there is a significant reduction of the impact pressures from pure water to aerated water. The maximum impact pressures measured in pure water were 0.27 bar, 0.38 bar, 0.56 bar and 0.2 bar for the broken, high aeration, flip-through and slightly breaking wave impacts, whereas those maximum impact pressures were only from 0.03 bar to 0.13 bar for wave impacts in aerated water. This reduction of the impact pressures was caused by increase in aeration in the water body (The aerated water with 0.6 % void fraction has its density of 992 kg/m³, while the pure water has its density of 998 kg/m³). In addition, the incident wave which was affected by the current

and turbulence induced by the bubble generator, lead to reduced impact pressures in aerated water. Significant reduction of the impact pressure from 5.5 bar in pure water to 0.9 bar in aerated water of 0.8 % void fraction, which was generated by a bubble curtain, was also found in the experimental work of Kimmoun et al. (2012). Figure 5-28 shows the mean values of the impact pressures in aerated water (dashed line) were much smaller than that in pure water (solid line).
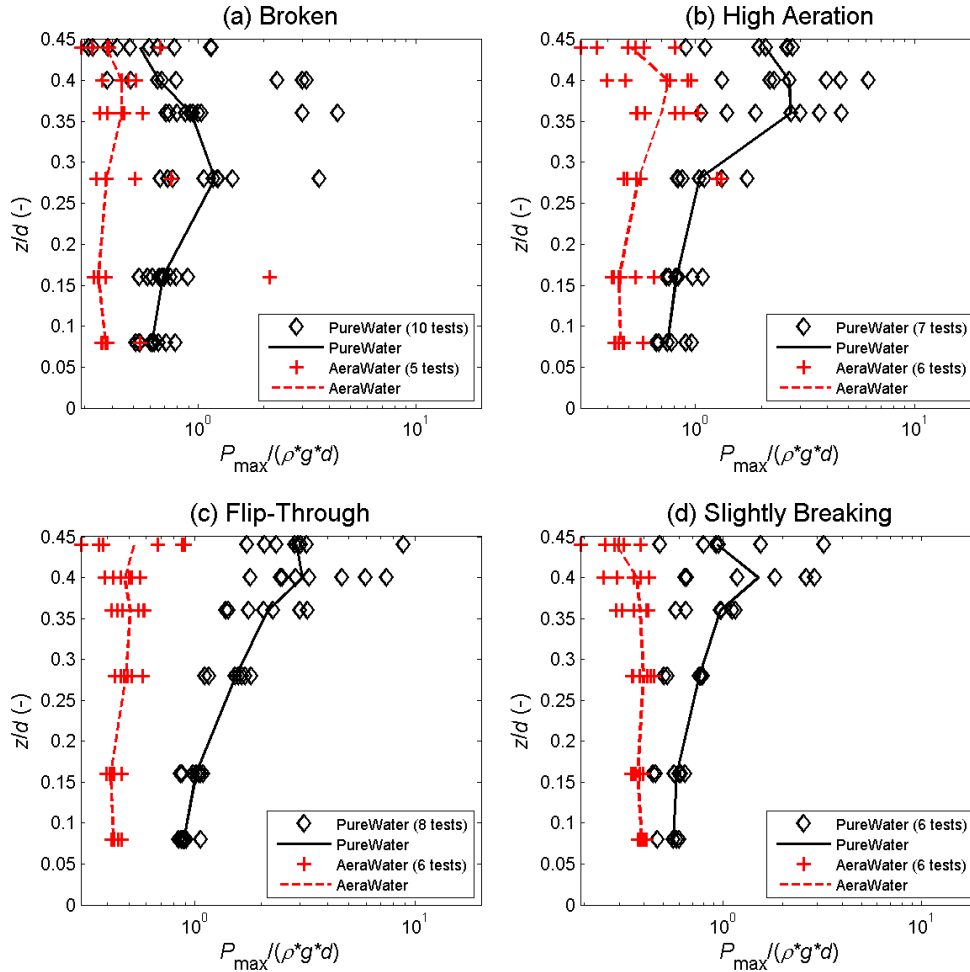
Figure 5-28: Impact pressures on rigid wall in pure and aerated water.

Pressure impulses on the vertical rigid wall are presented in Figure 5-29 for pure and aerated water. The black diamond marker and solid line are the pressure impulse and the medium value at the measured levels in pure water, respectively. The red plus marker and dashed line are for the aerated water. The results show that the pressure impulses in aerated water are smaller than those in pure water for all types of wave impacts (broken,

high aeration, flip-through and slightly breaking). Pressure impulses decrease with increasing the level on the wall for both pure and aerated water.
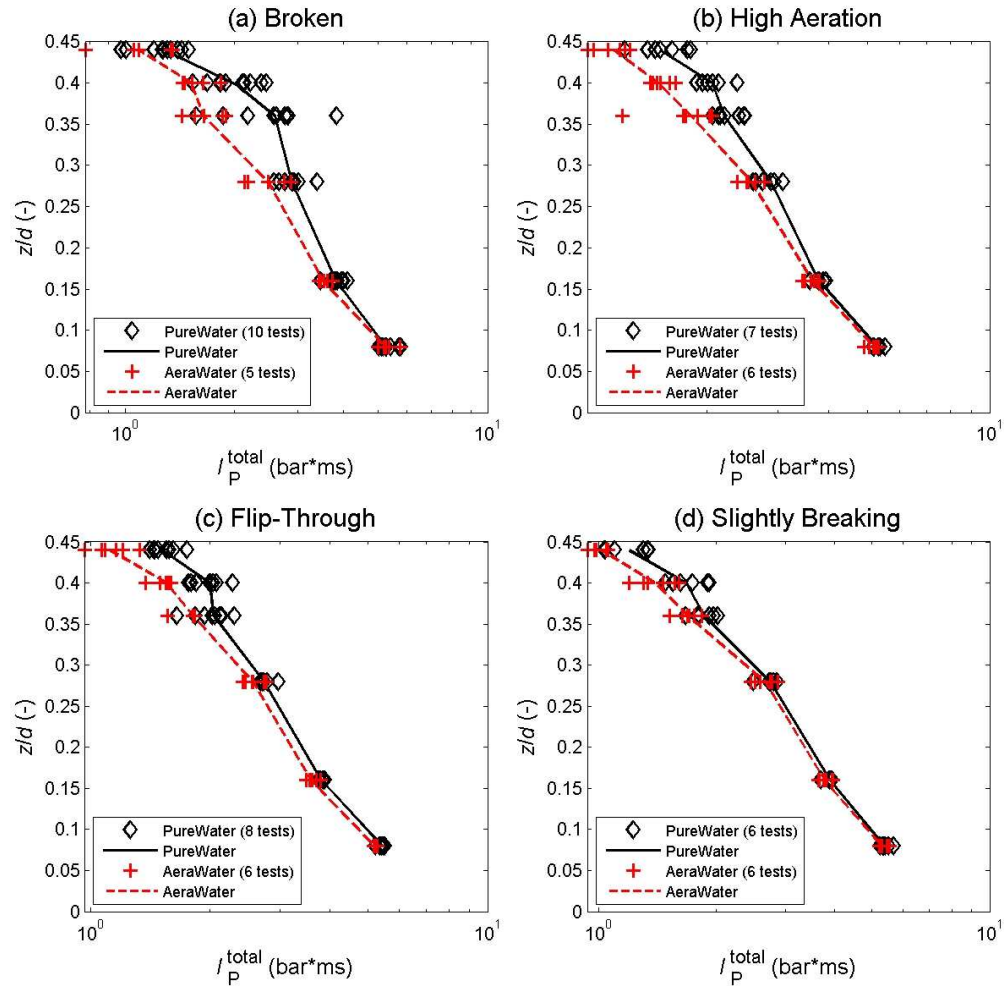
Figure 5-29: Pressure impulses on rigid wall in pure and aerated water.

5.2.2 Impact force and impulse in pure and aerated water

Figure 5-30 presents the mean value and its variation of the impact forces and force impulses on the rigid wall in pure and aerated water for the tested wave impacts. It is shown that the impact forces in pure water are significantly higher than the impact force in aerated water (Figure 5-30a). In both pure and aerated waters, the flip-through impact resulted in the highest impact force and the lowest impact force is for the broken wave impact. The aerated water was also found to decrease the overall load which was integrated from the measured pressures in Kimmoun et al. (2012). In general, the average values of the total force impulses in pure water are higher than those in aerated

107

water but their variation is quite large where in some events the total force impulse in aerated water is larger than that in pure water (Figure 5-30b).
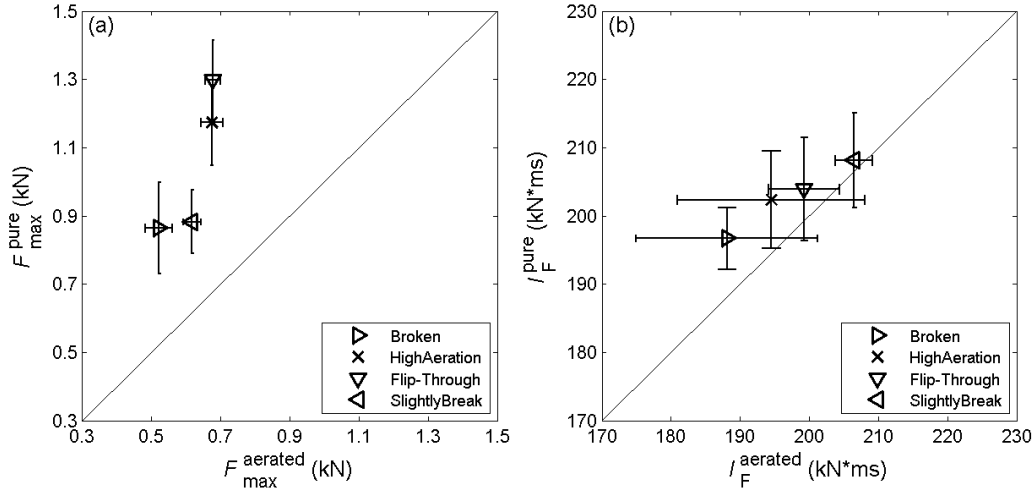
Figure 5-30: (a) Impact force and (b) force impulse on rigid wall in pure and aerated water.

5.3   Discussion of hydroelasticity effect on wave impacts

5.3.1 Comparison of acceleration, force, deflection and pressures on the rigid and elastic walls

Typical time histories of acceleration, force, deflection of springs and pressures on the rigid and elastic walls are presented in Figure 5-31 to Figure 5-40. The corresponding FFT spectra are also presented in those figures. It can be clearly seen that the low oscillation frequency (~37 Hz) after impact in the time histories and FFT spectra of acceleration, force and deflection of springs of the tested walls (Figure 5-31, Figure 5-33, Figure 5-35, Figure 5-37 and Figure 5-39). Evidence of this low frequency can also be seen in the pressure signals under high aeration and flip-through wave impacts on the rigid and elastic walls (Figure 5-36 and Figure 5-38). Acceleration of the impact walls increases with increasing flexibility of the wall and there are higher oscillation frequencies for the more flexible wall (Figure 5-31a-b, Figure 5-33a-b, Figure 5-35a-b, Figure 5-37 a-b and Figure 5-39 a-b). Maximum force of the wall also decreases with increasing flexibility of the wall, except for the slightly breaking wave impact whereas the maximum force on the elastic wall 1 is higher than that on the rigid wall (Figure

5-39c). This reduction of the maximum force can be clearly seen for the high aeration and flip-through wave impacts (see Figure 5-35c and Figure 5-37c). As expected, deflection of springs increases significantly with decreasing stiffness of spring under the tested wave impacts (Figure 5-31e, Figure 5-33e, Figure 5-35e, Figure 5-37e and Figure 5-39e). Pressures on the tested walls are found to be very sensitive under wave impacts and it is difficult to assess how hydroelasticity affects the pressure on the walls by comparing single test cases between the tested walls (Figure 5-32, Figure 5-34, Figure 5-36, Figure 5-38). However, for the slightly breaking wave, which is known to be more stable than the other wave impact types, as also found for the force on the wall, the pressures on the elastic wall 1 are higher than those on the rigid wall, although they are seen to decrease with the more flexible wall (Elastic wall 2), see Figure 5-40. The respective FFT spectra are presented in the right hand plots in Figure 5-32 to Figure 5-40 for the time histories of pressures presented in the left hand plots. The spectra are plotted on the lin-log scale (with logarithmic scale for the y-axis) to show more detail of the spectral tail form. There are many high frequencies of the corresponding discrete events in the time histories of the measured pressure signals.
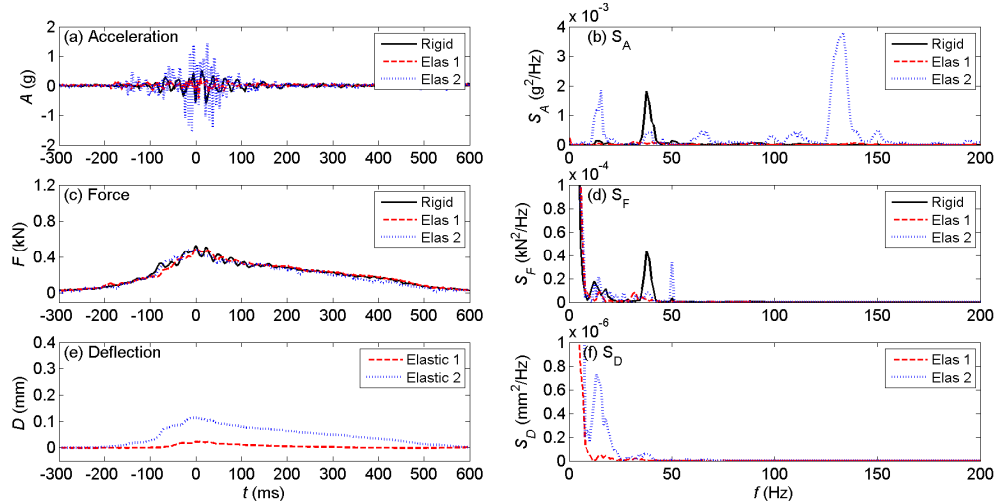
Figure 5-31: Time histories (left) and their spectra (right) of acceleration, force and deflection due to early broken wave impact.
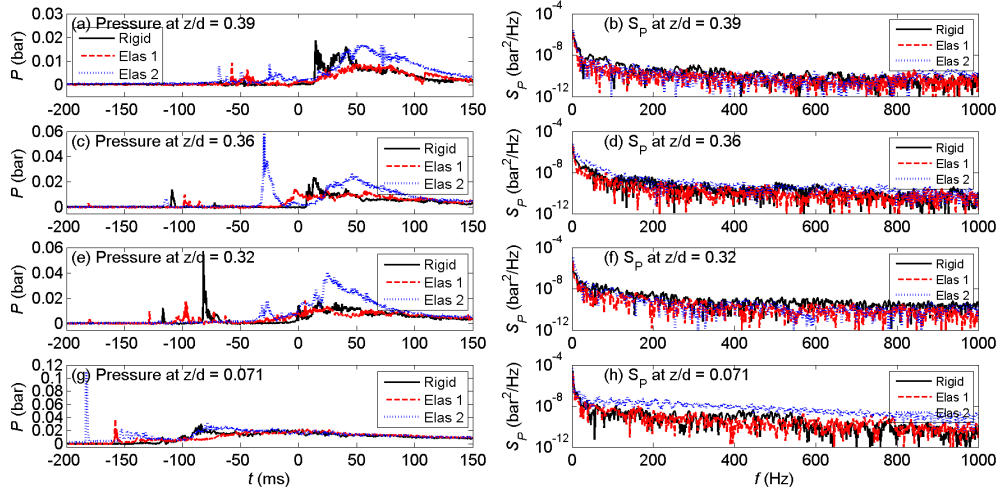
Figure 5-32: Pressure time histories (left) and their spectra (right) due to early broken wave impact on the walls. Note the different vertical scales.
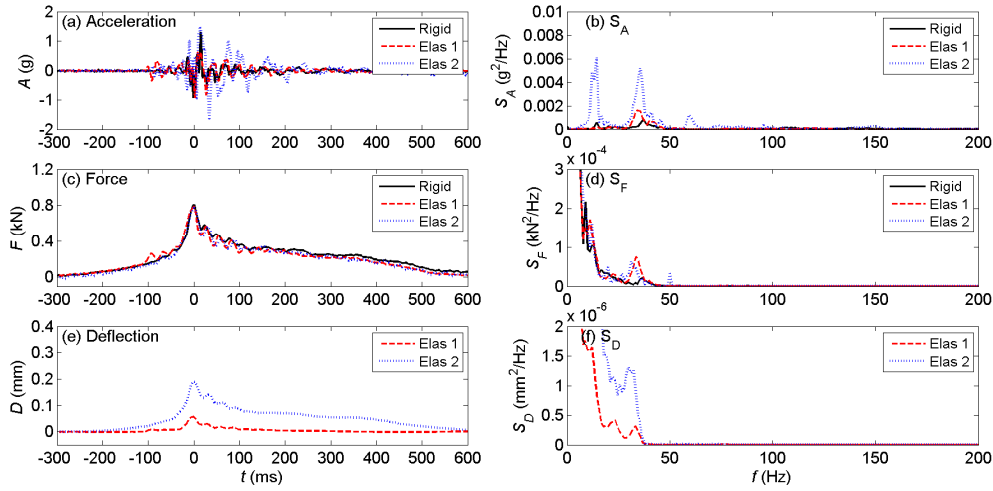
Figure 5-33: Time histories (left) and their spectra (right) of acceleration, force and deflection due to broken wave impact.
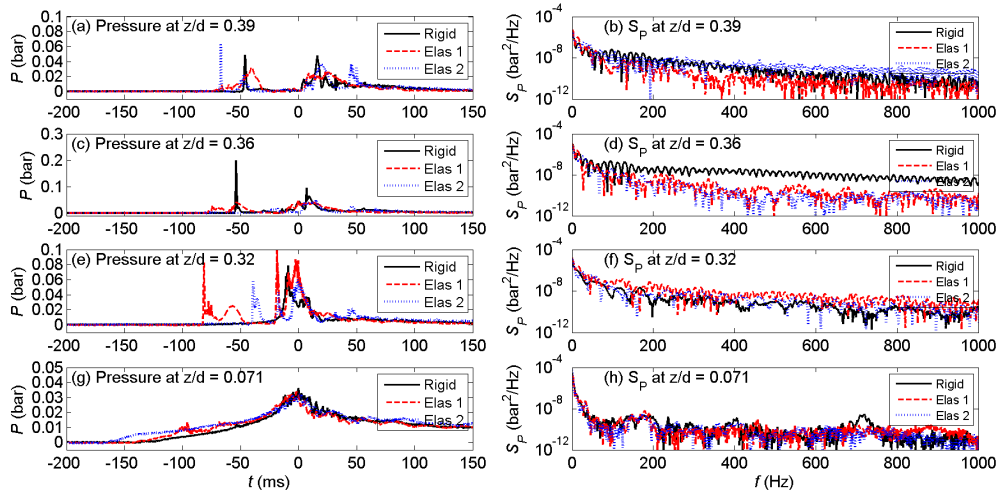
Figure 5-34: Pressure time histories (left) and their spectra (right) due to broken wave impact on the walls. Note the different vertical scales.
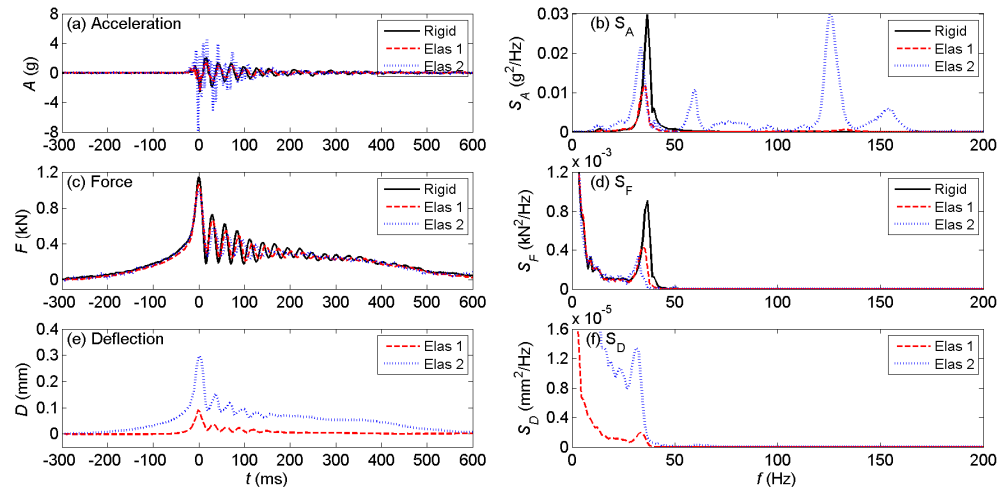
Figure 5-35: Time histories (left) and their spectra (right) of acceleration, force and deflection due to high aeration impact.
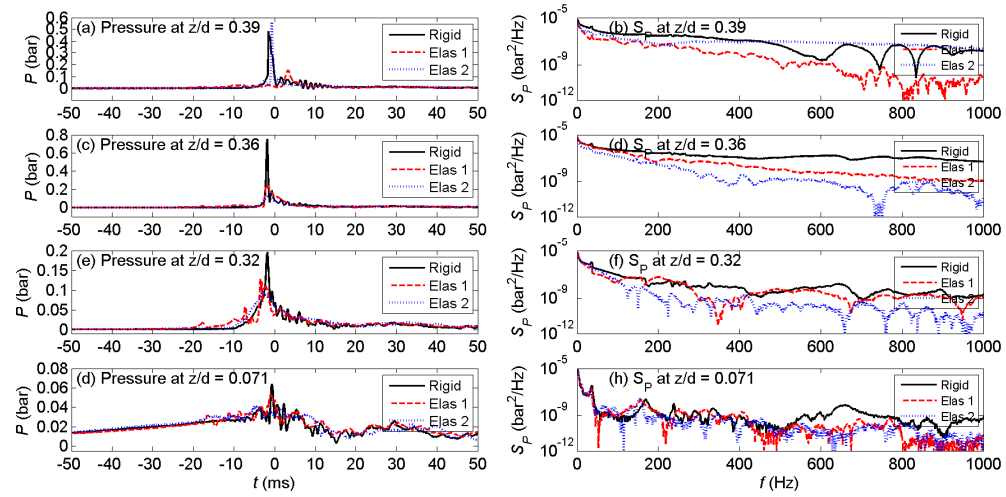
Figure 5-36: Pressure time histories (left) and their spectra (right) due to high aeration wave impact on the walls. Note the different vertical scales.
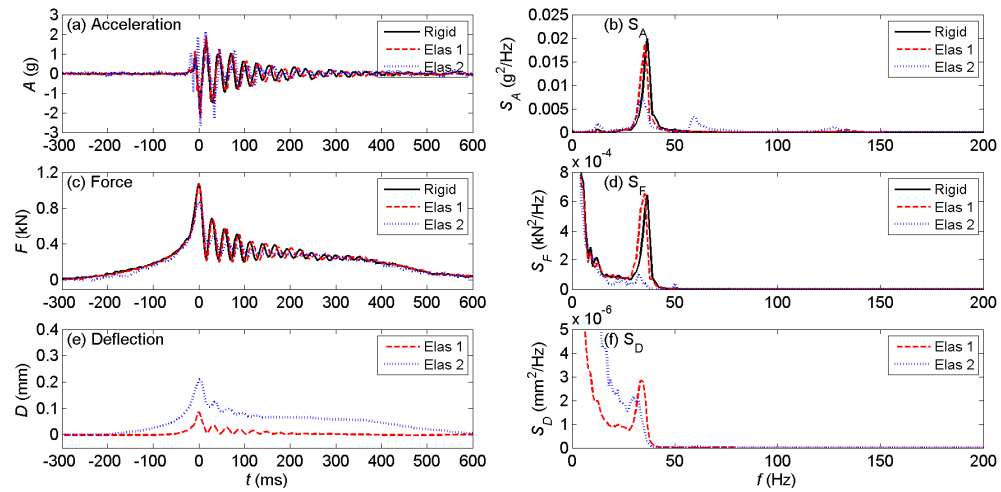
Figure 5-37: Time histories (left) and their spectra (right) of acceleration, force and deflection due to flip-through impact.
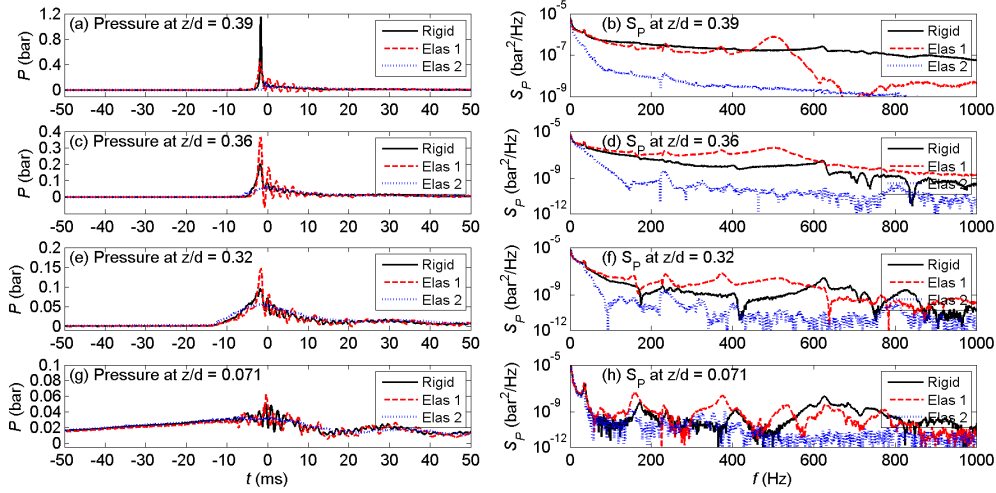
Figure 5-38: Pressure time histories (left) and their spectra (right) due to flip-through wave impact on the walls. Note the different vertical scales.
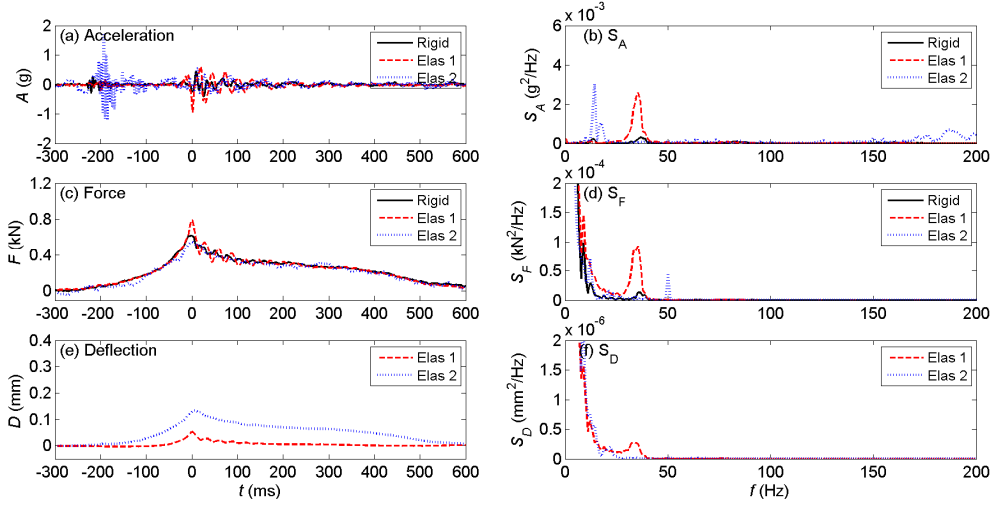
Figure 5-39: Time histories (left) and their spectra (right) of acceleration, force and deflection due to slightly breaking wave impact.
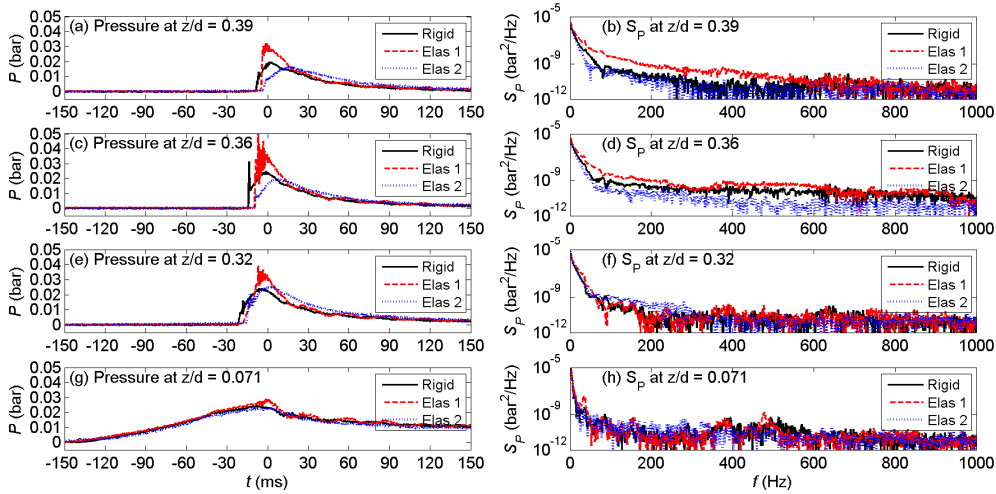
Figure 5-40: Pressure time histories (left) and their spectra (right) due to slightly breaking wave impact on the walls. Note the different vertical scales.

5.3.2 Impact pressure and impulse on rigid and elastic walls

The maximum pressures at various levels (z/d = 0.071 to 0.39) are presented in Figure 5-41 for different types of wave impact on the rigid and elastic walls. For the tested elastic wall 2, pressures were only measured at four levels of z/d = 0.071, 0.32, 0.36 and 0.39. The vertical axis is the dimensionless level z/d of the measured points on the wall and SWL is represented by z/d = 0. The horizontal axis is the logarithm of dimensionless impact pressure, $P_{max}/(\rho gd)$. In each plot of Figure 5-41, the black circle represents the impact pressures on the rigid wall, while the red cross and blue square are respectively for the elastic walls 1 and 2. The solid, dashed and dotted lines connect the mean values of the measured maximum pressure at each level on the rigid wall, elastic walls 1 and 2, respectively. Note these results were obtained from the tests with the water depth of 0.7 m. It can be seen from Figure 5-41 that the distributions of the impact pressures on the tested walls are different under various wave impact types (early broken, broken, high aeration, flip-through and slightly breaking) and the highest impact pressures were attained at the levels above SWL which is similar to the finding by Hofland et al. (2011), while most previous works found the highest impact pressures occurred at and around SWL (Hattori et al., 1994; Oumeraci et al., 1993; Hull and Müller, 2002; Bullock et al., 2007). For the early broken wave impact, the highest medium value of the impact pressures occurred at level of z/d = 0.25 for all the rigid and elastic walls (Figure 5-41a). At levels of z/d = 0.25 to 0.32, high impact pressures on the rigid and elastic walls were attained under broken wave impact (Figure 5-41b). Under high aeration wave and flip-through impacts, the impact pressures are significantly higher further up the wall (greater z/d), except for the high aeration wave impact in which the medium value of the impact pressures at level z/d = 0.39 is slightly smaller than that at level z/d = 0.36 on both the rigid wall and the elastic wall 1 (Figure 5-41c,d). For the high aeration case the impact pressure appears to peak at level z/d =

0.36, while for the flip-through the impact pressure continues to increase with distance up the wall. The highest impact pressure on the rigid wall and the elastic wall 1 were 1.15 bar ($P_{max}/\rho gd$ = 16.8) and 0.44 bar ($P_{max}/\rho gd$ = 6.4) which were both recorded at level z/d = 0.39 under the flip-through impacts (Figure 5-41d). On the other hand, the highest impact pressure of 0.56 bar ($P_{max}/\rho gd$ = 8.2) was measured at z/d = 0.36 on the elastic wall 2 under high aeration wave impact (Figure 5-41c). Figure 5-41e illustrates the distribution of the impact pressures on the rigid and elastic walls under the slightly breaking wave impacts. The impact pressures at the high levels (z/d = 0.25 to 0.39) are slightly larger than those at lower levels for all the tested walls. The impact pressures due to the slightly breaking wave impacts are much lower than those due to other wave impact types (early broken, broken, high aeration and flip-through). The early broken wave generated a water-air mixture turbulent bore (Figure 5-3) which caused the impact pressures at the lower levels z/d = 0.071 to 0.14 to be much higher than those due to the other wave impacts, in which the impact pressures were more likely caused by the run-up of the wave trough on the walls at these lower levels (Figure 5-6, Figure 5-9, Figure 5-12 and Figure 5-15). Considering single impact events, the highest impact pressures on the rigid wall (P_{max} = 1.15 bar) are much higher than those on the elastic walls (P_{max} = 0.44 bar for the elastic wall 1; P_{max} = 0.56 bar for the elastic wall 2). However, the medium values of all recorded impact pressures are more or less the same for the rigid and elastic walls at all levels, except the impact pressures on the elastic wall 2 are much smaller than those on the rigid wall and the elastic wall 1 under the flip-through impact (Figure 5-41d). Large scatter of the impact pressures was observed at all levels on the walls for the early broken wave impacts (Figure 5-41a). For the broken, high aeration and flip-through wave impacts, large scatter of the impact pressures was also found at high levels (z/d = 0.25 to 0.39) on the walls (Figure 5-41b,c,d). Stability of the slightly breaking wave impact caused the smallest scatter of impact pressures at all levels,

whereas the evolution of pressures on the wall is simply as the hydrostatic pressures on the walls (Figure 5-41e). The large scatter of the impact pressures on a vertical wall under different wave impacts were also observed in previous studies (Hattori et al., 1994; Oumeraci et al., 1993; Hull and Müller, 2002; Bullock et al., 2007).
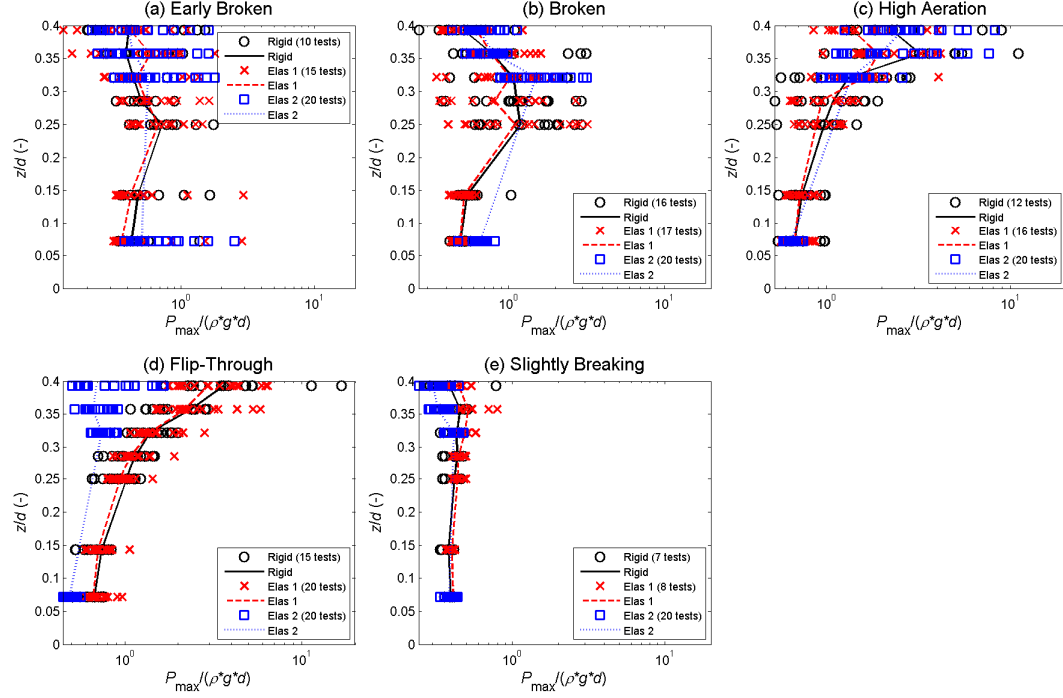
Figure 5-41: Impact pressures ($P_{max}/\rho g d$) on the walls in pure water ($d = 0.7$ m).

The total pressure impulses ($I_P{}^{total}$) were obtained by integrating pressure values over the impact duration. Figure 5-42 present the total pressure impulses at different levels on the rigid and elastic walls under the tested wave impact types. The black circle, red cross and blue square markers represent the total pressure impulses on the rigid wall, the elastic walls 1 and 2, respectively. The line joining mean values of the total pressure impulses are also presented in each plot of Figure 5-42. It can be seen that the total pressure impulses on the rigid wall (the black solid lines) are approximately the same on the elastic wall 1 (the red dashed lines) at all levels due to the tested wave impact types. On the elastic wall 2, pressure impulses at levels from $z/d = 0.071$ to 0.32 are slightly higher than those on the rigid wall and the elastic wall 1 due to all wave impact types (Figure 5-42a-e). In general, the total pressure impulse decreases with increasing level

on the walls and this is because of the submerged duration at low level is higher than those at higher level even the maximum pressure at low level is much smaller than that at high level. This can be seen from the time histories of pressures at different levels on the wall under wave impacts presented in previous sections (Figure 5-2, Figure 5-5, Figure 5-8, Figure 5-11 and Figure 5-14).
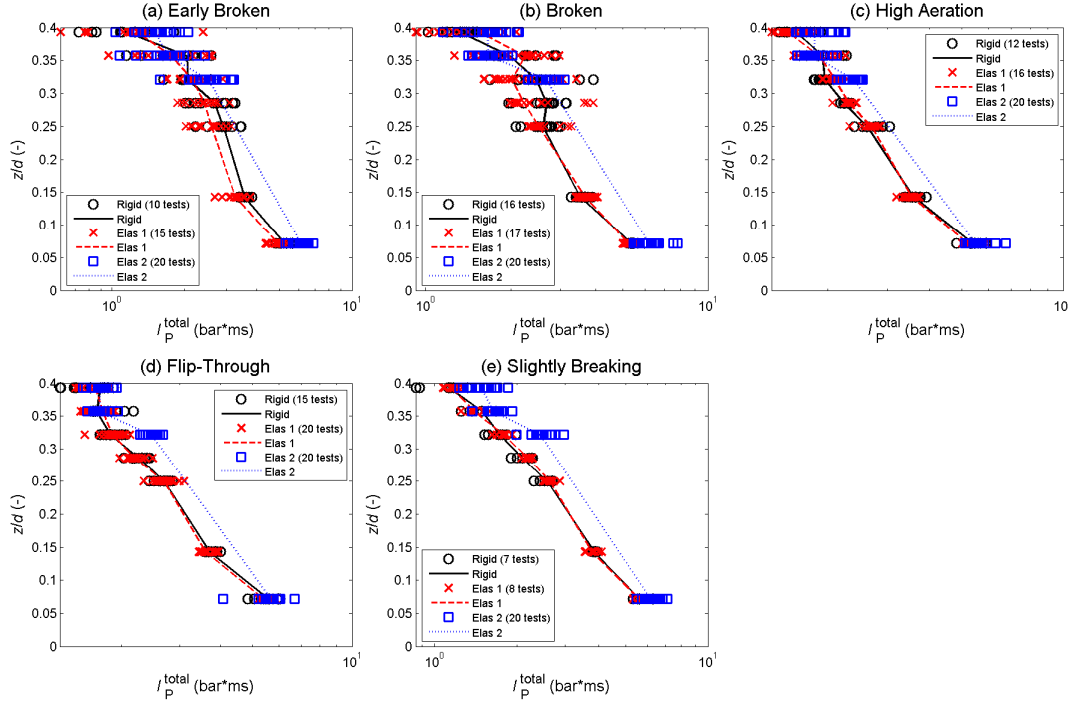
Figure 5-42: Pressure impulses (I_P^{total}) on the walls in pure water (d = 0.7 m).

5.3.3 Impact force and impulse on rigid and elastic walls

The mean impact force (F_{max}) and force impulse (I_F) on the rigid and elastic walls due to different wave impacts are presented in Figure 5-43. In each plot, the horizontal axis represents the impact force (Figure 5-43a) and total force impulse (Figure 5-43b) on the elastic wall, while the vertical axes represent those on the rigid wall. The black and red markers represent the elastic walls 1 and 2 data, respectively. The diagonal solid line in each plot is the 1:1 line.

It can be seen from Figure 5-43a that the mean impact forces on the rigid wall are the same as those on the elastic wall 1 due to the tested impact types, except for the slightly breaking wave impact whereas the impact force on the rigid wall is slightly smaller than

that on the elastic wall 1. In contrast, average impact forces on the elastic wall 2 are smaller than those on the rigid wall for the high aeration, flip-through and slightly breaking wave impacts. Due to the early broken wave impact, the impact forces on the rigid wall and the elastic wall 2 are approximately the same, but the force on the elastic wall 2 is higher than that on the rigid wall under the broken wave impact.

Figure 5-43b shows that the mean total force impulses on the rigid wall are higher than those on the elastic walls for the broken, high aeration, flip-through and slightly breaking impacts, while for the early broken wave impact the mean of total force impulses on the rigid and elastic walls are nearly the same. The total force impulses on the elastic wall 2 are significantly smaller than those on the elastic wall 1 for the broken, high aeration, flip-through and slightly breaking wave impacts. The scatters in the total force impulses (Figure 5-43b) are much larger than those of the impact forces (Figure 5-43a).
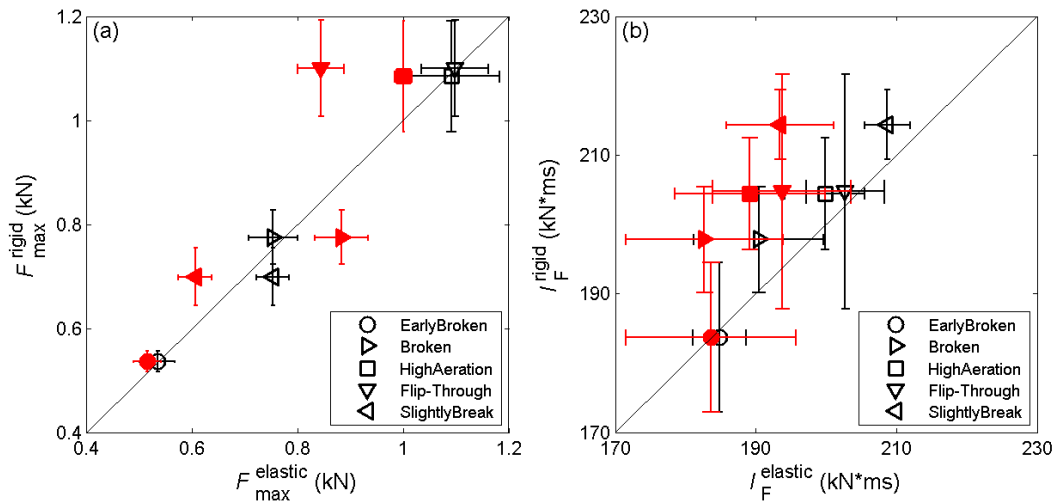
Figure 5-43: (a) Impact forces and (b) total force impulses on the walls in pure water ($d = 0.7$ m): Elastic wall 1 vs. Rigid wall (filled markers); Elastic wall 2 vs. Rigid wall (empty markers). The diagonal solid line is the 1:1 line.

5.3.4 Maximum deflection and impulse of springs

The mean maximum deflections of the springs used to create elastic walls are presented in Figure 5-44a. Due to the high aeration and flip-through impacts, the average deflections of the springs of the elastic wall 1 are approximately the same (~0.09 mm)

and they are nearly double the average deflections due to the broken and slightly breaking wave impacts (~0.05 mm) and triple the average deflection due to the early broken wave impact (~0.03 mm). The highest average deflection of springs of the elastic wall 2 is found for the high aeration wave impact (~0.3 mm). The average deflection due to the broken wave impact (~0.24 mm) is higher than that of the flip-through impact (~0.2 mm). The early broken wave impact caused the smallest average deflection of springs of the elastic wall 2 (~0.12 mm). Overall, the average deflections of the springs of the elastic wall 2 are much higher than those for the elastic wall 1. These are simply due to the spring rate of the elastic wall 2 (CL51x254: $k = 4*35$ N/mm) is nearly one-third of the spring rate of the elastic wall 1 (CL51x102: $k = 4*94$ N/mm). The total deflection impulses are presented in Figure 5-44a, whereas we can see that the total deflection impulses of the elastic wall 2 are about ten times those of the elastic wall 1.
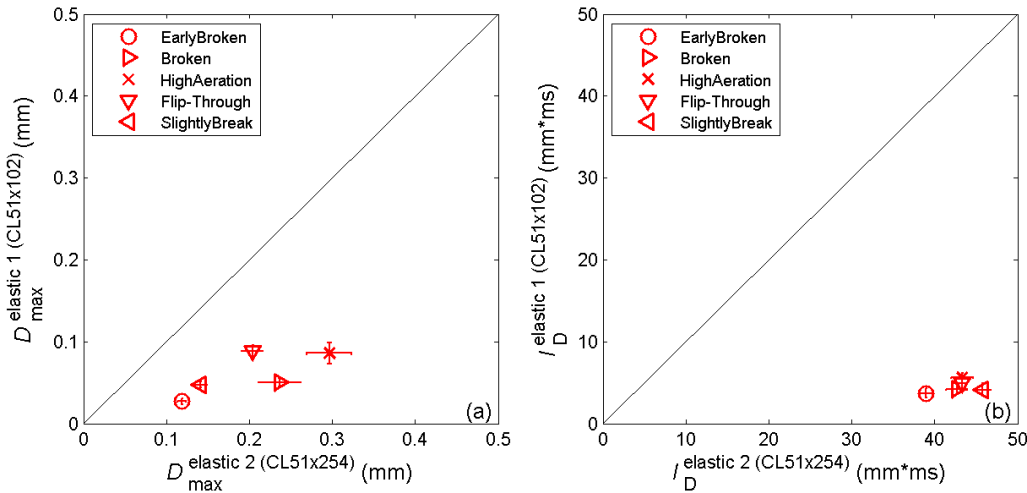
Figure 5-44: (a) Maximum deflection and (b) total deflection impulses of the springs. The diagonal solid line is the 1:1 line.

5.4 Conclusions of wave impacts

This chapter presents an experimental investigation of different wave impacts on a truncated wall in pure and aerated water. The wall can be changed from the rigid wall to elastic wall to investigate hydroelasticity effects on the wave impacts. The wave impact

types include the early broken, broken, high aeration, flip-through and slightly breaking wave impacts. The results of the study show that:

- Oscillations observed in time histories of pressures and total horizontal force are due to elasticity of the tested models, pressure wave reflections and trapped air bubbles.

- High aeration and flip-through wave impacts are found as the violent impacts on the hulls of offshore structures, which can produce very high both impact pressure and horizontal force on the hulls. These wave impact types should be considered for offshore structure design.

- In contrast to the drop test (slamming impacts), pressure measurement due to wave impact on the truncated vertical wall was unrepeatable, but the total force on the wall was found to be repeatable.

- Impact pressure on the wall due to flip-through impact decrease with increasing elasticity of the wall. However, the total pressure impulse on the wall increases with the more flexible wall.

- Impact force is reduced with the more flexible wall due to high aeration, flip-through and slightly breaking wave impacts. Additionally, there is a significant hydroelasticity effect on the total force impulse on the vertical wall under all wave impact types, whereas the total force impulse decreases as increasing elasticity of the wall.

- Aeration did significantly reduce peak wave loads (both pressure and force) on the wall, but impulses were not much reduced.

- Implications for design are that maximum instantaneous loads may be conservative in the presence of aerated water.

CHAPTER 6: WAVE-STRUCTURE INTERACTIONS OF FPSO MODELS

In this chapter, experimental results of wave-structure interactions of simplified FPSO-shaped bodies are presented and discussed, with the aim of understanding more about the wave-structure interaction, particularly the generation of scattered waves, the mooring line force and structural response, which may affect the local and global loadings of ship and offshore structures under non-breaking wave environment. These tests were carried out in the Ocean Basin at Plymouth University's COAST Laboratory where the effects on the wave-structure interaction of model length, wave steepness and incident wave direction were investigated. A detailed description of the experiment has been fully presented in Section 3.3. The non-dimensional ratio D/L_p of the tested waves varies from 0.09 to 0.11 (with the linear component), from 0.37 to 0.43 (with the second-harmonic), from 0.83 to 0.98 (with the third-harmonic) and from 1.48 to 1.74 (with the four-harmonic). Due to $D/L_p < 0.2$, the diffraction of the linear component is much weaker than those of the higher harmonic components (second-, third- and four-harmonics) which have $D/L_p > 0.2$.

6.1 Results of wave scattering around fixed models

6.1.1 Effect of model length on wave scattering
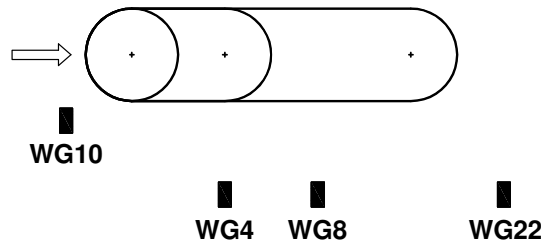
Figure 6-1. Location of WG4, 8, 10 & 22 for models 1, 2 & 3.

Wave gauges were positioned close to the tested models (see Figure 3-22) in order to examine how the model length affects the scattered wave field. Two locations were investigated, close to the bow (WG10) and at a fixed distance from the stern of the three models (WG4 for Model 1, WG8 for Model 2 and WG22 for Model 3), as shown in Figure 6-1, with exact gauge locations given in Figure 3-23. Results are presented for the steepest wave ($kA = 0.21$).

6.1.1.1 Near the bow

By applying the phase-based harmonic separation method introduced in Section 3.3.2, the linear and the higher harmonic components of the free-surface elevation ($\eta_{22}+\eta_{42}$, η_{33}, η_{44}) can be obtained at the bow of the models (for WG10 just upstream of the front stagnation point on the bow). The amplitude spectra that correspond to the time history of the separated components are shown in Figure 6-2. Comparing these spectra for the tests with and without the models in place indicates the considerable enhancement of the spectra due to the interaction of the incident waves with the models. This is evident in the importance of the second, third and fourth harmonics. In addition, it is found that the enhancement of the amplitude spectrum of the higher harmonics ($\eta_{22}+\eta_{42}$, η_{33}, η_{44}), due to wave interaction with Model 1 (the cylinder), are strongest in comparison with the interactions observed with Models 2 and 3. The amplitude spectra of the linear and higher harmonics caused by the presence of Models 2 and 3 are approximately the same, except the second harmonic (η_{22}), which is greater for Model 3 than for Model 2.

Figure 6-2. Amplitude spectra of the separated components near the bow of the models for $kA = 0.21$ (WG10). Note the different vertical scales.

The corresponding time histories of the separated harmonic components are derived by performing an inverse FFT of the corresponding filtered amplitude spectrum. These are presented in Figure 6-3 for the waves with and without the models in place. Significant enhancement of the free-surface elevation of the linear and higher harmonics due to wave scattering from the models can be clearly seen. The local free-surface elevation of the linear component has a lower crest and higher trough, in the presence of Model 1, than with Models 2 and 3 in place (Figure 6-3a). In contrast, the local free-surface elevations of the second, third and fourth harmonics have the highest crest and lowest trough with Model 1 and these are approximately the same with Models 2 and 3 (Figure 6-3b, c, d). For the second harmonic, the incident bound and scattered wave fields are roughly comparable (Figure 6-3b). However, the third and fourth harmonics indicate that the scattered wave field is significantly larger than the incident bound wave component (Figure 6-3c, d).

Figure 6-3. Time histories of the separated components near the bow of the models for $kA = 0.21$ (WG10). Note the different vertical scales.

Data on the scattered wave only are obtained by subtraction of the time histories with and without the models in place (Equation (3-10)); these are shown in Figure 6-4. As previously seen in Figure 6-3, the scattered waves of the second, third and fourth harmonics are strongest with Model 1 in place (Figure 6-4b, c, d). The third harmonic scattered wave is reduced as the model length is increased. It can be observed in Figure 6-4c & d that there is a second pulse in the third and fourth harmonics of the scattered wave fields, arriving about 1.5 s later than the first pulse. This may induce a second load cycle for the structure. It should be noted that this is entirely separated from the double frequency error wave off the paddles which arrived at the model at around $t = +13$ s in the time histories of the second harmonic components (Figure 3-27b), and will then diffract in a predominately linear manner.
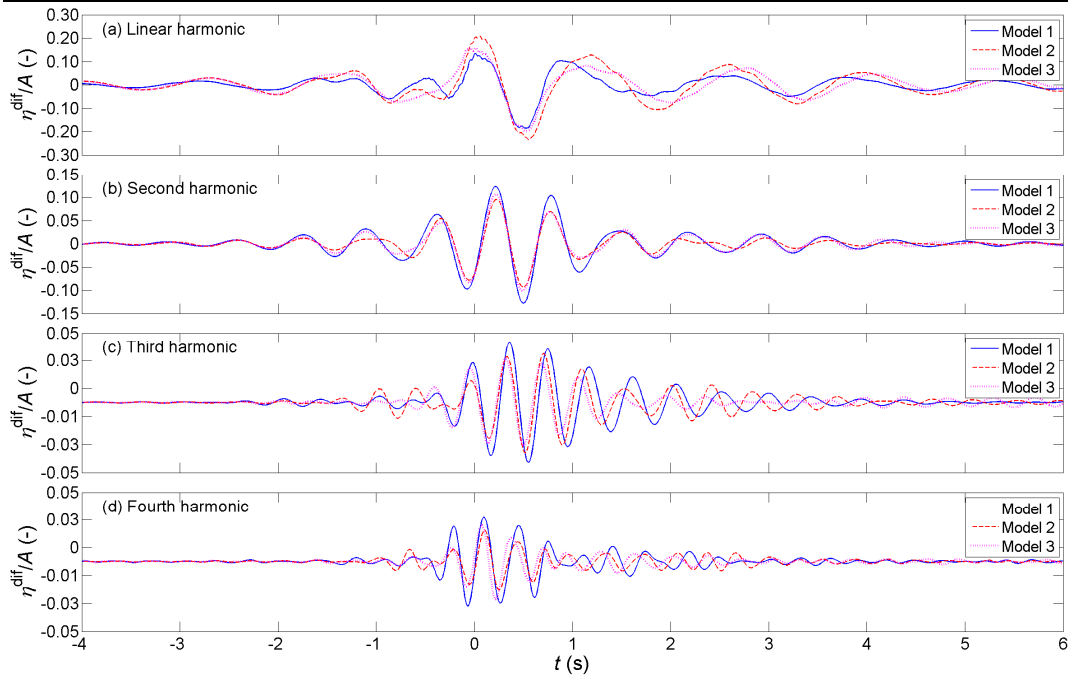
Figure 6-4. Time histories of the scattered waves near the bow of the models for $kA = 0.21$ (WG10). Note the different vertical scales.

6.1.1.2 Near the stern

Wave scattering at the stern of three models is investigated using wave gauges WG4, WG8 and WG22 shown in Figure 6-1, all of which have the same relative distance from the stern of Models 1, 2 and 3 respectively. The linear and higher-harmonic sum frequency harmonic components are separated by applying the phase-based method as before, and are presented in Figure 6-5 for the tests with and without models. The amplitude spectra of the linear harmonics with models in place are smaller than those without models (Figure 6-5a), but the amplitude spectra of the higher harmonics increase with models in place (Figure 6-5b, c, d). Furthermore, it is shown that the amplitude spectrum of the linear component decreases slightly as model length increases (Figure 6-5a). The amplitude spectra of the second- and third-harmonic sum frequency terms are highest in the presence of Model 2, while they are approximately the same with Models 1 and 3 (Figure 6-5b, c). For the fourth-harmonic sum frequency, the amplitude spectra are quite similar in magnitude but rather wiggly for all three models (Figure 6-5d). The harmonic extraction process is sensitive to the accuracy of

124

the time alignment of the four phase combinations, but the results presented here are very clearly separated between the different harmonics and we cannot see any significant leakage between harmonics.

Figure 6-5. Amplitude spectra of the separated components near the stern for $kA = 0.21$. Note the different vertical scales.

The time histories of the separated harmonics from the corresponding filtered amplitude spectra are shown in Figure 6-6. Data are also shown for the test without the models in place for comparison. The linear components are slightly smaller with the models in place (Figure 6-6a, e, i). The difference in the free surface elevation with and without the models in place is much more significant for the second-, third- and fourth-order sum frequency terms (Figure 6-6b-d, f-h, j-l). A second wave group due to diffraction from the model is observed in the second-, third- and fourth-harmonic sum frequency terms, and this appears to come later than the first pulse by about 3 s for the second harmonic (Figure 6-6b, f, j) and about 1.5 s for the third and fourth harmonics (Figure 6-6c, g, k & Figure 6-6d, h, l). The second wave packet is significantly lower in amplitude than the first group for the second harmonic (Figure 6-6b, f, j), while the second pulse is slightly higher than the first pulse for the third-order sum frequency component (Figure 6-6c, g, k). At the fourth-harmonic sum frequency, the first and second pulses are approximately the same amplitude, and it seems there is a third pulse in the free-surface elevation at about $t = 5.5$ s (Figure 6-6d, h, l). The second and third wave packets are clearly separated from and arrive much earlier than the double

frequency error wave trains off the wave paddles which arrived at the model position at $t = +13$ s (Figure 3-27b).

The time histories of the linear and higher harmonic scattered waves near the stern of the models presented in Figure 6-7 indicate the effect of wave-structure interaction on the linear component is quite weak (Figure 6-7a, e, i), but this effect is relatively much stronger for the higher harmonic components (Figure 6-7b-d, f-h, j-l). The free-surface elevations of second and fourth harmonic scattered waves are reduced as the model length increases (Figure 6-7b, f, j for the second harmonic & Figure 6-7d, h, l for the fourth harmonic). For the third harmonic component, the free-surface elevation of the scattered wave is strongest with Model 2 and it is nearly the same with Model 1 and 3 (Figure 6-7c, g, k).

One may speculate that this is an interference effect with substantial nonlinear scattering off the bow first and later off the stern. Both scattered components reach the downstream offset wave gauges but with different time delays for the different length models, so with different degrees of overlap in time.
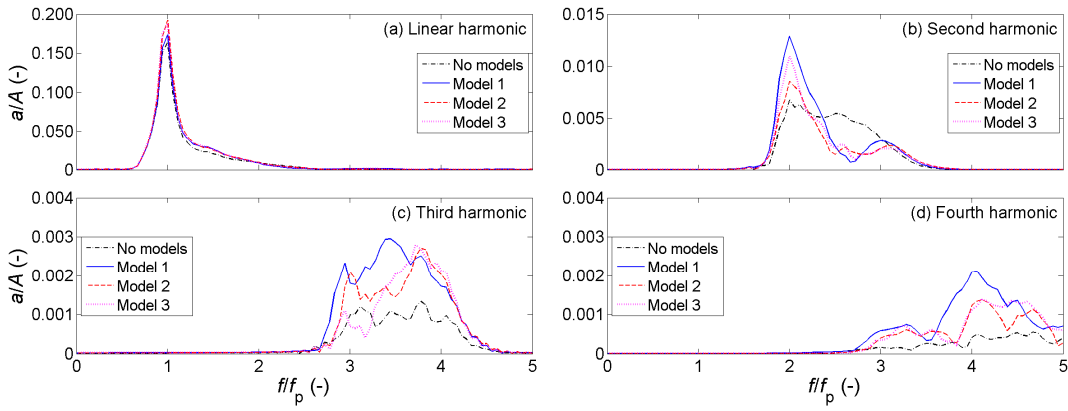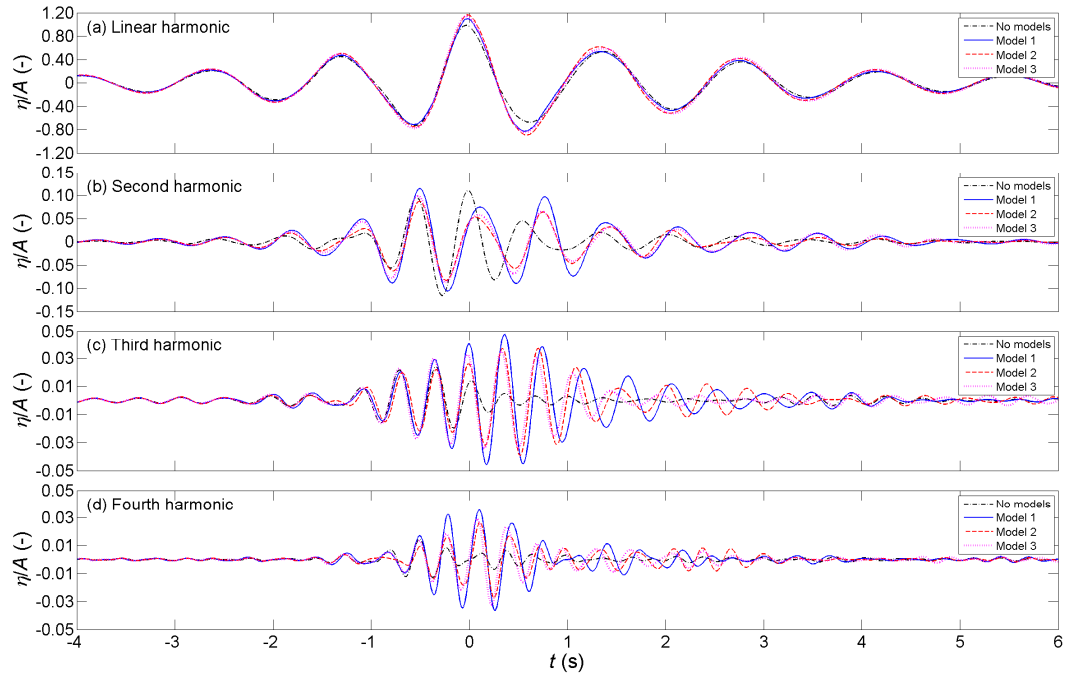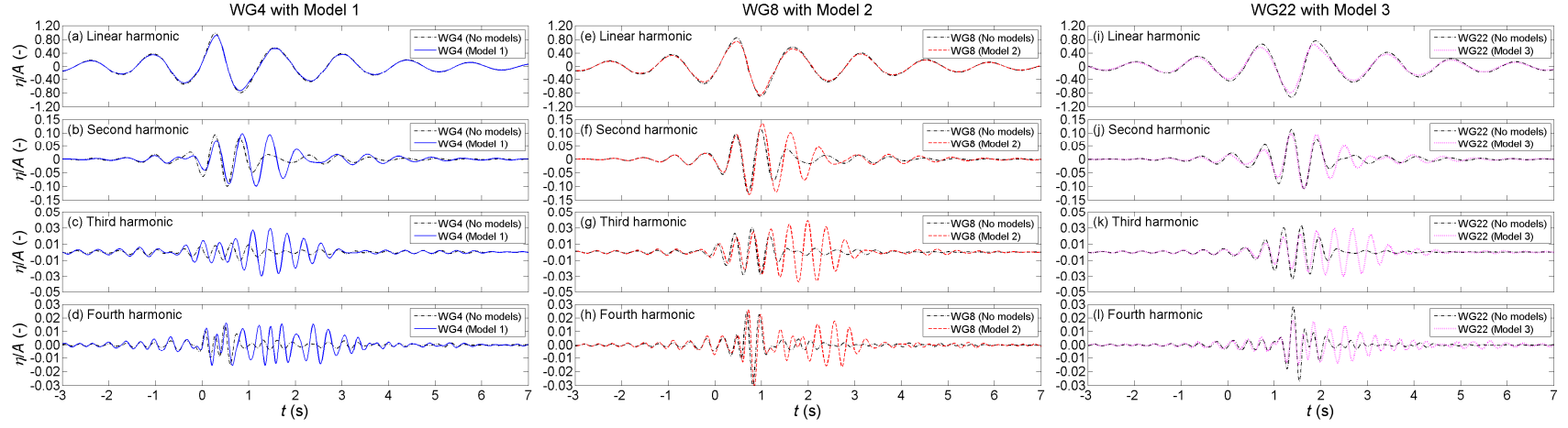
Figure 6-6. Time histories of the separated components near the stern of the models for $kA = 0.21$. Note the different vertical scales.

Figure 6-7. Time histories of the scattered waves near the stern of the models for $kA = 0.21$. Note the different vertical scales.

127

6.1.2 Effect of wave steepness on wave scattering

The input wave groups used in these experiments are defined assuming linear paddle transfer functions and then linear propagation and frequency dispersion on finite depth. For finite amplitude waves, cubic wave-wave interactions can occur which lead to changes in both the amplitude and phase of the waves away from linear predictions. This type of modulational instability was first observed by Benjamin and Feir (1967) for regular waves, see the review by Yuen and Lake (1980). For wave groups these effects are cumulative, increasing at increasing distance from the wave maker (see, for example, Baldock et al., 1996; Ning et al., 2009; and Adcock and Taylor, 2009 & 2016). Since it is necessary to change the amplitude of the incident packet to explore the amplitude ordering of the various scattered wave harmonics, it is important to establish whether nonlinear evolution is significantly changing the structure of the incident wave group when it interacts with the models.
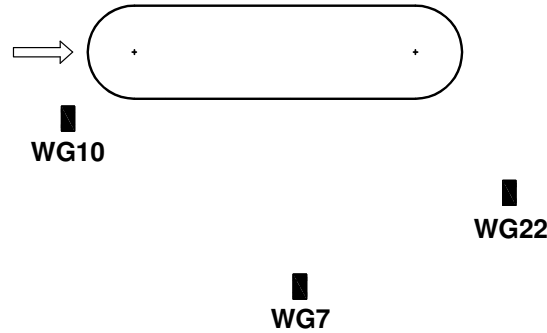
Figure 6-8. Location of WG7, 10 & 22 w.r.t Model 3.

The effect of wave steepness on the scattering is reported for Model 3, shown in Figure 6-8, with the focused wave groups of two different steepnesses and three gauge locations: near to the bow (WG10), to the side (WG7) and near to the stern (WG22). Results are presented for wave steepness kA = 0.13 and 0.18.

Time histories of the linear harmonics of the tested focused wave groups with steepness kA = 0.13 and 0.18, at the location near the bow of Model 3 (WG10) but with the model removed are presented in Figure 6-9. The solid line represents the scaled time history of the linear harmonic of the focused wave group with kA = 0.13 (by a scaling factor of

0.18/0.13 = 1.38), the dashed line for $kA = 0.18$ and the dotted line is the difference between the solid and dashed lines. It is shown that the solid and dashed lines are almost identical. Therefore, there is apparently no evidence of significant cumulative evolution beyond linear as the wave propagates from the paddle to the position of the model. The incident linear components can then be treated as identical in shape, simply with an amplitude scaling.
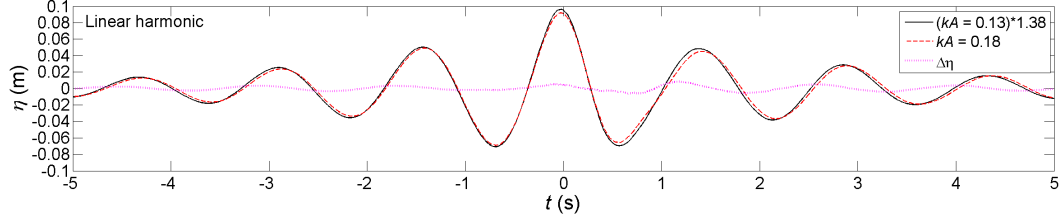
Figure 6-9. Comparison of the linear component of the tested wave groups ($kA = 0.13$ & 0.18).

Applying the phase-based separation method presented in Section 3.3.2, the amplitude spectra of the linear and second, third and fourth harmonics of the separated components are examined. Only the more interesting higher harmonics are presented in this section to examine the effect of wave steepness on the wave-structure interaction, because the linear component simply scaled with wave steepness, except for a slight difference at the spectral tail high frequencies. Amplitude spectra of the second, third and fourth harmonics of the separated components are presented in Figure 6-10, Figure 6-11 and Figure 6-12 for the location near the bow (WG10), to the side (WG7) and near the stern (WG22) of Model 3, respectively. In general, as would be expected, the amplitude spectra of the higher harmonics are seen to increase as the wave steepness is increased from $kA = 0.13$ (solid line) to $kA = 0.18$ (dashed line). The amplitude spectrum of the second harmonic near the bow of the model is significantly higher than those at the side and near the stern (Figure 6-10a, Figure 6-11a & Figure 6-12a), and there is slight difference in the amplitude spectra of the third and fourth harmonic components at those locations (Figure 6-10b-c, Figure 6-11b-c & Figure 6-12b-c). The steepness of the wave appears to have its greatest effect on the third harmonics where some of the values nearly double near the stern (Figure 6-12b).

129
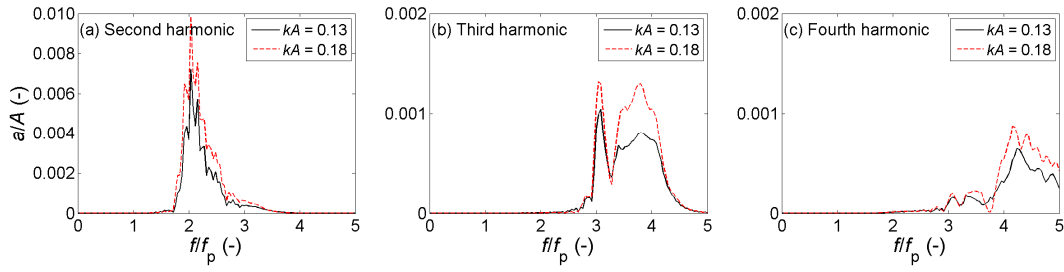
Figure 6-10. Amplitude spectra of the separated components near the bow of Model 3 (WG10). Note the different vertical scales.
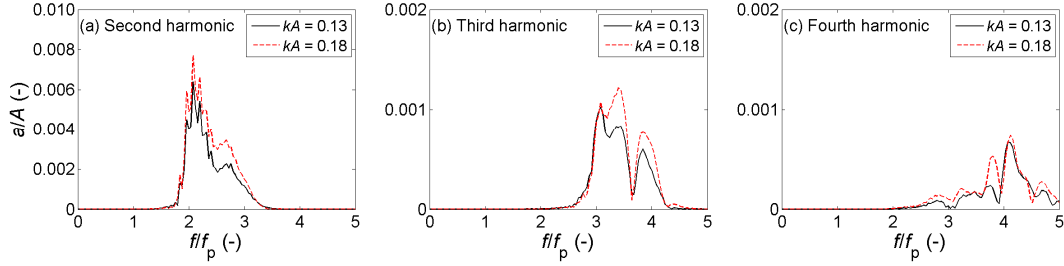
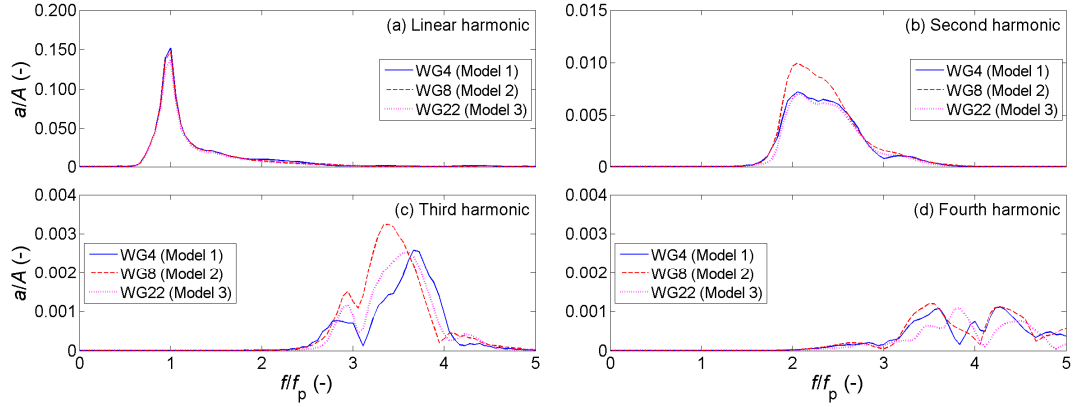Figure 6-11. Amplitude spectra of the separated components alongside Model 3 (WG7). Note the different vertical scales.
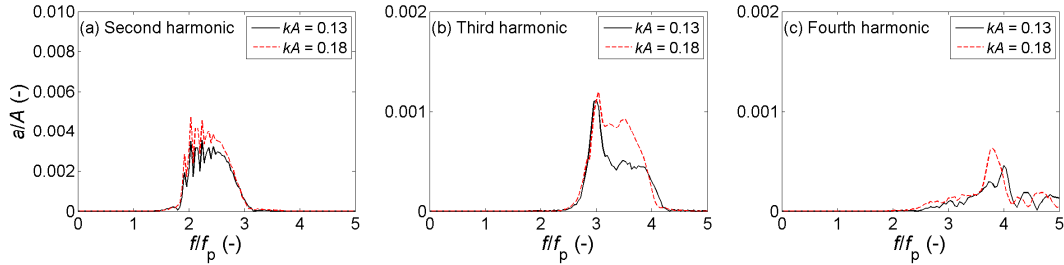
Figure 6-12. Amplitude spectra of the separated components near the stern of Model 3 (WG22). Note the different vertical scales.

The corresponding filtered time histories of the higher harmonics of the scattered wave fields at locations near the bow, to the side and near the stern of Model 3 are presented in Figure 6-13, Figure 6-14 and Figure 6-15, respectively. At the bow there is considerable amplification of the second and fourth harmonics (Figure 6-13a, c). A significant effect of the wave steepness can also be found at the third harmonic of the scattered wave near the stern (Figure 6-15b) as might be expected from the amplitude spectrum. The fourth harmonic component near the bow is much higher than that to the side and near the stern of the model (Figure 6-13c, Figure 6-14c and Figure 6-15c). This is at least due to WG10 being closer to the model so the radiated field has not decayed in amplitude significantly due to geometric spreading, whereas for the other gauge positions spreading is more important.
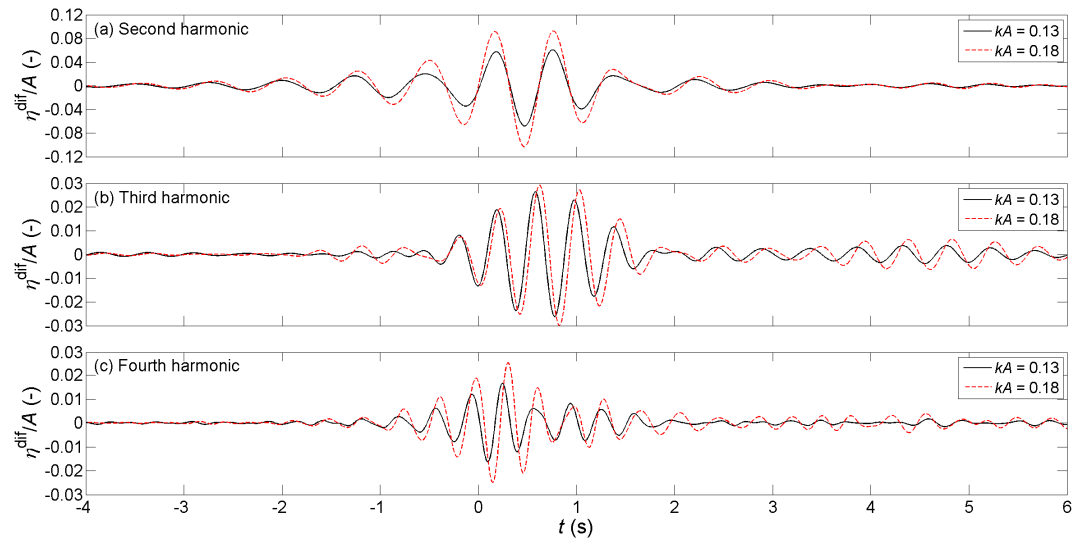
Figure 6-13. Time histories of the scattered waves near the bow of Model 3 (WG10). Note the different vertical scales.
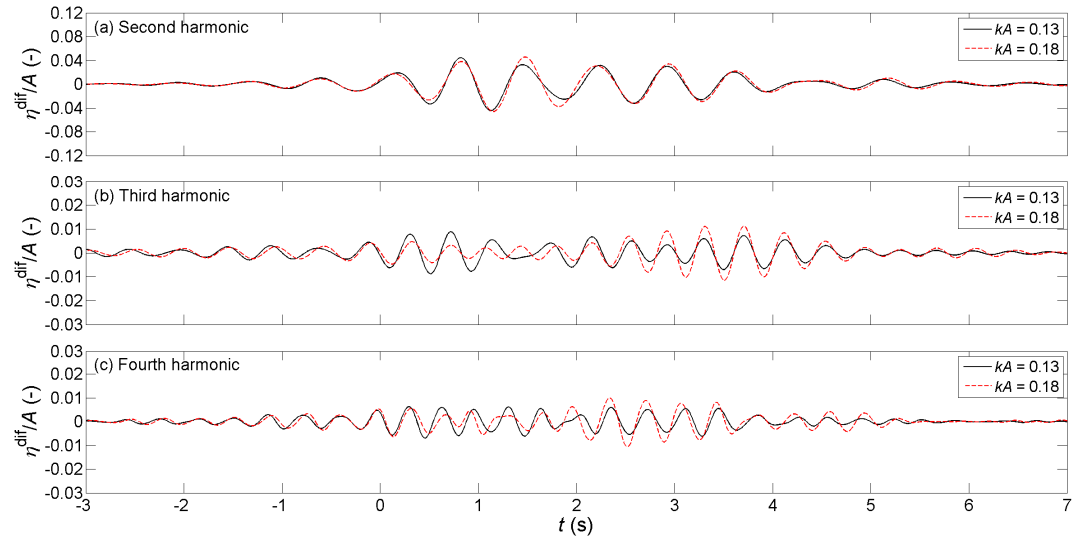
Figure 6-14. Time histories of the scattered waves alongside Model 3 (WG7). Note the different vertical scales.

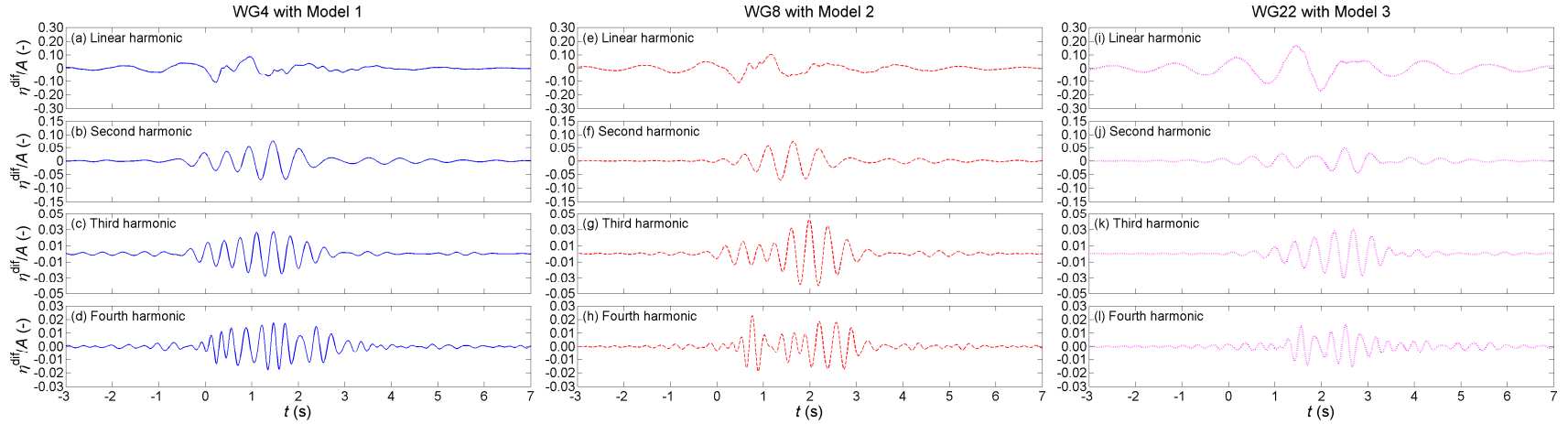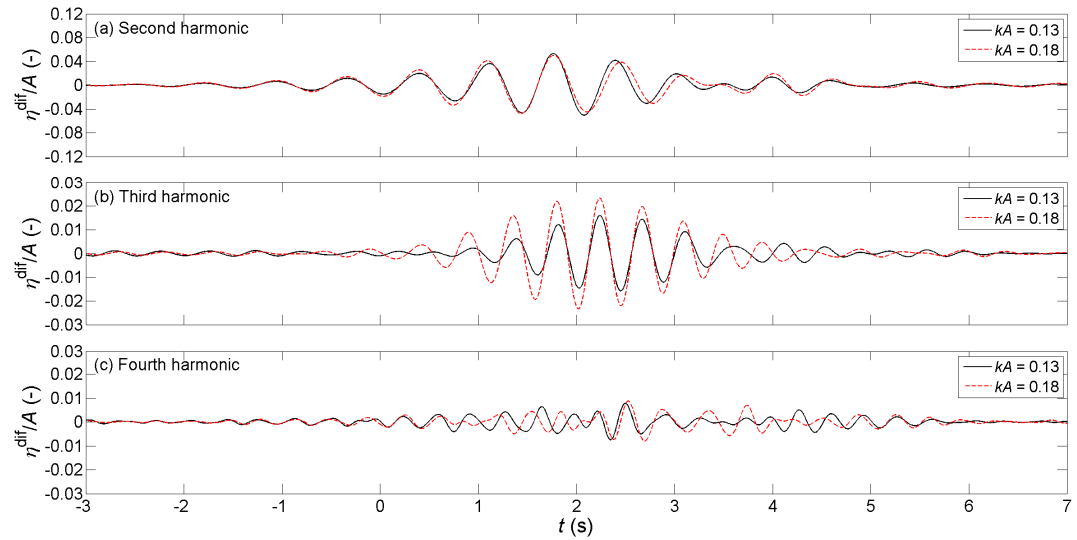

Figure 6-15. Time histories of the scattered waves near the stern of Model 3 (WG22). Note the different vertical scales.

131

6.1.3 Effect of incident wave angle on wave scattering
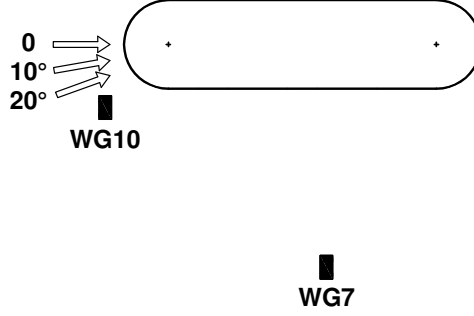
Figure 6-16. The tested incident wave angles with model 3.

Different incident wave angles were tested to investigate the effect of wave direction on scattering. Tests were conducted with incident wave directions of 0°, 10° and 20° (Figure 6-16) with a wave steepness $kA = 0.17$. In this case, only the crest focused wave group (η^0) and the trough focused wave group (η^{180}) were tested. Therefore, the odd and even harmonics were separated using the simple phase-inversion separation method which has been presented in previous studies (Baldock et al., 1996; Zang et al., 2006; Fitzgerald et al., 2014).

$$(\eta^0 - \eta^{180})/2 = \eta_{11} + \eta_{31} + \eta_{33} \qquad (6\text{-}1)$$

$$(\eta^0 + \eta^{180})/2 = \eta_{20} + \eta_{40} + \eta_{22} + \eta_{42} + \eta_{44} \qquad (6\text{-}2)$$

The odd and even harmonics are separated using Equation (6-1) and (6-2), respectively. Frequency filtering is applied to extract the higher harmonic amplitude spectra from the odd and even harmonics, and then the free-surface elevations of those higher harmonic terms ($\eta_{22}+\eta_{42}$, η_{33}, η_{44}) are obtained using inverse FFT of the filtered amplitude spectra.

Amplitude spectra of the linear and the higher harmonic components for the location near the bow (WG10) and to the side (WG7) of Model 3, due to different incident wave angles, are presented in Figure 6-17 and Figure 6-18, respectively. It can be seen that the amplitude spectra of the harmonic components increase as the incident wave angle increases from 0° to 20°, but are most energetic at the incident angle of 10°, except for

the third harmonic to the side where the amplitude spectrum decreases with increasing the wave angle (Figure 6-18c).

It is striking that the amplitude spectra are generally of comparable shape for the linear and second harmonics, as the approaching direction is altered. In contrast, the shape of the fourth harmonic spectrum changes somewhat and the third harmonic spectrum changes significantly, suggesting that third harmonic is in some sense 'different'.

The time histories of the scattered wave corresponding to the amplitude spectra near the bow and to the side are presented in Figure 6-19 and Figure 6-20. The linear, third and fourth harmonics are reduced with increasing angle of incidence for both locations (Figure 6-19a, c, d and Figure 6-20a, c, d). On the contrary, the second harmonic is greatest for the 10° wave (Figure 6-19b and Figure 6-20b). The third and fourth harmonics at the location near the bow (Figure 6-19c, d) are significantly larger than those to the side of the model (Figure 6-20c, d).
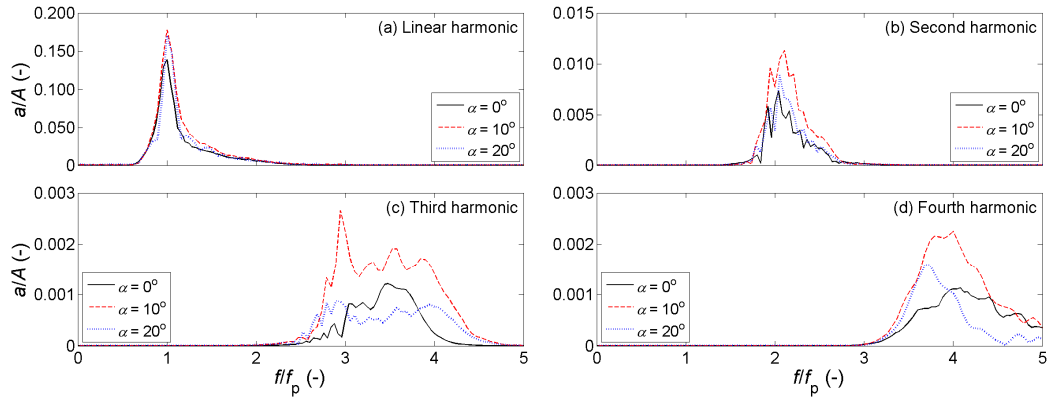
Figure 6-17. Amplitude spectra of the separated components near the bow of Model 3 for *kA* = 0.17 (WG10). Note the different vertical scales.
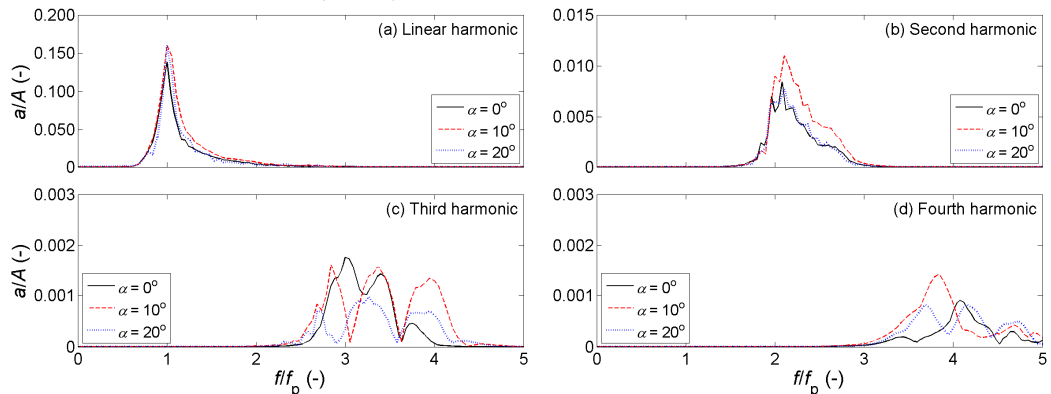
Figure 6-18. Amplitude spectra of the separated components alongside of Model 3 for *kA* = 0.17 (WG7). Note the different vertical scales.

133
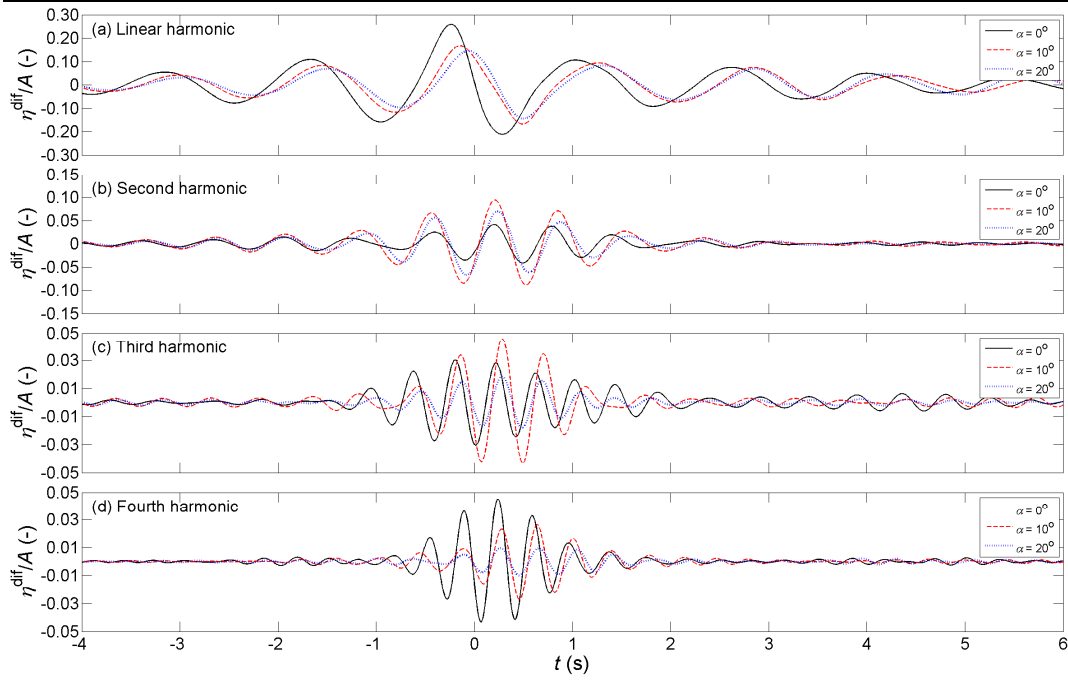
Figure 6-19. Time histories of the scattered waves near the bow of Model 3 for *kA* = 0.17 (WG10). Note the different vertical scales.
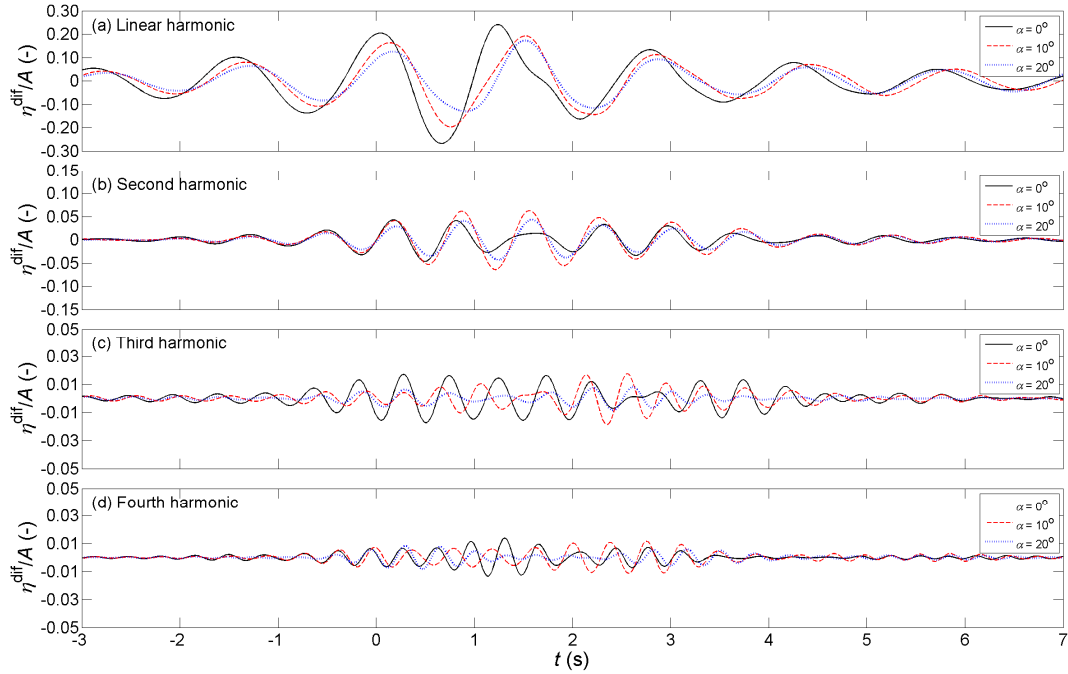
Figure 6-20. Time histories of the scattered waves alongside of Model 3 for *kA* = 0.17 (WG7). Note the different vertical scales.

6.1.4 Discussion of the results for the fixed models

This experimental work has shown that there are the second, third and fourth harmonic scattered waves upstream of the bow, out to the side and downstream of all three tested models. These findings are consistent with Fitzgerald et al. (2014) where their analysis

of a 0.25 m diameter cylinder interacting with a focused wave group with $kA = 0.1$ gives results with strong similarities to Model 1 (Figures 8, 9, 11 and 12). However, their analysis of the cylinder simulations did not stress the structure of the fourth harmonic components, due to concerns about grid resolution. Similar second harmonic scattered waves were also found on the upstream side of a FPSO model, which is similar to Model 3 in this paper, by Zang et al. (2006) and Siddorn (2012), but their work did not identify significant third and fourth harmonic scattered waves on the upstream side comparable to our experimental observations for Model 3 (Figure 6-3, Figure 6-4 and Figure 6-13). Siddorn (2012) simulated wave-structure interaction of the FPSO model presented by Zang et al. (2006) and found a third harmonic scattered wave to the side and downstream of the FPSO model comparable to those reported here (Figure 6-6, Figure 6-7, Figure 6-14 and Figure 6-15). In the present study, a second wave packet in the second, third and fourth harmonics has been found at almost all the observed locations surrounding the models. These second pulses are entirely separate from and occur much earlier than the error wave train off the wave paddles. So these second pulses are excited by the main incident group, and they may induce a second load cycle on the structure.

The linear, second, third and fourth harmonic scattered waves near the bow of models in our experiment increased their maximum amplitudes by 21%, 13%, 4% and 3% of the undisturbed incident linear amplitude, respectively (Figure 6-4). These components are much larger at locations closer to the bow of the model i.e. at WG16 located at 0.01 m from the bow (see Figure 3-23). At this location, effectively the front stagnation point, the linear, second, third and fourth harmonic scattered wave amplitudes increase up to 33%, 27%, 8% and 4% of the incident linear wave, respectively (Figure 6-21). Zang et al. (2006) found that near the bow the linear and second order diffraction increased by 45% and 30% the undisturbed incident crest elevation and these are quite similar to our

findings here. The linear and higher harmonic scattered wave amplitudes near the stern of the models are comparable with those near the bow, except for the linear components at the stern (WG24 in Figure 3-23) of Model 1 and 2. These increase by up to 120% and 90% the undisturbed incident linear wave amplitude (Figure 6-22) and it is clearly seen that the model length significantly affects the linear diffraction term at the stern (the shorter the model length the higher the linear diffraction). The fourth harmonic scattered wave amplitude can be seen to be as much as 8% of the undisturbed incident linear component if the two phase separation method is applied (Figure 6-19). Evidence of the second scattered wave packets is also found for the third and fourth harmonics at the bow, from $t = +1$ s to $+4$ s (Figure 6-21c, d), and at the stern, from $t = +2.5$ s to $+5.5$ s (Figure 6-22c, d), of the models. It would be expected that the higher harmonic wave field saturates when the input wave amplitude is sufficiently large (Grue, 1992), but these present tests are likely to be well short of this stage when the whole idea of a Stokes-type expansion breaks down.
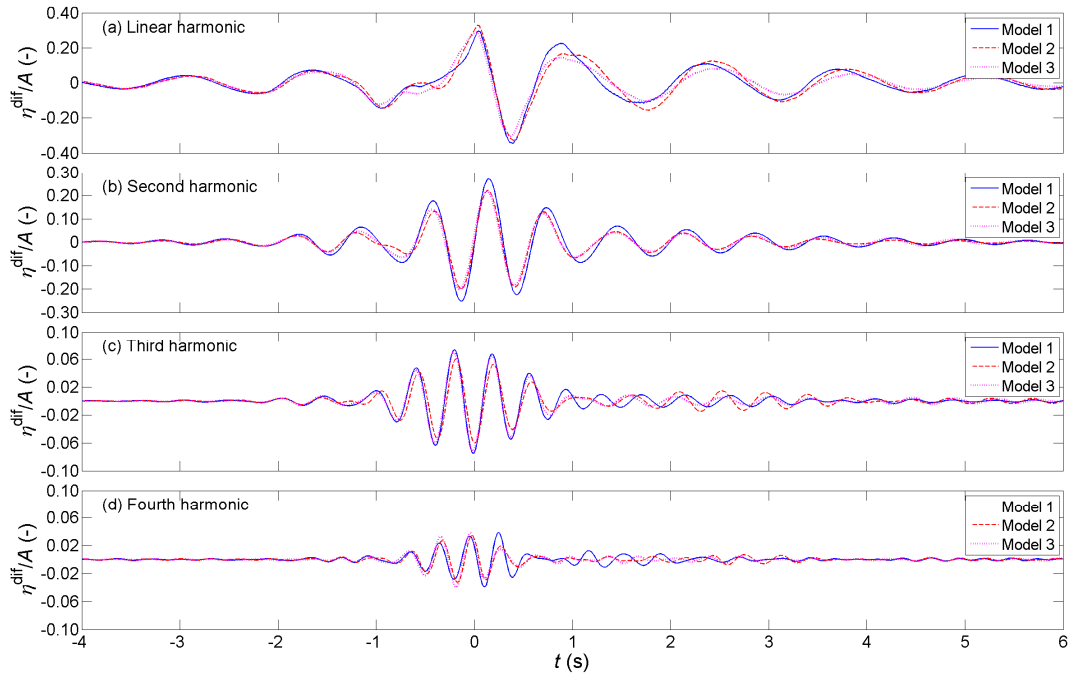
Figure 6-21. Time histories of the scattered waves at the bow of the models for $kA = 0.21$ (WG16). Note the different vertical scales.
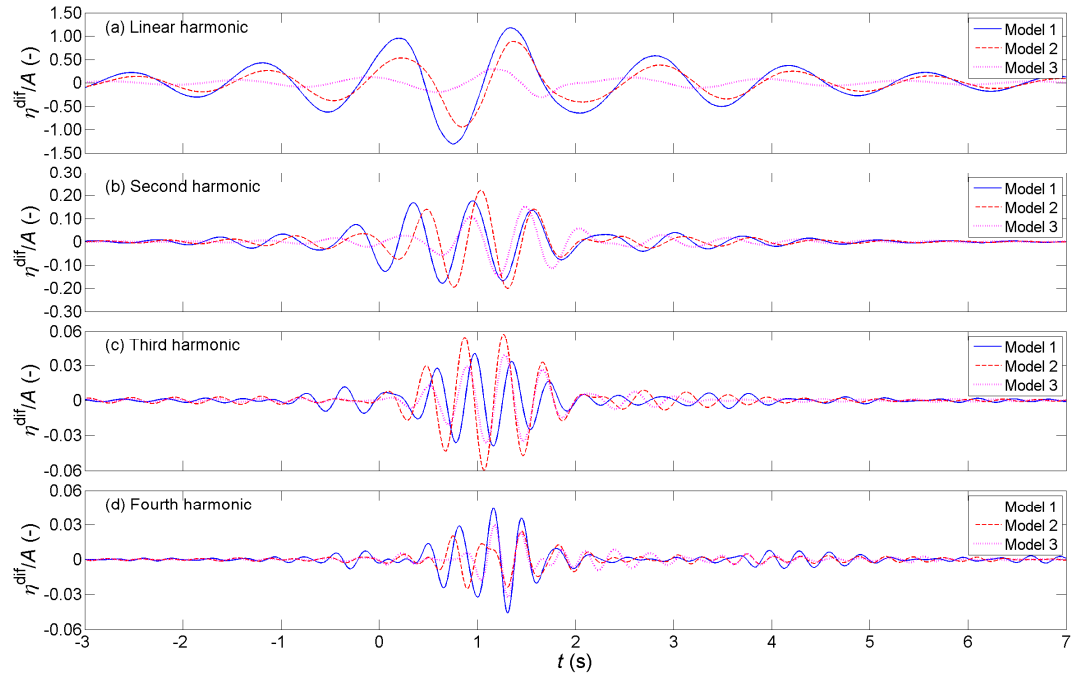
Figure 6-22. Time histories of the scattered waves at the stern of the models for $kA = 0.21$ (WG24). Note the different vertical scales.

The interaction of the incoming wave group with the bow of each of the models results in a second difference frequency component (η_{20}). This is a long bound wave and significantly contributes to the local free surface elevation at the bow (up to about 10% of the undisturbed linear harmonic amplitude), see Figure 6-23, Figure 6-24 and Figure 6-25. It is interesting to see that there is a considerable set-*up* of the water surface at the bow (focal location) with each of the models in place, and this should be contrasted with the smaller set-*down* at the focal location without the models (Figure 6-23). This behaviour of the second difference component with and without models is similar to the results presented in Zang et al. (2006) where they showed the excellent agreement between the experiments and second-order diffraction calculations. Figure 6-23 also shows that the local second difference component set-*up* is unaffected by the model lengths. Indeed, with three different lengths of the models (Models 1, 2 and 3), the second difference components are almost identical at the bow. In contrast, the second difference component is dependent on the wave steepness and wave direction, scaling simply as the square of the wave group linear amplitude (again consistent with 2nd

137

order diffraction) as shown in Figure 6-24. Furthermore, it is unchanged with wave direction from head-on $\alpha = 0°$ to an approach angle of 10°, but reduced at least at the gauge position for a wave approach angle of $\alpha = 20°$ off head-on, as shown in Figure 6-25.
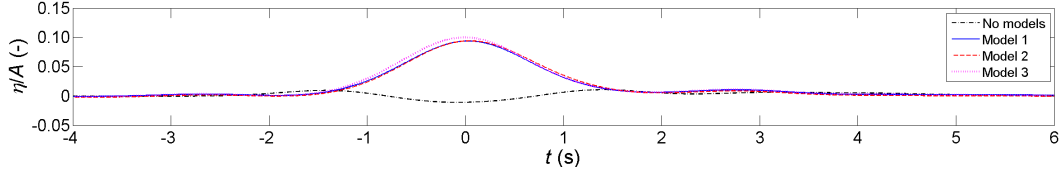
Figure 6-23. Time histories of the second difference component (η_{20}) at the bow of the models (WG16) for $kA = 0.21$.
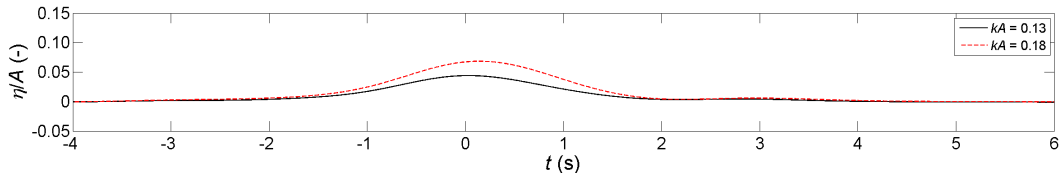
Figure 6-24. Time histories of the second difference component (η_{20}) at the bow of Model 3 (WG16) for $kA = 0.13$ & 0.18.
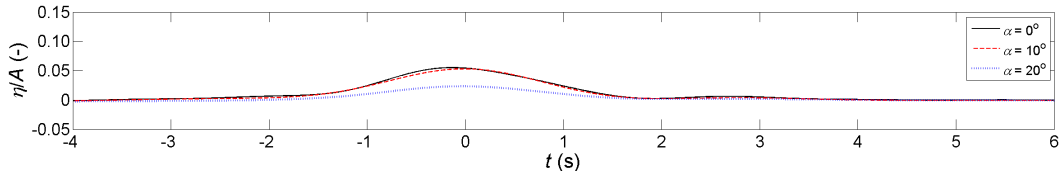
Figure 6-25. Time histories of the second difference component (η_{20}) at the bow of Model 3 (WG16) for $kA = 0.17$ and $\alpha = 0°$, 10° & 20°.

In practical applications, the third- and fourth-order frequency components obtained from the model test should be taken into account to assess wave loading for offshore structure design and ringing-type structural response in fixed and taut moored structures, and numerical modelling should be carefully designed to make sure these effects can be captured. Some traditional numerical modelling approaches are based on linear theory and cannot predict these strongly nonlinear effects (Det Norske Veritas, 2010) and so high order or fully nonlinear approaches should be taken. The effects on crest elevation, which is contributed from the linear, superharmonics (up to fourth-order) and the second difference component (η_{20}), should also be considered for design of the air gap and position of accommodation in offshore structures.

6.2   Results of the free floating Model 3

In this section, the effects of wave steepness and wave direction on the mooring line force and motion response of the free floating Model 3 are investigated. The mooring line used in this experiment was a single taut mooring line. Therefore, as the taut moored model fluctuated the mooring line force was generated within the duration of one wave group (typically x sec). Only the crest focused wave group (η^0) and the trough focused wave group (η^{180}) were tested for the free floating Model 3. Therefore, the simple *phase-inversion* separation method in combination with frequency filtering, which is presented in Section 6.1.3, is applied to extract the linear and the higher harmonic components of the free-surface water elevation and also the mooring line force of the free floating Model 3. The layout of the single mooring line system is presented in Figure 3-24. Two wave gauge locations were investigated, close to the bow (WG10) and to the side (WG7) of Model 3, as shown in Figure 6-26.

WG10

WG7
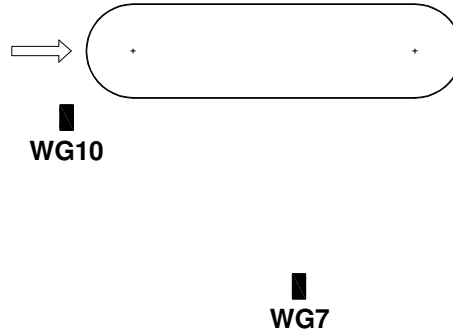
Figure 6-26: Location of WG7 & 10 w.r.t Model 3.

Typical time histories of the mooring line force and motion response of the floating Model 3 are presented in Figure 6-27 and Figure 6-28 for the wave steepness $kA = 0.13$. The undisturbed water elevation at the focal location (WG11) is included in Figure 6-27a and Figure 6-28a. The vertical axis is the dimensionless values, in which F_1^{max} and R_{Y1}^{max} are the total linear amplitude of the mooring line force and pitch motion, respectively. Unfortunately, the measurement signal of the motion in yaw was lost as shown in Figure 6-27b and Figure 6-28b.
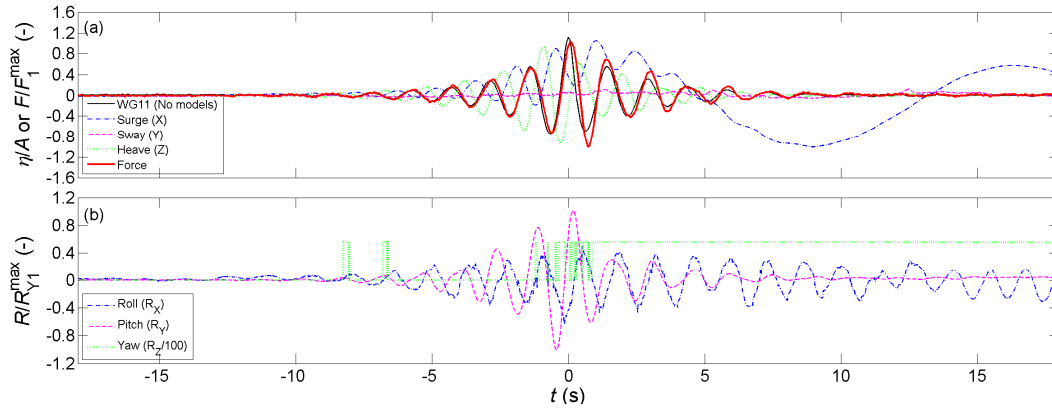
Figure 6-27: Typical time histories of the mooring line force and motion response of the floating Model 3 ($kA = 0.13$, Phase $\theta = 0°$).
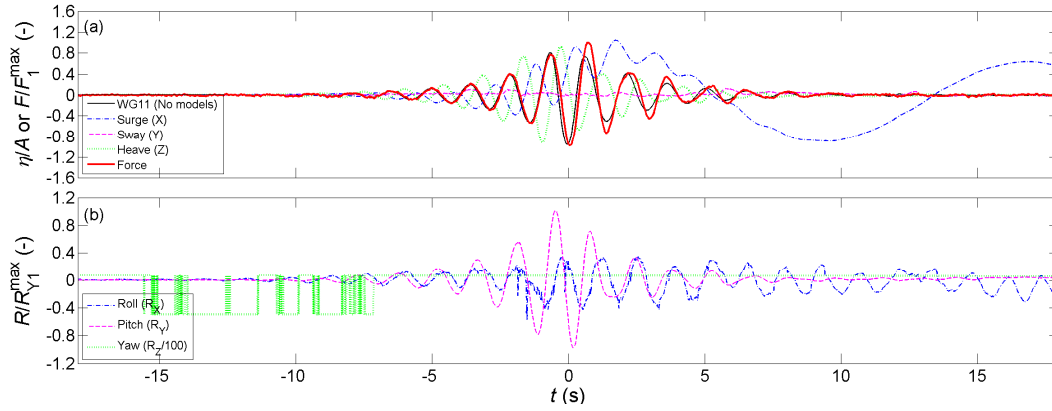
Figure 6-28: Typical time histories of the mooring line force and motion response of the floating Model 3 ($kA = 0.13$, Phase $\theta = 180°$).

6.2.1 Wave scattering around the fixed and floating Model 3

The water elevations at two locations (WG7 & 10) are analysed in order to examine how the floating model affects the scattered wave field. Results are presented for the steepest wave ($kA = 0.17$) tested with the floating model.

Near the bow

By applying the phase-inversion separation method introduced in Section 3.3.2, the linear and the higher harmonic components of the free-surface elevation (η_{11}, η_{22}, η_{33}, η_{44}) can be obtained at the bow of the models (for WG10 just upstream of the front stagnation point on the bow). The amplitude spectra that correspond to the time history of the separated components are shown in Figure 6-29. Comparing these spectra for the tests with and without the models in place indicates the considerable enhancement of

140

the spectra due to the interaction of the incident waves with the models, except the linear harmonic (η_{11}), which is smaller for the floating model than for without model and with the fixed model (Figure 6-29a). In addition, it is found that the enhancement of the amplitude spectrum of the second and fourth harmonics (η_{22} & η_{44}), due to wave interaction with the floating model, are stronger in comparison with the interactions observed with the fixed model (Figure 6-29b, d). The amplitude spectra of the third harmonic (η_{33}) caused by the presence of the fixed and free floating models are approximately the same (Figure 6-29c).
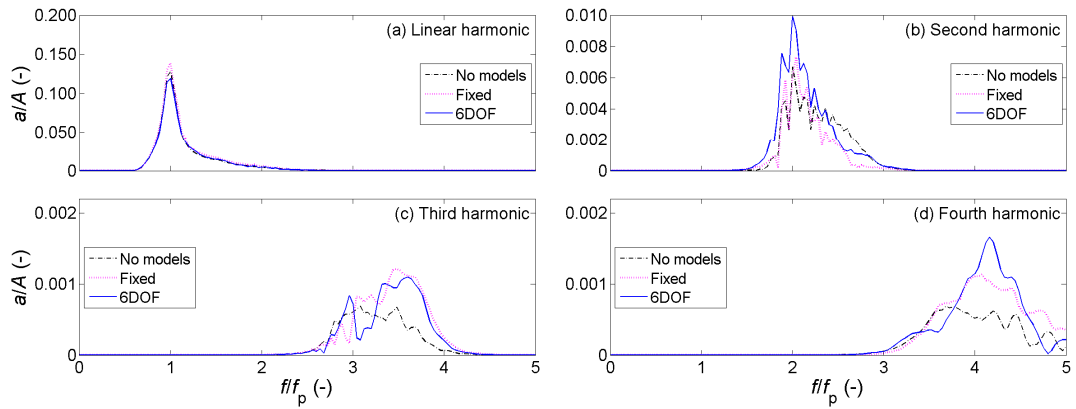
Figure 6-29: Amplitude spectra of the separated components near the bow of Model 3 (Fixed and free floating) for *kA* = 0.17 (WG10). Note the different vertical scales.

The corresponding time histories of the separated harmonic components are derived by performing an inverse FFT of the corresponding filtered amplitude spectrum. These are presented in Figure 6-30 for the waves with and without the models in place. Significant enhancement of the free-surface elevation of the linear and higher harmonics due to wave scattering from the models can be clearly seen. The local free-surface elevation of the linear component has a lower crest and higher trough, in the presence of the free floating model, than with the fixed model in place (Figure 6-30a). In contrast, the local free-surface elevations of the second harmonic have the highest crest and lowest trough with the floating model (Figure 6-30b), and the third and fourth harmonics are approximately the same with both fixed and floating model (Figure 6-30c, d).
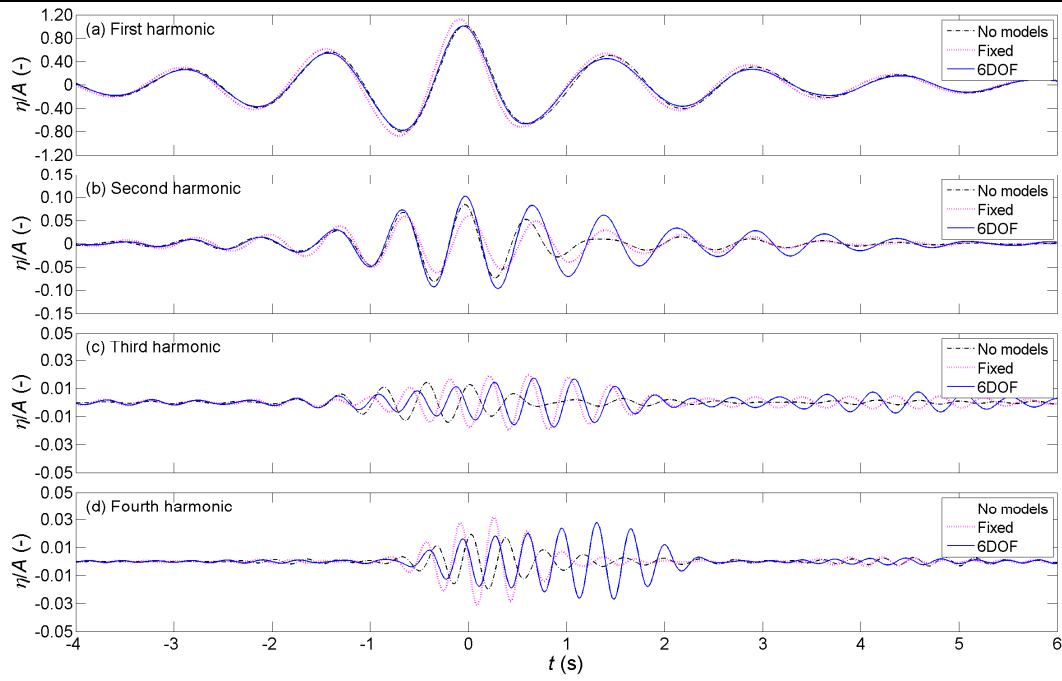
Figure 6-30: Time histories of the separated wave components near the bow of Model 3 (Fixed and free floating) for *kA* = 0.17 (WG10). Note the different vertical scales.

Data on the scattered wave only are obtained by subtraction of the time histories with and without the models in place (Equation (3-10)); these are shown in Figure 6-31. The scattered waves of the linear, third and fourth harmonics are strongest with the fixed model in place (Figure 6-31a, c, d). In contrast, the second harmonic scattered wave is strongest with the floating model (Figure 6-31b). As observed before, it can be seen in Figure 6-31c & d that there is a second pulse in the third and fourth harmonics of the scattered wave fields, arriving at about *t* = +3.5 s which may induce a second load cycle for the structure.
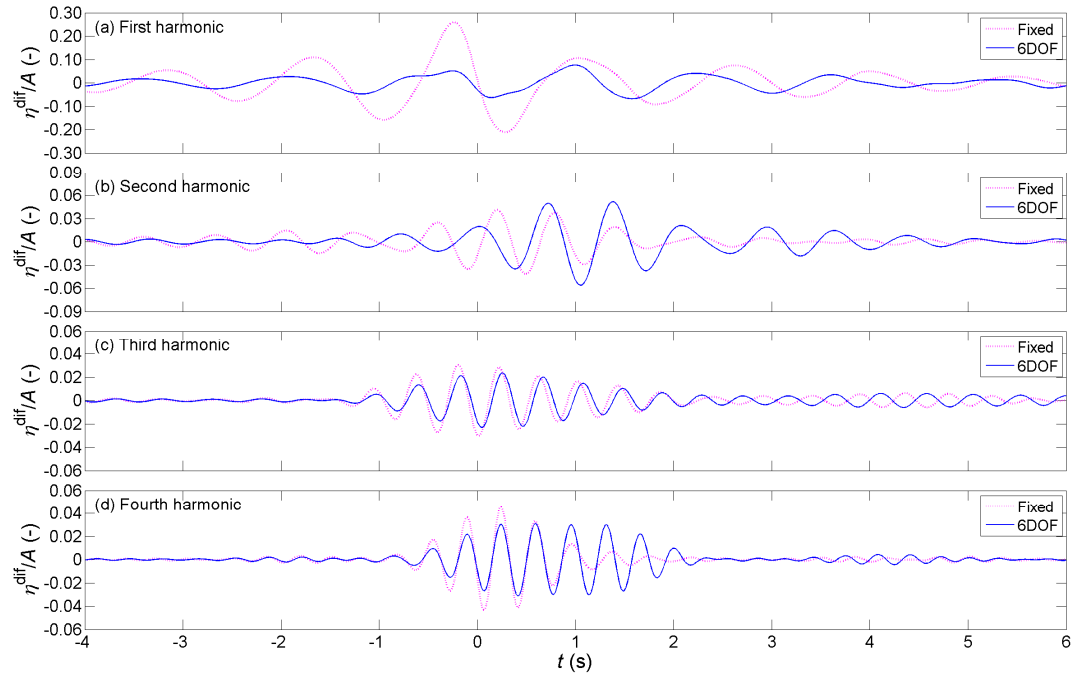
Figure 6-31: Time histories of the scattered waves near the bow of Model 3 (Fixed and free floating) for $kA = 0.17$ (WG10). Note the different vertical scales.

Alongside

Wave scattering alongside of the fixed and floating models is investigated using wave gauges WG7 shown in Figure 6-26. Amplitude spectra of the linear and higher harmonic components are presented in Figure 6-32. Similar to the observed at location near the bow, it is also shown that the amplitude spectrum of the linear component is lower with the floating model than with the fixed model and without model (Figure 6-32a). The amplitude spectra of the second and third harmonics are highest in the presence of the floating model (Figure 6-32b, c); while the fourth harmonics are approximately the same but rather wiggly for the fixed and floating models (Figure 6-32d); possibly a reflection that the harmonic extraction process is sensitive to the accuracy of the time alignment of the two phase combinations, and the 4th-harmonic has the higher sensitivity.
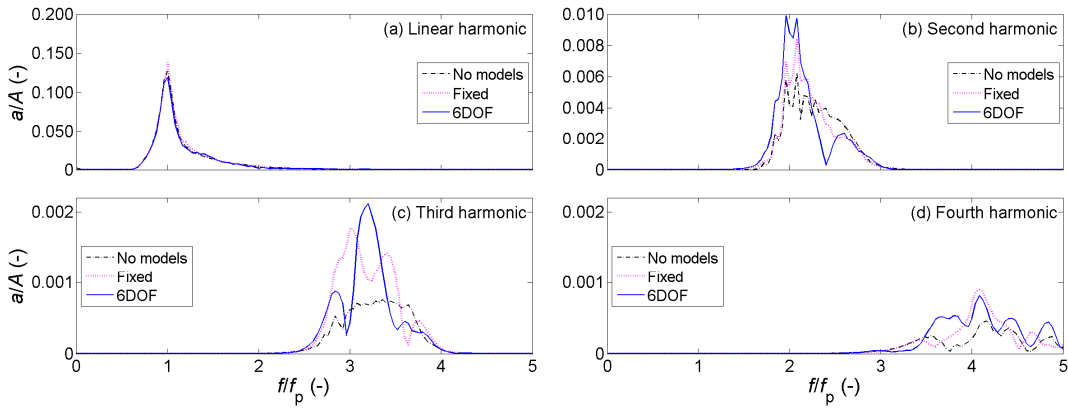
Figure 6-32. Amplitude spectra of the separated components alongside Model 3 (Fixed and free floating) for $kA = 0.17$ (WG7). Note the different vertical scales.

The time histories of the linear and higher harmonic scattered waves alongside of the fixed and floating models presented in Figure 6-33. It is indicated that the effect of wave-structure interaction on the linear component is quite weak for the floating model in comparison with the fixed model (Figure 6-33a), but this effect is relatively much stronger for the second harmonic component (Figure 6-33b). For the third and fourth harmonic components, the free-surface elevations of the scattered wave are nearly the same with the fixed and floating models (Figure 6-33c, d).
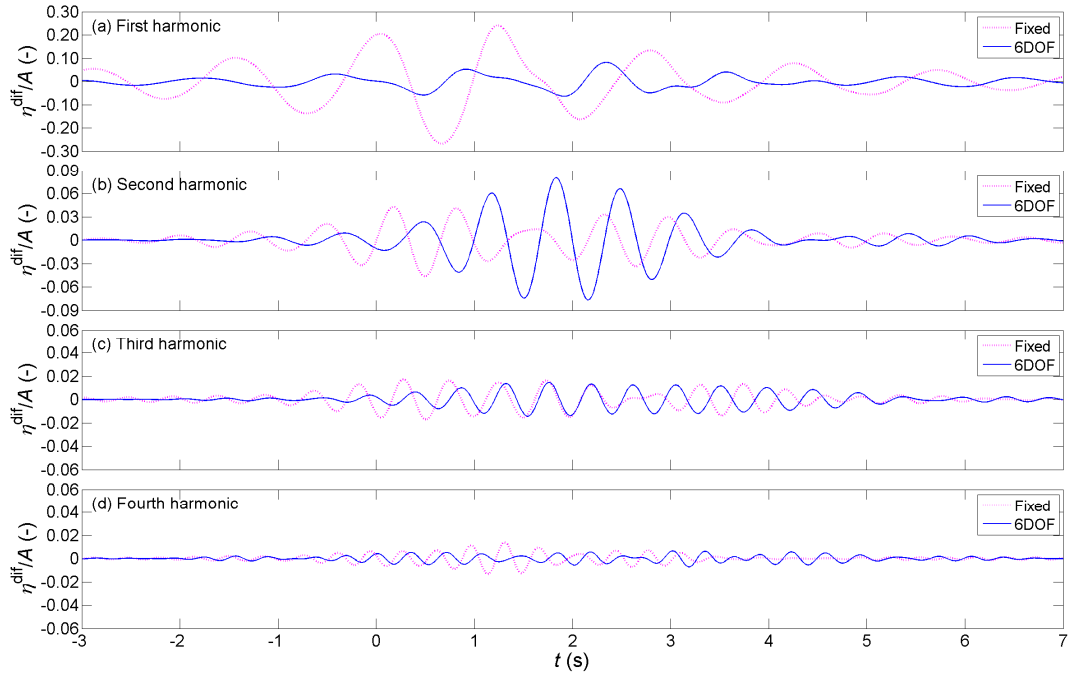
Figure 6-33. Time histories of the scattered waves alongside Model 3 (Fixed and free floating) for $kA = 0.17$ (WG7). Note the different vertical scales.

6.2.2 Effect of wave steepness on wave scattering, mooring line force and motion response

The effects of wave steepness on the wave scattering, mooring line force and motion response are reported for the free floating Model 3, shown in Figure 3-24, with the focused wave groups of two different steepness (kA = 0.13 and 0.17), at two gauge locations: near to the bow (WG10) and to the side (WG7), the single mooring line force and the motion response in heave and pitch.

Applying the simple phase-inversion separation method in combination with frequency filtering presented in Section 3.3.2, the amplitude spectra of the linear and second, third and fourth harmonics of the separated components are examined. Similar to the fixed model presented in Section 6.1.2, only the more interesting higher harmonics are presented in this section to examine the effect of wave steepness on the wave-structure interaction of the free floating model. Amplitude spectra of the second, third and fourth harmonics of the separated components are presented in Figure 6-34 and Figure 6-35 for the location near the bow (WG10) and to the side (WG7) of the floating model, respectively. In general, as would be expected and similar to the results of the fixed model, the amplitude spectra of the higher harmonics are seen to increase as the wave steepness is increased from kA = 0.13 (solid line) to kA = 0.17 (dashed line). The amplitude spectrum of the second harmonic near the bow of the model is significantly higher than those at the side for kA = 0.13, but they are approximately the same for kA = 0.17 (Figure 6-34a & Figure 6-35a). There is a slight difference in the amplitude spectra of the third and fourth harmonic components at those locations (Figure 6-34b-c & Figure 6-35b-c). The steepness of the wave appears to have its greatest effect on the third and fourth harmonics where some of the values nearly double at the location near the bow (Figure 6-34b-c).

Figure 6-34. Amplitude spectra of the separated components near the bow of the free floating Model 3 (WG10). Note the different vertical scales.

Figure 6-35. Amplitude spectra of the separated components alongside the free floating Model 3 (WG7). Note the different vertical scales.

The corresponding filtered time histories of the higher harmonics of the scattered wave fields at locations near the bow and to the side of the free floating Model 3 are presented in Figure 6-36 and Figure 6-37, respectively. At the bow there is slight amplification of the second harmonic (Figure 6-36a). There is a significant effect of the wave steepness at the third and fourth harmonics of the scattered wave near the bow (Figure 6-36b, c) as might be expected from the amplitude spectrum. A significant effect of wave steepness can also be found at the second harmonic to the side (Figure 6-37a). Amplitudes of the third harmonics to the side seem not to be affected by the wave steepness (Figure 6-37b), but the amplitude of the fourth harmonic is decreased as the wave steepness increasing (Figure 6-37c). Similar to the finding with the fixed model presented in Section 6.1.2, the fourth harmonic component near the bow is much higher than that to the side of the floating model (Figure 6-36c and Figure 6-37c). As discussed in previous section, this is due to geometric spreading, whereas the gauge position spreading is more important.

146
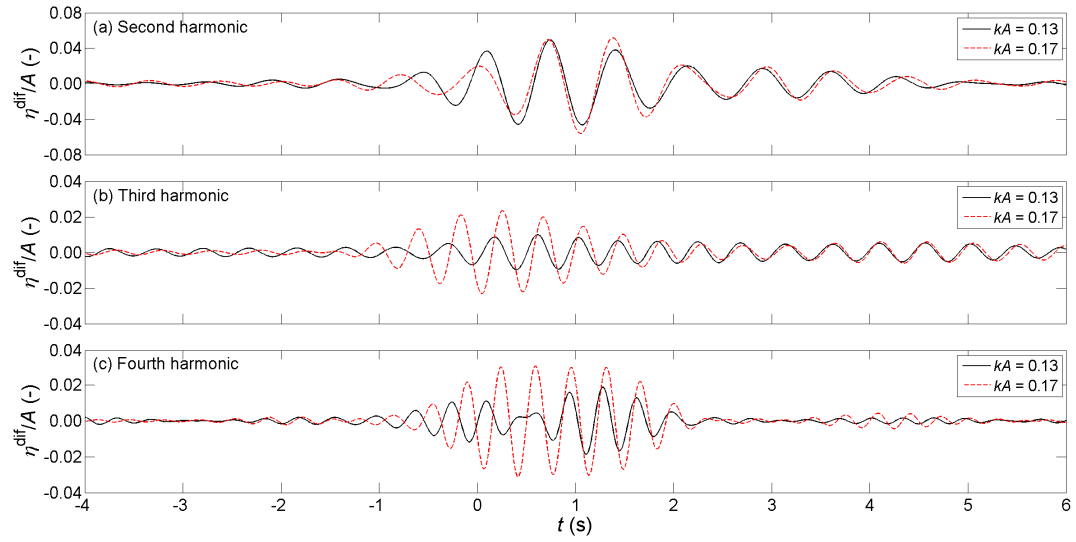
Figure 6-36. Time histories of the scattered components near the bow of the free floating Model 3 (WG10). Note the different vertical scales.
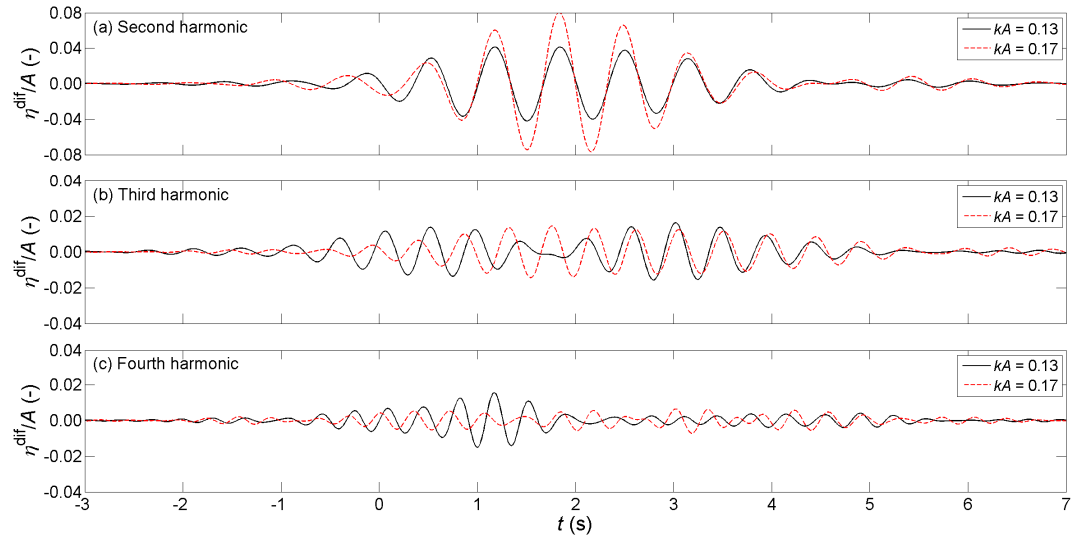
Figure 6-37. Time histories of the scattered components alongside the free floating Model 3 (WG7). Note the different vertical scales.

The linear and the higher harmonic components of the mooring line force, the heave and pitch motions of the free floating Model 3 were extracted using the phase-inversion method which has been applied for the free-surface elevation. Amplitude spectra and time histories of the higher harmonics of the mooring line force are presented in Figure 6-38 and Figure 6-39, respectively. The vertical axis is the dimensionless force, in which F_1^{max} is the total linear amplitude of the mooring line force. It can be seen that the amplitude spectra of the second and third harmonics increase significantly as the wave steepness increases from $kA = 0.13$ to $kA = 0.17$ (Figure 6-38a, b), but the amplitude

147

spectra of the fourth harmonics are nearly the same (Figure 6-38c). Indeed, the evidence for a significant effect of the wave steepness at the second and third harmonics of the mooring line force can be found on the time histories of those harmonics presented in Figure 6-39a-b, whereas as the wave steepness increases from $kA = 0.13$ to $kA = 0.17$ the amplitudes of the second and third harmonics increase by three and two times, respectively. Amplitudes of the fourth harmonic are more or less the same for both $kA = 0.13$ & 0.17 (Figure 6-39c).
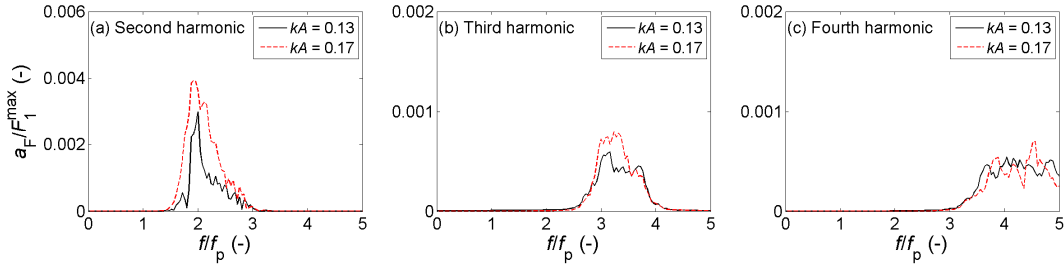
Figure 6-38. Amplitude spectra of the separated components of the mooring line force of the free floating Model 3. Note the different vertical scales.
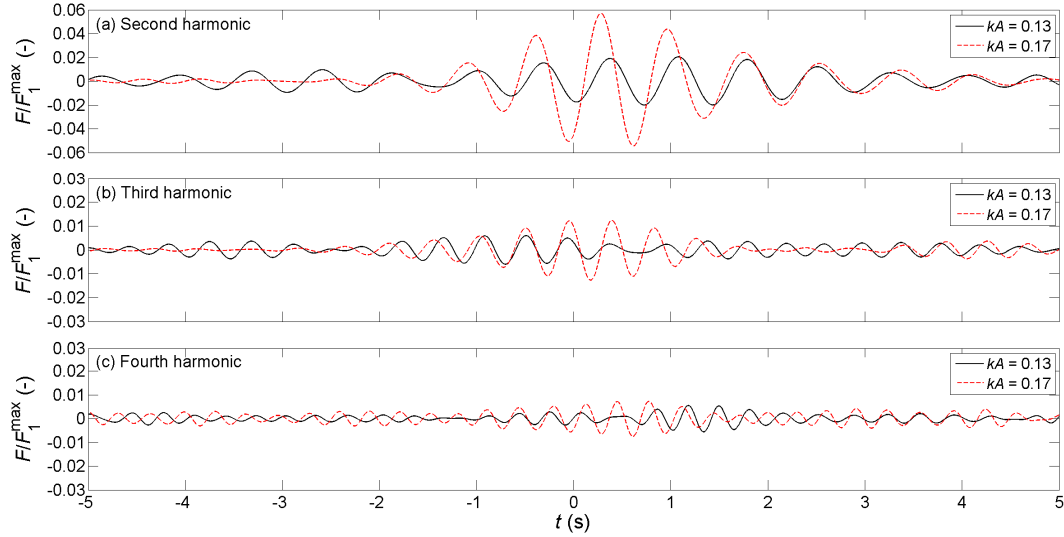
Figure 6-39. Time histories of the separated components of the mooring line force of the free floating Model 3. Note the different vertical scales.

Amplitude spectra of the heave and pitch motions of the free floating Model 3 are presented in Figure 6-40 and Figure 6-42, respectively. Similar to the behaviour of the mooring line force, the amplitude spectra of the second and third harmonics of the heave and pitch motions increase significantly as increasing wave steepness (Figure 6-40a, b and Figure 6-42a, b). In addition, the amplitude spectrum of the fourth

harmonic increases slightly as the wave steepness increases (Figure 6-40c and Figure 6-42c). Corresponding time histories of the higher harmonics of the heave and pitch motions are presented in Figure 6-41 and Figure 6-43, and they show clearly a significant effect of the wave steepness on the motion response of the floating Model 3 as the findings from the mooring line force presented in Figure 6-39.
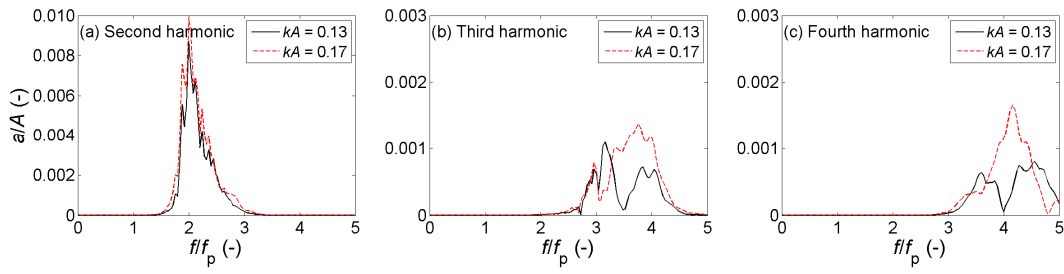

Figure 6-40. Amplitude spectra of the separated components of the heave motion of the free floating Model 3. Note the different vertical scales.

Figure 6-41. Time histories of the separated components of the heave motion of the free floating Model 3. Note the different vertical scales.

Figure 6-42. Amplitude spectra of the separated components of the pitch motion of the free floating Model 3. Note the different vertical scales.
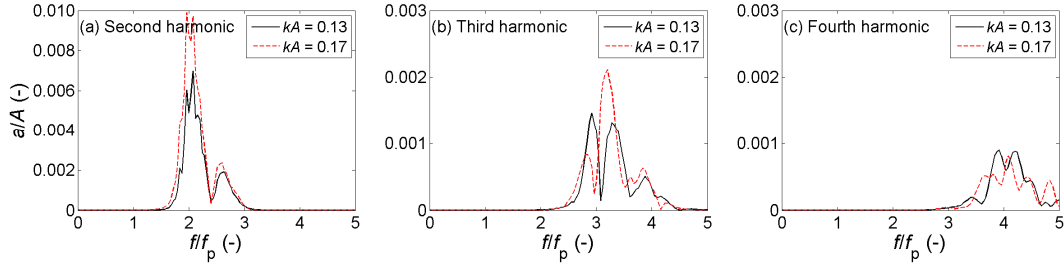
Figure 6-43. Time histories of the separated components of the pitch motion of the free floating Model 3. Note the different vertical scales.

6.2.3 Effect of incident wave angle on wave scattering, mooring line force and motion response

Amplitude spectra of the linear and the higher harmonic components for the location near the bow (WG10) and to the side (WG7) of the free floating Model 3, due to different incident wave angles ($\alpha = 0°$, $10°$ & $20°$), are presented in Figure 6-44 and Figure 6-45, respectively. In contrast with the findings for the fixed model presented in Section 6.1.3, the amplitude spectra of the harmonic components decrease as the incident wave angle increases from $0°$ to $20°$ for the floating model, but similar to the fixed model that they are also most energetic at the incident angle of $10°$ at the higher harmonics, except for the second harmonic to the side where the amplitude spectrum decreases with increasing the wave angle (Figure 6-45b).

The time histories of the scattered wave corresponding to the amplitude spectra near the bow and to the side are presented in Figure 6-46 and Figure 6-47. The linear harmonic is increased with increasing the incident angle for both locations (Figure 6-46a and Figure 6-47a). On the contrary, the second harmonic to the side is significantly reduced as the incident angle increased (Figure 6-47b). The third harmonics at the locations near the bow and to the side are strongest for the $10°$ wave (Figure 6-46c and Figure 6-47c).

Similar to the fixed model, due to the gauge location spreading the third and fourth harmonics at location to the side (Figure 6-47c, d) are significantly smaller than those near the bow of the floating model (Figure 6-46c, d).
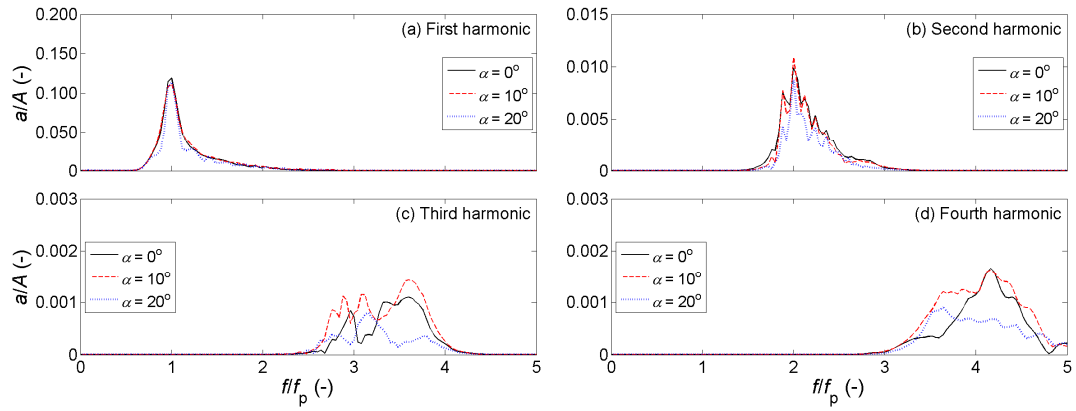
Figure 6-44. Amplitude spectra of the separated components near the bow of the free floating Model 3 for $kA = 0.17$ (WG10). Note the different vertical scales.
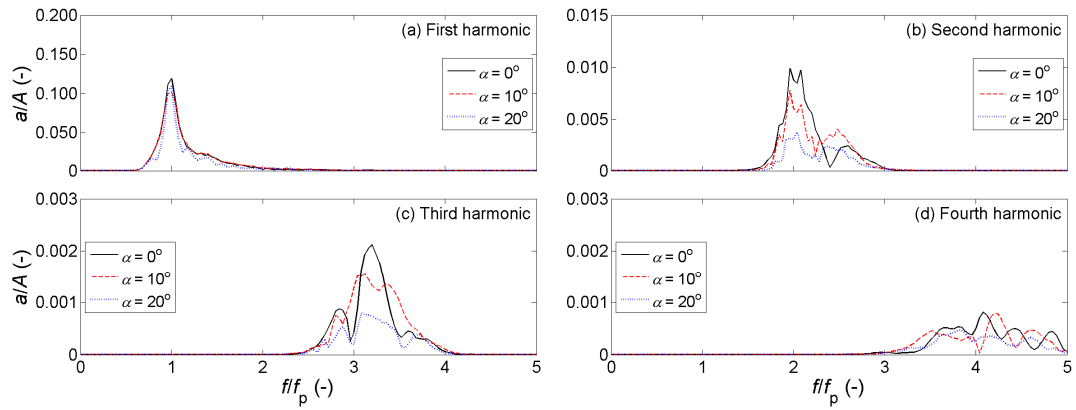
Figure 6-45. Amplitude spectra of the separated components alongside the free floating Model 3 for $kA = 0.17$ (WG7). Note the different vertical scales.
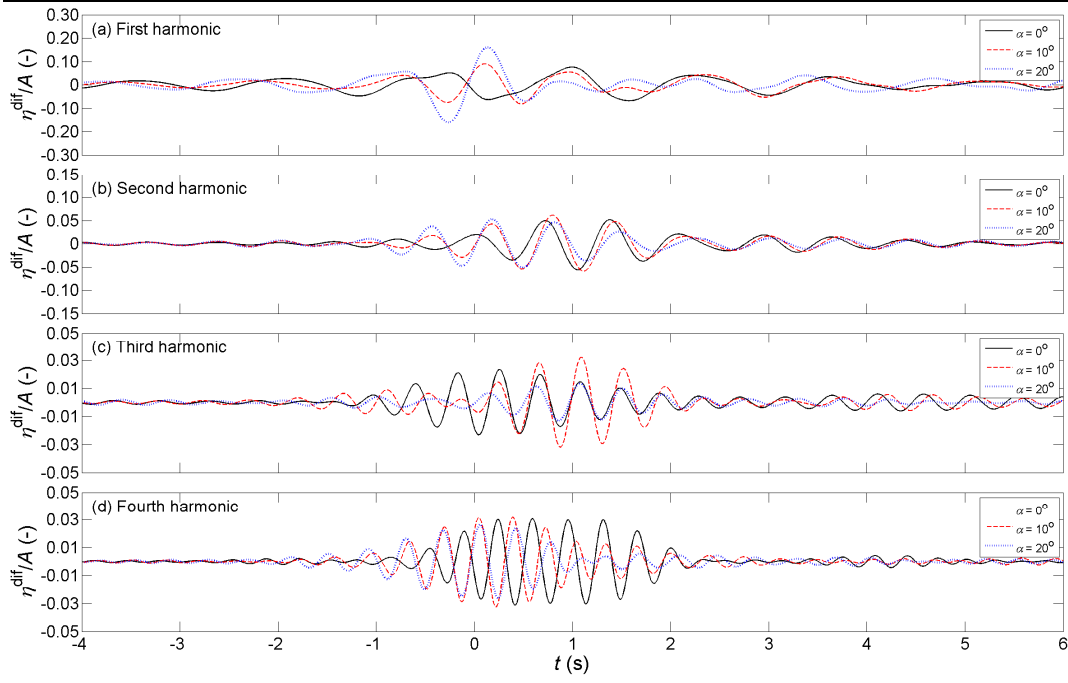
Figure 6-46. Time histories of the scattered waves near the bow of the free floating Model 3 for *kA* = 0.17 (WG10). Note the different vertical scales.
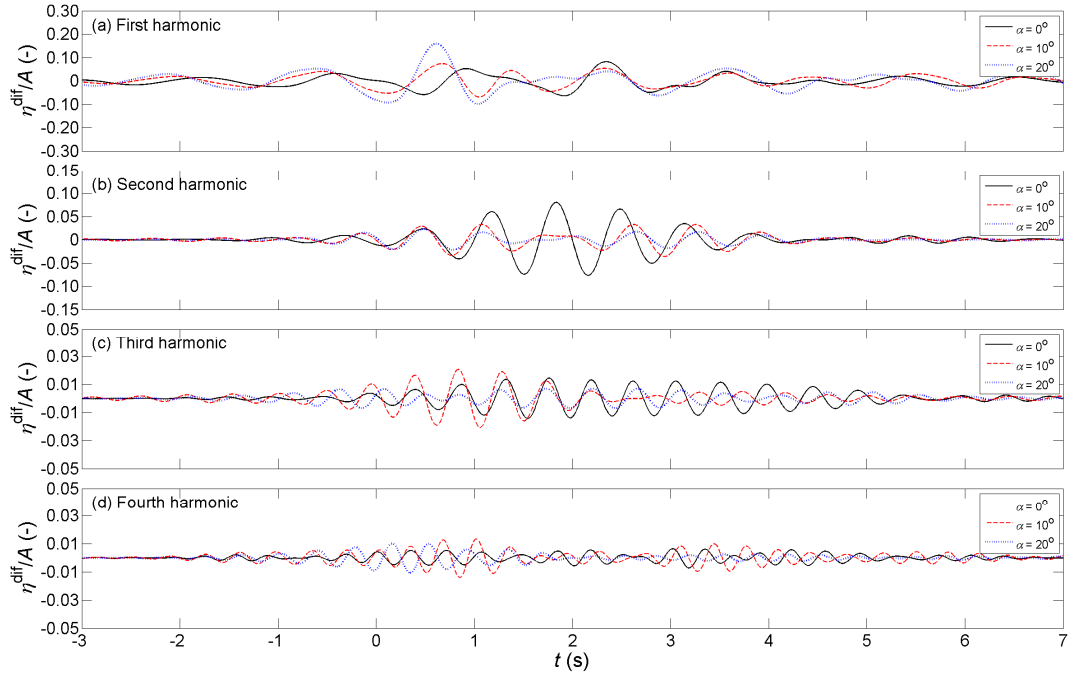
Figure 6-47. Time histories of the scattered waves alongside the free floating Model 3 for *kA* = 0.17 (WG7). Note the different vertical scales.

Amplitude spectra of the linear and the higher harmonics of the mooring line force, the heave and pitch motions are presented in Figure 6-48, Figure 6-49 and Figure 6-50 for different incident wave angles. It can be seen that the linear and the higher harmonics of the mooring line force, the heave and pitch motions are reduced with increasing the

152

angle of incidence, but similar to the higher harmonics of the free-surface elevation at location near the bow of the floating model, the second and third harmonics of the mooring line force, the heave and pitch motions are also most energetic at the 10° wave (Figure 6-48b, c, d, Figure 6-49b, c, d and Figure 6-50b, c, d). Time histories of the higher harmonics of the mooring line force, the heave and pitch motions show indeed the evidence of the most energetic at the incident angle of 10° for the higher harmonics (Figure 6-51b, c, d, Figure 6-52b, c, d and Figure 6-53b, c, d). It can be clearly seen from Figure 6-51, Figure 6-52 and Figure 6-53 that the linear and the higher harmonics of the mooring line force, the heave and pitch motions are significantly decreased as the incident angle increases from 0° to 20°.
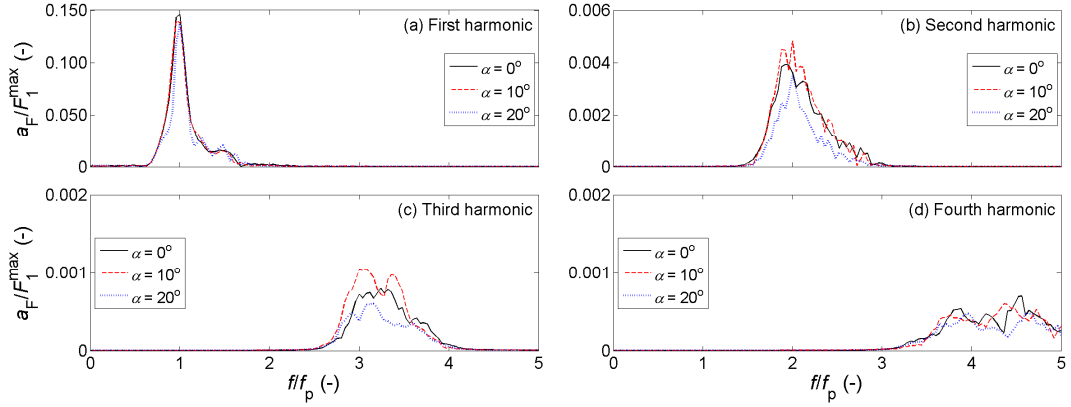
Figure 6-48. Amplitude spectra of the separated components of the mooring line force of the free floating Model 3 for *kA* = 0.17. Note the different vertical scales.
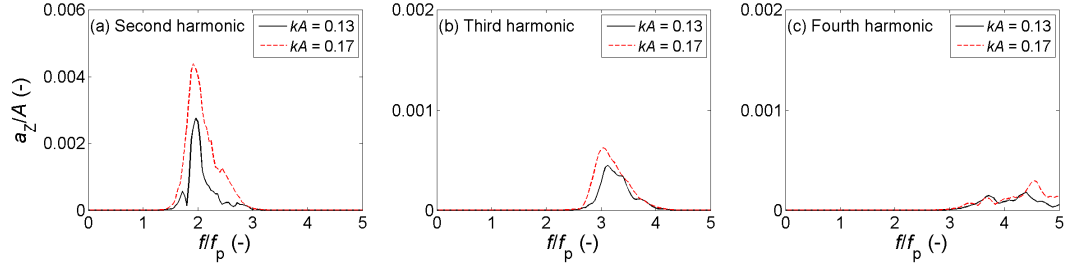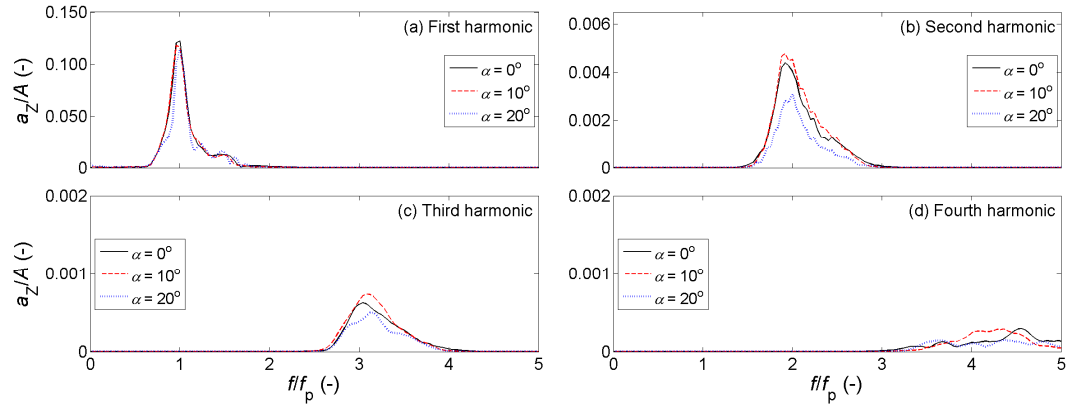

Figure 6-49. Amplitude spectra of the separated components of the heave motion of the free floating Model 3 for *kA* = 0.17. Note the different vertical scales.
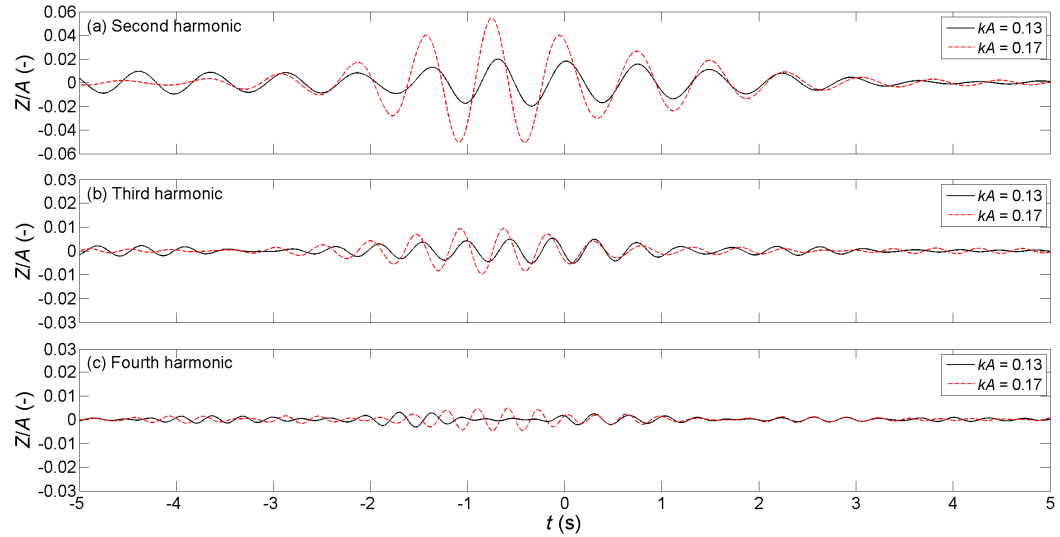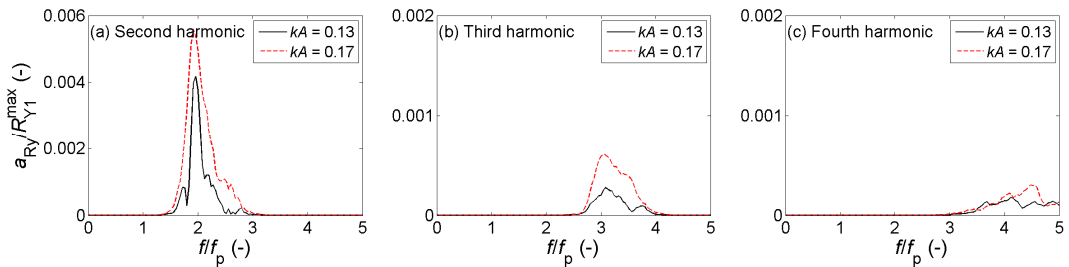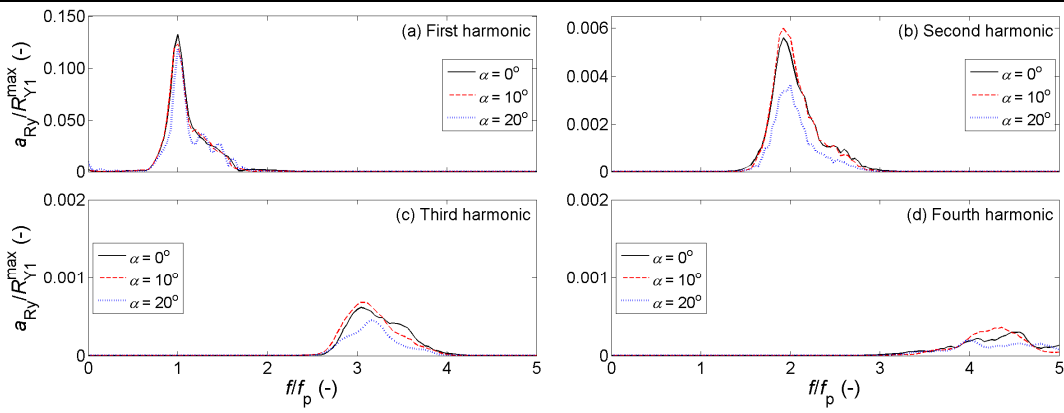
Figure 6-50. Amplitude spectra of the separated components of the pitch motion of the free floating Model 3 for *kA* = 0.17. Note the different vertical scales.
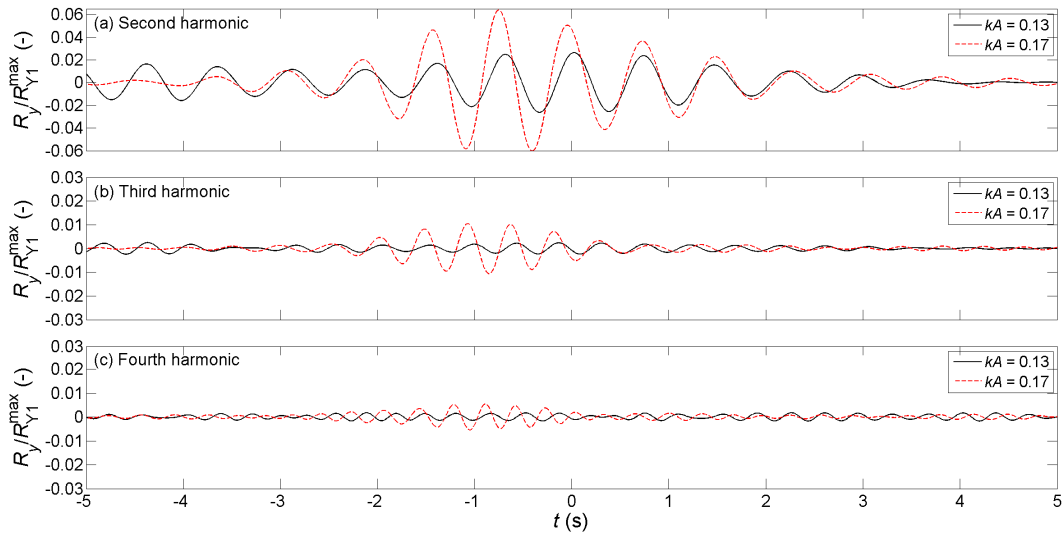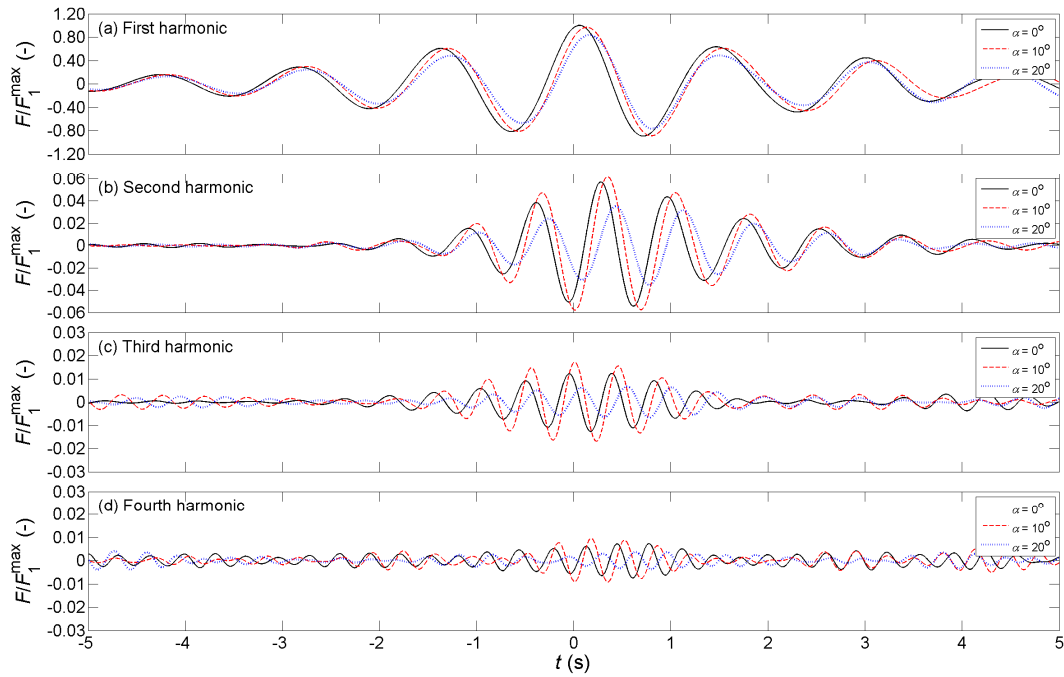

Figure 6-51. Time histories of the separated components of the mooring line force of the free floating Model 3 for *kA* = 0.17. Note the different vertical scales.
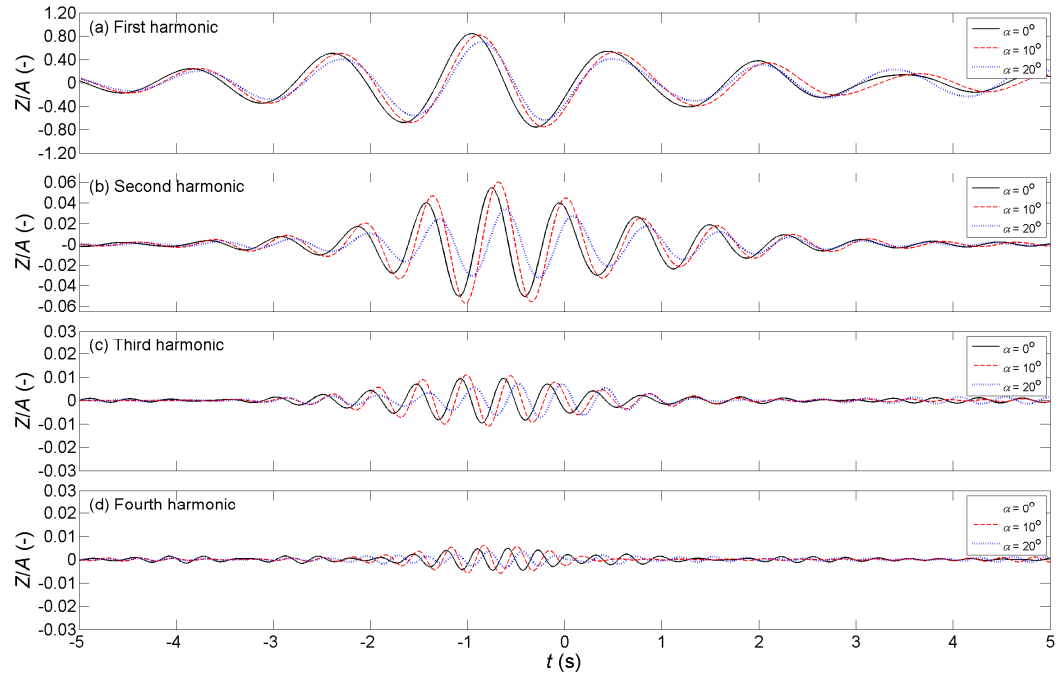
Figure 6-52. Time histories of the separated components of the heave motion of the free floating Model 3 for $kA = 0.17$. Note the different vertical scales.
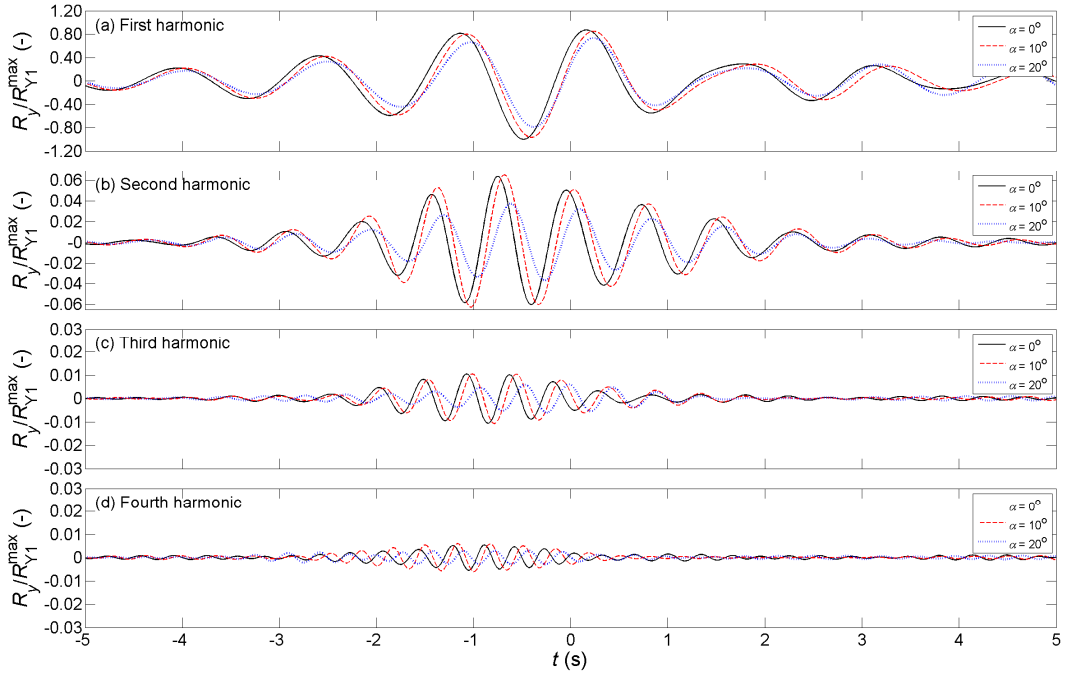
Figure 6-53. Time histories of the separated components of the pitch motion of the free floating Model 3 for $kA = 0.17$. Note the different vertical scales.

6.2.4 Discussion of the results for the free floating Model 3

This experimental work has shown the floating effect on scattered wave fields upstream and at the side of an FPSO-shaped model (Model 3), which was fixed or free floating. When the FPSO is floating, the linear harmonic scattered waves are significantly

155

reduced, but the second harmonic scattered waves both upstream and to the side of the model, are significantly increased. The third and fourth harmonic scattered waves are approximately the same for the fixed and floating models. At the bow of the model (WG16), the linear harmonic wave component is relatively smaller than the linear harmonics of the undisturbed incident wave and the wave with the fixed model (Figure 6-54a). Consequently, the linear harmonic scattered wave at the bow of the floating model is significantly larger than that of the fixed model (Figure 6-55a). On the other hand, the second and third harmonic waves at the bow increased significantly with the floating model than without and with the fixed model (Figure 6-54b, c) and the second and third harmonic scattered waves were therefore increased with the floating model as well (Figure 6-55b, c). The fourth harmonics of the disturbed wave and the scattered wave at the bow of the floating model are smaller than those with the fixed model (Figure 6-54d and Figure 6-55d).
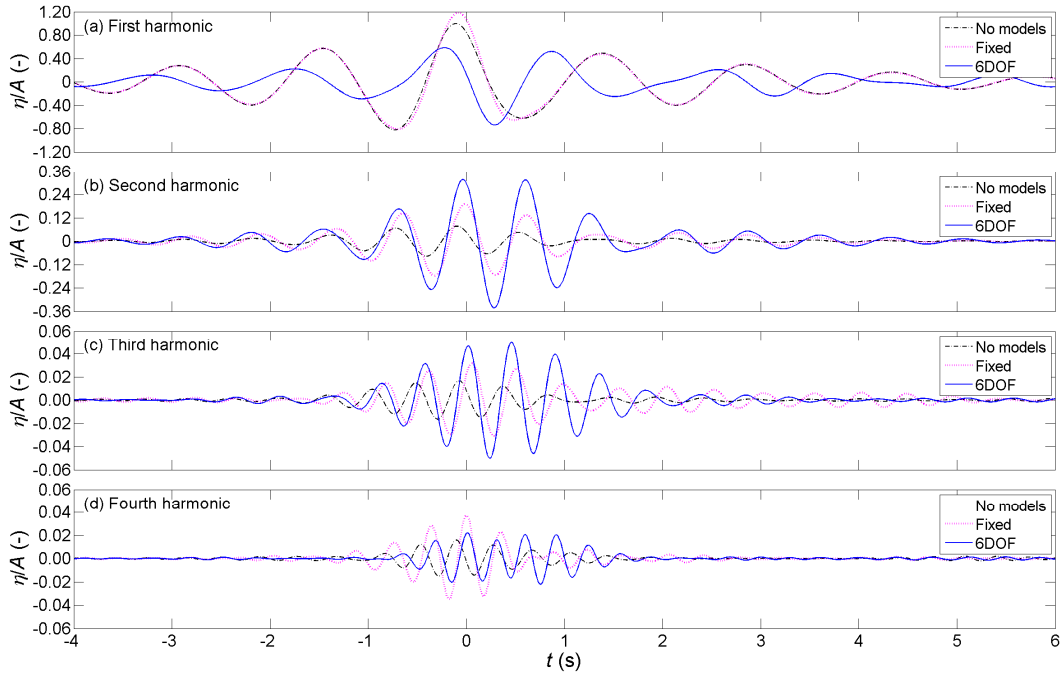
Figure 6-54. Time histories of the separated wave components at the bow of Model 3 (Fixed and free floating) for *kA* = 0.17 (WG16). Note the different vertical scales.
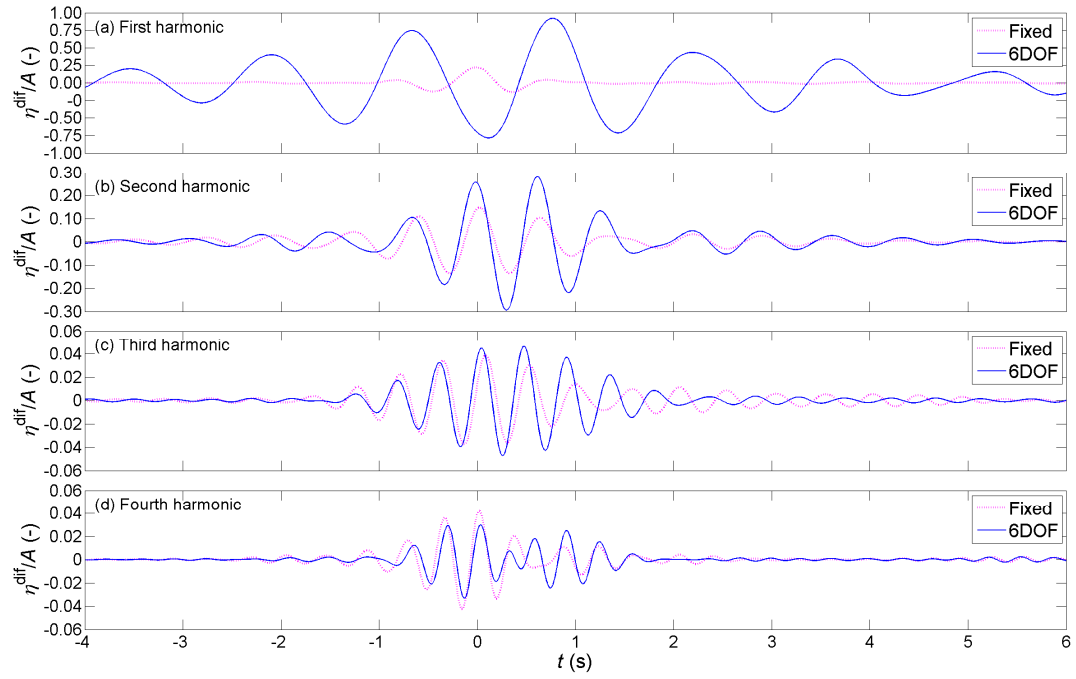
Figure 6-55. Time histories of the scattered waves at the bow of Model 3 (Fixed and free floating) for *kA* = 0.17 (WG16). Note the different vertical scales.

Similar to the free surface elevation around the model, the second, third and fourth harmonics of the mooring line force of the free floating model are also found from this experimental work and their maximum amplitudes are about 6 %, 1.7 % and 1 % of the linear harmonic mooring line force (see Figure 6-39 and Figure 6-51). These findings are comparable with Fitzgerald et al. (2014) where their analysis of a 0.25 m diameter cylinder interacting with a focused wave group with *kA* = 0.1 gives results with the second, third and fourth harmonic inline forces, which were calculated using the Stokes expansion with wave-to-force quadratic transfer functions, were about 14 %, 4 % and 1.5 % of the linear component, but their model was a fixed model.

The second difference frequency components (η_{20}) at the bow of the fixed and floating models are presented in Figure 6-56. It is clearly seen that, due to the interaction of the incoming wave group with the bow of the fixed model, the second difference frequency component is significantly higher than that with the floating model. As shown in Figure 6-57 and Figure 6-58, the wave steepness has a significant effect on the second difference components of the free surface elevation at the bow (η_{20}) and the mooring

157

line force (F_{20}) of the floating model, scaling simply as the square of the wave group linear amplitude (again consistent with 2nd order diffraction). In addition, as the wave direction changes from head-on $\alpha = 0°$ to an approach angle of 10°, the second difference components (η_{20} and F_{20}) are unchanged, but they reduced for a wave approach angle of $\alpha = 20°$ off head-on, as shown in Figure 6-59 and Figure 6-60. It is found that there is a significant difference in the shape of wave packages for the second difference mooring line force from this experimental work (Figure 6-58 and Figure 6-60) to the second difference inline force presented in Fitzgerald et al. (2014).
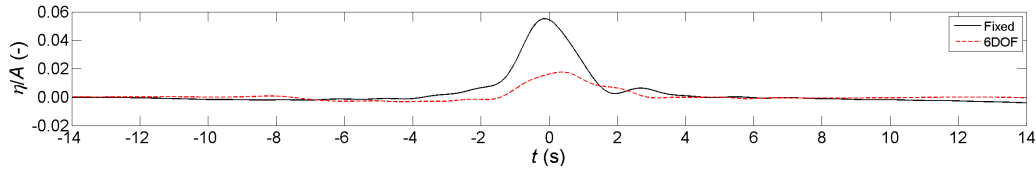
Figure 6-56. Time histories of the second difference component (η_{20}) at the bow of the fixed and free floating Model 3 (WG16) for $kA = 0.17$ and $\alpha = 0°$.
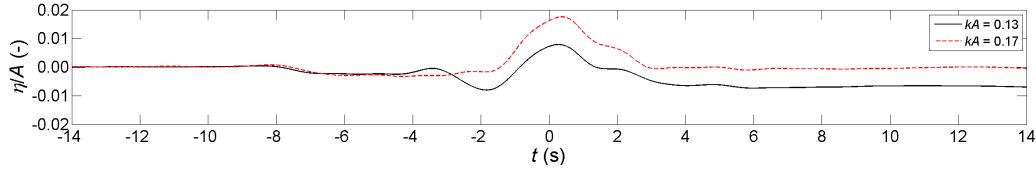
Figure 6-57. Time histories of the second difference component (η_{20}) at the bow of the free floating Model 3 (WG16) for $kA = 0.13$ & 0.17 and $\alpha = 0°$.
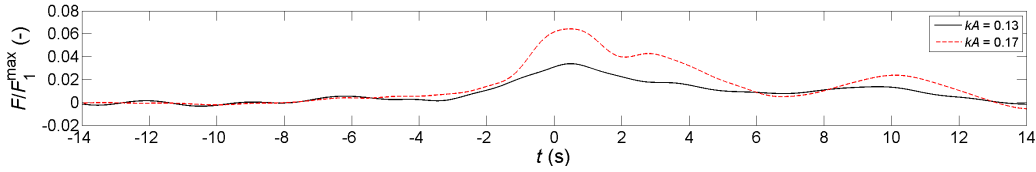
Figure 6-58. Time histories of the second difference component (F_{20}) of the mooring line force of the free floating Model 3 for $kA = 0.13$ & 0.17.
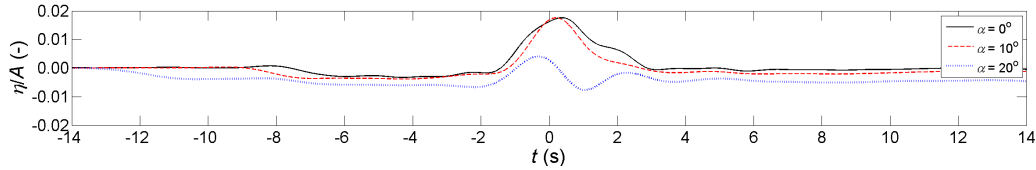
Figure 6-59. Time histories of the second difference component (η_{20}) at the bow of the free floating Model 3 (WG16) for $kA = 0.17$ and $\alpha = 0°$, 10° & 20°.
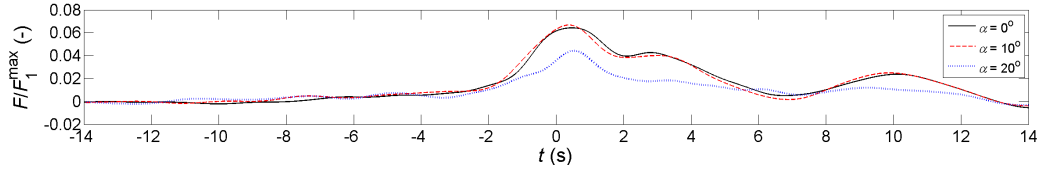
Figure 6-60. Time histories of the second difference component (F_{20}) of the mooring line force of the free floating Model 3 for $kA = 0.17$ and $\alpha = 0°$, $10°$ & $20°$.

6.3 Conclusions of wave-FPSO interaction

Experiments have been performed to examine wave-structure interactions for simplified FPSO geometries. These explore the effects of model length, wave steepness and the incident wave angle on the structure of the total local wave field and also the scattered wave components. An existing general phase-based harmonic separation method has been successfully applied to extract the linear and higher harmonic wave components of the free-surface elevation around the models. In addition, wave-structure interactions of a free floating FPSO model were also investigated for the mooring line force and wave scattering.

It is noted that the results reported here are for relatively small models in long waves ($D/L_p \sim 0.09$, where L_p is the wave length and D the body width), so the effect of linear diffraction is relatively modest. However, this study does observe significant nonlinearity in the scattered field, for which a Stokes-type expansion is appropriate. For relatively larger bodies, linear diffraction will be more important and the nature of the nonlinear scattered components of the waves may change. The key findings of this study are as follows.

6.3.1 For the fixed models

- At locations having the same relative distance to the bow of the models, the highest amplitude scattered waves are obtained with the shortest model (the cylinder). In each case, the second harmonic scattered wave field is comparable in magnitude to the component in undisturbed incident wave, whereas the third-

and fourth harmonics are significantly larger than the equivalent incident bound components.

- At locations having the same relative distance to the stern, the linear harmonic increases as model length decreases but the nonlinear harmonics are similar for all three models and slightly smaller for the longest model at the second harmonic component.

- As the incident wave steepness increased, the non-linear scattered wave increases and a second pulse is evident in the higher harmonics of the scattered wave fields (at second-, third- and fourth-order).

- It is found that the second harmonic scattered wave is greatest near the bow for the incident wave angle of 10° and the third and fourth harmonic scattered waves reduce as the incident wave angle increases from 0° to 20°. The incident wave angle affects the maximum crest height and wave loading and therefore it should be considered in design.

- The second order difference long-wave component is a robust feature of these experiments. This interaction produces a substantial and relatively long-lasting set-up at the bow for all three models. All other higher frequency components ride on the local hill, so the implications of this behaviour for green water on deck are clear.

- In a generic sense, this experimental work observes that the third harmonic of the scattered wave field shows the most complex structure in time, and also in the spectrum. This is consistent with the discussion of the extra complexity of the third harmonic force component in time on a single cylinder given by Fitzgerald et al. (2014).

- Although these results are for contributions to the surface elevation around the models, the third- and fourth-order wave components contribution to global force and to local pressures on the body surface should also be considered for assessing wave loading and structural response in offshore structure design, which may result in ringing-type load effects for some structures.

- Higher order components i.e. the third and four harmonics are significant (up to 8% of overall crest height) so a design method that includes these effects should be applied. This could be achieved using a fully nonlinear numerical method (CFD) solving the Navier-Stokes equations, high-order BEM or FEM schemes for fully nonlinear potential flow, and of course more physical experiments.

- The contributions of the third- and fourth-harmonics and the second difference term to the surface elevation need to be taken into account in design of the air gap and the level of accommodation for offshore structures.

6.3.2 For the free floating model

- In comparison with the fixed model, the linear harmonic scattered waves reduced significantly with the floating model. However, the second harmonic scattered waves increased significantly both upstream and to the side of the floating model.

- Similar to the fixed model, the higher harmonic scattered waves increased with increase wave steepness.

- As the incident wave steepness increased, the higher harmonics of the mooring line force, heave and pitch motions increased.

- In contrast with the fixed model, the linear and the higher harmonic wave components decreased with increase the incident wave angle. The third

harmonic scattered waves are strongest both near the bow and to the side for the incident wave direction of 10°.

- The second, third and fourth harmonics of the mooring line force, heave and pitch motion responses are greatest with the 10° wave. The linear and higher harmonics of the mooring line force, heave and pitch motions reduce as the incident wave angle increases from 0° to 20°.

- The second difference long-wave component reduced significantly with the floating model. The second difference wave at the bow of the floating model also increased with the wave steepness increases, but it reduced as the incident wave angle increases from 0° to 20°.

- Similar to the second difference wave at the bow of the floating model, the second difference component of the mooring line force increased with increasing wave steepness.

- As the incident wave angle increased from 0° to 20°, there is significant reduction of the second difference mooring line force.

CHAPTER 7:   CONCLUSIONS AND RECOMMENDATIONS

This study brings together three different types of hydrodynamic interactions to shed light on the role of (i) aeration and hydroelasticity in slamming and wave impacts and (ii) wave-structure interaction in wave loading. These can have both local and global effects on offshore structures and ships, and may cause local damage and/or structural vibrations. The effects of model length, wave steepness and incident wave angle is also considered on wave scattering from offshore structures and ships, mooring line force and structural response. These effects are important as they may affect global load and potentially lead to damage or catastrophic failure. Three different experiments were conducted: (i) free-falling of a flat plate (rigid or elastic) onto pure and aerated water surfaces, which is designed to represent severe slamming impacts with zero degree deadrise angle; (ii) different types of wave impacts on a truncated vertical rigid or elastic wall in pure and aerated water; and (iii) wave-structure interaction of FPSO-shaped bodies. In the following, conclusions and recommendations found from this experimental study are given relating to local and global loads on offshore structures and ships, which need to be assessed as part of the marine structure design process.

7.1   Impacts in pure water

Physical modelling of slamming impacts by freely dropping a flat plate onto a pure water surface was investigated in this experimental study. It has been found that the spatial distribution of impact pressures depends on the impact velocities (which varied from 1 m/s to 7 m/s in this study). The largest maximum pressure always occurred at the centre of the plate, while the maximum pressure at locations near the edges is about 80 % of the pressure at the centre of the plate for $v < 2$ m/s and about 40 % for $v > 2$ m/s. In addition, the impact loadings on the tested plate are proportional to the square of the

impact velocity and the empirical factors of this relationship are found to depend on the body mass and the location on the plate. These empirical factors may be used for design process of the bow or bottom slamming of offshore structures and ships.

Another aspect of impact on a large offshore structure (such as an FPSO vessel) is offshore breaking wave impact on the hull of ship structure. In this study, wave impacts on a truncated vertical wall, designed to represent a vertical section of an FPSO hull, was experimentally explored for various wave impact types, i.e. early broken, broken, high aeration (large air pocket), flip-through and slightly breaking wave impacts. It is found that the high aeration and flip-through wave impacts are the most severe impact types and they should be considered for offshore structure design.

Post-impact high frequency oscillations of pressures were observed for both the slamming and wave impacts, and these oscillations are due to repeated compression and expansion of the trapped air between the impact plate and water surface, or the trapped air between wave front and the truncated wall. Furthermore, post-impact low frequency oscillation, with a frequency similar to the natural frequency of the wall, was discovered in the time histories of acceleration, pressures and total force of the wall for all tested wave impact types. Those local loading oscillations (high and low frequencies) may need to be assessed for the fatigue analysis of a section of the structure hull or whole ship structure.

7.2   Effects of aeration on impacts

Aeration has an important effect on the slamming and wave impacts, both considered in the present experimental study. There is a significant reduction in the hydrodynamic impact loadings (pressure and force) for those measured in aerated water compared to those in pure water. In addition, significant reductions in the pressure and force impulses of the first positive phase are also found from the slamming impacts in aerated water compared with pure water, but there is nearly no reduction of the total loading

164

impulses for both slamming and wave impacts. The variation of impulsive loadings is less sensitive than the peak loadings for both slamming and wave impacts. Therefore, implications for design are that maximum instantaneous loads may be conservative in the presence of aerated water. The loading amplitude and spatial/temporal evolution is fundamental to be considered in the analysis of structural response.

An exponential relationship of the maximum force and the void fraction has been proposed with its coefficients found from the slamming impacts in this study. These empirical coefficients may be considered as a reference for marine structure design if the effect of aeration needs to be assessed for slamming impacts, and can be used for numerical modelling of aeration effect on slamming impacts.

The repeatability of the pressure time histories (for both magnitude and rise time) was severely affected by aeration of the air-water mixture. This is believed to be caused by the presence of the bubbles in the air-water medium, which create random disturbance in the body of the fluid and at the free surface. This surface distortion also affects the impact pressures in the slamming impact test (drop test).

7.3   Effects of hydroelasticity on impacts

The elasticity of the tested plates and/or walls has a significant effect on the hydrodynamic impact loadings for both slamming and wave impacts, in which the impact loadings are reduced with the more flexible plate/wall. In addition, the elasticity has also an effect on the post-impact oscillations of the pressures for the slamming impacts. The impulsive loadings of the first positive phase decreases as increasing the elasticity of the plate for the slamming impacts. Similarly, the total force impulse decreases as increasing elasticity of the wall for wave impacts, but the total pressure impulse on the wall increases with the more flexible wall. The effects of elasticity on hydrodynamic impact loadings need to be considered to assess the local/global loads which may cause local damage of a hull section or global structural response.

7.4   Wave-structure interactions of FPSO models

Experiments of wave-structure interaction of FPSO-shaped bodies was carried out to investigate the effects of model length, wave steepness and wave direction on wave scattering around the models, mooring line force and responses of the model, all of which may affect the local pressures and global structural response. The models were fixed or free floating with a single mooring line.

7.4.1 Effects of model length

Scattered waves were generated from the interaction of focused wave groups with different FPSO-shaped models. The results show that the geometry of offshore structures and ships has significant effects on wave scattering around the structure, in which the highest amplitude scattered waves near the bow are obtained with the shortest model (the cylinder) but the nonlinear harmonics near the stern are similar for all tested models. Significant third and fourth harmonic scattered waves were observed for all tested models and these non-linear harmonic wave components may induce the ringing-type loading on offshore structures and ships. Therefore, physical model test should be carried out to assess for design processing for a particular geometry of a ship or offshore structure.

7.4.2 Effects of wave steepness

As the incident wave steepness increased the non-linear scattered wave increases and a second pulse is evident in the higher harmonics of the scattered wave fields for both the fixed and floating models. These may increase local pressure loading on structure surface in its magnitude and loading cycle, which can contribute to fatigue load of an offshore structure or ship hull section. In addition, the higher harmonics of the mooring line force, heave and pitch motions also increased with the wave steepness increasing and these will affect the global loading of structure. The highest wave steepness in a

particular operation area/location of offshore structures and ships should be tested/investigated to understand how it affects the local and global loading of the structures.

7.4.3 Effects of directionality

The incident wave direction has considerable effects on the scattered wave field, mooring line force and structural response of the ship and offshore structure, and its effects depend on the geometry and situation (fixed or floating) of the structure. It would therefore be advisable to obtain exact information from model testing with various incident wave direction to determine which one is critical for design of a particular ship or offshore structure, in particular the 10° wave was found in this experimental study to have a significant effect on scattered waves, mooring line force and structural response.

7.5   Recommendations for future work

The finding of this experimental study might be useful to assess in design processing of offshore structures and ships, and also for comparison with numerical simulations. The author recommends further experimental study of the following factors.

- Future research should use underwater high speed cameras with suitable lighting to capture the trapped air pocket between the impact plate and fine detail of the water surface in slamming impacts. This will be useful to estimate the frequency of the air pocket for comparison with the post-impact oscillation frequency observed in pressure time history.

- Different deadrise angles should be considered for slamming impact test in both pure and aerated water in future study.

- Future study should also consider both compression and extension of springs used to form the elastic plate/wall tests.

- A single mooring line was used for FPSO-shaped model tests in the present study, therefore a mooring line system, which is similar to the mooring system used at sea, should be interested for model testing in future.

- Combination of wave and current should be tested to investigate their interaction with FPSO models.

REFERENCES

Aarsnes J., (1994). "An Experimental Investigation of the Effect of Structural Elasticity on Slamming Loads and Structural Responses." Technical report, MARINTEK A/S, Trondheim, Norway.

Adcock, T.A.A., Taylor, P.H. (2009). "Focusing of unidirectional wave groups on deep water: An approximate nonlinear Schrödinger equation-based model." *Proceedings of the Royal Society A: Mathematical, Physical and Engineering Sciences*, 465 (2110), pp. 3083-3102. (2009)

Adcock, T.A.A. and Taylor, P.H. and Gibbs, R. (2016) "Non-linear evolution of uni-directional focussed wave-groups on deep water: A comparison of models." *Applied Ocean Research* **59**, 147-152.

Bachynski, E. E. and Moan, T. (2014). "Ringing loads on tension leg platform wind turbines." Ocean Engineering **84**: 237-248.

Baldock, T. E., Swan, C., Taylor, P. H. (1996). "A Laboratory Study of Nonlinear Surface Waves on Water." Philosophical Transactions of the Royal Society of London A: Mathematical, Physical and Engineering Sciences **354**(1707): 649-676.

Battley M., Allen T., Pehrson P., Stenius I., and Rosen A., (2009). "Effects of Panel Stiffness on Slamming Responses of Composite Hull Panels." in *17th International Conference on Composite Materials*, ICCM17, Edinburgh International Convention Centre (EICC), Edinburgh, UK.

Benjamin, T. Brooke; Feir, J.E. (1967). "The disintegration of wave trains on deep water. Part 1. Theory." *Journal of Fluid Mechanics* **27** (3): 417-430. DOI: 10.1017/S002211206700045X.

Bishop R. and Price W., (1979). "Hydroelasticity of Ships", Cambridge University Press.

Blanchard, D. C., and Woodcock, A. H. (1957). "Bubble formation and modification in the sea and its meteorological significance." *Tellus, * **9,** 145-158.

Borthwick, A. G. L., Hunt, A. C., Feng, T., Taylor, P. H., Stansby, P. K. (2006). "Flow kinematics of focused wave groups on a plane beach in the U.K. Coastal Research Facility." Coastal Engineering **53**(12): 1033-1044.

Bredmose, H., A. Hunt-Raby, et al. (2009). "The ideal flip-through impact: experimental and numerical investigation." Journal of Engineering Mathematics **67**(1-2): 115-136.

Bullock, G. N., Crawford, A. R., et al. (2001). "The influence of air and scale on wave impact pressures." *Coastal Engineering* 42(4): 291-312.

Bullock, G. N., C. Obhrai, et al. (2007). "Violent breaking wave impacts. Part 1: Results from large-scale regular wave tests on vertical and sloping walls." Coastal Engineering **54**(8): 602-617.

Buchner, B., Hodgson T., Voogt, A.J. (editors), Ballard, E., Barltrop, N., Falkenberg, E., Fyfe, S., Guedes Soares, C., Iwanowski, B., Kleefsman, T. (2004). "Summary report on design guidance and assessment methodologies for wave slam and green water impact loading", *MARIN Report No. 15874-1-OE*, Wageningen, The Netherlands.

Chan, E. S. and W. K. Melville (1988). "Deep-Water Plunging Wave Pressures on a Vertical Plane Wall." Proceedings of the Royal Society of London A: Mathematical, Physical and Engineering Sciences **417**(1852): 95-131.

Chanson, H., S.-i. Aoki, et al. (2002). "Unsteady air bubble entrainment and detrainment at a plunging breaker: dominant time scales and similarity of water level variations." *Coastal Engineering* **46**(2): 139-157.

Chaplin, J.R., Rainey, R.C.T. and Yemm, R.W. (1997). "Ringing of vertical cylinder in waves." *Journal of Fluid Mechanics*, **350**: 119-147.

Chuang, S.-L. (1966a). "Slamming of rigid wedge-shaped bodies with various deadrise angles." David Taylor Model Basin, Washington DC, Report 2268.

Chuang, S.-L. (1966b). "Experiments on flat-bottom slamming", *Journal of Ship Research*, **10**(1), 10-17.

Chuang, S. (1970). "Investigation of impact of rigid and elastic bodies with water." *Naval Ship Research and Development Center: Report No.* **3248**.

Cooker, M. J. & Peregrine, D. H. (1990). "Computation of violent wave motion due to waves breaking against a wall." *In Proceedings of the 22nd International Conference on Coastal Engineering*, Delft, The Netherlands, pp. 164–176. ASCE.

Cooker, M. J. and D. H. Peregrine (1995). "Pressure-impulse theory for liquid impact problems." *Journal of Fluid Mechanics* **297**: 193-214.

Deane, G. B. and M. D. Stokes (1999). "Air Entrainment Processes and Bubble Size Distributions in the Surf Zone." *Journal of Physical Oceanography* **29**(7): 1393-1403.

Det Norske Veritas (2010). "Environmental conditions and environmental loads". Recommended Practice DNV-RP-C205.

Det Norske Veritas (2010). "Global performance analysis of deep-water floating structures". *Recommended Practice* DNV-RP-F205.

Detsch, R., & Harris, I. (1989). "Dissolution and rise velocity of small air bubbles in water and salt water." *In OCEANS'89. Proceedings IEEE*, Vol. **1**, pp. 286-291.

El Malki Alaoui, A., A. Nême, et al. (2012). "Experimental study of coefficients during vertical water entry of axisymmetric rigid shapes at constant speeds." *Applied Ocean Research* **37**(0): 183-197.

El Malki Alaoui, A., A. Nême, et al. (2015). "Experimental investigation of hydrodynamic loads and pressure distribution during a pyramid water entry." *Journal of Fluids and Structures* **54**(0): 925-935.

Faltinsen, O. (1993). *Sea Loads on Ships and Offshore Structure* (Cambridge University Press).

Faltinsen, O. M., Newman, J. N. and Vinje, T. (1995). "Nonlinear wave loads on a slender vertical cylinder." *Journal of Fluid Mechanics*, **289**, pp 179-198 doi:10.1017/S0022112095001297

Faltinsen, O. M. (1997). "The effect of hydroelasticity on ship slamming." *Philosophical Transactions of the Royal Society of London A: Mathematical, Physical and Engineering Sciences* **355**(1724): 575-591.

Faltinsen, O. (2000). "Hydroelastic slamming." *Journal of Marine Science and Technology* **5**(2): 49-65. http://dx.doi.org/10.1007/s007730070011.

Faltinsen, O., M. Landrini, et al. (2004). "Slamming in marine applications." *Journal of Engineering Mathematics* **48**(3-4): 187-217.

Faltinsen, O. M. (2014). "Hydrodynamics of marine and offshore structures." *Journal of Hydrodynamics*, Ser. B **26**(6): 835-847.

Fenton, J. D. (1985). "A fifth-order Stokes theory for steady waves." *J. Waterway Port Coastal and Ocean Engineering. ASCE.* **111**: 216-234.

Fitzgerald, C. J., Taylor, P. H., Taylor, R. E., Grice, J., Zang, J. (2014). "Phase manipulation and the harmonic components of ringing forces on a surface-piercing column." *Proceedings of the Royal Society of London A: Mathematical, Physical and Engineering Sciences* **470**(2168)

References

Franz, G. J. (1959). "Splashes as sources of sound in liquids." *J. Acoust. Soc. Amer.,* **31,** 1080-1096.

Frieze, P. A. (2011). "Offshore structure designs and construction", in Ships and Offshore Structures, in Encyclopedia of Life Support Systems (EOLSS), Developed under the Auspices of the UNESCO, Eolss Publishers, Paris, France, [http://www.eolss.net].

Grabemann, I., Weisse, R. (2008). "Climate change impact on extreme wave conditions in the North Sea: an ensemble study." *Ocean Dynamic* **58**:199–212

Grue, J. (1992). "Nonlinear water waves at a submerged obstacle or bottom topography." *Journal of Fluid Mechanics*, **244**, pp 455-476.

Gulev, S.K., Grigorieva, V. (2004). "Last century changes in ocean wind wave height from global visual wave data." *Geogr Res Lett* **31**: L24302. doi:10.1029/2004GL021040

Hancock, N. (2014). "Calibration of aeration data for drop impact testing." Project II of MEng (Hons) Civil and Coastal Engineering at Plymouth University.

Hann, M., Greaves, D., Raby, A. (2014). "A new set of focused wave linear combinations to extract non-linear wave harmonics." *In Twenty-ninth Int. Workshop on Water Waves and Floating Bodies*, Osaka, Japan, 30 March - 2 April, 61–64 (http://www.iwwwfb.org/Abstracts/iwwwfb29/iwwwfb29_16new.pdf)

Hattori, M., A. Arami, et al. (1994). "Wave impact pressure on vertical walls under breaking waves of various types." *Coastal Engineering* 22 (1 - 2): 79-114.

Hofland, B., Kaminski, M., & Wolters, G. (2011). "Large scale wave impacts on a vertical wall." *Coastal Engineering Proceedings, 1*(**32**), structures.15. doi:http://dx.doi.org/10.9753/icce.v32.structures.15

HR Wallingford Ltd (2002). "FPSO response in long and short crested seas." *HSE OT Report 2002/018.*

Hull, P. and G. Müller (2002). "An investigation of breaker heights, shapes and pressures." *Ocean Engineering* **29**(1): 59-79.

Hunt, A., P. H. Taylor, Borthwick, A., Stansby, P., Feng, T. (2003). "Kinematics of a Focused Wave Group on a Plane Beach: Physical Modelling in the UK Coastal Research Facility." *Coastal Structures* **2003**: 740-750.

Huseby M., Grue J. (2000). "An experimental investigation of higher-harmonic wave forces on a vertical cylinder". *Journal of Fluid Mechanics***, 414**: 75-103.

Kapsenberg, G. K. (2011). "Slamming of ships: Where are we now?," *Philos. Trans. R. Soc., A* **369**, 2892–2919. http://dx.doi.org/10.1098/rsta.2011.0118.

Kay, J. (2014). "UK storms destroy railway line and leave thousands without power," BBC News, available at http://www.bbc.co.uk/news/uk-26042990.

Kimmoun, O., Malenica, et al. (2009). "Fluid structure interactions occurring at a flexible vertical wall impacted by a breaking wave." *Proc. of 19th International Offshore and Polar Engineering Conference,* 21-26 July, Osaka, Japan.

Kimmoun, O., A. Ratouis, and L. Brosset (2012). "Influence of a Bubble Curtain on the Impact of Waves on a Vertical Wall." *Proc. of 22nd International Offshore and Polar Engineering Conference*. International Society of Offshore and Polar Engineers, 17-22 June, Rhodes, Greece.

Kreyszig, E. (2006). "Advanced Engineering Mathematics, 9th Edition", John Wiley & Sons, 1246 pages. ISBN: 9780470458365.

Kvålsvold J., (1994). "Hydroelastic Modelling of Wet-Deck Slamming on Multi-Hull Vessels." *Mta-report 1994: 100*, Department of Marine Hydrodynamics, The Norwegian Institute of Technology, Norway.

Kwon, S.H., Jung, D.J. et al. (2003). "An Alternative Experiment for Slamming Using an Air Pressure Cylinder." *Proceeding of the 13th International Offshore and Polar Engineering Conference (ISOPE)*, Honolulu, Hawaii, USA, pp. 542-548.

Lafeber, W., H. Bogaert, et al. (2012). <u>Comparison of wave impact tests at large and full scale: Results from the sloshel project</u>. *Proc. of 22nd International Offshore and Polar Engineering Conference*. International Society of Offshore and Polar Engineers, 17-22 June, Rhodes, Greece.

Lang, N. A., Rung, T. (2011). "Impact Tests in Pure and Aerated Water." *Proceeding of the 30th International Conference on Ocean, Offshore and Arctic Engineering* (OMAE), Rotterdam, The Netherlands, June 19–24.

Lefebvre, S. and Collu, M. (2012). "Preliminary design of a floating support structure for 5 MW offshore wind turbine." *Ocean Engineering* **40**: 15 - 26.

Lewison, G., Maclean, W. M. (1968). "On the cushioning of water impact by entrapped air." *Journal of Ship Research*, **12**(2), 116-130.

Lewison, G. R. G. (1970). "On the reduction of slamming pressures." *Publication of: Royal Institution of Naval Architects*, **112**(3).

Liger-Belair, G., Marchal, R., Robillard, B., Dambrouck, T., Maujean, A., Vignes-Adler, M. and Jeandet, P. (2000). "On the Velocity of Expanding Spherical Gas Bubbles Rising in Line in Supersaturated Hydroalcoholic Solutions: Application to Bubble Trains in Carbonated Beverages." *Langmuir* **16** (4), 1889-1895. DOI: 10.1021/la990653x

Longuet-Higgins, M. S. (1993). "Bubble noise mechanisms - A review". *Natural Physical Sources of Underwater Sound,* B. R. Kerman, Ed., Kluwer Academic, 419–452.

Ma, Z. H., Causon, D. M., Qian, L., Mingham, C. G., Mai, T., Greaves, D. & Raby, A. (2016). "Pure and aerated water entry of a flat plate." *Physics of Fluids* **28**(1): 016104. DOI: http://dx.doi.org/10.1063/1.4940043

Mai, T., Greaves, D. and Alison, R. (2014). "Aeration effects on impact: Drop test of a flat plate". *Proceedings of the 24th International Ocean and Polar Engineering Conference* (ISOPE2014), Busan, Korea. Vol 3, pp. 703-709.

Mai, T., Hu, Z. Z., Greaves, D. and Alison, R. (2015). "Investigation of Hydroelasticity: Wave Impact on a Truncated Vertical Wall". *Proceedings of the 25th International Ocean and Polar Engineering Conference* (ISOPE2015), Hawaii, USA. Vol.3, pp 647-654.

Medwin, H. (1977). "In situ acoustic measurements of microbubbles at sea." *Journal of Geophysical Research* **82**(6): 971-976.

Melville, W. K. (1996). "The role of surface-wave breaking in air-sea interaction." *Annu. Rev. Fluid Mech.,* **28,** 279–321.

Mercier, J. A. (1982). "Evolution of tension leg platform technology." *Proc 3rd Int. Conf. Behaviour of Offshore Structures*, Massachusetts Institute of Technology, Cambridge, MA.

Minnaert, M. (1933). "On musical air bubbles and the sounds of runningwater." *Philos. Mag.,* **16,** 235–248.

Molin, B., F. Remy, O. Kimmoun and E. Jamois (2005). "The role of tertiary wave interactions in wave-body problems. " *Journal of Fluid Mechanics*, **528**, pp 323-354

Monahan, E. C. (1993). "Occurrence and evolution of acoustically relevant sub-surface bubble plumes and their associated, remotely monitorable, surface whitecaps." *Natural Physical Sources of Underwater Sound,* B. R. Kerman, Ed., Kluwer Academic, 503-517.

Ning, D.Z., Zang, J., Liu, S.X., Eatock Taylor, R., Teng, B., Taylor, P.H. (2009). "Free-surface evolution and wave kinematics for nonlinear uni-directional focused wave groups." *Ocean Engineering*, 36 (15-16), pp. 1226-1243.

References

Oh, S. H. , Kwon, S. H., et al. (2009), "A close look at air pocket evolution in flat impact." *Proc. of 24th International Workshop on Water Waves and floating Bodies*, Zelenogorsk, Russia.

Oumeraci, H., H. W. Partenscky, et al. (1992). "Impact loading and dynamic response of caisson breakwaters." *Coastal Engineering Proceedings* **1** (23), 1475-1488.

Oumeraci, H., P. Klammer, et al. (1993). "Classification of Breaking Wave Loads on Vertical Structures." *Journal of Waterway, Port, Coastal, and Ocean Engineering* **119**(4): 381-397.

Pumphrey, H. C., and Elmore, P. A. (1990). "The entrainment of bubbles by drop impacts". *J. Fluid Mech.,* **220,** 539–567.

Rodgers, L. and Bryson, M. (2014). "10 key moments of the UK winter storms," BBC News, available at http://www.bbc.co.uk/news/uk-26170904.

Rosén A., (2004). "Loads and Responses for Planing Craft in Waves." *PhD Thesis*, Royal Institute of Technology, KTH Centre for Naval Architecture, Stockholm, Sweden.

Siddorn, P. D. (2012). "Efficient numerical modelling of wave-structure interaction." DPhil. University of Oxford.

Shao Y. L., Faltinsen O. M. (2014). "A harmonic polynomial cell (HPC) method for 3D Laplace equation with application in marine hydrodynamics." *Journal of Computational Physics*, **274**: 312-332.

Smith, N. J., Stansby, P. K., et al. (1998). "The slam force on a plate in free flight due to impact on a wave crest". *Journal of Fluids and Structures*, vol. 12, 183-196.

Stapelberg, R. F. (2009). "Handbook of Reliability, Availability, Maintainability and Safety in Engineering Design." Springer London. DOI:10.1007/978-1-84800-175-6. ISBN: 978-1-84800-174-9 (Print) 978-1-84800-175-6 (Online).

Stenius, Ivan (2009). *Hydroelasticity in Marine Hull Bottom Panels - Modeling and Characterization.* Stockholm: KTH. ISBN: 978-91-7415-389-7.

Stenius, I., Rosén, A., Battley, M., Allen, T., & Pehrson, P. (2011a). Hydroelastic effects in slamming loaded panels. In *11th. International Conference on Fast Sea Transportation (FAST 2011), Honolulu, Hawaii, USA* (pp. 644-652).

Stenius, I., Rosén, A., Kuttenkeuler, J. (2011b). "Hydroelastic interaction in panel-water impacts of high-speed craft." *Ocean Engineering* **38**(2–3): 371-381.

Stenius, I., Rosén, A., Battley, M., & Allen, T. (2013). Experimental hydroelastic characterization of slamming loaded marine panels. *Ocean Engineering*, *74*, 1-15.

Temarel, P. (2008). "Hydroelasticity of Ships: Taking Stock and Moving Forward." *in 22nd Asian-Pacific Technical Exchange and Advisory Meeting on Marine Structures*, TEAM 2008, Istanbul, Turkey.

Tenzer, M., Moctar, O. e. & Schellin, T. E. (2015). "Experimental investigation of impact loads during water entry." *Ship Technology Research*, **62**:1, 47-59

Tromans, P.S., Anaturk, A.R., and Hagemeijer, P. (1991). "A new model for the kinematics of large ocean waves - application as a design wave." *Proc. 1st Int. Offshore and Polar Eng. Conf.*, Edinburgh, U.K., 11-16 August, 64-71.

U.S. Energy Information Administration (www.eia.gov).

U.S. Energy Information Administration (2016). "International Energy Outlook 2016" . Report Number: DOE/EIA-0484(2016) at www.eia.gov/ieo.

Van Nuffel, D., K. Vepa, et al. (2013). "A comparison between the experimental and theoretical impact pressures acting on a horizontal quasi-rigid cylinder during vertical water entry." *Ocean Engineering*.

Verhagen, J.H.G. (1967). "The impact of a flat plate on a water surface." *Journal of Ship Research* **10**, 211–223.

von Karman, T. (1929). "The impact on seaplane floats during landing." National Advisory Committee for Aeronautics. *Technical Note*, vol. 321.

Voogt, A.J. and Buchner, B. (2004). "Prediction of Wave Impact Loads on Ship-type Offshore Structures in Steep Fronted Waves." *Proceedings of the ISOPE2004*, paper no. 2004-JSC-343

Wagner, H. (1932). "Über Stoß- und Gleitvorgänge an der Oberfläche von Flüssigkeiten." *ZAMM - Journal of Applied Mathematics and Mechanics / Zeitschrift für Angewandte Mathematik und Mechanik* 12(4): 193-215.

Wienke, J. and H. Oumeraci (2005). "Breaking wave impact force on a vertical and inclined slender pile - theoretical and large-scale model investigations." Coastal Engineering **52**(5): 435-462.

Williams, M. O. (2008). "Wave mapping in UK waters: Supporting document." *Health and Safety Executive*, Research Report RR621, pp 38.

Wilson, W. D. (1960). "Speed of Sound in Sea Water as a Function of Temperature, Pressure, and Salinity." *The Journal of the Acoustical Society of America* **32**(6): 641-644.

Xu L., Barltrop N. and Okan B. (2008a). "Bow impact loading on FPSOs 1 - experimental investigation." *Ocean Engineering* Vol **35**, No 11-12, pp1148 - 1157 http://dx.doi.org/10.1016/j.oceaneng.2008.04.013

Xu L. and Barltrop N., (2008b). "Bow impact loading on FPSOs 2 - theoretical investigation." *Ocean Engineering* Vol **35**, No. 11-12, pp1158-1165 http://dx.doi.org/10.1016/j.oceaneng.2008.04.012

Yuen, H.C.; Lake, B.M. (1980). "Instabilities of waves on deep water." *Annual Review of Fluid Mechanics* **12**: 303-334. DOI: 10.1146/annurev.fl.12.010180.001511.

Young, R.I., Zieger, S., Babanin, A.V. (2011). "Global trends in wind speed and wave height." *Science* **332**(22):451-455

Zang, J., Gibson, R., Taylor, P. H., Eatock Taylor, R., and Swan, C. (2006). "Second order wave diffraction around a fixed ship-shaped body in unidirectional steep waves." *Journal of Offshore Mechanics and Arctic Engineering*, **128**(2): 89.

Zhu, L. (1995). "Structural Response of Ship Plates in Slamming-Drop Test Results and Analysis", University of Glasgow, Department of Naval Architecture and Ocean Engineering-Reports-NAOE.

APPENDIX A:

A.1   Volumetric method

This method was developed by Kurt Langfeld - Professor in Theoretical Physics, Plymouth University.

Let us put a cylinder of cross section A and length L into the bubble bath of depth L (see Figure A-1 below).
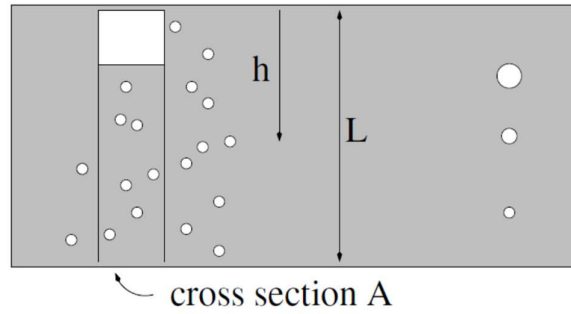
Figure A-1: Air flow rate measured by a vertical cylinder.

Let's call t_{full} the time needed to completely fill the cylinder with air. We also introduce t_b, which is the time a bubble needs to surface.

The rate R of air delivery is then given by

$$R = AL \frac{1}{t_{full}} \qquad \text{(A-1)}$$

The amount of air in the basin (within the same volume than the cylinder) is then given by R_{tb} leaving us with a void fraction of:

$$\beta = \frac{V_{air}(L)}{V} = AL \frac{1}{t_{full}} t_b / AL = \frac{t_b}{t_{full}} \qquad \text{(A-2)}$$

In the remainder, we correct for the fact that the bubbles are expanding during the ascent. We introduce the surface pressure p, the pressure p_h at depth h and Δp the change in pressure given by the weight of the water column:

$$p(h) = p + \Delta p, \qquad \Delta p = \rho g h \tag{A-3}$$

If $v(h)$ denotes the volume of a bubble at depth h, we use an adiabatic gas equation:

$$p(h)v(h)^\kappa = pv(0)^\kappa \tag{A-4}$$

The average bubble size is then given by:

$$v_{av} = \frac{1}{L}\int_0^L v(h)dh = \frac{1}{L}\int_0^L \frac{v(0)}{(1+\rho g h / p)^{1/\kappa}}dh = \frac{p}{\Delta p}\frac{\kappa}{\kappa-1}\left[\left(1+\frac{\Delta p}{p}\right)^{1-1/\kappa}-1\right]v(0) \tag{A-5}$$

Using

$$v(0) = \left(\frac{p(h)}{p}\right)^{1/\kappa} v(L) = \left(1+\frac{\Delta p}{p}\right)^{1/\kappa} v(L) \tag{A-6}$$

We find:

$$v_{av} = \frac{p}{\Delta p}\frac{\kappa}{\kappa-1}\left[\left(1+\frac{\Delta p}{p}\right)-\left(1+\frac{\Delta p}{p}\right)^{1/\kappa}\right]v(L) \tag{A-7}$$

Assuming that $\Delta p \ll p$, we find:

$$\frac{v_{av}}{v(L)} = 1 + \frac{1}{2\kappa}\frac{\Delta p}{p} + O\left(\frac{\Delta p^2}{p^2}\right) \tag{A-8}$$

The air in the (full) cylinder is exposed to the pressure $p(L)$. The corrected void fraction is given by:

$$\beta = \frac{V_{av}}{V} \approx \left[1+\frac{1}{2\kappa}\frac{\Delta p}{p}\right]\frac{V(L)}{V} = \left[1+\frac{1}{2\kappa}\frac{\Delta p}{p}\right]\frac{t_b}{t_{full}} \tag{A-9}$$

For L = 0.5 m and using the adiabatic coefficient $\kappa \approx 5/3$, we find:

$$\frac{\Delta p}{p} \approx \frac{5000}{10^5} = 5\% \tag{A-10}$$

Therefore,

176

$$\beta = 1.015 \frac{t_b}{t_{full}} \tag{A-11}$$

Hence, the effect of the growing bubbles during ascent is a small correction.

A.2   Probability of non-exceedance of P_{max} in aerated water for drop test

Figure A-2. CDF of P_{max} on the 45kg elastic plate 1 in aerated water (β = 0.8 %).

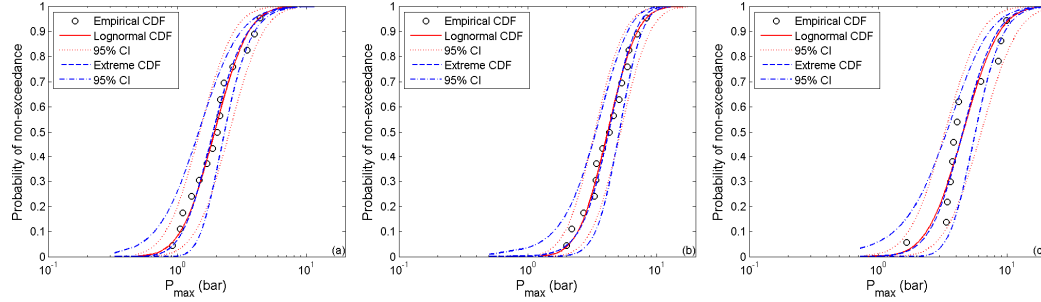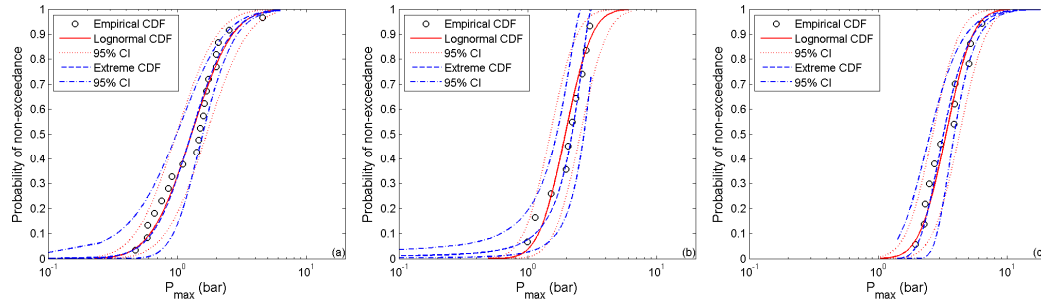Figure A-3. CDF of P_{max} on the 45kg elastic plate 1 in aerated water (β = 1 %).

Figure A-4. CDF of P_{max} on the 45kg elastic plate 1 in aerated water (β = 1.6 %).
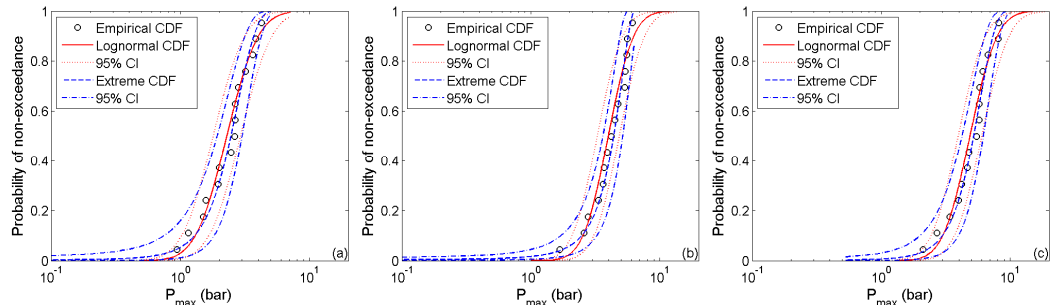
Figure A-5. CDF of P_{max} on the 52kg elastic plate 1 in aerated water (β = 0.8 %).
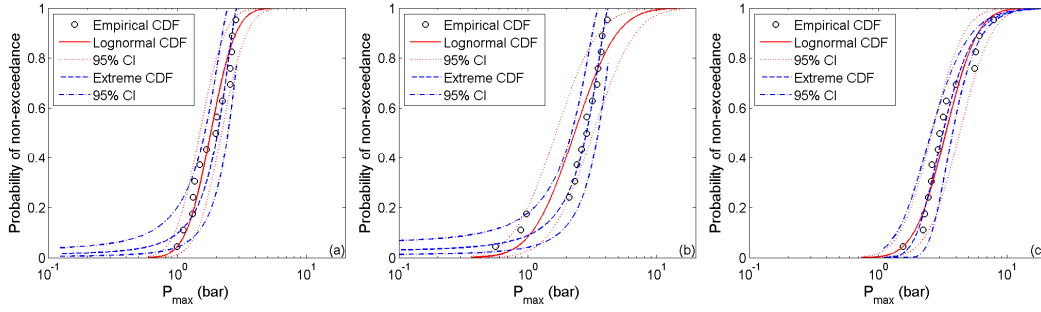
Figure A-6. CDF of P_{max} on the 52kg elastic plate 1 in aerated water (β = 1 %).
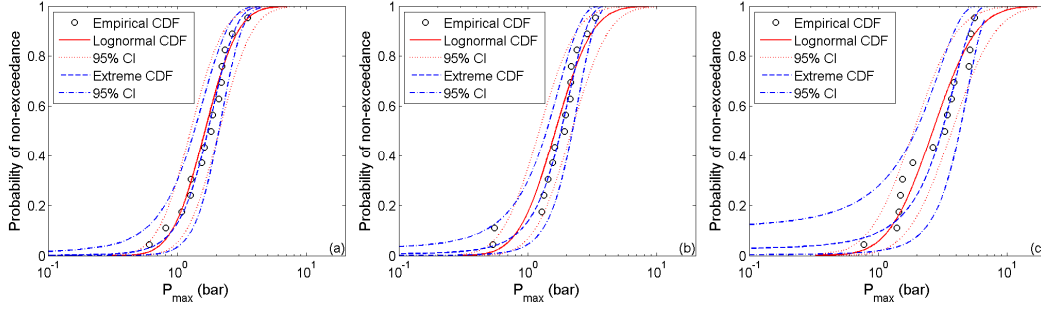
Figure A-7. CDF of P_{max} on the 52kg elastic plate 1 in aerated water (β = 1.6 %).
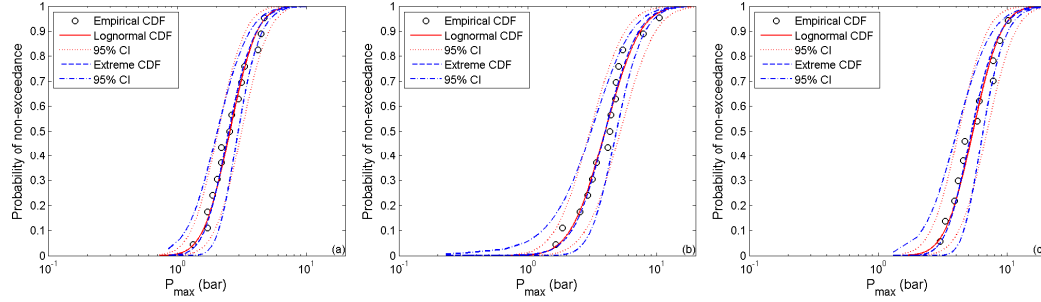
Figure A-8. CDF of P_{max} on the 52kg elastic plate 2 in aerated water (β = 0.8 %).

Figure A-9. CDF of P_{max} on the 52kg elastic plate 2 in aerated water (β = 1 %).

Figure A-10. CDF of P_{max} on the 52kg elastic plate 2 in aerated water (β = 1.6 %).

APPENDIX B: REPEATABILITY OF WAVE IMPACTS

B.1   Repeatability of wave impacts in pure water
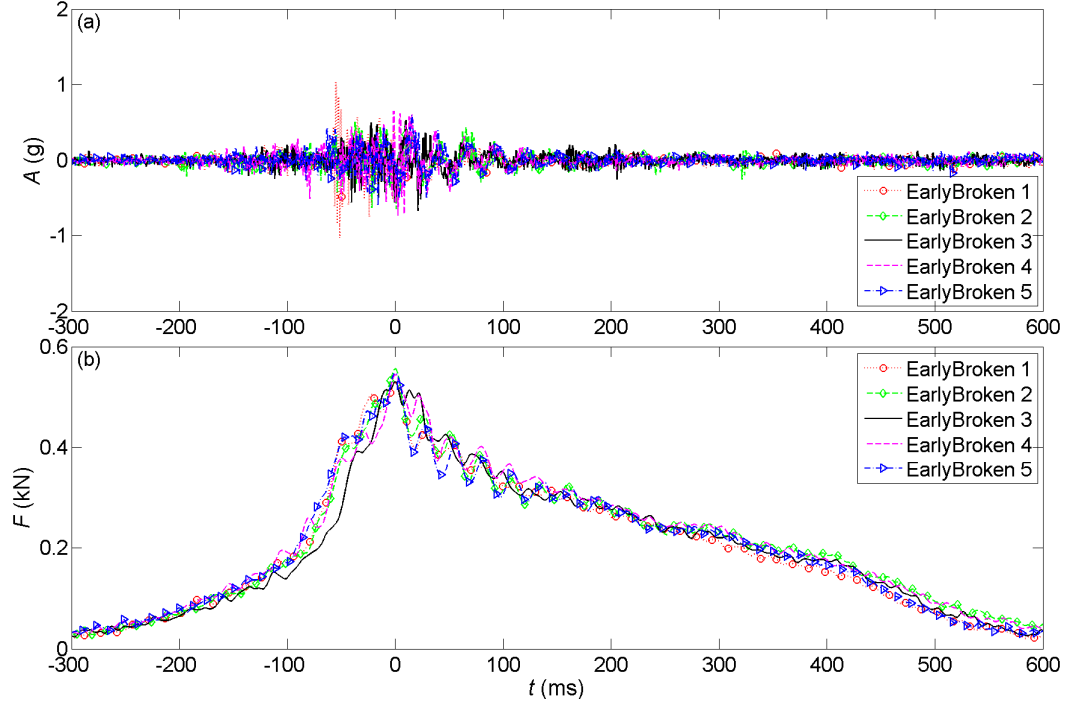
Figure B-1: Repeatability of acceleration and force traces on rigid wall under early broken wave impact in pure water (d = 0.7 m).
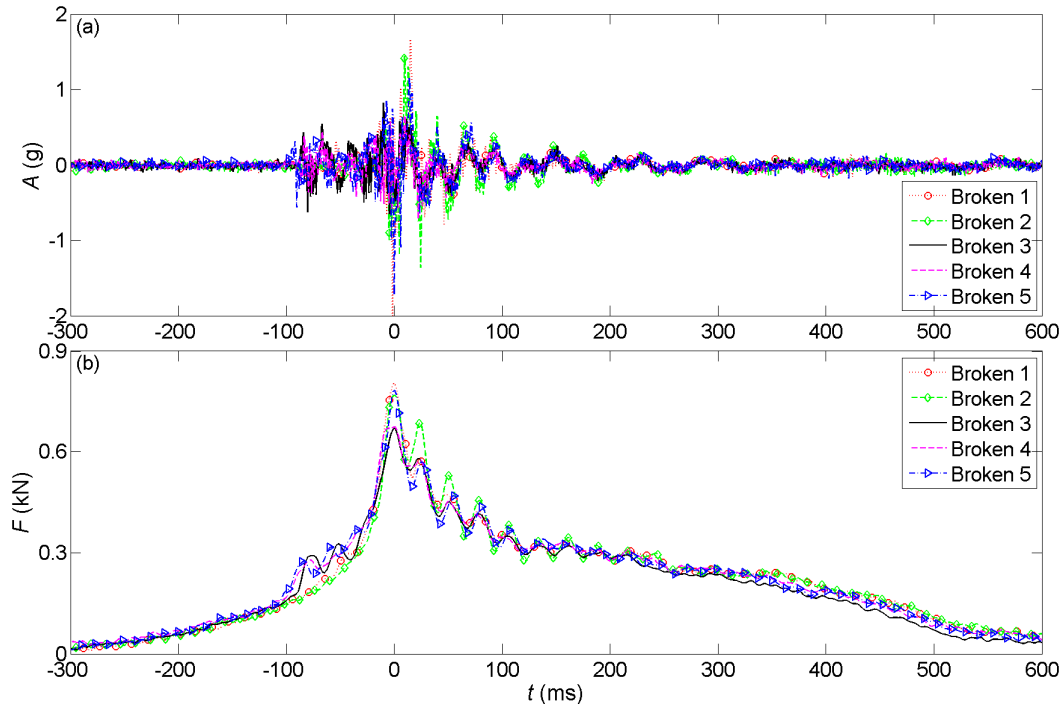
Figure B-2: Repeatability of acceleration and force traces on rigid wall under broken wave impact in pure water (d = 0.7 m).
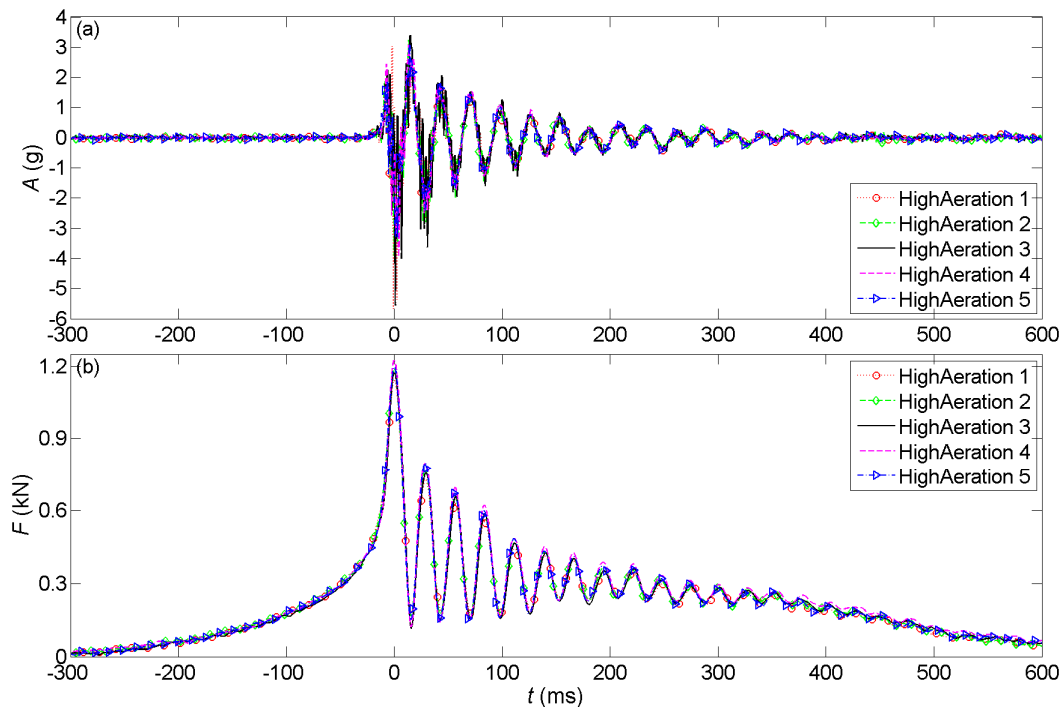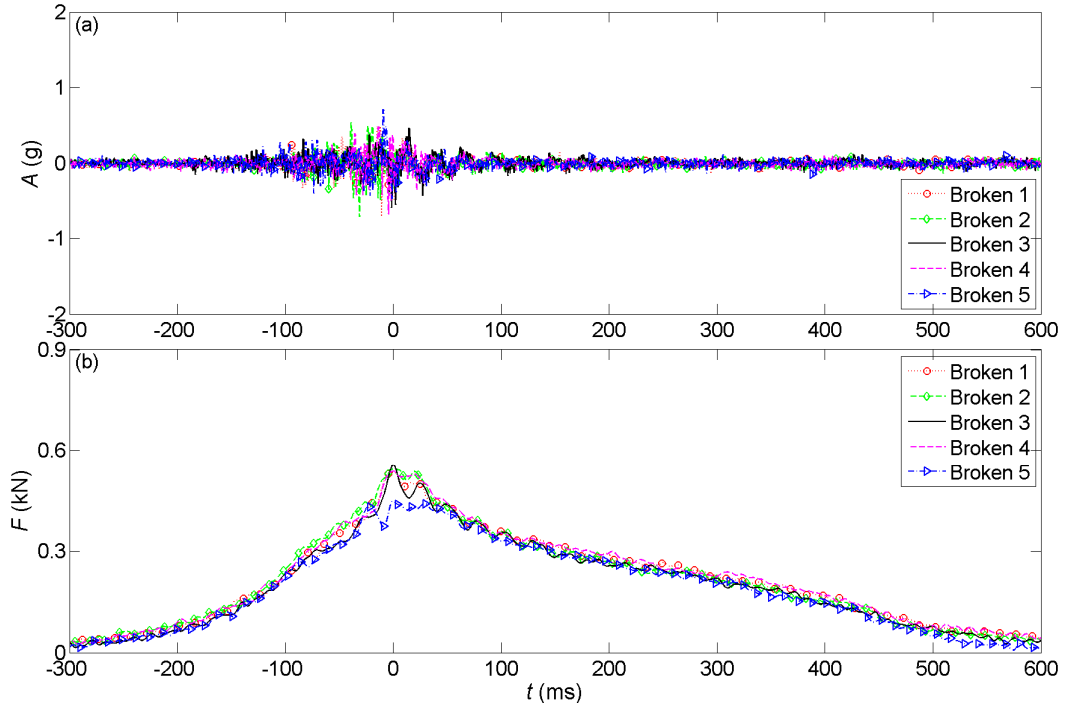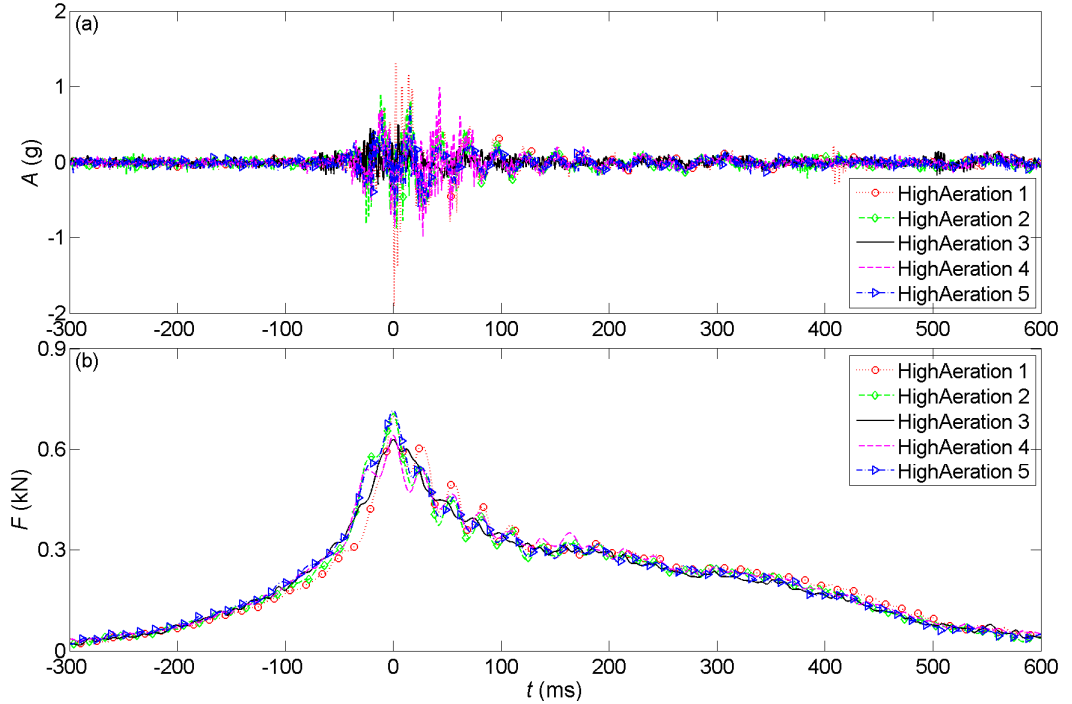

Figure B-3: Repeatability of acceleration and force traces on rigid wall under high aeration wave impact in pure water (d = 0.7 m).
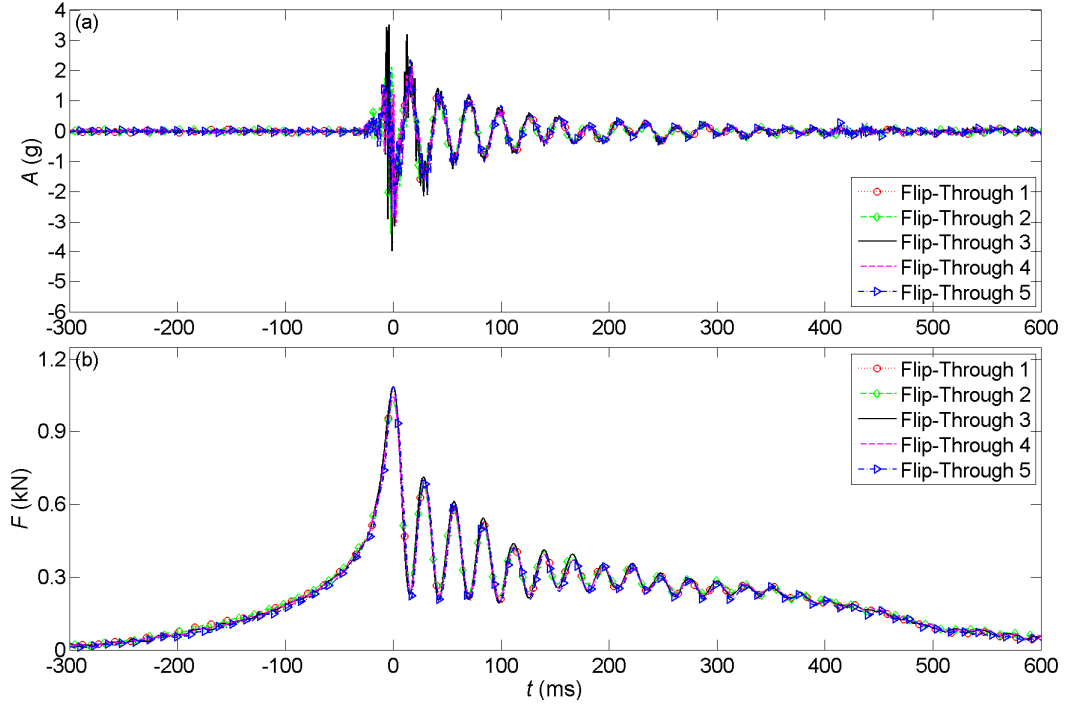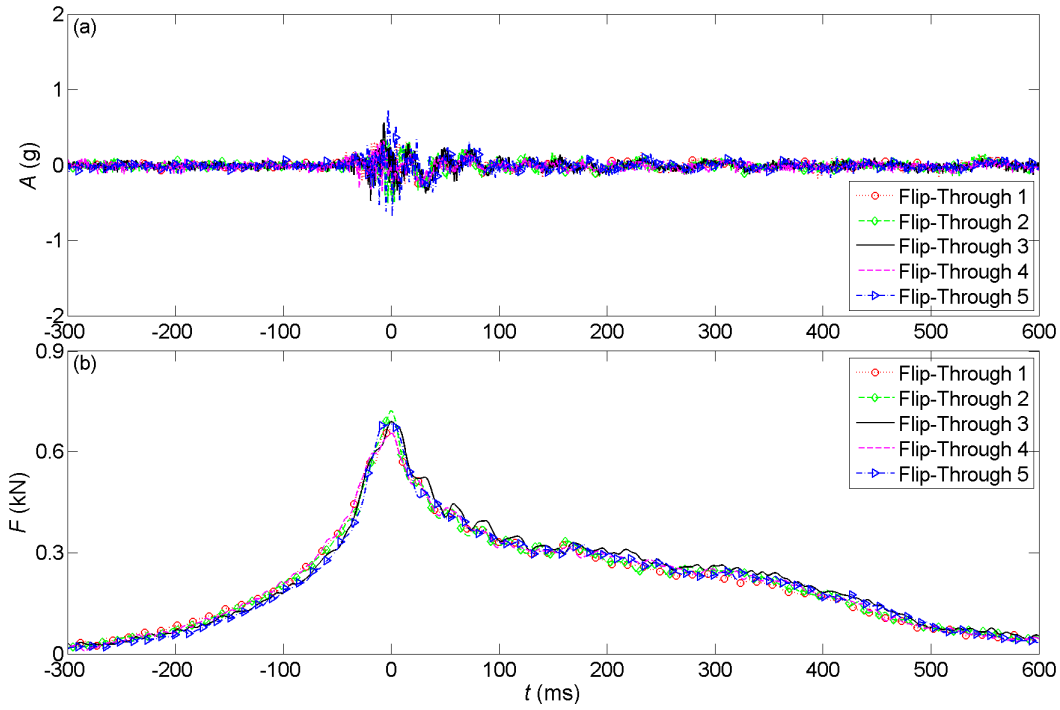
Figure B-4: Repeatability of acceleration and force traces on rigid wall under flip-through wave impact in pure water (d = 0.7 m).
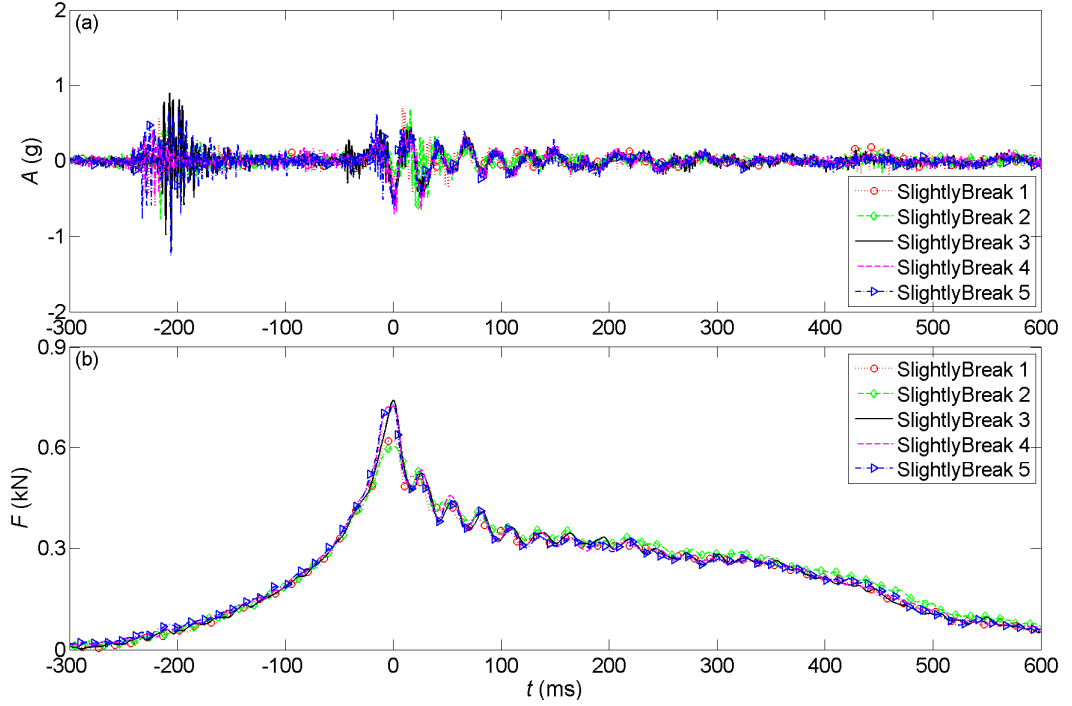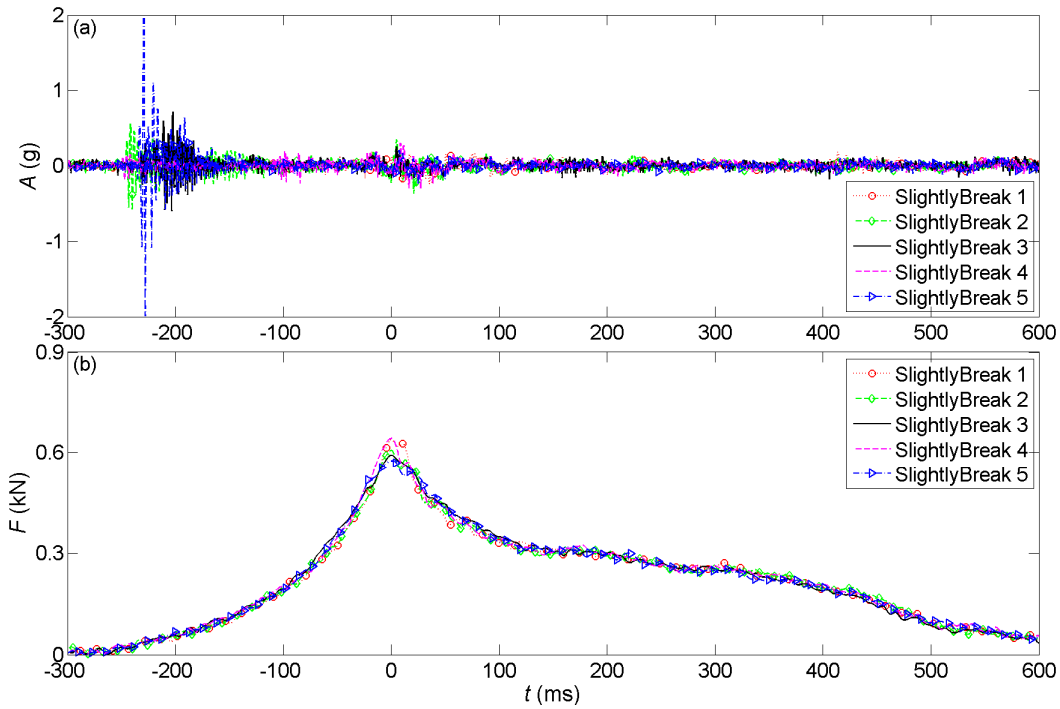

Figure B-5: Repeatability of acceleration and force traces on rigid wall under slightly breaking wave impact in pure water (d = 0.7 m).
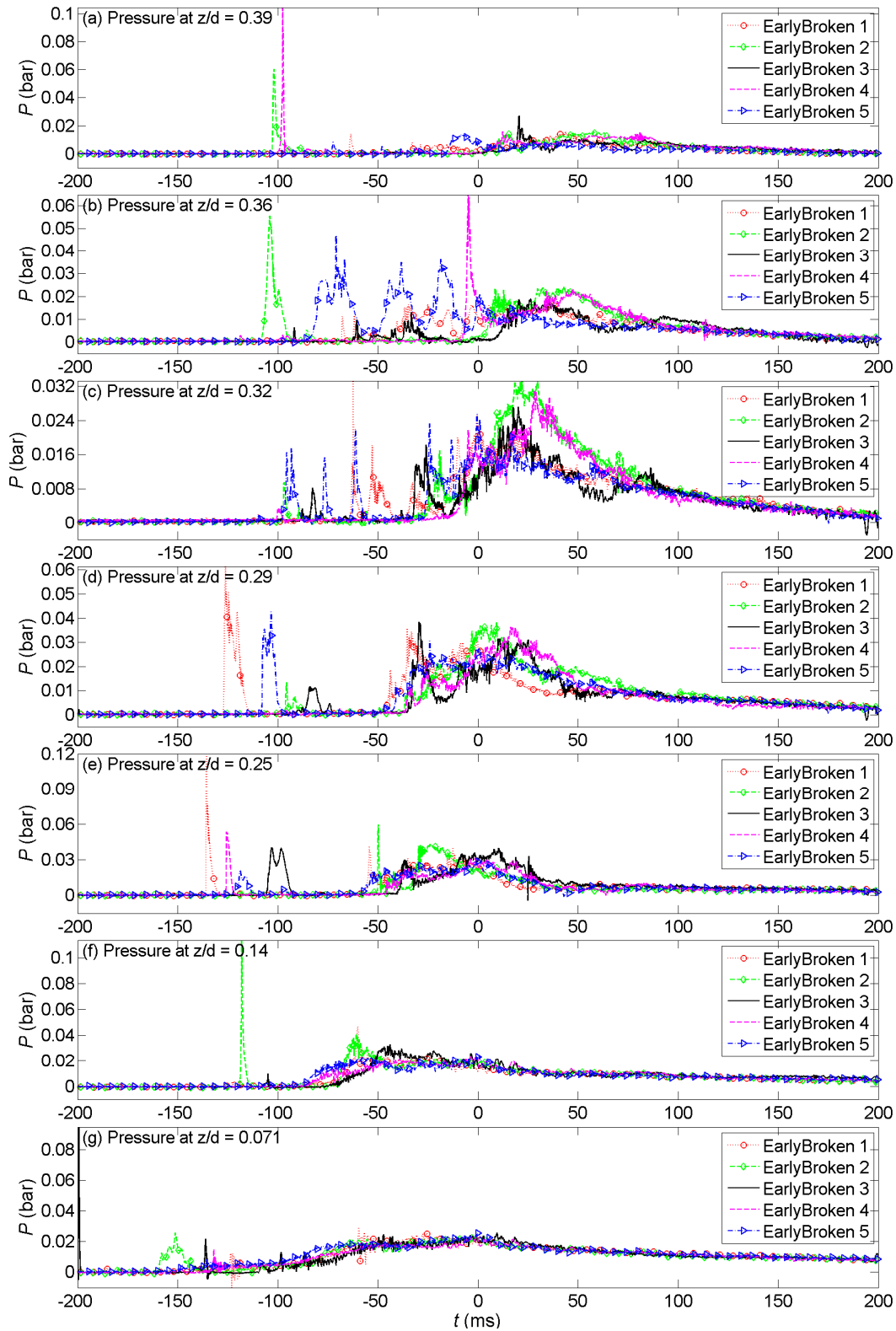
Figure B-6: Repeatability of pressure traces on rigid wall under early broken wave impact in pure water (*d* = 0.7 m).
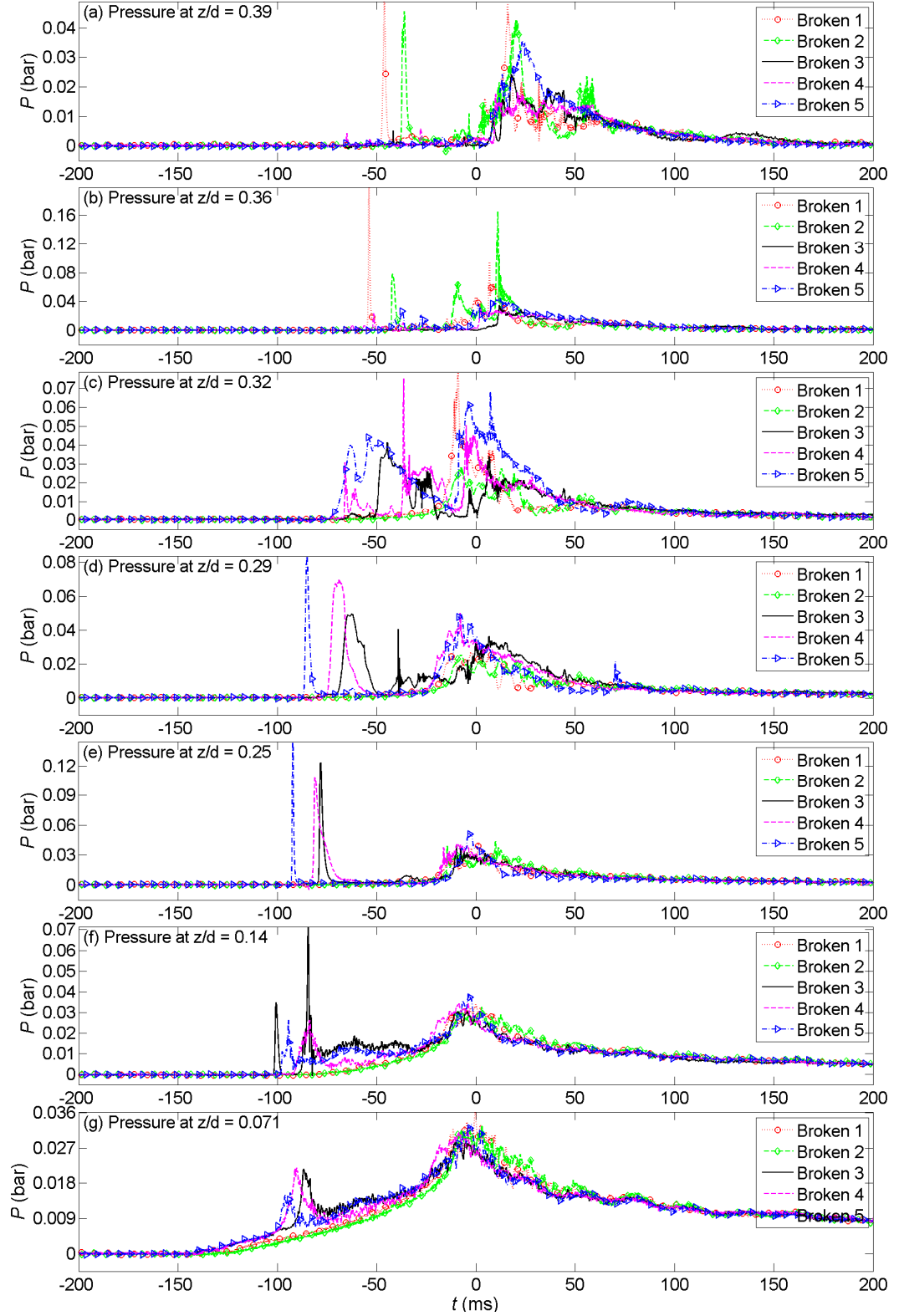
Figure B-7: Repeatability of pressure traces on rigid wall under broken wave impact in pure water ($d = 0.7$ m).
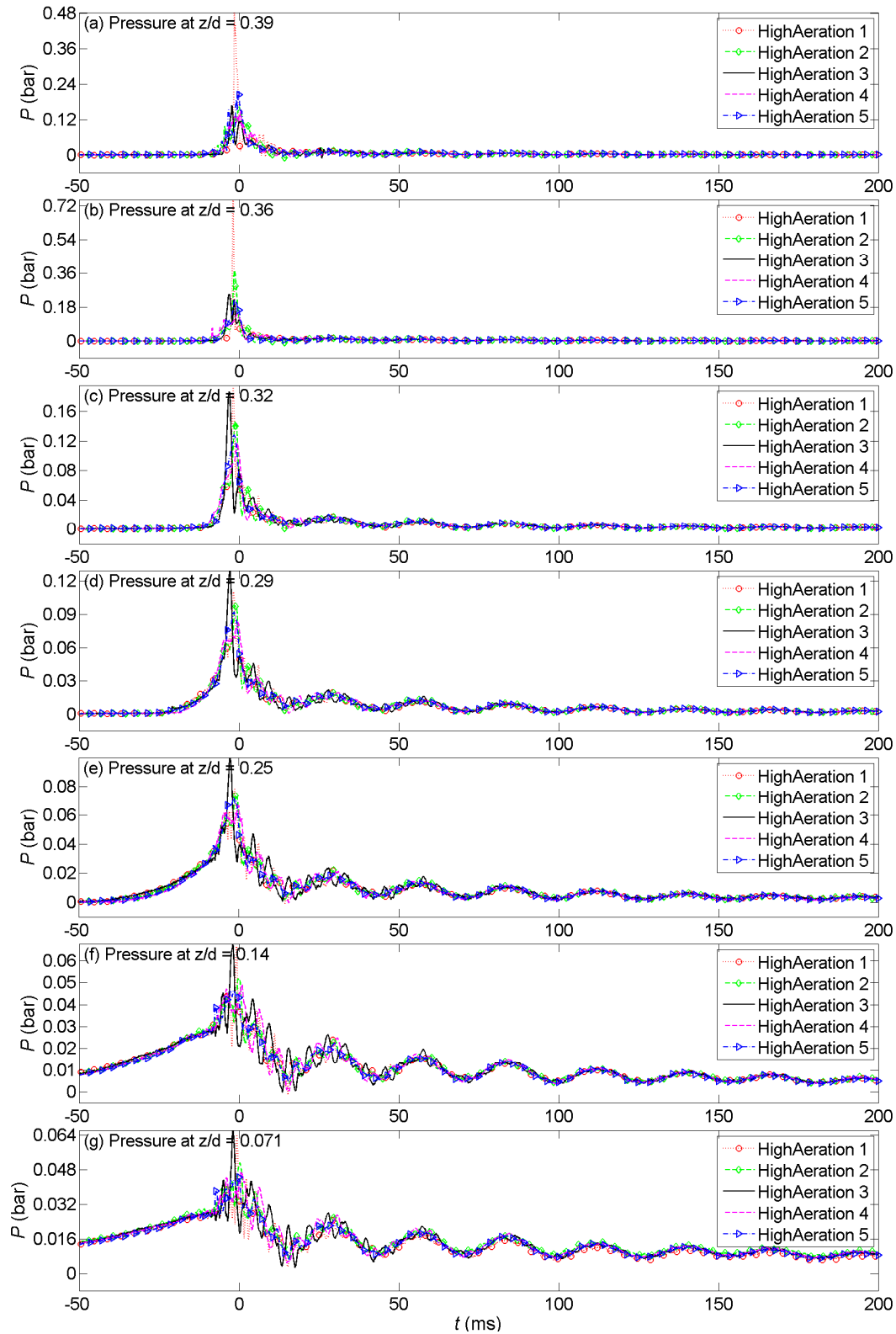
Figure B-8: Repeatability of pressure traces on rigid wall under high aeration wave impact in pure water (d = 0.7 m).
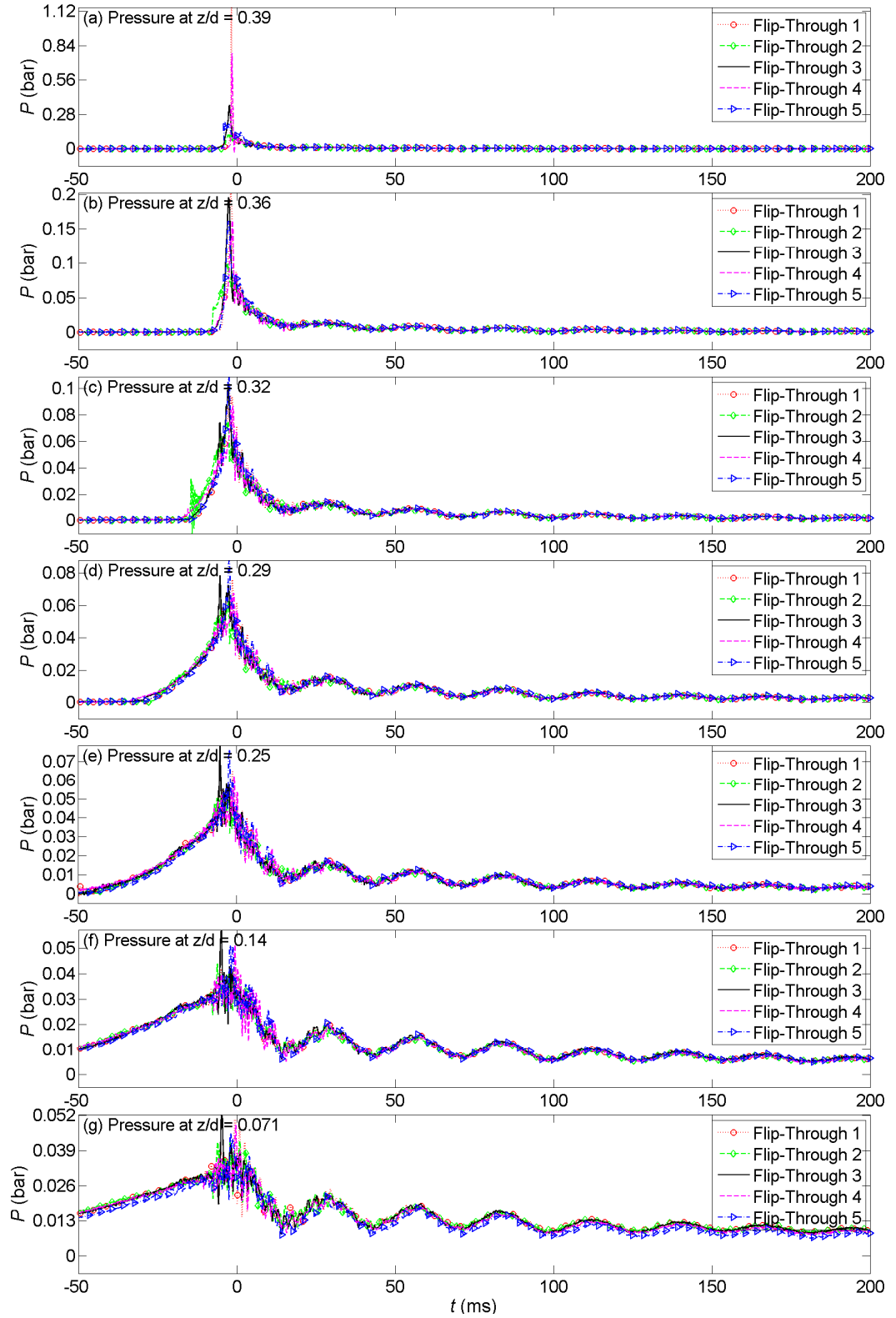
Figure B-9: Repeatability of pressure traces on rigid wall under flip-through wave impact in pure water (d = 0.7 m).
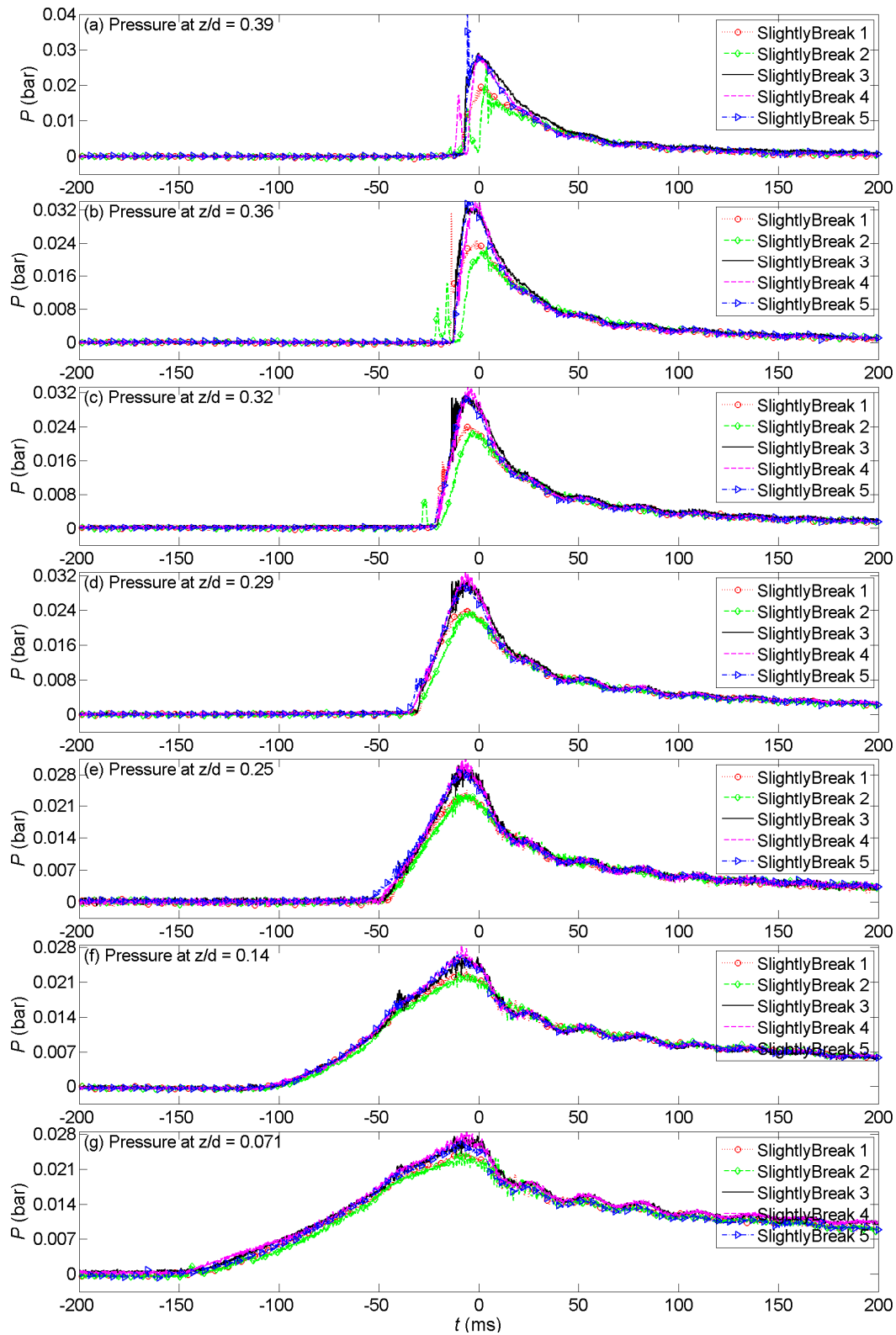
Figure B-10: Repeatability of pressure traces on rigid wall under slightly breaking wave impact in pure water (d = 0.7 m).

B.2   Repeatability of wave impacts in aerated water

Figure B-11: Repeatability of acceleration and force traces on rigid wall under broken wave impact in aerated water ($d = 0.625$ m).
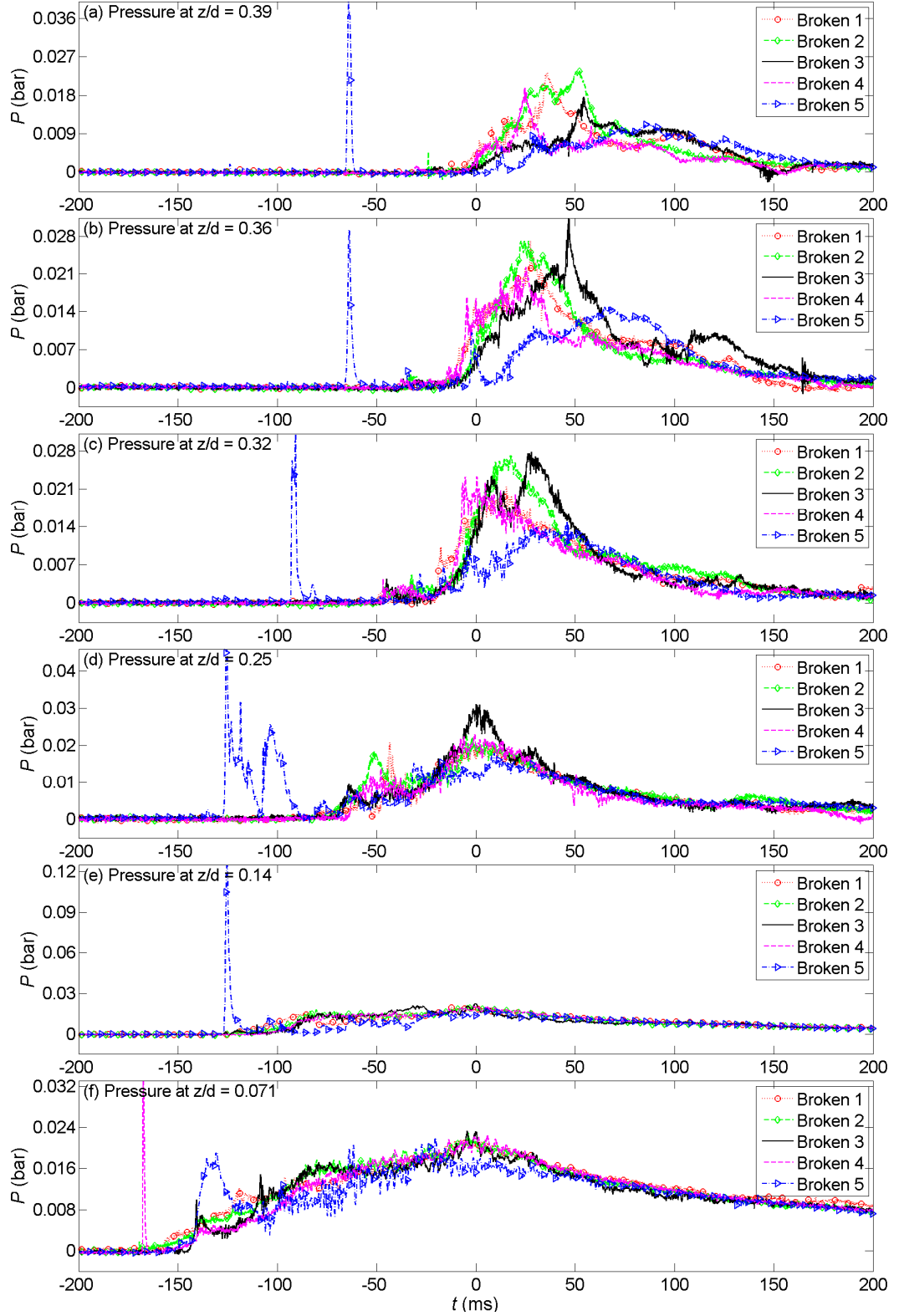

Figure B-12: Repeatability of acceleration and force traces on rigid wall under high aeration wave impact in aerated water ($d = 0.625$ m).

Figure B-13: Repeatability of acceleration and force traces on rigid wall under flip-through wave impact in aerated water (d = 0.625 m).

Figure B-14: Repeatability of acceleration and force traces on rigid wall under slightly breaking wave impact in aerated water (d = 0.625 m).

Figure B-15: Repeatability of pressure traces on rigid wall under broken wave impact in aerated water (*d* = 0.625 m).
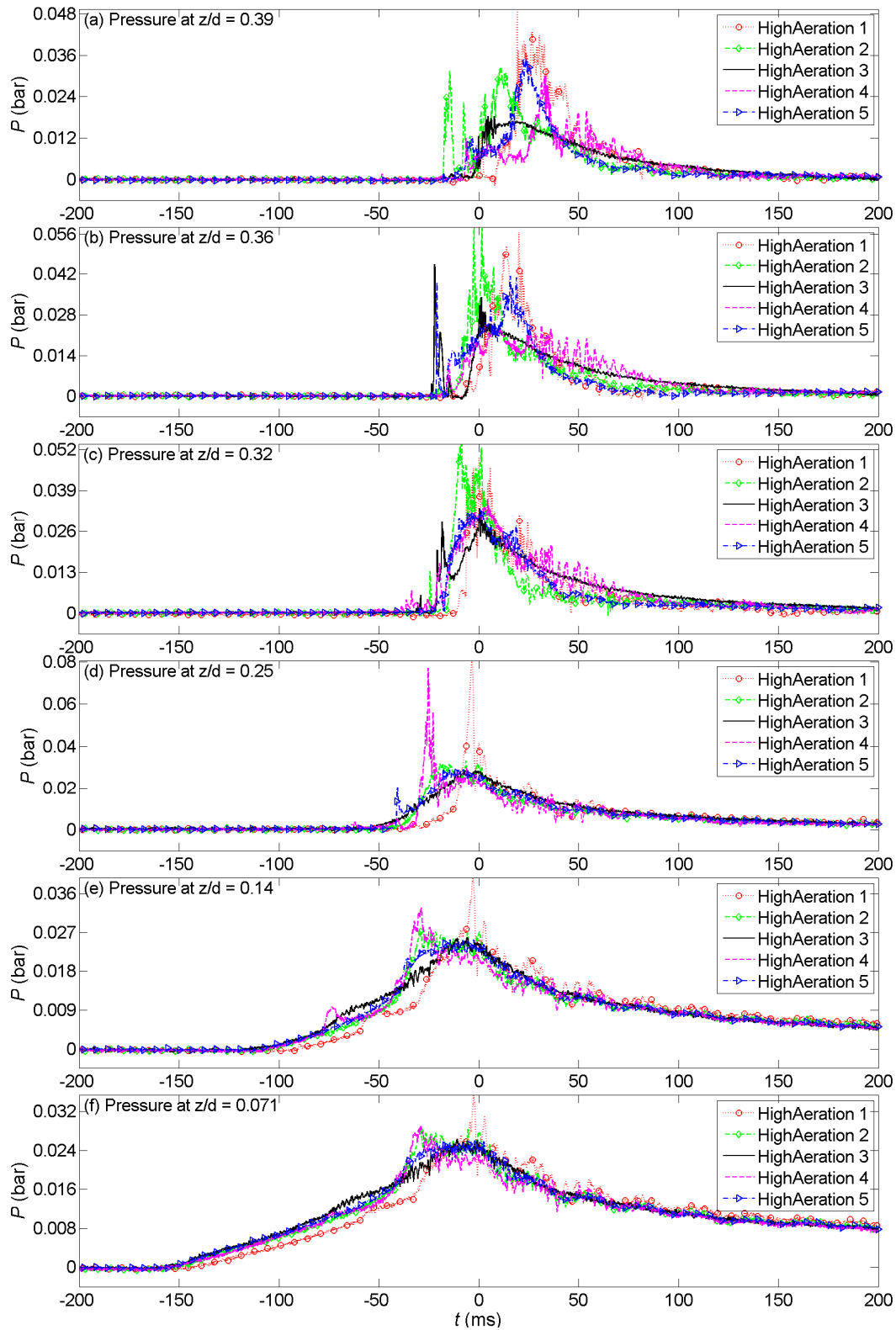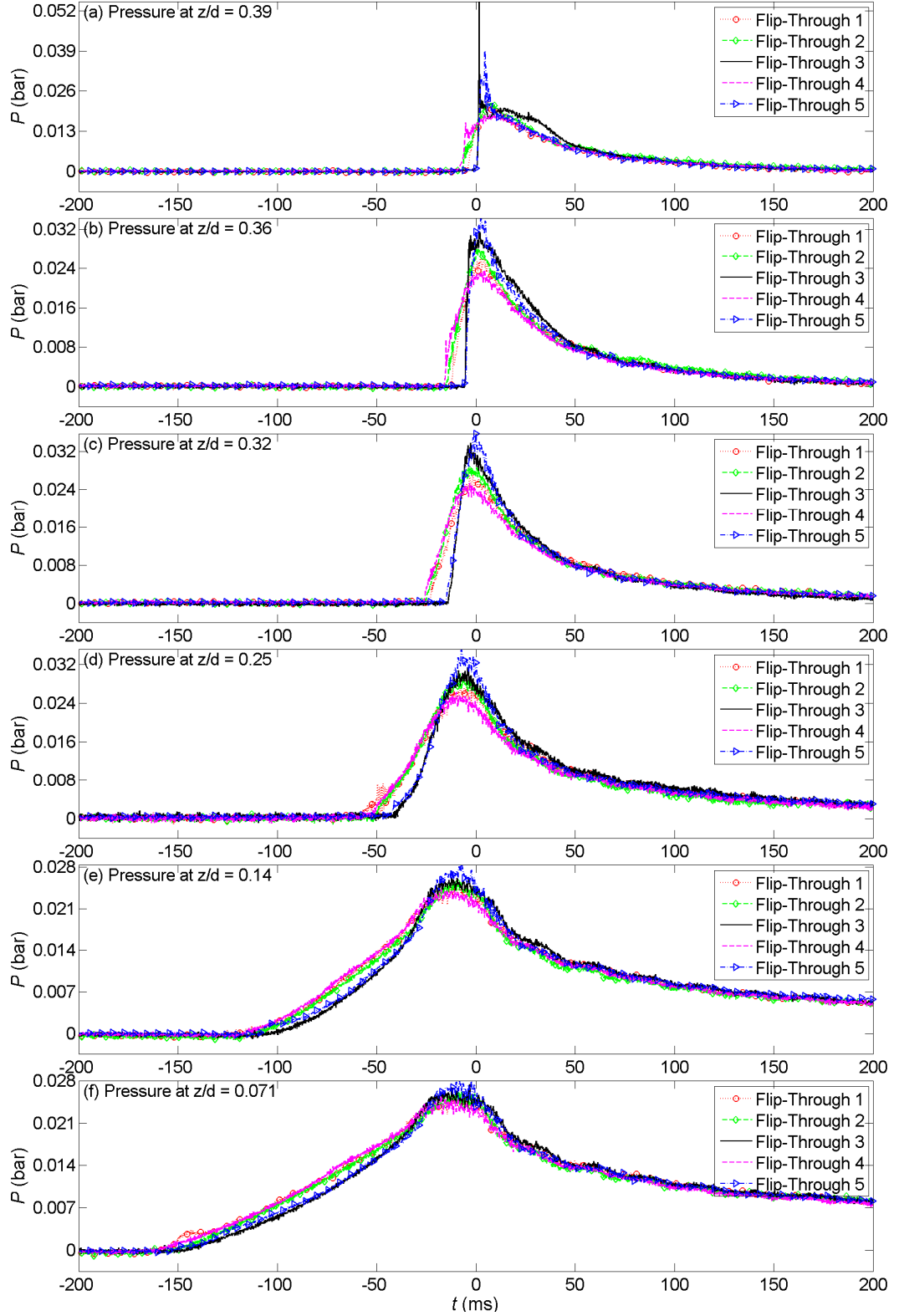
Figure B-16: Repeatability of pressure traces on rigid wall under high aeration wave impact in aerated water (d = 0.625 m).

Figure B-17: Repeatability of pressure traces on rigid wall under flip-through wave impact in aerated water (d = 0.625 m).
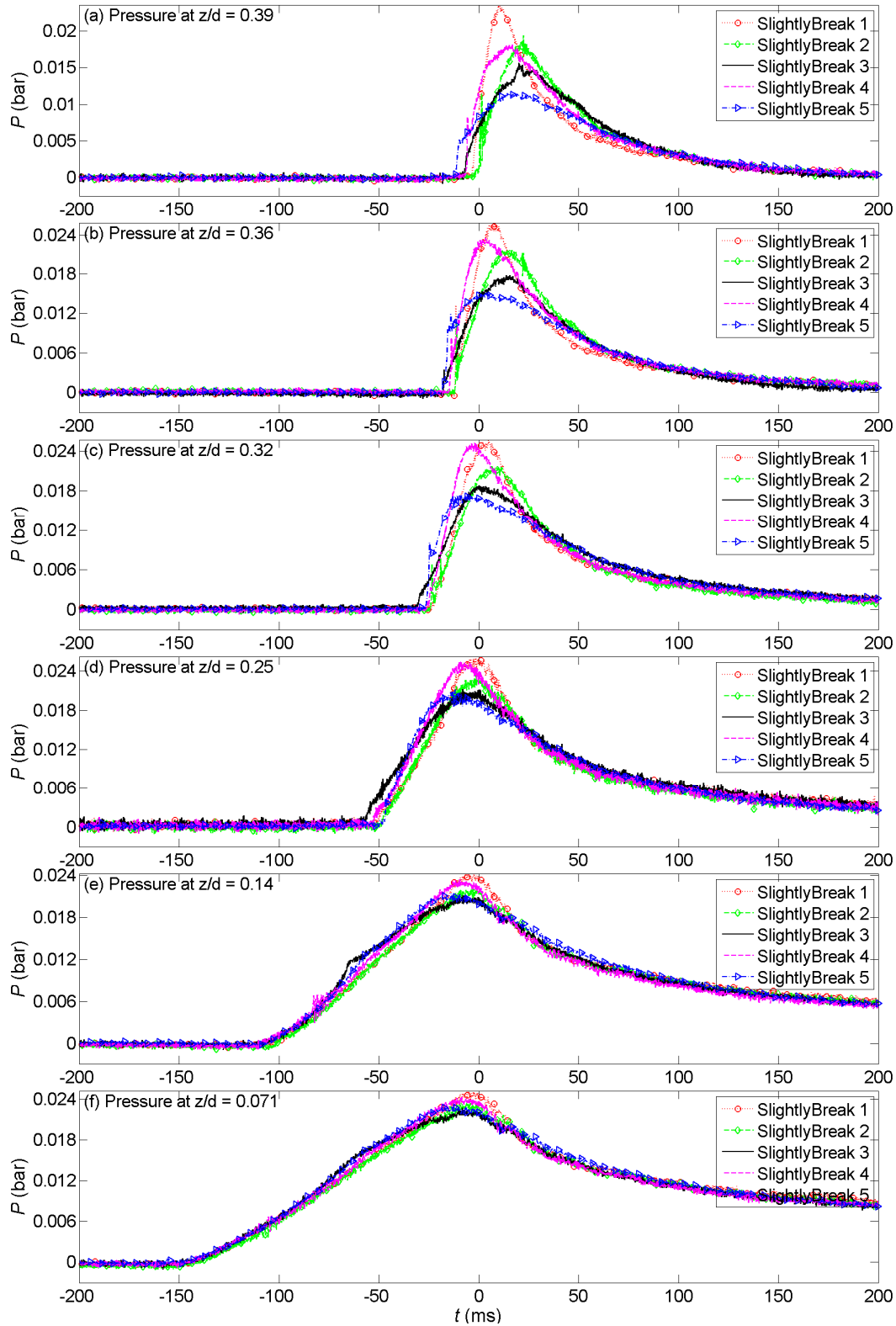
Figure B-18: Repeatability of pressure traces on rigid wall under slightly breaking wave impact in aerated water (d = 0.625 m).

APPENDIX C: PROBABILITY OF NON-EXCEEDANCE OF WAVE IMPACT PRESSURES IN AERATED WATER (D = 0.625 M)
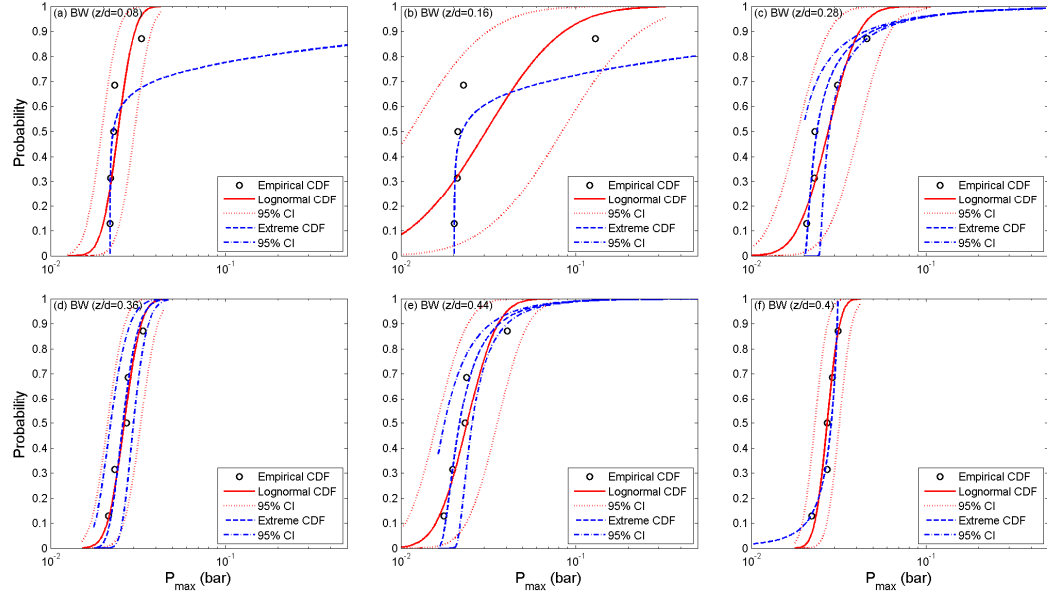

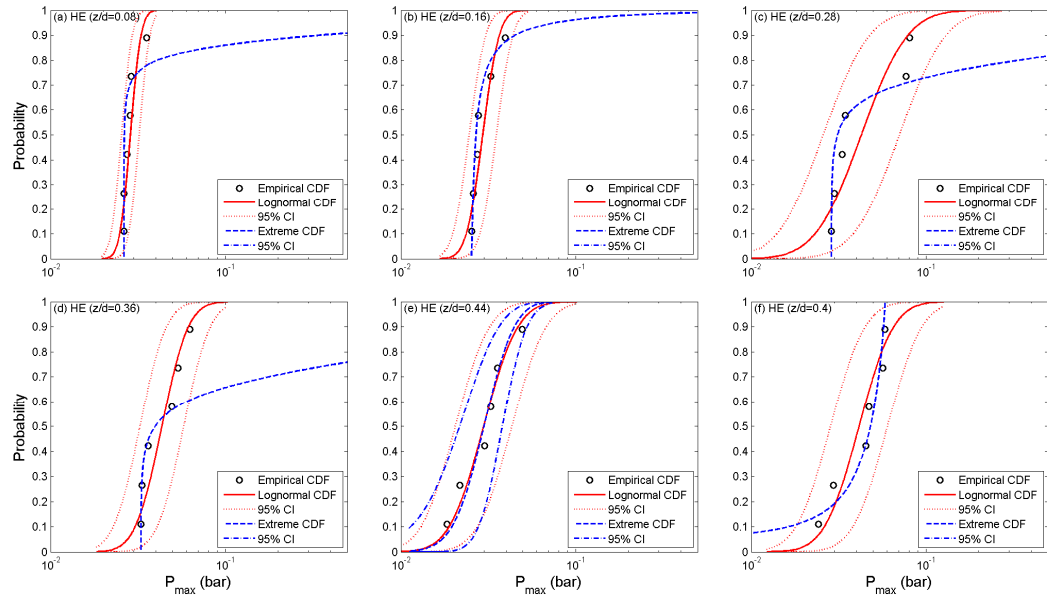Figure C-1. CDF of P_{max} on the rigid wall due to broken wave impact in aerated water (β = 0.6 %).

Figure C-2. CDF of P_{max} on the rigid wall due to high-aeration wave impact in aerated water (β = 0.6 %).
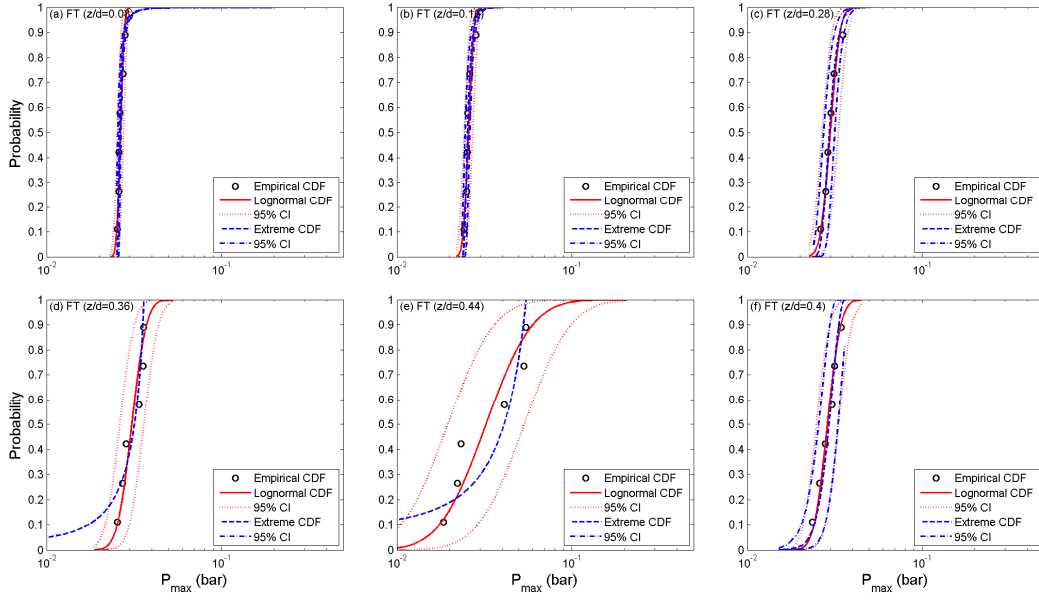
Figure C-3. CDF of P_{max} on the rigid wall due to flip-through wave impact in aerated water (β = 0.6 %).
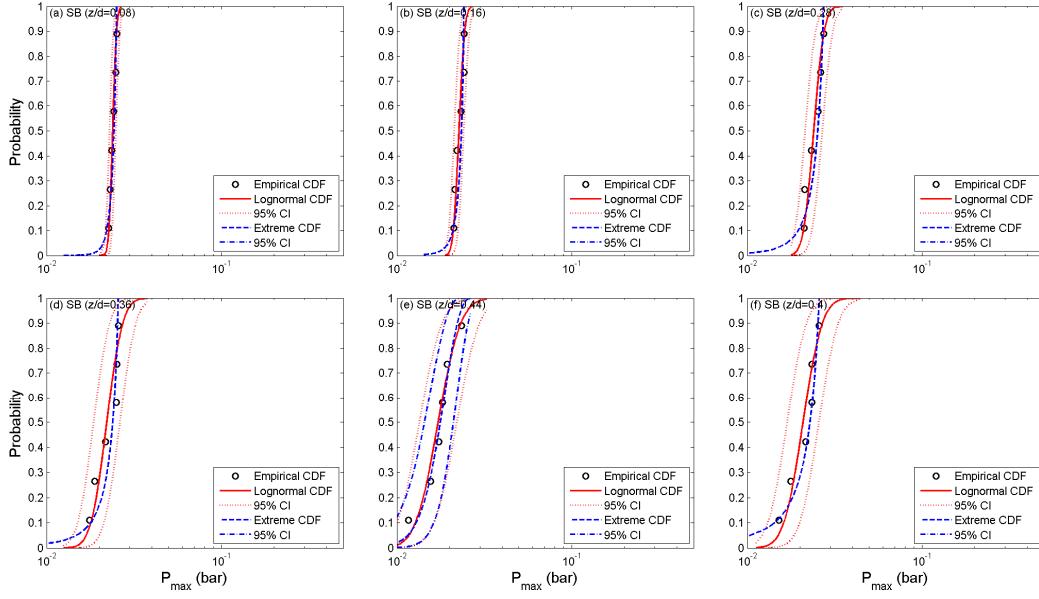

Figure C-4. CDF of P_{max} on the rigid wall due to slightly breaking wave impact in aerated water (β = 0.6 %).